Momentum correlations in strongly-depleted 4He* Bose-Einstein condensates

Gaétan Hercé

université PARIS-SACLAY

Momentum correlations in strongly-depleted ^{4}He* Bose-Einstein condensates

Corrélations en impulsion dans des condensats de Bose-Einstein de $^4He^*$ fortement déplétés

Thèse de doctorat de l'université Paris-Saclay

École doctorale n° 527 Ondes et Matière (EDOM)
Spécialité de doctorat: Physique
Graduate School : Physique, Référent : Institut d'Optique

Thèse préparée dans l'unité de recherche **Université Paris-Saclay, Institut d'Optique, CNRS, Laboratoire Charles Fabry, 91127 Palaiseau France** sous la direction de **David CLÉMENT**, Maîtres de conférences.

Thèse soutenue à Paris-Saclay, le 17 janvier 2023, par

Gaétan HERCÉ

Composition du jury

Membres du jury avec voix délibérative

Alice SINATRA Professeure des universités, Université de la Sorbonne	Présidente & Examinatrice
Sylvain NASCIMBENE Maître de conférences, École Normale Supérieure Paris	Rapporteur & Examinateur
Bruno LABURTHE-TOLRA Directeur de recherche, Université Sorbonne Paris Nord	Rapporteur & Examinateur
Nicolas PAVLOFF Professeur des universités, Université Paris-Saclay	Examinateur
Lauriane CHOMAZ Tenure-Track Professor, Université de Heidelberg	Examinatrice

Membres du jury sans voix délibérative

Quentin GLORIEUX Maître de conférences, Université de la Sorbonne	Membre invité
David CLÉMENT Maître de conférences, Université Paris-Saclay	Directeur de thèse

THESE DE DOCTORAT
NNT : 2023UPASP001

université PARIS-SACLAY | ÉCOLE DOCTORALE Ondes et matière (EDOM)

Titre: Corrélations en impulsion dans des condensats de Bose-Einstein de $^4He^*$ fortement déplétés

Mots clés: Gaz quantiques, Problème à N corps, Détection d'atomes uniques, Réseau optique, Corrélations en impulsion, Condensats de Bose-Einstein fortement déplétés

Résumé: Ce manuscrit est centré sur l'étude de systèmes quantiques à N corps, des gaz quantiques d'atomes d'hélium 4 métastable, dans le régime de fortes interactions. Ce régime est atteint dans un réseau optique 3D où les atomes simulent l'hamiltonien de Bose-Hubbard. En augmentant la profondeur du réseau, le système subit une transition de phase induite par les interactions entre un superfluide et un isolant de Mott. La détection d'atomes uniques d'hélium métastable dans l'espace des impulsions nous permet de caractériser le système par le biais des corrélations en impulsion entre atomes.

À impulsions proches, ces corrélations identifient les états quantiques, des superfluides et des isolants de Mott, via leur cohérence à N corps. L'extension de ces corrélations jusqu'au sixième ordre met en évidence la contribution de la déplétion aux propriétés statistiques du condensat. À impulsions opposées, les corrélations entre atomes révèlent la présence du mécanisme d'appariement de Bogoliubov au sein de la déplétion quantique de condensats de Bose-Einstein à l'équilibre et dans le régime de faibles interactions. Plusieurs signatures de l'origine quantique de ces paires d'atomes confirment cette prédiction vieille de 70 ans.

L'augmentation du potentiel du réseau dans le régime superfluide nous permet d'étendre ces mesures au cas des condensats de Bose-Einstein fortement déplétés. À impulsion nulle, le régime de fortes interactions est caractérisé par des déviations plus importantes de la cohérence à N corps du condensat comparé à la prédiction pour un état cohérent. D'autre part, la suppression du signal des paires de Bogoliubov bien avant la transition de Mott reflète la non-validité de cette prédiction aux plus fortes interactions. Cela suggère également la présence de triplets d'atomes corrélés en impulsion, que nous n'avons pas encore pu observer.

Dans ce manuscrit, la région critique de la transition de Mott est explorée à l'aide de mesures 3D de la densité en impulsion résolues à l'échelle de l'atome unique. Cette observable contient des signatures de la criticalité de la transition au-delà du champ moyen. La capacité à capturer la physique particulière du système près de la transition est prometteuse pour étendre les mesures de corrélation à ce régime, où des corrélations non triviales pourraient signaler que le système devient fortement corrélé.

Title: Momentum correlations in strongly-depleted $^4He^*$ Bose-Einstein condensates

Keywords: Quantum gases, Many-body problem, Single-atom detection, Optical lattice, Momentum correlations, Strongly-depleted Bose-Einstein condensates

Abstract: This manuscript focuses on studying quantum many-body systems, quantum gases of metastable Helium-4 atoms, in the strongly-interacting regime. This regime is reached in a 3D optical lattice where atoms simulate the Bose-Hubbard Hamiltonian. Increasing the lattice depth, the atomic cloud undergoes an interactions-induced transition from a superfluid to a Mott insulating phase. The single-atom detection of metastable Helium atoms in momentum space allows us to characterize the many-body system through the atom momentum correlations.

At close-by momenta, these correlations identify quantum states, Bose superfluids and Mott insulators, via their many-body coherence. Extending these correlations up to the sixth order highlights the depletion's contribution to the condensate's statistical properties. At opposite momenta, atom correlations reveal the presence of Bogoliubov's pairing mechanism in the quantum depletion of weakly-interacting Bose-Einstein condensates at equilibrium. Several signatures of the quantum origin of these atom pairs confirm this 70-year-long prediction.

Ramping up the lattice potential in the superfluid regime allows us to extend these measurements to the case of strongly-depleted Bose-Einstein condensates. At zero momenta, the strongly-interacting regime is characterized by larger deviations from the many-body coherence of the condensate compared to the prediction for a coherent state. On the other hand, the suppression of the Bogoliubov paring signal well before the Mott transition reflects the breaking of this approximation's validity at stronger interactions. It also suggests the presence of momentum-correlated triplets of atoms, which we have yet to be able to observe.

In this manuscript, the critical region of the Mott transition is explored using single-atom resolved 3D measurements of the momentum density. This observable contains signatures of the criticality of the transition beyond the mean-field level. The ability to capture the particular physics of the system near the transition holds promise for extending correlation measurements to this regime, where non-trivial correlations may signal that the system is becoming strongly correlated.

Remerciements

Ce manuscrit est le fruit d'un peu plus de trois années de thèse à l'Institut d'Optique dans le groupe gaz quantique, sous la supervision de David Clément. J'ai eu la chance au cours de cette période d'évoluer dans une atmosphère chaleureuse, amicale, et bienveillante, dont j'aimerais ici remercier les principaux acteurs. Ces remerciements s'adressent bien évidemment en premier lieu à David Clément. Merci à toi de m'avoir pris sous ton aile durant cette thèse, après m'avoir donné durant le M2 Laser Optique Matière un premier avant-goût de l'interaction lumière-matière. Pour être honnête, mes souvenirs de ce cours sont diffus car, comme tu l'auras sûrement remarqué après ces trois années, j'ai une mémoire capricieuse. Ce dont je me souviens, c'est l'impression d'avoir eu pour professeur quelqu'un d'investi et patient, désireux de transmettre ses connaissances à ses étudiants. Plus que le contenu du cours en lui-même, je pense que c'est cela qui m'a poussé à vouloir faire une thèse avec toi. Trois ans et demi plus tard, je ne regrette pas ce choix, et l'impression que j'avais au master reste intacte. Merci donc pour tout ce que tu m'as transmis : les connaissances théoriques, le savoir-faire expérimental, la méthode de travail, et la curiosité intellectuelle. J'ai hâte de continuer à développer tout cela dans la suite de ma carrière professionnelle. Merci également pour ton exigence et ton souhait que les doctorants s'approprient leur sujet d'étude. Ces deux aspects m'ont fait gagner en autonomie et ont été une motivation certaine. Je finirai par te remercier pour ta disponibilité et ton investissement pendant toute la durée de cette thèse, notamment lorsqu'il a fallu corriger ce manuscrit. Je sais bien que cela fait partie de ton rôle d'encadrant, mais j'ai connu suffisamment de doctorants moins bien lotis pour réaliser la chance que j'ai eu.

Il va de soi que le contenu de ce manuscrit n'est pas le résultat de ma seule contribution. Aussi, j'aimerais remercier tous mes collègues de l'équipe « Helium-Lattice » que j'ai pu côtoyer durant cette thèse. Les thésards: Cécile, Antoine, JP, et Maxime. Les post-docs: Alexandre et Raphaël. Les étudiants en stage: Chao, Antoine et Tangy. Sans oublier Tommaso Roscilde de l'ENS Lyon. La plupart de ces personnes ont contribué de façon plus ou moins directe au contenu de ce manuscrit, et toutes ont participé à la bonne ambiance au sein de l'équipe. Je tiens à remercier tout particulièrement Antoine et JP avec qui nous avons formé pendant longtemps l'équipe HBT (Hercé-Bureik-Ténart). Cela a été un réel plaisir d'apprendre à utiliser l'expérience avec toi, Antoine, et je garderai

longtemps en mémoire nos longues heures de débogage et d'alignement des réseaux à nous relayer sur Spotify pour le choix des musiques. Je devrais d'ailleurs en toute rigueur remercier La Femme, Maître Gims (Indochine ?) et bien d'autres... Merci également à toi JP pour ces années passées ensemble, pour tout ce que tu as mis en place sur l'expérience et tout ce que tu as organisé pour moi le jour de ma soutenance. Je garderai là aussi longtemps ton superbe chapeau !

Bien entendu, je voudrais également remercier l'intégralité des membres du groupe Gaz Quantiques. À la fois les membres permanents pour leur bienveillance et conseils durant ma thèse, ainsi que tous les doctorants que j'ai pu côtoyer durant ces trois ans et demi. Je ne prendrai pas le risque de les citer, par peur d'en oublier. Ils se reconnaîtront. Merci également au reste des membres du Laboratoire Charles Fabry. À son directeur, Patrick Georges, pour son investissement auprès des doctorants. À Hélène, pour sa bonne humeur et son franc-parler du temps où elle animait la cafétéria de l'Institut. À l'équipe enseignante du LEnsE (Fabienne, Lionel, Cédric, Thierry) pour m'avoir permis d'enseigner à l'Institut durant ma thèse. Cela aura été une expérience à la fois enrichissante et gratifiante. C'est d'ailleurs dans le calme d'une salle de classe de l'Institut, où j'ai été tantôt élève tantôt enseignant, que je me suis installé pour rédiger ces remerciements. La nostalgie sûrement.

Le mot de la fin sera bien sûr pour mes amis et mes proches. Un grand merci aux amis du M2 LOM (Lionel, Christian, Yohann, Lucas, Elise) parce que l'on a tous été dans le même bateau, et bon courage aux retardataires pour leur fin de thèse. Merci également à Laura qui venait périodiquement nous apporter sa bonne humeur à l'Institut. Evidemment, il y a une mention spéciale pour Lionel et Christian, avec qui nous avons formé la coloc « Le Trépied » pendant ces trois années. Faire cette coloc aura sûrement été la deuxième meilleure décision de mon année de M2, après le choix de la thèse, pour tout un tas de raisons (Monopoly Deal, study group, mama kitchen, le népotisme, la conquête de Mars...) sans oublier cette expérience particulière qu'est le confinement pour cause de crise sanitaire internationale. Je remercie aussi les amis de fac et ceux de longue date. Enfin, bien évidemment, je remercie ma famille et Alice parce qu'il n'y a pas que la thèse dans une vie de thésard et que cela fait du bien de s'en rappeler, notamment à l'approche de la fin.

Résumé en français

Ce manuscrit traite de l'étude expérimentale de condensats de Bose-Einstein (BEC) à fortes interactions au travers des moments et corrélations d'ordre supérieur dans l'espace des impulsions. Nous accédons à ces quantités en exploitant la détection électronique d'atomes individuels d'hélium-4 métastables (^{4}He*) à l'aide de galettes à microcanaux après une longue expansion en chute libre. Cette méthode de détection nous permet également d'obtenir les distributions en impulsion à 3D, avec une résolution et une gamme dynamique inégalées.

Cette gamme dynamique sur la mesure des densités en impulsion à 3D s'est avérée essentielle, notamment pour la thermométrie de gaz de bosons sur réseaux de quelques milliers d'atomes développée en collaboration avec Tommaso Roscilde (ENS Lyon) et présentée dans le chapitre 2. Nous avons montré que cette thermométrie sature la limite théorique fixée par l'information de Fisher (associée à la comparaison de $\rho(\boldsymbol{k})$ avec des simulations ab-initio QMC). Plus important encore, cette thermométrie nous a permis de démontrer l'adiabaticité du chargement des réseaux optiques, et donc la préparation d'états stationnaires du modèle de Bose-Hubbard. En particulier, le protocole de chargement ne souffre pas du spectre d'excitation continu dans le régime superfluide ni du voisinage du point critique quantique proche de la transition. Du point de vue de la simulation quantique, ces résultats confirment la capacité des plateformes d'atomes froids à préparer des états quantiques fortement corrélés de faible entropie (en l'absence de réservoir pour fixer la température).

Cette certification a jeté les bases de l'étude de la région critique de la transition de Mott à faible entropie. La suppression de $\rho(\boldsymbol{k} = \boldsymbol{0})$ en augmentant la profondeur du réseau conduit à un paramètre d'interaction critique compatible avec celui prédit par les simulations QMC pour le système homogène à remplissage unitaire et à la température de l'expérience, plutôt qu'avec celui d'une prédiction de type champ moyen à $T = 0$. En outre, la suppression de $\rho(\boldsymbol{k} = \boldsymbol{0})$ est compatible avec une variation critique dont l'exposant serait celui attendu pour le modèle $3DXY$, une propriété confirmée par les données QMC. Ces résultats diffèrent de plusieurs études expérimentales précédentes sur la région critique de la transition de Mott, une spécificité qui résulte de notre accès unique à $\rho(\boldsymbol{k} = \boldsymbol{0})$ et d'un choix judicieux du nombre d'atome dans les condensats pour obtenir

un remplissage unitaire du réseau.

Dans le chapitre 3, nous profitons d'une amélioration de notre efficacité de détection pour étudier la statistique de comptage complète (FCS) et les moments d'ordre élevé (jusqu'à $n = 6$) de l'occupation des modes en impulsion dans des gaz de Bose superfluides et des isolants de Mott détectés en champ lointain. Les statistiques de comptage mesurées sont cohérentes avec celles attendues pour une description en termes d'états purs, à savoir une distribution de Poisson pour le condensat et une distribution thermique pour l'isolant de Mott. Ces résultats sont corroborés par la cohérence multi-corps dans ces systèmes, quantifiée par l'amplitude normalisée $g^{(n)}(0)$ des corrélations locales d'ordre n. Cette dernières est mesurée avec un contraste parfait via une approche originale basée sur les moments factoriels. Concernant le mode du condensat en $\boldsymbol{k} = \mathbf{0}$ de gaz de Bose superfluides, nous observons de légères déviations $\left(g^{(n)}(0) > 1\right)$ à la cohérence multi-corps parfaite $g^{(n)}(0) = 1$ prédite par Glauber pour un état cohérent. Nous introduisons un modèle heuristique pour expliquer ces déviations, puisque les calculs ab-initio des corrélations à plusieurs particules ne sont pas réalisables dans le régime de fortes interactions de notre expérience. Malgré sa simplicité, notre modèle capture quantitativement les déviations $g^{(n)}(0) > 1$ observées expérimentalement et les attribue à la fraction d'atomes déplétés. Le modèle explique également pourquoi le rôle de la déplétion n'a pu être observé lors d'une étude précédente [1]. Ayant identifié la cause des déviations, nos mesures confirment la nature cohérente des condensats produits dans les expériences jusqu'au sixième ordre des corrélations au moins. Atteindre ce niveau de certification est d'une importance primordiale pour des investigations plus poussées de ces fluctuations dans le régime fortement corrélé près de la transition de Mott, où des signatures de non-Gaussianité, si elles sont présentes, apparaîtraient dans les fonctions de corrélation d'ordre élevé ($n \geq 3$).

Dans le chapitre 4, les corrélations à deux corps entre modes d'impulsion opposés $\boldsymbol{k}$ et $\boldsymbol{-k}$ révèlent des paires d'atomes (à impulsions opposées) dans la déplétion de gaz de Bose en interaction à l'équilibre. Cette observation confirme au niveau microscopique la prédiction faite par N. Bogoliubov il y a plus de 70 ans pour la déplétion quantique. La présence de ces paires dans l'état fondamental à N corps du système résulte des fluctuations quantiques induites par les interactions microscopiques entre particules à température nulle. Cette origine est confirmée par plusieurs observables: l'extrême sensibilité du signal aux effets de température finie, la variation de l'amplitude du signal analogue à celle mesurée pour des états comprimés à deux modes, la violation de l'inégalité de Cauchy-Schwartz, et la réduction des fluctuations relatives du nombre d'atome entre modes d'impulsion opposés. Ce signal d'appariement a pu être observé grâce à notre efficacité de détection améliorée et grâce aux réseaux optiques qui nous permettent d'atteindre le régime de basse température.

Ce dernier offre la possibilité de tester les prédiction de l'approche perturbative de Bogoliubov dans le régime fortement intéragissant en augmentant la profondeur des réseaux. La probabilité pour un atome déplété d'appartenir à une paire $\boldsymbol{k}/\boldsymbol{-k}$ présente une variations non-monotone avec la fraction condensée. Sa croissance initiale est compatible avec le régime de Bogoliubov, dans lequel des interactions plus fortes augmentent le nombre de paires dans la déplétion. Cependant, la suppression de l'amplitude du signal d'appariement à des fractions condensées plus petites (mais non-nulles) signale une rupture de la validité de cette approximation. Cette rupture apparaît pour des fractions condensées compatibles avec celles trouvées dans des systèmes homogènes [2]. Les premières recherches de triplets corrélés en impulsion dans la déplétion, qui résulteraient de processus d'interaction au-delà de la théorie de Bogoliubov, ont été infructueuses. Cette exploration a été jusqu'à présent

purement expérimentale puisque aucune prédiction théorique n'existe pour les corrélations entre particules dans notre système (même au second ordre), illustrant la complexité de la physique explorée par notre simulateur quantique.

Contents

Introduction

M. Plank's derivation of the black-body radiation formula in 1900 [3] and A. Einstein's understanding of the photoelectric effect in 1905 [4] both relied on the description of light fields in terms of discrete energy quanta. These were the first times that a corpuscular description of light was required to explain a physical effect, and marked the birth of Quantum Physics. In 1924, L. De Broglie theorized the concept of wave-particle duality [5] according to which any particle of mass m and velocity v behaves as a wave over the typical distance set by the De Broglie wavelength:

$$\lambda = \frac{h}{mv} \tag{1}$$

with h is the Planck constant. The experimental proof of the wave-particle duality was provided in 1927 by C. J. Davisson and L. H. Germer [6] who observed the diffraction of electrons by the atoms of Nickel crystals.

Reaching the quantum realm with cold atoms experiments

The averaged (or thermal) De Broglie wavelength generalizes the concept of wave-particle duality to ensembles of massive particles at thermal equilibrium at temperature T:

$$\lambda_{dB} = \frac{h}{\sqrt{2\pi m k_B T}} \tag{2}$$

with k_B the Boltzmann constant. The description of (possibly large) systems of particles requires the formalism of Quantum Physics as soon as the phase-space density, defined as $n\lambda_{dB}^3$ with n the system's density, is of the order of unity. Above this threshold, the system is said to be in the quantum degeneracy regime. In nature, this regime can be found for instance in the core of neutron stars, where the huge pressure increases the phase-space density up to $n\lambda_{dB}^3 \sim 10^5$ despite a temperature of $\sim 10^9$ K. Such pressures cannot be achieved in experiments. However, the advent of lasers and laser cooling techniques[1] made it possible for experimentalists to reduce the temperature of dilute atomic clouds

[1] See for instance the Nobel lectures of S. Chu [7], C. Cohen-Tannoudji [8], and W. Ketterle [9]

below the micro kelvin, hence the name "cold atoms" associated with this field of research. Combined with optical and magnetic trapping, the phase-space density of atomic clouds can be brought above the quantum degeneracy threshold. Degenerate quantum gases were first produced in 1995 with the realization of Bose-Einstein condensates (BECs) of Rubidium atoms in the group of C.E. Wieman and E.A. Cornel at JILA [10] and of Sodium atoms in the group of W. Ketterle at the MIT [11]. For these achievements, C.E. Wieman, E.A. Cornel, and W. Ketterle were awarded the Nobel Prize in Physics in 2001. These pioneering works opened the way towards investigations of quantum many-body systems with unrivaled level of control and a wealth of detection techniques.

Quantum simulation with quantum gases

Quantum many-body systems are systems made of interacting quantum particles, in which the interplay between quantum fluctuations and interactions gives rise to complex physics that cannot be captured by mean-field descriptions. Many-body correlations occurring at the vicinity of quantum phase transitions (such as the superfluid-to-Mott transition) or many-particle entanglement are examples of this peculiar physics. Exact descriptions of many-body systems are restricted to small ensembles of particles (a few dozen) since the Hilbert space grows exponentially with the number of degrees of freedom. Because of this limitation, the wave function of real-life many-body systems is unreachable to modern simulations with classical computers. In 1982 [12], R. Feynman proposed the alternative of using quantum systems, which inherently obey the laws of Quantum Mechanics, as quantum simulators of specific Hamiltonians. Today, the "Quantum Simulation" field of research envisioned by Feynman is flourishing as experimentalists successfully implemented various platforms for quantum simulation [13]. This manuscript focuses on quantum gases, but one can also cite trapped ions [14], arrays of Rydberg atoms [15], superconducting qubits [16], or polar molecules [17]. Since the first BECs, quantum gases have become central in the quantum simulation of interacting many-body systems. A reason for that comes from the possibility to set manually and precisely some microscopic parameters driving the physics of the system, such as the interactions between the particles (strength, sign, range), the dimensionality, or the energy landscape seen by the atoms (disorders, optical lattices, box traps). This versatility has permitted the implementation of numerous Hamiltonians with quantum gases [18].

An ideal testbed: the Bose-Hubbard model

The first Hamiltonian realized with quantum gases was the Bose-Hubbard Hamiltonian, which is one of the conceptually simplest Hamiltonians inspired by condensed-matter physics. It was first implemented with quantum gases loaded inside 3D optical lattices in the group of I. Bloch in 2002 [19], following the suggestion of D. Jaksch *et al.* [20]. This Hamiltonian describes the behavior of bosons inside a periodic potential. Physics is set by two energy scales U and J, associated respectively with on-site interactions and tunnelling (see Figure 1). Despite its apparent simplicity, the $T = 0$ phase diagram of this Hamiltonian contains a quantum phase transition resulting from the competition between the tunnelling effect, which favors a disordered (superfluid) phase, and repulsive interactions, which favors an ordered (Mott Insulator) phase. This transition was first observed in [19], by driving the depth of the optical lattice. The Bose-Hubbard model is an ideal test bed for the quantum simulation of many-body systems where interactions

play a central role. It has been studied in detail over the last twenty years but still contains unanswered questions, especially concerning the quantum critical point of the transition. This Hamiltonian is one of our team's main objects of study, and the second chapter of this manuscript is directly related to its investigation.

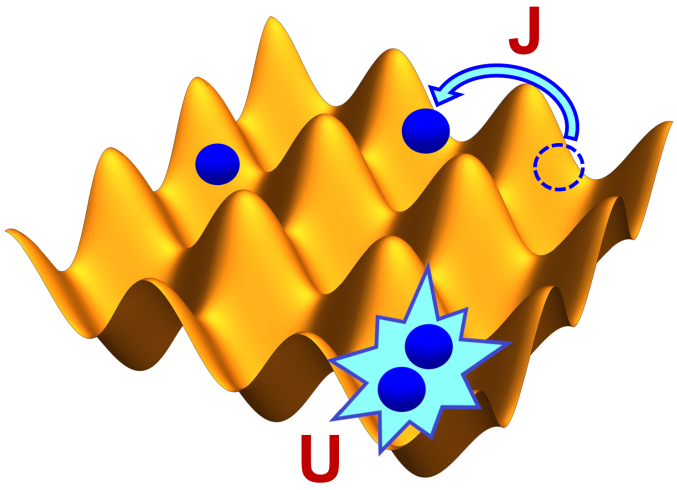

Figure 1: **Schematics representation of atoms in a 2D optical lattice.** The periodic potential confines the atoms on the lattice sites. The possible microscopic processes are tunnelling from one site to another or repulsive interactions between atoms at the same site. The energy costs of these processes are, respectively, the parameters J and U of the Bose-Hubbard Hamiltonian.

Detection techniques with cold atoms

A complete understanding of quantum many-body systems requires keeping track of the correlations between individual degrees of freedom (positions, momenta, spins) of the elementary constituents (atoms, ions, molecules). These correlations are only accessed via measurements of the full particle distribution in the degree of freedom considered, and require local probes able to resolve the particles individually.

Cold atoms platforms benefit from a vast panel of optical imaging techniques which can be destructive (fluorescence and absorption imaging) or non-destructive (phase contrast imaging). In their simplest implementation, these techniques are global probes of the system sensitive to the atomic density rather than individual atoms. However, several single-particle resolved probes have been developed on cold atoms platforms [21]. On the one hand, fluorescence imaging has been upgraded to collect the photons emitted by single emitters, the latter being either ions in magnetic traps [22], Rydberg atoms in optical tweezers [23], or neutral atoms in 2D optical lattices [24]. These measurements access the in-situ positions of the particles, but single-atom sensitivity with fluorescence imaging has also been demonstrated in time-of-flight images [25]. On the other hand, non-optical techniques can also provide single-atom resolved detection. These techniques rely, for instance, on high-finesse optical cavities to which individual atoms can couple [26], on ionization of particle and detection of the resulting ions [27], or on multi-channel plates that detect metastable noble gas atoms [28]. Our experiment belongs to this last category.

Electronic detection of metastable Helium atoms

Helium being a noble gas, the metastable state (in which condensation is reached) has a ~ 20 eV internal energy exceeding by far that of any other atomic specie brought to degeneracy. Thanks to this specificity, metastable Helium benefits from an alternative detection technique to optical imaging. This technique, commonly found in high-energy physics, relies on Micro-Channel Plates (MCPs) to detect electronically individual metastable Helium (^{4}He*) atoms after a time-of-flight (TOF). With the conditions (verified experimentally) that the cloud undergoes a free fall and is probed in the far-field regime of expansion, the spatial coordinates $\boldsymbol{r}$ of each atom yield the in-trap momentum coordinates $\boldsymbol{k}$ via the ballistic relationship:

$$\hbar \boldsymbol{k} = \frac{m\boldsymbol{r}}{t_{\mathrm{TOF}}} \tag{3}$$

with $t_{\mathrm{TOF}} = 297$ ms the TOF duration. Therefore, working with ^{4}He* atoms provides unique access to a singular quantity in cold atoms experiments: the 3D *distribution* of the momentum occupation number. Averaging experimental realizations of such distributions yields the 3D momentum density $\rho(\boldsymbol{k}) = \langle \hat{a}^\dagger(\boldsymbol{k})\hat{a}(\boldsymbol{k})\rangle$ with unmatched resolution and dynamical range due to the single-atom resolved detection after a long TOF. But most importantly, momentum distributions provide the moments of the momentum occupation number beyond the mean and variance, and enable the computation of momentum correlations between individual atoms. These quantities are crucial to investigate many-body systems, as they should contain signatures of the strongly-correlated regime.

Outline of the manuscript

The manuscript is organized into four chapters:

- Chapter 1 presents the experimental apparatus producing ^{4}He* BECs, whose cycle duration was improved from 6.8 s to 4 s during the course of this thesis. The electronic detection of individual ^{4}He* atoms in the far-field regime of expansion from an optical lattice is also detailed. Finally, special emphasis is placed on the experimental calibration of the MCPs' detection efficiency ($\eta_{\mathrm{MCP}} = 53(2)\%$) and on a two-photon Raman transfer that was implemented to multiply by a factor of two the statistics on the momentum distributions.

The following three chapters illustrate the formidable capacity of combining 3D optical lattices with the electronic detection of individual ^{4}He* atoms in the momentum space:

- Chapter 2 presents a thorough investigation of the average momentum occupation number $\rho(\boldsymbol{k}) = \langle \hat{a}^\dagger(\boldsymbol{k})\hat{a}(\boldsymbol{k})\rangle$ across the superfluid-to-Mott transition. More specifically, this study relies on the 3D momentum densities to certify the adiabatic preparation of equilibrium states of the Bose-Hubbard model [29], and on the peak momentum density $\rho(\boldsymbol{k} = \boldsymbol{0})$ to locate the transition and reveal the critical scaling [30].
- Chapter 3 reports the Full Counting Statistics and high-order moments (up to $n = 6$) of the momentum occupation number for two iconic states of the Bose-Hubbard model: Bose superfluids and Mott insulators [31]. These measurements provide an unprecedented characterization of these strongly-interacting systems via their many-body coherence.

- Finally, Chapter 4 presents the observation of the $\boldsymbol{k}$/-$\boldsymbol{k}$ pairs in the depletion of interacting Bose gases [32]. This signal, predicted by N. Bogoliubov more than 70 years ago [33], is revealed by the correlations at opposite momenta contained within the momentum distributions of lattice bosons. These atom pairs at opposite momenta, together with more complex correlated clusters, are then investigated in stronger interaction regimes for which Bogoliubov's approximation is expected to fail.

Chapter 1

1. Experimental setup

Helium was first brought to degeneracy in 2001 in the groups of A. Aspect [34] and C. Cohen-Tannoudji [35]. These experiments were performed with bosonic Helium-4 atoms, and a similar achievement was later performed in 2006 with Helium-3, a fermionic isotope, in the group of W. Vassen [36]. Nowadays, only a few experiments are working with Helium-4 in the world: one in Amsterdam led by K. Eikema [37], one in Canberra led by A. Truscott [38], one in Vienna led by A. Zeilinger [39], and two here in Palaiseau, ours led by D. Clément and the original one led by D. Boiron, C. Westbrook, and A. Aspect [40]. This small number of experiments results probably from the technical difficulties associated with cooling metastable Helium gases to quantum degeneracy. A first difficulty is that Helium-4 can only be laser-cooled in its metastable $2\,^3S_1$ state, noted $^4He^*$, from which transitions to the $2\,^3P_{0,1,2}$ states can be addressed with commercial lasers operating at 1083 nm. Therefore, the first step for any Helium-4 experiment is to produce $^4He^*$ atoms starting from the ground state, which necessitates implementing a plasma discharge. Another difficulty comes from the low atomic mass of Helium atoms, which requires pre-cooling the source with liquid nitrogen and a long Zeeman slower to decrease the atoms' velocity within the capture range of a Magneto-Optical Trap (MOT). Finally, the huge internal energy of the metastable state, 19.8 eV, drastically increases the rate of light-assisted Penning collisions [41, 42]. During this interaction process, one atom falls back into the ground state while the other is ionized, resulting in a loss of two metastable atoms:

$$He^* + He^* \rightarrow He + He^+ + e^- \tag{1.1}$$

Fortunately, Penning collisions can be suppressed by working with spin-polarized gases for which the collision rate is reduced by four orders of magnitude for Helium [43]. Nevertheless, these collisions limit the maximum atomic density achievable when the gas is unpolarized, as in the MOT or Molasses stages.

Despite all these difficulties, Helium is worth bringing to degeneracy because its high internal energy is sufficient to extract an electron from a metallic surface, paving the way to an electronic detection of single Helium atoms [28, 44]. To do this, the cloud is released from a magnetic or optical trap and dropped onto a special detector called a Micro-Channel Plate (MCP). A detailed description of how it enables detecting individual $^4He^*$ atoms is given in Section 1.3. Before reaching this detector, the cloud undergoes a time-of-flight

(TOF) which maps the measured spatial distribution onto the momentum distribution. Therefore, Helium-4 experiments are particularly well suited for investigating momentum correlations between individual atoms (see Chapters 3 and 4).

This first chapter describes the experimental set-up and the work done during this thesis to improve it. Section 1.1 summarizes the path towards quantum degeneracy with ^{4}He* atoms, while Section 1.2 presents the work done to save 3.8 seconds on the experimental sequence duration. Section 1.3 focuses on the electronic detection chain that enables the measurement of individual ^{4}He* atoms, which is necessary for all the results reported in this manuscript. Section 1.4 describes a two-photon Raman transfer that we implemented to increase the statistics of the measured atomic distributions by a factor of two. Finally, Section 1.5 highlights the specificities of a TOF expansion from an optical lattice, corresponding to the experimental conditions in which all the data presented this manuscript were taken. Note that the physics of ultracold lattice bosons will be discussed in detail in the next chapter.

1.1 Condensation of metastable Helium 4 atoms

The first ^{4}He* BECs were obtained in tens of seconds [34, 35]. In 2015, our team reported a faster experimental scheme of ~ 6 s [45] whose main innovation was replacing the long evaporation in a magnetic trap with a much shorter one in a hybrid magnetic-optical configuration. Since 2021, the Australian team has held the record for the fastest production of ^{4}He* BECs, achieved in 3.3 s in a magnetic trap [38]. For us, the experimental sequence nowadays is pretty much the same as in 2015. For the sake of completeness of this manuscript, all the different stages toward condensation are reminded in this first section in a hopefully synthetic and pedagogical way. Of course, more detailed information can be found in the team's previous manuscripts [46–49].

1.1.1 ^{4}He energy levels of interest

Figure 1.1 presents the relevant energy levels of ^{4}He, whose experimental uses are described throughout this chapter. The starting point is the metastable $2\,^3\mathrm{S}_1$ state, which acts as an effective ground state since its ~ 8000 s lifetime is long enough to safely neglect the probability for a ^{4}He* atom to return to the true ground state $1\,^1\mathrm{S}_0$ during an experimental cycle. An asset of this metastable state is its 19.8 eV internal energy, resulting from the fact that Helium is a noble atomic species and is thus hard to excite. This energy scale is much larger than any other atomic specie brought to degeneracy and is at the origin of the capability to detect ^{4}He* atoms individually. Finally, laser cooling is achievable from the metastable state by addressing either the transitions to the $2\,^3\mathrm{P}_2$ or $2\,^3\mathrm{P}_1$ states, depending on whether Doppler cooling or Sub-Doppler cooling is performed. On the other hand, the large energy difference between the $2\,^3\mathrm{P}_0$ state and the other two states is used to perform two-photon Raman transfer. All these $2\,^3\mathrm{P}_{0,1,2}$ states have a natural linewidth $\Gamma = 2\pi \times 1.6$ MHz and are addressed from the metastable $2\,^3\mathrm{S}_1$ state with resonant light close to 1083 nm.

Two different laser sources are used for laser cooling. The $2\,^3\mathrm{S}_1 \rightarrow 2\,^3\mathrm{P}_2$ transition is addressed by a 50 kHz wide mono-mode fiber laser (NKT Photonics) which is amplified by

an Ytterbium-doped fiber amplifier (Keopsys) delivering a total of 2 W of optical power. To address the $2\,^3S_1 \rightarrow 2\,^3P_1$ transition, we use a Distributed Bragg Reflector diode of ~ 5 MHz bandwidth, amplified to 800 mW by a second Ytterbium-doped fiber amplifier from Keopsys. The frequencies of both lasers are locked to their respective transitions thanks to a saturated absorption spectroscopy signal obtained from a Helium plasma, generated inside a Helium cell by a homemade high-voltage circuit [50].

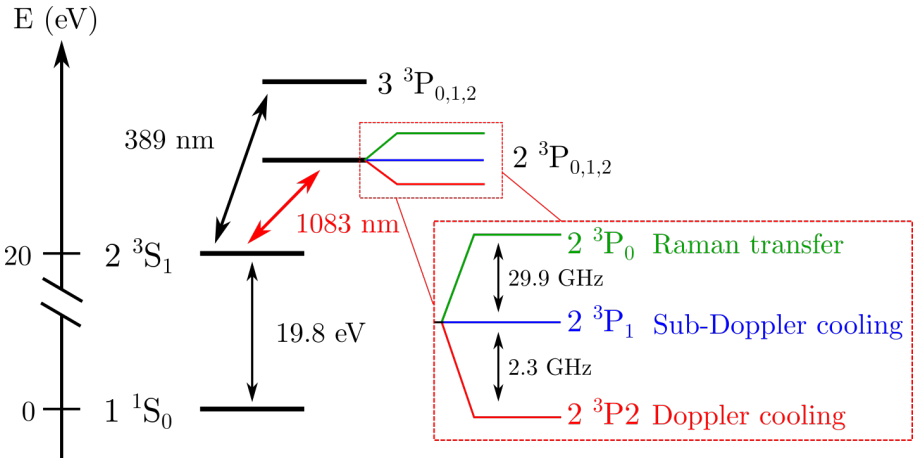

Figure 1.1: **^{4}He energy levels.** Starting from the $2\,^3S_1$ metastable state, transitions to the $2\,^3P_{0,1,2}$ states are used for either cooling, imaging, or manipulating the atoms. These transitions have a wavelength of ~ 1083 nm.

1.1.2 A source of $^4He^*$ atoms

The first step of our experimental sequence is the production of $^4He^*$ atoms from the ground state $1\,^1S_0$. This is done similarly to all other Helium experiments worldwide by applying a plasma DC-discharge onto the atoms. Figure 1.2 (a) schematically describes how this process works in our experiment. A flux of Helium atoms is confined inside a glass tube, which contains a metallic needle connected to a high voltage power supply. A 3.0 kV voltage applied to the needle ignites a plasma between its tip and a grounded perforated metallic plate, called a skimmer, located a few centimeters away. The skimmer's role is to cut into the transverse velocity distributions of the Helium atoms flux after the discharge. Multiple excited states are populated by the discharge. Only the metastable one is laser cooled, while the atoms in the other states are pumped. Due to Helium atoms' lightness, metastable atoms produced by the plasma are too fast to be trapped inside the science chamber after a Zeeman slower of reasonable length. To slow them down, a first cooling stage consists in having the atoms pass through a narrow hole drilled inside a cold piece of boron nitride (BN). The boron nitride is mounted inside a Copper (Cu) cylinder, cooled by having liquid Nitrogen flowing through it. The Copper cylinder cools the boron nitride, which in turns cools the atoms colliding with the walls of the narrow hole. All these elements are mounted on a single metallic frame shown in Figure 1.2 (b). The whole structure, affectionately called the "source", is quite fragile and must be carefully handled any time some maintenance must be performed. And there were ! Here is a short review of what can possibly happen:

- The glass tube can crack due to the leverage exerted by the (heavy) metallic cross to which it is attached. The latter is also connected to the plastic tube of the Helium

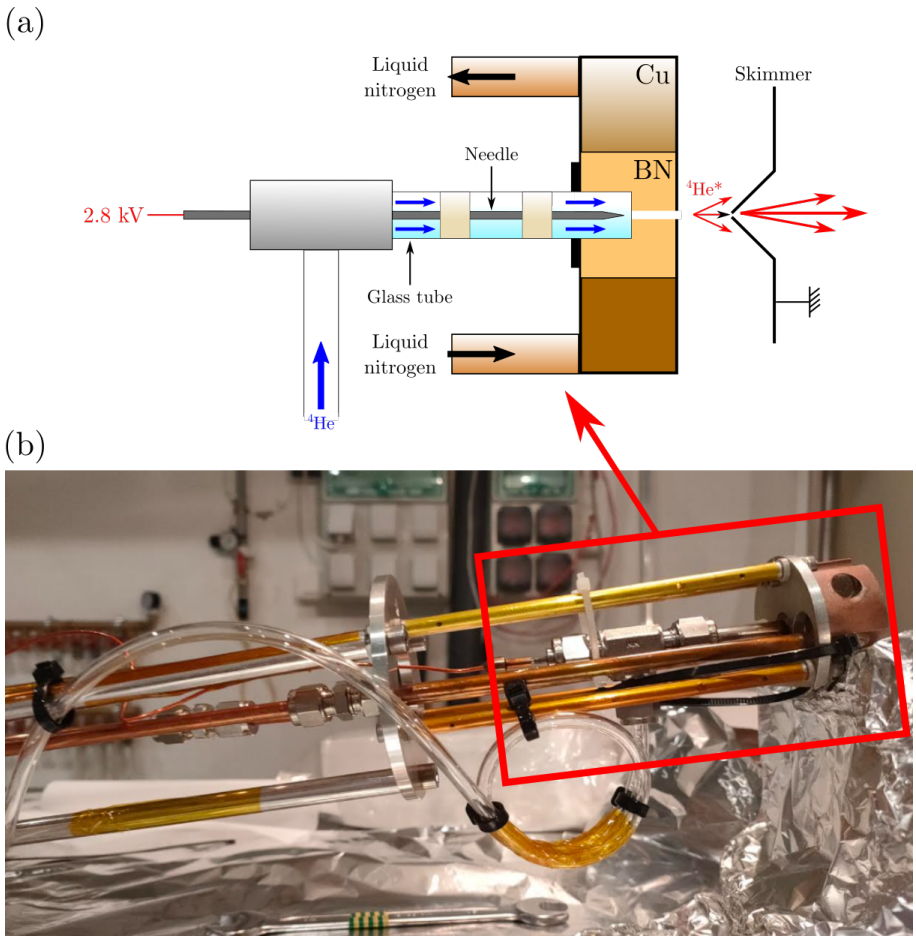

Figure 1.2: **Schematics and picture of the source.** (a) Schematics of the source. ^{4}He atoms circulate through a glass tube where a plasma discharge excites a fraction (10^{-4}) of them into the metastable state. Atoms then pass through a hole in a piece of boron nitride (BN) cooled by the Copper mount (Cu) in which liquid Nitrogen flows. Finally, a skimmer filters the atoms exiting the boron nitride with large transverse velocities. (b) Picture of the metallic frame holding all the pieces of the source together. The red rectangle illustrates the part that corresponds to figure (a).

inlet, whose elasticity adds mechanical stress to the cross. For these reasons, the cross and the plastic tube are both attached to the metallic frame by cable ties (in black and white in the figure).

- A plastic gasket, in black in figure (a), is glued at the interface between the glass tube and the boron nitride. Every time the experiment is started, the glue contract at low temperatures and may eventually crack itself or the glass tube. One has to use an "elastic" glue that can deform to prevent this.
- The boron nitride inner and outer diameters must match exactly with those of the glass tube and the hole in the Copper mount. If the first condition is not met, not all Helium atoms flow into the hole in the boron nitride. The second condition is necessary for the boron nitride to be cooled effectively by the Copper mount. Otherwise, the longitudinal velocities of Helium atoms would be too large. The laboratory's mechanical workshop precisely machines those boron nitride elements.
- The needle is nibbled by the plasma and must be changed occasionally. In addition,

some metallic powder can clog the narrow hole in the boron nitride.
- If the needle is too far from the skimmer, the plasma may ignite inside the plastic tube rather than at the needle tip. The needle orientation also strongly affects the flux of Helium atoms reaching the science chamber. Therefore, some wedges in the glass tube maintain the needle aligned with the hole in the boron nitride. Those are represented in white in figure (a).

Each troubleshooting allowed us to gradually optimize the source until the latest version shown in Figure 1.2 (b), dated May 2021. The plasma current has been stable since then ($\sim$ 12.5 mA), and no further openings of the source has been needed, confirming the robustness of our latest design.

1.1.3 A word about Doppler and Sub-Doppler cooling

Cold atoms experiments rely on laser cooling techniques to slow down large ensembles of particles, and Doppler cooling is always used as a first cooling stage. It involves the radiation pressure felt by a two-level atom doing cycles of absorption and spontaneous emission with resonant photons. In our case, the two-level configuration is obtained by addressing the $2\,^3S_1 \rightarrow 2\,^3P_2$ transition of ^{4}He with σ^+ polarized light, so that the atoms end up cycling between respectively the $m_J = 1$ and $m_J = 2$ sublevels of these states. The radiation pressure writes:

$$\boldsymbol{F} = \hbar \boldsymbol{k} \frac{\Gamma}{2} \frac{s}{s+1} \quad \text{, with} \quad s = \frac{I/I_{sat}}{1 + 4\Delta^2/\Gamma^2} \tag{1.2}$$

where s is the saturation parameter, whose definition involves the detuning to the resonance Δ and the saturation intensity I_{sat} (for us $I_{sat} = 0.16\ \mathrm{mW/cm^2}$). Due to the Doppler effect, an atom moving with a velocity $\boldsymbol{v}$ sees the effective detuning $\Delta' = \Delta - \boldsymbol{k}\cdot\boldsymbol{v}$, and the radiation pressure then depends on the orientation between the laser beam and the atom's trajectory. To decelerate the atom, one must use a contra-propagating laser beam with a negative detuning Δ (red-detuned) so that the Doppler effect brings the atoms back on resonance with the photons.

In addition to a deceleration process, Doppler cooling allows the accumulation of large ensembles (millions) of atoms in small volumes on the order of cubic centimeters. This trapping process is achieved by illuminating an ensemble of two-level atoms with three orthogonal and contra-propagating pairs of Doppler beams. Such a system is referred to as a Red Molasse and was first realized experimentally in 1985 [51]. The equilibrium temperature of a Red Molasse, set by the competition between the friction of the radiation pressure and the momentum diffusion induced by spontaneous emission processes, writes as:

$$k_B T = \frac{\hbar}{2} \frac{\Delta^2 + \Gamma^2/4}{|\Delta|} \tag{1.3}$$

The minimum temperature is called the Doppler limit [52], and is reached for $\Delta = -\Gamma/2$:

$$k_B T_{\mathrm{D}} = \frac{\hbar\Gamma}{2} \tag{1.4}$$

For ^{4}He*, the Doppler limit corresponds to $T_{\mathrm{D}} \simeq 39\ \mu$K [53]. For most atomic species, this limit is not observed experimentally as Sub-Doppler mechanisms spontaneously take place and reduce the temperature further. However, these Sub-Doppler mechanisms do

not occur spontaneously with Helium, as their capture velocity is smaller than the Doppler limit. This specificity has allowed our team to measure this limit for Helium in 2014 [54].

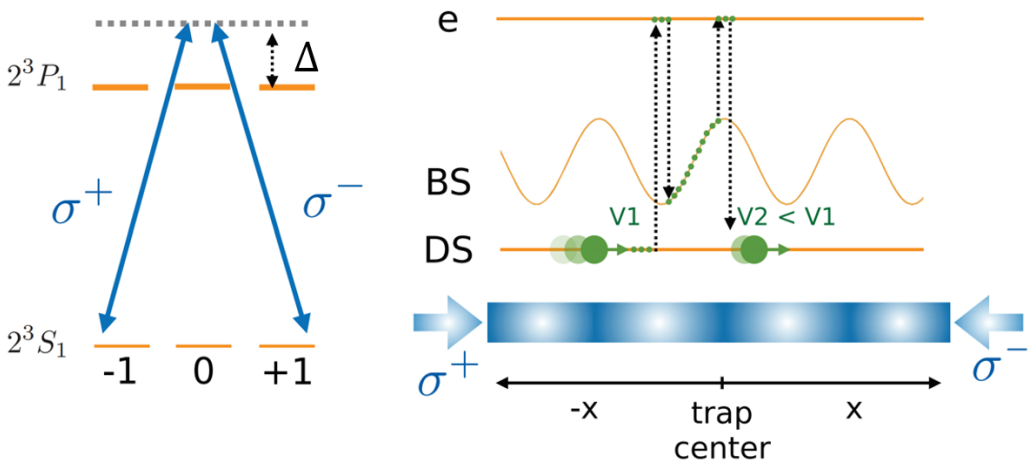

Figure 1.3: **Sisyphus cooling on the transition $2\,^3S_1 \rightarrow 2\,^3P_1$.** Left: a Λ-configuration is achieved via pairs of $\sigma^+ - \sigma^-$ polarized beams. Both beams have the same Rabi frequency and positive detuning from the $^3P_1$ state. Right: The contra-propagation of the $\sigma^+ - \sigma^-$ beams modulates spatially the lightshift of $|\Psi_{BS}\rangle$, while that of $|\Psi_{DS}\rangle$ remains zero. An atom initially in $|\Psi_{DS}\rangle$ is transferred to $|\Psi_{BS}\rangle$ near the bottom of a potential energy hill. It then loses kinetic energy by climbing that hill before being optically pumped back into $|\Psi_{DS}\rangle$. The repetition of these processes continuously slows down the atom and is called Sisyphus cooling.

Several Sub-Doppler mechanisms can lower the temperature beyond the Doppler limit. They originate from the presence of a degenerate ground state in the transition addressed, contrary to the simple two-level system required for Doppler cooling. In our experiment, Sisyphus cooling is performed with the transition $2\,^3S_1 \rightarrow 2\,^3P_1$. This $J_g = 1 \leftrightarrow J_e = 1$ configuration allows the implementation of a so-called Gray Molasse, whose first realization dates back to 1992 [55]. Three orthogonal pairs of contra-propagating beams illuminate the atoms. Each pair contains a σ^+ and a σ^- beam, which share the same Rabi frequency Ω_0 and detuning to the excited state Δ. Let us consider the motion of an atom along the direction z of one of these pairs. Because the transition between both $m_J = 0$ sublevels is forbidden, the $\sigma^+ - \sigma^-$ beams implement a Λ-configuration between the two ground states $|g_+\rangle = |2\,^3S_1, m_J = +1\rangle$, $|g_-\rangle = |2\,^3S_1, m_J = -1\rangle$, and the excited state $|e\rangle = |2\,^3P_1, m_J = 0\rangle$ (see left panel of Figure 1.3). The interference between the $\sigma^+ - \sigma^-$ beams leads to spatially modulated Rabi frequencies:

$$\Omega_\pm(z) = \Omega_0 \cos(kz \pm \phi/2) \tag{1.5}$$

where ϕ is the relative phase between the beams. For a sufficiently large detuning Δ, the population of the excited state is negligible, and the atoms are in one of the following coherent superpositions of $|g_+\rangle$ and $|g_-\rangle$:

$$|\Psi_{BS}\rangle \propto \Omega_+(z)\,|g_+\rangle + \Omega_-(z)\,|g_-\rangle \quad \text{, with} \quad \hbar\omega_{BS} \simeq \frac{\hbar\Omega^2}{4\Delta}\left(\Omega_+(z)^2 + \Omega_-(z)^2\right) \tag{1.6}$$

$$|\Psi_{DS}\rangle \propto \Omega_+(z)\,|g_+\rangle - \Omega_-(z)\,|g_-\rangle \quad \text{, with} \quad \hbar\omega_{DS} = 0 \tag{1.7}$$

The dark state (DS) is uncoupled to the excited state $|e\rangle$, and its lightshift is zero. On the contrary, the lightshift of the bright state (BS) is positive for $\Delta > 0$ and spatially

modulated. As the definitions of $|\Psi_{\mathrm{BS}}\rangle$ and $|\Psi_{\mathrm{DS}}\rangle$ involve z, the motion of an atom creates a coupling between both states. One can show that the highest probability for an atom initially in $|\Psi_{\mathrm{DS}}\rangle$ to switch to $|\Psi_{\mathrm{BS}}\rangle$ is reached at the positions z where the lightshifts are the closest, namely down the hills of $\hbar\omega_{\mathrm{BS}}$. This is referred to as motional coupling, whose strength is inversely proportional to the energy difference (hence it happens preferentially when the lightshift in $|\Psi_{\mathrm{BS}}\rangle$ is small). Conversely, an atom in $|\Psi_{\mathrm{BS}}\rangle$ can be optically pumped towards $|\Psi_{\mathrm{DS}}\rangle$, with a maximum probability at the top of the hills because the optical pumping rate is $\Gamma s/2$, *i.e.* maximum when the lightshift is maximum. Because climbing the hill of potential energy slows down the atom, the latter returns to $|\Psi_{\mathrm{DS}}\rangle$ with a smaller velocity than when it left. Going back and forth between $|\Psi_{\mathrm{BS}}\rangle$ and $|\Psi_{\mathrm{DS}}\rangle$ keeps slowing down the atom as it propagates along z. This mechanism, shown in the right panel of Figure 1.3, is called Sisyphus cooling by analogy with the endless movement of Sisyphus' rock in Greek mythology. In the case of the atom, the temperature does not decrease endlessly. Sisyphus cooling stops when the atom's kinetic energy is of the order of the height of the hill, namely when $k_B T \sim \hbar\Omega_0^2/|\Delta|$. The Rabi frequency Ω_0 cannot be chosen arbitrarily small as the final velocity must remain smaller than the capture velocity for Sub-Doppler mechanisms ($\propto \Omega_0^2$). In practice, the smallest velocities obtained with Sisyphus cooling are of the order of a few times the recoil velocity $v_r = \hbar k/m$.

1.1.4 Description of the laser cooling stages

After having reminded some commonly used laser cooling techniques, this section briefly presents their actual implementation in our experiment, in chronological order. The optical accesses of the different cooling beams around the science chamber are schematically presented in Figure 1.4.

Zeeman slower

Right after exiting the source, the atomic jet of ^{4}He* atoms is collimated by Transverse Molasses (TMs), namely two pairs of contra-propagating beams implementing Doppler cooling along the directions orthogonal to the propagation axis. The atoms then enter a $\sim$ 2.5 m long Zeeman slower, in which they are continuously decelerated by a contra-propagating beam along the longitudinal direction. This Zeeman slower is a vacuum tube surrounded by magnetic coils. Those produce a Zeeman shift of the atomic energy levels to keep the atoms in resonance with the light (whose frequency is fixed) as they get slowed down. This technique was first implemented by W. D. Phillips [56] in 1982 to decelerate an atomic jet of Sodium atoms and allows us to decrease the atomic longitudinal velocity from $\sim$ 1200 m/s at the exit of the source to $\sim$ 50 m/s on reaching the science chamber.

Magneto-Optical Trap

The longitudinal velocity of the atoms after the Zeeman slower is sufficiently small to trap them inside a MOT. The latter combines the Doppler effect with the Zeeman shift induced by a magnetic gradient to spatially confine the atoms. Its first implementation dates back to 1987 [57]. For the laser part, three orthogonal pairs of laser beams cross each other at the center of the science chamber. The beams are red-detuned compared to the $2\,^3\mathrm{S}_1 \rightarrow 2\,^3\mathrm{P}_2$ transition, and each pair is $\sigma^+ - \sigma^-$ polarized. In addition, two coils in anti-Helmoltz configuration produce a magnetic quadrupole in the science chamber,

whose center coincides with the crossing of the laser beams. Due to the local magnetic gradient, an atom moving away from the trap center is only resonant with a contra-propagating beam, whose radiation pressure brings it back to the center. Therefore, this joint mechanism allows to confine atoms into a given volume in space. The capture range of a MOT is also larger than that of a bare optical Molasse, as the magnetic gradient allows for atoms with larger velocities to be resonant with the light.

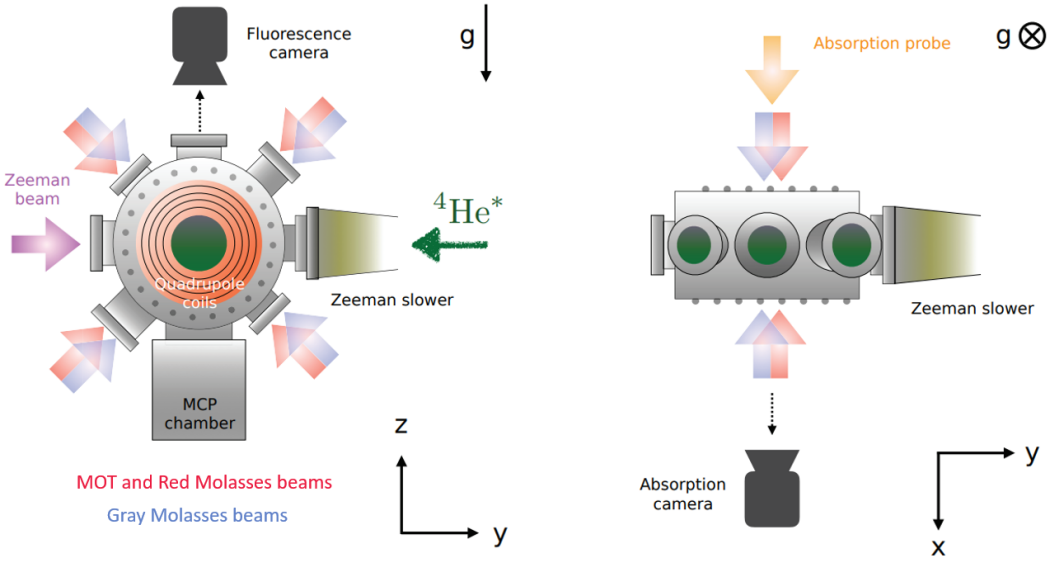

Figure 1.4: **Scheme of the cooling beams around the science chamber.** The Zeeman beam is in the opposite direction to the incoming flux of ^{4}He* atoms exiting the Zeeman slower. Although coming from two different lasers, the six Red Molasses and Gray Molasses beams are delivered to the science chamber by the same optical fibers. The figure also shows the position of the fluorescence and absorption imaging cameras. A specific beam is used for absorption imaging, while the MOT beams are tuned to resonance for fluorescence imaging.

In the experiment, the magnetic coils are positioned along the x-axis, roughly 10 cm away from the science chamber center. To load the MOT, a current of 16 A is applied to the coils, creating a magnetic gradient of 25 G/cm on the atoms. The detuning of the laser beams is set to $\Delta = -60\ \Gamma$, and the intensity to 15 I_{sat} per beam. A large detuning ensures a large velocity capture range and also limits the rate of Penning collisions. These settings allow us to capture $\sim 2 \times 10^9$ atoms in 2 s. The MOT is then compressed by decreasing the detuning to $\Delta = -12\ \Gamma$, which increases the density by a factor ~ 10 . At the same time, the intensity per beam is reduced to $\sim 0.1\ I_{sat}$ to keep a low amount of Penning collisions. The resulting cloud contains $N \sim 2 \times 10^9$ atoms at a temperature $T \simeq 1.2$ mK, with a density $n \sim 7 \times 10^9$ atoms/cm^3.

Red Molasses

Once the MOT loaded, the magnetic quadrupole is switched off and one ends up with a Red Molasse, where regular Doppler cooling is the only process in place. However, the cloud temperature is still far from the Doppler limit $T_D \simeq 38$ µK, reached for $\Delta = -\Gamma/2$. To get closer, the detuning is reduced to $\Delta \sim -\Gamma$, which is possible thanks to the narrow 50 kHz bandwidth of the laser. To avoid large Penning collisions, the intensity is simultaneously

lowered to 0.05 I_{sat} per beam. After 5 ms, the Red Molasse typically contains $N \simeq 1.8\times10^9$ atoms at $T \simeq 100$ µK. Getting closer to the Doppler limit would induce strong losses due to the vanishing intensity $s \ll 1$ required to reach this limit, and is not needed as the equilibrium temperature is now small to proceed with Sub-Doppler cooling.

Gray Molasses

The capture velocity for traditional Sisyphus configurations, such as the lin $\perp$ lin or $\sigma^+ - \sigma^-$ polarization gradient cooling [58], is below the Doppler limit for ^{4}He* atoms [54]. As described in Section 1.1.3, Sub-Doppler temperatures can still be achieved via Gray Molasses, implemented on the $2\,^3S_1 \rightarrow 2\,^3P_1$ transition. For that, the detuning of the light is set to $\Delta = 8\ \Gamma$ and the intensity to $\sim 4.7\ I_{sat}$ per beam. After 5 ms, typically $N \simeq 1.7 \times 10^9$ atoms are trapped at a temperature $T \simeq 15$ µK. Although below the Doppler limit, the temperature is not small enough to reach condensation. This is also the consequence of the density being limited by the Pennings collisions, resulting in a phase-space density of only a few 10^{-5} at this stage. Therefore, the cloud must now be polarized to increase its density further, and cooled via evaporative cooling.

1.1.5 Description of the evaporative cooling stages

Evaporative cooling removes the hottest particles from a sample and allows the rest to thermalize at a lower temperature when elastic collisions are sufficiently large. It is encountered in everyday life, for example when blowing on a cup of coffee, and is the final step in all experiments with cold atoms to achieve condensation. Experimentally, it is implemented either in a magnetic trap or in an optical trap. The first realizations of ^{4}He* BECs were all performed by extensive evaporation in a magnetic trap [34, 35, 39, 59, 60]. However, this technique has two drawbacks. Firstly, achieving condensation requires long evaporation ramps (~ 10 s) in a magnetic trap. Secondly, the light mass of ^{4}He* makes it particularly susceptible to Majorana spin flips at the center of a magnetic quadrupole, where the field cancels out [61]. Particular trapping geometries, such as the "cloverleaf" design, can circumvent this effect, but induce large atom number fluctuations at the end of evaporation. On the other hand, early work on all-optical evaporation of Rubidium atoms demonstrated the stability and speed of evaporation inside optical traps [62, 63]. However, this technique cannot be implemented with ^{4}He* atoms because Penning collisions would limit the density in this unpolarized case. In 2009, the authors of [64] reported the condensation of Rubidium atoms in a combined magnetic and optical trap. Inspired by this approach, our team has set up a similar scheme for ^{4}He* atoms [54]. This hybrid configuration combines the efficient loading of a magnetic quadrupole with fast optical evaporation ramps.

Magnetic trap

Before being loaded into the magnetic quadrupole, ^{4}He* atoms are optically pumped to the $m_J = 1$ sublevel of the $2\,^3S_1$ state by addressing the transition to the $2\,^3P_1$ state with σ^+ light. This optical pumping stage is required because only the $m_J = 1$ sublevel is magnetically trapped: the $m_J = 0$ is insensitive to the magnetic field, and the $m_J = -1$ is anti-trapped. To define a quantization axis during this stage, two coils in Helmoltz configuration produce a bias field along the z-axis. The quadrupole is produced with the

same coils as for the MOT, and corresponds to a magnetic gradient of ~ 5 G/cm. Around $N \simeq 1.7 \times 10^9$ atoms are loaded into the quadrupole, which corresponds to almost all the atoms of the gray molasses. Polarizing the atoms decreases the Pennings collisions rate by a factor $\sim 10^4$ [65], which allows us to increase the density. To this end, the gradient is increased to ~ 35 G/cm. Finally, the cloud is cooled via radio-frequency (RF) evaporation [9]. The idea of this technique is to selectively couple the hottest atoms to the $m_J = 0$ and $m_J = 1$ sublevels using RF waves. Due to the spatial dependence of the Zeeman shift, progressively decreasing the RF frequency allows to expel atoms which are located closer to the trap center, namely colder atoms. In our experiment, RF evaporation is performed in ~ 3 s, during which the RF frequency is linearly decreased from 40 MHz to 6 MHz. At the end of the evaporation, $N \simeq 120 \times 10^6$ atoms are trapped with a density $n = 6.6 \times 10^{11}$ at/cm^3 and at a temperature $T \simeq 70$ µK. Even though this temperature is larger than the one of the Gray Molasses, the phase-space density has increased by almost two orders of magnitude due to the higher density.

Optical Dipole Trap

After the RF evaporation, the cloud is sufficiently cold and dense to be loaded into a crossed Optical Dipole Trap (ODT). The latter is produced by a far red-detuned laser beam at 1550 nm (from IPG Photonics), so that atoms are trapped at the maxima of the light intensity [66]. Consequently, the beam is tightly focused on the atoms and reflected on itself with an angle of 20° to produce a cigar-shaped trap (see Figure 1.19). The forward and return beams are referred to as ODT1 and ODT2, and their waists are respectively 133 µm and 63 µm. An Acousto-Optic Modulator (AOM) shifts the frequency of ODT2 by a few tens of MHz to prevent interference effects with ODT1. The ODT trap is loaded by switching on ODT1 and ODT2 at full power (18 W for ODT1) and decreasing the quadrupole current in 500 ms with exponential decaying ramps. This transfer is optimized by slightly offsetting the position of the magnetic zero compared to the center of the ODT. This is done with magnetic biases, and limits Majorana losses that would be too high if both centers were superimposed [47]. Due to its narrowness, only $N \simeq 5 \times 10^6$ atoms are loaded into the ODT. Simultaneously, the density increases by more than two orders of magnitude, and the temperature is divided by two. Note that a bias field is applied along the x-axis while the atoms are in the ODT to maintain their polarization and avoid Pennings losses. Final evaporation in the ODT allows condensation to be reached. The laser intensity is progressively decreased with a PID loop to let the hottest particles escape. The trap opens during the process, meaning that the trapping frequencies and the density decrease during the evaporation, contrary to the magnetic case. Nevertheless, the temperature is cooled faster, and condensation is reached after typically ~ 600 ms. The final ODT intensity determines the BEC atom number and the trapping frequencies. The largest BECs corresponds to $N \simeq 10^6$ atoms and $(\omega_x, \omega_y, \omega_z) = 2\pi \times (81, 352, 320)$ Hz, with no thermal fraction distinguishable on absorption images (see next paragraph). All the results presented in this manuscript required significantly smaller BECs, for which the evaporation was pushed further. These smaller BECs corresponds to $N \simeq 5 \times 10^3$ atoms or less, and trapping frequencies of the order of $(\omega_x, \omega_y, \omega_z) = 2\pi \times (41, 173, 180)$ Hz. The evolution of the phase-space density throughout the experimental sequence is summarized in Figure 1.5.

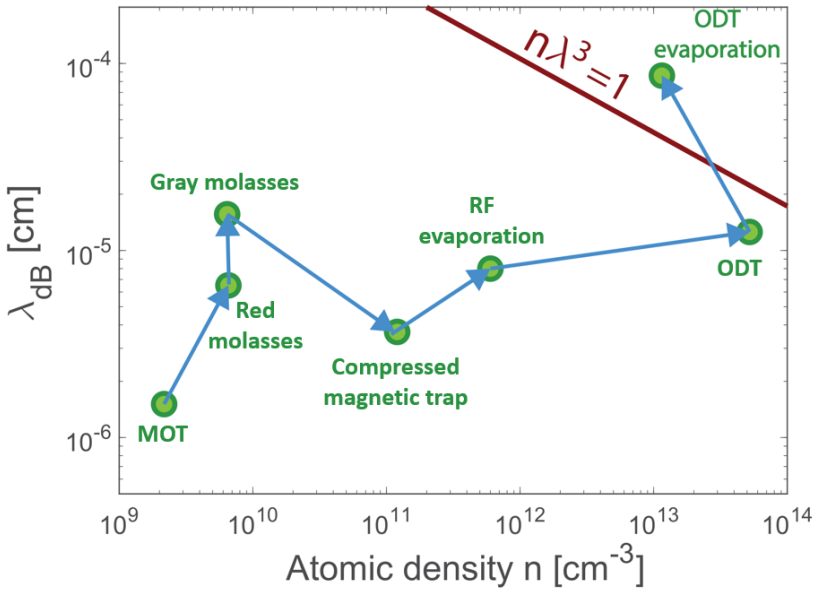

Figure 1.5: **Phase-space density $n\lambda_{\mathrm{dB}}^3$ in the different experimental stages.** The phase-space density corresponds to the product of the atomic density n with the third power of the (thermal) De Broglie wavelength $\lambda_{\mathrm{dB}} = h/\sqrt{2\pi k_B T}$. A BEC is obtained when the phase-space density exceeds one, which is achieved by cooling ($\lambda_{\mathrm{dB}} \nearrow$) and compressing ($n \nearrow$) the atomic clouds.

1.1.6 Optical imaging

In complement to the electronic detection permitted by ^{4}He* atoms, our experiment implements traditional fluorescence and absorption imaging techniques. Optical detection is essential for diagnosing the cloud temperature and atom number via the density profiles of the atomic distribution after Time-Of-Flight (TOF). Fluorescence imaging is achieved by illuminating the atoms with the MOT beams on resonance for 100 µs. The fluorescence photons, emitted isotropically, are collected by an InGaAs camera above the science chamber (see Figure 1.4). This camera contains 256×320 pixels of (30×30) µm^2, and its 125 µm resolution in the image plane is appropriate for imaging the cloud until the end of the RF evaporation. To characterize the clouds after the loading into the ODT, absorption imaging is performed with a probe beam of weak intensity $I_{\mathrm{sat}}/5$ addressing the $2\,^3\mathrm{S}_1 \rightarrow 2\,^3\mathrm{P}_2$ transition. This beam illuminates the atoms from the side of the science chamber, and the cloud shadow is imaged by a second InGaAs camera whose optical axis forms an angle with the xy plane due to geometrical constraints. The resolution of this detection scheme is 13 µm, which is enough to resolve a BEC after a short TOF. In particular, the BEC atom number N_{BEC} is extracted from the Thomas-Fermi profiles measured after a TOF of a few milliseconds.

1.2 Reducing the experimental sequence duration

The first ^{4}He* BECs obtained by our team in 2015 [45] were produced every 6 seconds, which was a factor of two faster than the state of the art at that time [35, 59, 60].

The main innovation for this improvement was to perform evaporative cooling in both a magnetic and an optical trap. In 2021, the Australian team reported the production of ^{4}He* BECs of $\sim 10^6$ atoms in 3.3 seconds [38]. They achieve such short cycle durations by by-passing the evaporative cooling stage in the magnetic trap. In their case, performing 1D Doppler cooling in the magnetic trap (QUIC configuration) is sufficient to load a crossed optical dipole trap. This is impossible for us because the cloud's density directly after loading the magnetic trap is too small ($\sim 10^{10}\,\mathrm{cm}^{-3}$). Therefore, we compress the magnetic trap to increase the density, which in turn heats the cloud and makes the RF evaporation mandatory before loading the ODT. Nevertheless, the work of the Australian team motivated us to try reducing our own sequence duration. Indeed, short experimental sequences are a prerequisite for extracting correlations, since each measurement usually requires thousands of experimental files to reach a satisfying signal-to-noise ratio.

1.2.1 Faster production of ^{4}He* BECs

At the beginning of my thesis, the experiment could typically produce ^{4}He* BECs of 6×10^6 atoms in $\sim$ 6.8 seconds. To do faster without major modifications of the experimental apparatus, we first tried to optimize the number of ^{4}He* atoms in the different steps of the experimental cycle. The most efficient lever was to increase the initial number of atoms trapped in the MOT. This number strongly depends on the plasma's "health", the pressure in the source vacuum chamber, and the orientation of the Helium beam. As mentioned in Section 1.1.2, the several attempts at improving the source design have allowed us to reach a situation where the plasma is stable. Combined with a thorough optimization of the source and MOT parameters (skimmer position, source pressure, alignment of the TMs/Zeeman/MOT beams, MOT detuning ...), both the loading rate and maximum atom number of the MOT can be significantly improved, as illustrated in Figure 1.6. This optimization typically permits the shortening of the MOT loading stage from 2 s to 1 s while keeping $\sim 2.5\times10^9$ atoms at the end of the MOT loading, which is already a significant improvement. Thanks to this higher atom number, the evaporation in the magnetic trap is more efficient and can be done faster. We found that we could keep more than 150×10^6 atoms at the end of the RF evaporation while *(i)* suppressing an unnecessary 1 s wait time at the beginning of the ramps and *(ii)* reducing the duration of the ramp from 2 s to 1.4 s. Finally, the transfer from the magnetic to the optical dipole trap was also shortened by 0.4 s by reducing the exponential decay time of the quadrupole current from $\tau = 100$ ms to $\tau = 85$. In total, the experimental cycle has been fastened from $\sim$ 6.8 s to $\sim$ 4 s without loosing in terms of BEC atom number ($5-6\times10^5$) or shot-to-shot atom number fluctuations ($\sim 8\%$).

1.2.2 Optical pumping of $m_J = 0$ atoms

As mentioned in the introduction of this chapter, using MCPs allows us to detect individual ^{4}He* atoms. One of the benefits of this detector is to measure very dilute signals. For instance, the results presented in Chapter 4 required to detect atomic clouds with momentum densities of typically $n = 0.5$ atom/cm^3. Therefore, such signals can easily be masked by the detection background on the MCPs if nothing is done to reduce it. This background (of ^{4}He* atoms) has two origins. The first contribution comes from the atoms ejected during the evaporation stages of the experimental sequence. In particular, the fraction ejected upwards in the science chamber may reach the MCPs at the same time

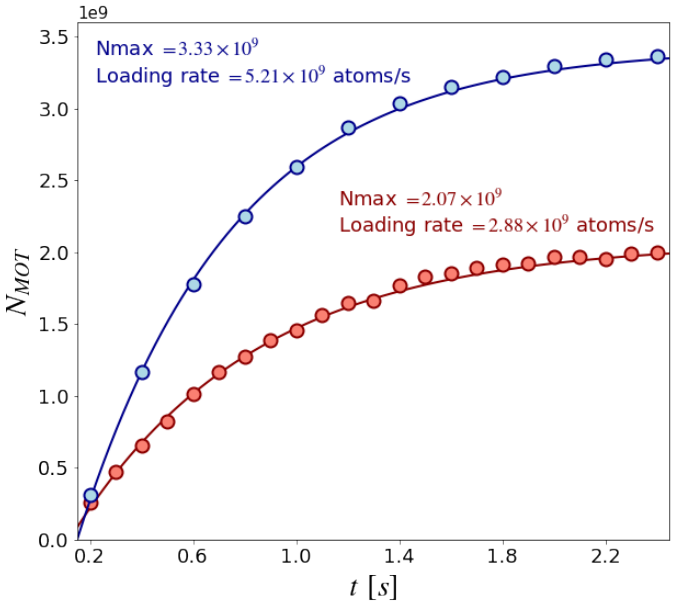

Figure 1.6: **Improvement of the MOT loading.** The atom number in the MOT is plotted versus the duration of the loading stage for an optimized (blue) and non-optimized (red) loading. Experimental points are fitted with the scaling $N_{\max}\left(1-\exp^{-(t-t_0)/\tau}\right)$ from which the maximum atom number $N_{\max}$ and the loading rate $N_{\max}/\tau$ are extracted.

as the atoms of interest. The second contribution corresponds to $m_J = 0$ atoms trapped inside the crossed ODT together with the $m_J = 1$ atoms. They originate from Majorana spin-flips occurring during the transfer from the magnetic to the optical trap. Both contributions are visible in the upper left and right panels of Figure 1.7. These are respectively the histogram of the number of counts detected by the MCP and a time-integrated top view of the atom's impacts on the MCP surface. For this measurement, a large BEC of hundreds of thousands of atoms was released from the ODT after 1 s of holding. We apply a magnetic gradient at the beginning of the expansion to push the condensate away so that the MCPs measure only background atoms. The atoms ejected during the evaporation (indicated by the orange dashed line) reach the MCP first and are delocalized over its entire surface. On the other hand, the colder $m_J = 0$ atoms that remained in the ODT until the end of evaporation have a narrower velocity distribution centered on the MCP ($\boldsymbol{k} \simeq \mathbf{0}$), and indicated by the pink dashed line. To reduce this background when taking data, a typical procedure consists in holding the BEC in the ODT for 3 s. The outcome is shown in the middle panels of Figure 1.7. The number of detected atoms has been divided by $373/102 \simeq 3.7$ compared to the previous case, and most of the delocalized background has been removed. However, doing this does not totally suppress the $m_J = 0$ atoms, and a faint cloud remains at the MCP's center. To reach faster experimental sequences, we thought of optically pumping these $m_J = 0$ atoms into the $|2\,^3\mathrm{S}_1\,, m_J = 1\rangle$ state. The idea behind this is to reduce the initial number of background atoms to avoid such a long holding time. The lower panels of Figure 1.7 show an example of the background reduction achieved by an additional optical pumping stage, the implementation of which is now described.

Optical pumping is realized at the end of the evaporation in the ODT. It is done similarly to the one in the Gray Molasses by addressing the $2\,^3\mathrm{S}_1 \rightarrow 2\,^3\mathrm{P}_2$ transition with

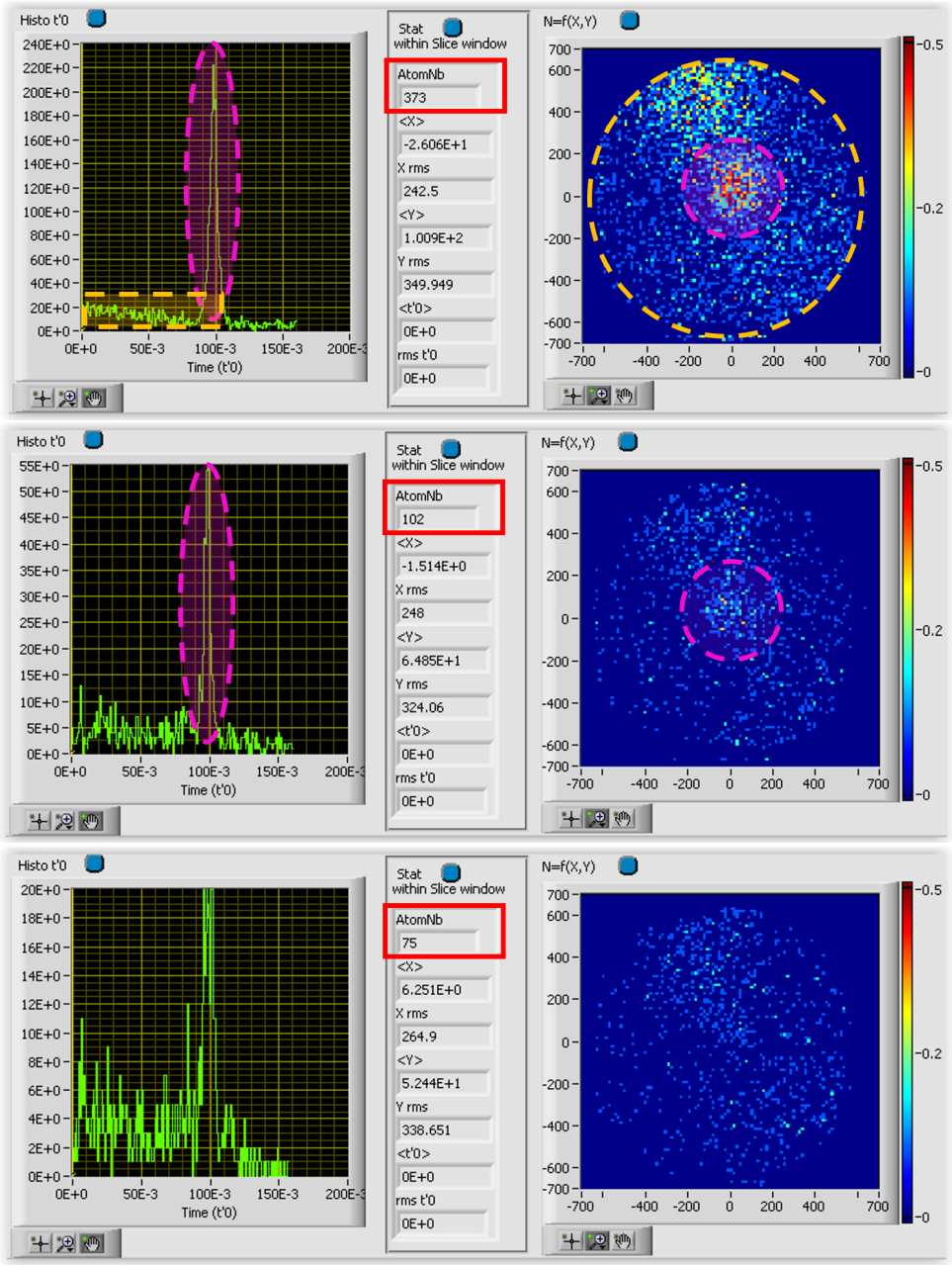

Figure 1.7: **MCP background versus holding time and optical pumping.** Left: histograms of the number of counts detected by the MCP. Right: time-integrated top views of the atom's impacts on the MCP surface. Both contributions to the background are indicated by the orange and pink dashed lines (see text). From top to bottom, the background is reduced by increasing the holding time in the ODT from 1 to 3 s, and from applying an optical pumping stage to further reduce the amount of $m_J = 0$ atoms in the pink dashed line of the upper panels.

σ^+ polarized light. The magnetic bias of the ODT along the x-axis is decreased to zero while that along the z-axis is increased to its maximum value ($\sim 4\,\mathrm{MHz}$) in 60 ms. The atoms are then illuminated by a 700 µs long pulse whose frequency is tuned via an AOM to match that of the $2\,^3\mathrm{S}_1 \rightarrow 2\,^3\mathrm{P}_2$ transition. After that, the magnetic biases are re-inverted in another 60 ms. We record the number of background atoms detected by the MCPs on varying the AOM frequency to observe the optical pumping effect. As illustrated in the left panel of Figure 1.8, we indeed observe a reduction of the number of $m_J = 0$ atoms around 235 MHz. After some optimization (for instance, passing from a pulse to a sweep), we tested this optical pumping in real data-taking conditions with lattice gases of a few thousand atoms. In particular, we investigated the background level reduction with the ODT's holding time for both configurations with and without optical pumping right after the end of evaporation. The results are presented in the right panel of Figure 1.8. Without optical pumping, the background level saturates around $3-4$ s of holding. This saturation is reached after only ~ 2 s when optical pumping is performed. Therefore, this optical pumping stage makes us gain one additional second on the total experimental cycle.

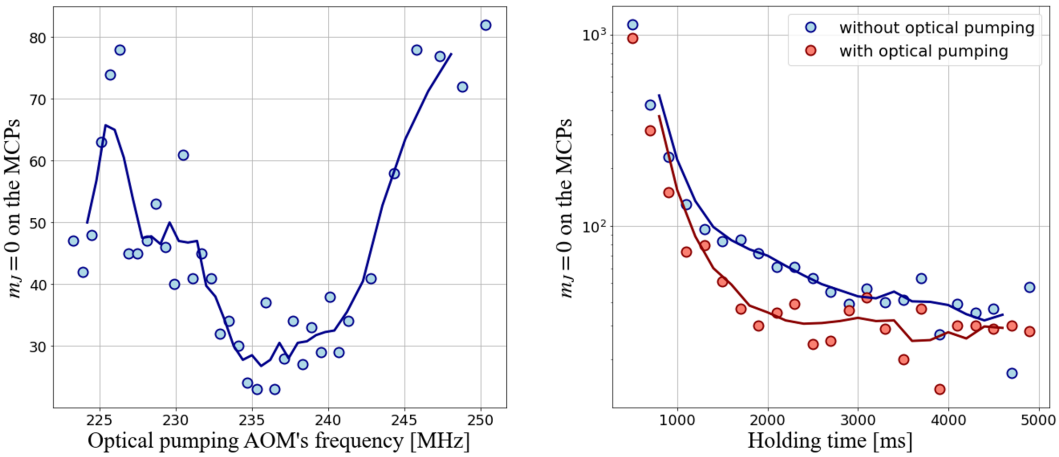

Figure 1.8: **Optical pumping after ramping down the ODT.** Left: background atoms on the MCPs versus optical pumping frequency. The dip in the number of $m_J = 0$ atoms around 235 MHz shows that the optical pumping reduces the background level. The solid line is a moving average of the experimental data. Right: background atoms on the MCPs versus ODT's holding time. Solid lines are also moving averages. Without optical pumping (blue data), the background level on the MCPs saturates after $\sim 3-4$ s. In contrast, a similarly good background can be reached in only ~ 2 s when optical pumping is performed (red data).

We comment here briefly on the difficulties encountered when trying to achieve optical pumping at maximum ODT intensity, namely before optical evaporation. Contrary to the previous case, we observe now a clear Lorentzian resonance associated with an increase of $m_J = 0$ atoms (see left panel of Figure 1.9). This observation, combined with a strong suppression of the $m_J = 1$ atoms at the same frequency (curve not shown), indicates that the optical pumping transfers atoms from the $m_J = 1$ to the $m_J = 0$ sublevel rather than the opposite. One reasonable explanation is that the light polarization is not σ^+ but rather π or σ^-. To confirm this hypothesis, we measured the resonance frequency for various ODT intensities and magnetic fields. The results are presented in the right panel of Figure 1.9. A first observation is that the resonance frequency decreases with the strength of the magnetic field (x-axis). This means that the energy levels addressed optically get closer

in energy the stronger the Zeeman shift. It thus excludes the possibility of a π polarized light, since the latter would address the transition between the states $|2\,^3\mathrm{S}_1\ ,\ m_J = 1\rangle$ and $|2\,^3\mathrm{P}_2\ ,\ m_J = 1\rangle$ whose energy difference remains constant. On the other hand, this measurement is consistent with a σ^- polarized light coupling the states $|2\,^3\mathrm{S}_1\ ,\ m_J = 1\rangle$ and $|2\,^3\mathrm{P}_2\ ,\ m_J = 0\rangle$. The shift between the resonance frequencies in the low/high ODT's intensity cases supports this conclusion. Indeed, the red-detuned ODT induces a negative lightshift on the energy levels, which increases the energy difference between the states $|2\,^3\mathrm{S}_1\ ,\ m_J = 1\rangle$ and $|2\,^3\mathrm{P}_2\ ,\ m_J = 0\rangle$. Therefore, the ODT seems to polarize the atoms in such a way that the optical pumping beam acts as a σ^- light. To see if the beam also contains a σ^+ component, we scanned the frequency range around 235 MHz trying to observe a similar dip to the one in Figure 1.8, without success. The result of these attempts is that the ODT-induced perturbation when the ODT is at maximum power is too strong to perform optical pumping before optical evaporation.

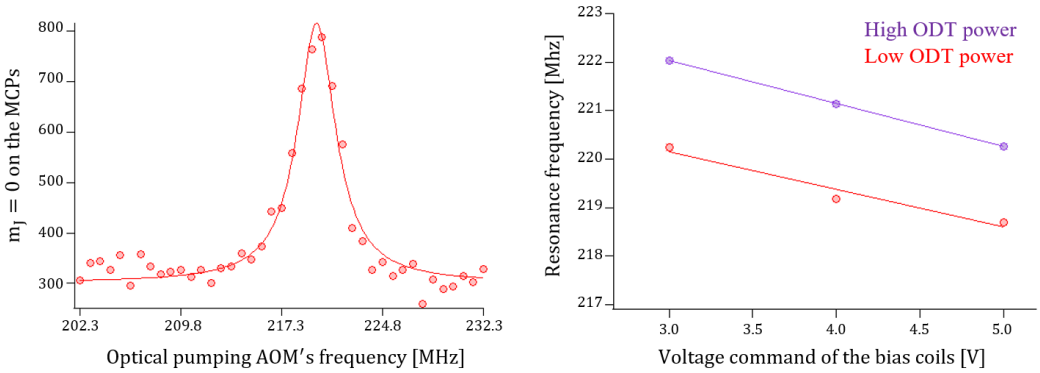

Figure 1.9: **Optical pumping before ramping down the ODT.** Left: background atoms on the MCPs versus optical pumping frequency. The solid line is a Lorentzian fit used to extract the resonance frequency. Right: Resonance frequency versus magnetic bias field, at two different ODT intensities. The magnetic field strength is quantified via the voltage command sent to the power supply of the coils.

To conclude this section, the entire experimental sequence for data taking has been reduced by 3.8 s to reach $\sim$ 8 s (accounting for the reset time). This improvement has a significant impact since it increases the maximum number of files that can be collected during a typical day of acquisition from $\sim$ 2400 to $\sim$ 3600. For comparison, all the results concerning momentum correlations between individual atoms (Chapters 3 and 4) were obtained by averaging over $\sim$ 2000 distributions for each set of parameters. Because half (at worse) of the measured distributions are thrown away due to atom number fluctuations, each dataset must contain about 4000 distributions to be confident that the statistic is sufficient. Two days of acquisition were needed per dataset with the old sequence, whereas one day is enough with the new one. In addition, collecting a dataset in a single day tends to limit variations in the experimental conditions between the distributions. Finally, we note that improving the shot-to-shot atom number fluctuations for our typical experimental conditions (lattice gases with a few thousand atoms) might be the next major step in reducing the total acquisition time.

1.3 Individual detection of ^{4}He* atoms

As mentioned in the introduction of this chapter, the 19.8 eV internal energy of ^{4}He* atoms allow them to be detected electronically using a Micro-Channel Plate (MCP). This kind of detector is widely used in high energy physics [67–69], but not commonly found in cold atoms experiments. The electronic detection is one of the main purposes of bringing ^{4}He* atoms to degeneracy. Combined with delay lines, it permits reconstructing the three momentum coordinates of individual atoms after a TOF. Consequently, the 3D momentum distribution of the released gas is accessible with an outstanding momentum resolution and a dynamic range of several orders of magnitude. In addition, this measurement is performed without line-of-sight integration, contrary to the case of optical imaging. All the results presented in this manuscript were achieved thanks to this particular detection method, whose key aspects are now presented.

1.3.1 Description of the MCPs

A Micro-Channel Plate is a thin metallic disc with a series of holes (or channels) in the micrometer range. Ours is the F9142-01 MOD6 Hamamatsu design whose open-to-air ratio, *i.e.* the ratio of the area of the holes to the total area of the MCP, is 90%. The total diameter of the disc is 8 cm, while that of the channels is $d_c = 12$ µm. These channels are drilled at an angle of 20° to the surface normal so that a Helium atom falling into one of them is sure to hit its surface at some point. When this happens, the high internal energy of the metastable atom compared to the work function of the metal ($\sim$ eV) makes the extraction of an electron from the surface possible [70]. By polarizing the MCP, this first electron is accelerated downwards and continues to extract other electrons by hitting

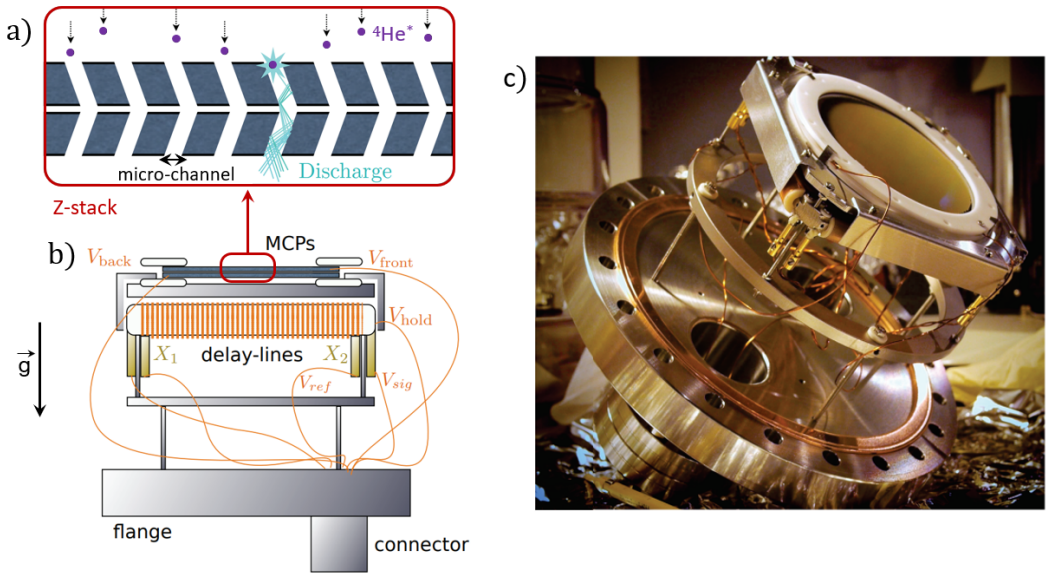

Figure 1.10: **Descriptions of the MCPs and delays lines.** (a) Schematic representation of the electronic discharge triggered by an initial ^{4}He* atom falling into a micrometer channel of two MCPs in a Z-stack configuration. (b) Schematic description of how the MCPs and the delay lines are mounted on a flange. (c) Photograph of the mounting represented in (b).

the surfaces, producing an avalanche process (see Figure 1.10). In our experiment, two MCPs are attached in a Z-stack configuration to amplify this electronic discharge further [71]. By applying a voltage of 2.4 kV between the plates, an initial ^{4}He* atom hitting the MCPs produces an electronic shower of $\sim 10^8$ electrons at the channel exit. By itself, this signal is insufficient to know when and where an atom has fallen. However, the position and arrival time of a ^{4}He* atom onto the MCPs can be inferred by coupling the electronic discharge to delay lines.

1.3.2 Delay lines and reconstruction of spatial distributions

Underneath the MCPs are two Roentdek delay lines, consisting of two metallic wires perpendicularly wrapped around a holding board about a hundred times (see Figure 1.11). The electronic discharge couples to these wires, resulting in the contra-propagation of two pulses towards the extremities of each waveguide. To reconstruct the 3D position of an atom, one must find its corresponding quadruplet $(t_{x_1}, t_{x_2}, t_{y_1}, t_{y_2})$ among the list of arrival times. This is the role of the "reconstruction algorithm", which operates in two steps. The algorithm first collects all the pulses in the channels x_1, x_2, y_1 and y_2 that belong to a time interval of 100 ns. This duration represents the longest time a pulse propagating at $v_g = 20$ cm/ns can spend inside the $L_{dl} = 20$ m long delay lines [72]. Consequently, the four pulses of a single detection event must be contained within this time window. The job is done if only one pulse in each channel satisfies this condition. Otherwise, the algorithm computes the quantity D:

$$D = t_{x_1} + t_{x_2} - (t_{y_1} + t_{y_2}) \tag{1.8}$$

for each possible quadruplet among the list of arrival times satisfying the first condition. By construction, D equals zero when the arrival times correspond to the same detection event. Therefore, the four pulses for which D is the closest to zero are assigned to the same atom. These times are removed from the list, and the procedure is repeated with the remaining ones until each detection event has been identified.

After having found the quadruplet $(t_{x_1}, t_{x_2}, t_{y_1}, t_{y_2},)$ of a single detection event, one can derive the impact position (x_i, y_i) of the discharge on the grid, which identifies with the position (x, y) of the initial ^{4}He* atom on the surface of the MCP:

$$x = \frac{1}{2}\left(t_{x_1} - t_{x_2}\right) v_g \tag{1.9}$$

$$y = \frac{1}{2}\left(t_{y_1} - t_{y_2}\right) v_g \tag{1.10}$$

The quadruplet $(t_{x_1}, t_{x_2}, t_{y_1}, t_{y_2},)$ also gives the impact time of the pulse:

$$t_i = t_{x_1} + t_{x_2} - \frac{L_{dl}}{v_g} = t_{y_1} + t_{y_2} - \frac{L_{dl}}{v_g} \tag{1.11}$$

The vertical coordinate of an atom is then obtained from $z = v_{COM} \times t_i$, with v_{COM} the vertical velocity of the cloud's center-of-mass when hitting the MCPs. The latter being located 43 cm below the center of the science chamber, the cloud's center-of-mass undergoes a TOF of $t_{TOF} = 297$ before reaching the MCPs with a velocity $v_{COM} = 2.9$ m/s. Therefore, the precise determination of the quadruplets $(t_{x_1}, t_{x_2}, t_{y_1}, t_{y_2})$ yields the 3D spatial coordinates of each atom reaching the MCPs.

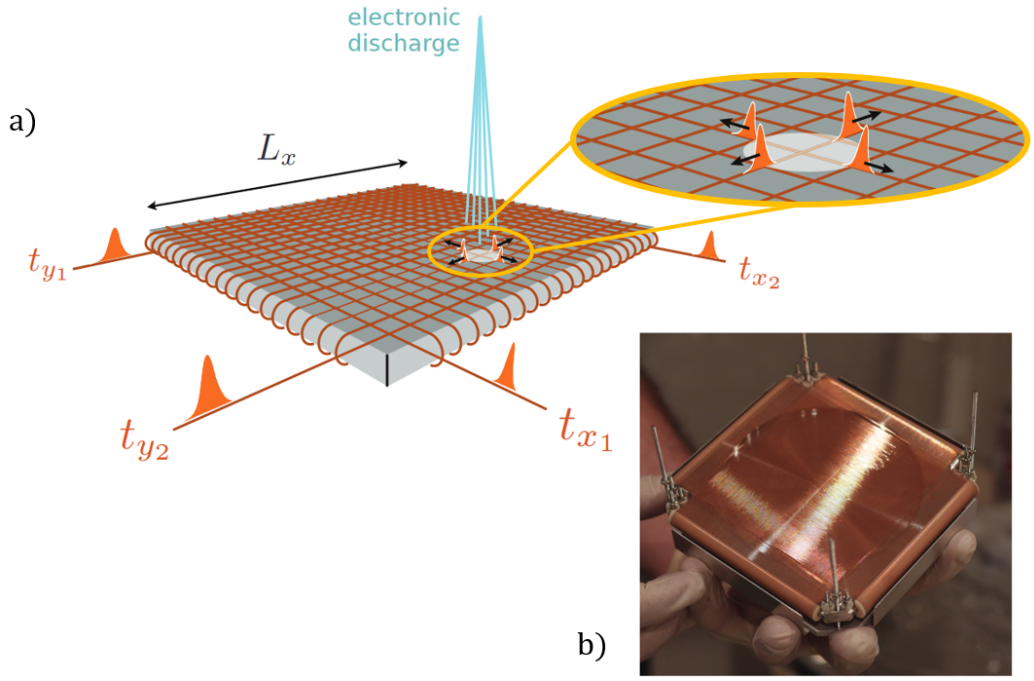

Figure 1.11: **Delay lines.** (a) Schematic representation of the delay lines. After the impact of an electronic discharge, two pulses propagate in opposite directions towards the extremities of both delay lines. Their arrival times $(t_{x_1}, t_{x_2}, t_{y_1}, t_{y_2})$ allows to reconstruct the spatial coordinates of the atoms. (b) Photograph of the delay lines.

1.3.3 Electronic chain and resolution of the detector

The resolution on the spatial distributions is directly determined by the temporal resolution on the pulse arrival times. For example, resolving two atoms separated by 1 mm on the MCPs plane and propagating along the x or y axis at speed $v_\perp = 10\,\text{cm} \times (v_g/L_{dl}) = 10^6$ m/s requires a temporal resolution of $2 \times 10^{-3}/10^6 = 2$ ns. We thus need fast electronics. In addition, assigning an arrival time to a pulse with such a precision is not straightforward when all pulses do not share the same amplitudes. Those depend on how well the electronic discharges couple to the delay lines, and strongly vary between the detection events. In this case, the naive approach of choosing as the arrival time the moment when a signal exceeds an amplitude threshold is not sufficiently sophisticated. Indeed, stronger pulses may be detected earlier than weaker ones, even if their arrival times are identical. This issue is overcome by using a Constant Fraction Discriminator (CFD), which determines the maximum of a pulse by finding the zero of its slope. To do that, the CFD transforms an initial pulse into a bimodal one:

$$V_{\text{CFD}}(t) = V_{\text{pulse}}(t) - f_c \times V_{\text{pulse}}(t - \tau) \tag{1.12}$$

using the so-called constant fraction $f_c \in [0, 1]$ and a delay τ. The zero-crossing of this bimodal pulse indicates when the maximum of the actual pulse is reached and is used to trigger a $0 - 1$ V signal with sharp rising edges. This signal is sent to an FPGA-based time-to-digital converter (TDC) [73] which converts it into digital time, with a coding step of $t_0 = 10$ ps.

This coding step gives us a first idea of the best resolution achievable by the whole detection chain. Along the lines of Equations 1.9 and 1.10, this minimum time interval

corresponds to a pixel size in the MCP plane given by:

$$\Delta x = \Delta y = \frac{1}{2} t_0 v_g = 60\,\mu\text{m} \tag{1.13}$$

which corresponds to the minimum bound of the in-plane resolution. However, any noise in the electronic chain affects the assignment of arrival times and consequently enlarges the resolution. This noise was measured experimentally in [48, 73] and yields the in-plane resolution:

$$\sigma_{x/y} \approx 120\,\mu\text{m} \tag{1.14}$$

At first glance, the situation is far more favorable for the vertical resolution. Indeed, the smallest vertical distance Δz resolved by the coding time and its value after accounting for the electronic noise are both much smaller than the horizontal resolution:

$$\Delta z = v_{\text{COM}} t_0 \simeq 0.35\,\text{nm} \tag{1.15}$$

$$\sigma_z \approx 0.5\,\text{nm} \tag{1.16}$$

However, the vertical resolution is actually limited by a geometrical constraint. As shown in Figure 1.12, the 20° angle of the channels implies that two atoms separated vertically by a distance smaller than $d_c/\tan(20)$ cannot be distinguished. This distance represents a minimum uncertainty in estimating the z coordinate of each atom, which limits the vertical resolution to:

$$\sigma_z = d_c/\tan(20) \approx 33\,\mu\text{m} \tag{1.17}$$

As it will be discussed in Section 1.5, the spatial atomic distribution after a TOF from an optical lattice can be related to the in-trap momentum distribution via the ballistic relationship:

$$\hbar \boldsymbol{k} = \frac{m\boldsymbol{r}}{t_{\text{TOF}}} \tag{1.18}$$

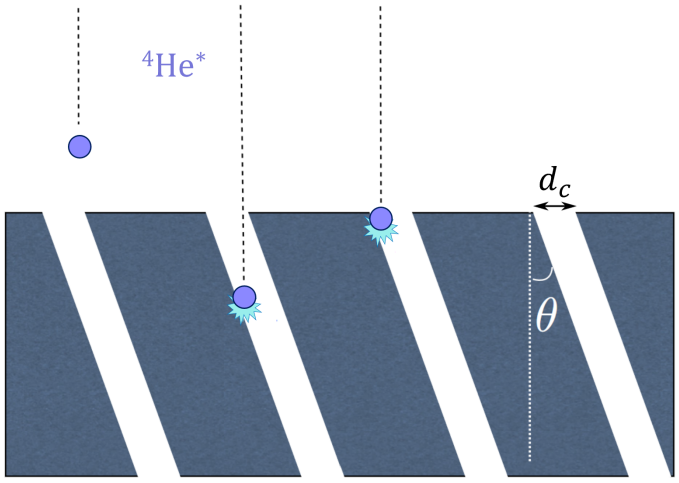

Figure 1.12: **Geometrical constraint on the vertical resolution.** The channels are drilled at an angle of $\theta = 20°$ to the normal to the MCP surface to ensure that a ^{4}He* atom hits the wall at some point. Because of this angle, both atoms A and B are detected simultaneously, although their arrival times differ. This effect limits the vertical resolution to $d_c/\tan(20) \approx 33$ µm.

Consequently, the spatial resolutions of Equations 1.14 and 1.17 converts into the momentum resolutions:

$$\sigma_{k_x/k_y} = \frac{m\,\sigma_{x/y}}{\hbar\,t_{\mathrm{TOF}}} \approx 3\times10^{-3}\,k_d \qquad \sigma_{k_z} = \frac{m\,\sigma_z}{\hbar\,t_{\mathrm{TOF}}} \approx 9\times10^{-4}\,k_d \tag{1.19}$$

where $k_d \simeq 8.1\ \mu\mathrm{m}^{-1}$ is our lattice wave vector. Verifying experimentally such small resolutions is not straightforward because it requires measuring momentum structures with sizes of the same order of magnitude. Sufficiently small structures can be obtained by considering the bunching peak associated with Hanbury-Brown and Twiss correlations. This effect is discussed in detail in section 3.2.2. In short, the second order correlation function $g^{(2)}(\boldsymbol{k},\boldsymbol{k'})$ of a bosonic system with Gaussian statistics should reach 2 when considering $\boldsymbol{k'} = \boldsymbol{k}$. However, this amplitude is reduced if the size of the associated correlation peak is of the order of the detector resolution. Therefore, the reduction of the peak amplitude compared to 2 provides a way to quantify the resolution. Since the size of the correlation peak is inversely proportional to the system size, the goal is to measure the bunching amplitude of large trapped systems with Gaussian statistics. The best candidate for us is a thermal cloud trapped in the ODT before the evaporation ramps. The cigar-shaped trap makes the gas more elongated along the x axis, and the bunching peak is consequently narrower in this direction. The associated bunching amplitude was reduced to 1.33(1), which allowed us to deduce a resolution $\sigma_{MCP} = 2.9(3)\times10^{-3}\ k_d$ compatible with the estimate based on the electronic noise measurement. Importantly, this measurement was voluntarily performed at high atom numbers to enlarge the system in the trap and decrease the bunching width further. However, all the results reported in this manuscript were obtained with much smaller atom numbers for which the correlation signals are wide enough not to be affected by the detector resolution.

1.3.4 Limitations of the detector

The combination of MCPs with delay lines and a long TOF allows the detection of individual atoms with an unprecedented resolution in momentum space. On the other hand, this detector suffers from several limitations. The main ones are its quantum efficiency, detection range, and saturation.

Quantum efficiency, noted η_{MCP}, is the ratio between the number of atoms detected and the number of atoms falling onto the MCP. It is limited by a low open-to-air ratio, which results in a high probability of an atom missing a micrometer channel. This cause affects us only slightly, as this ratio is 90% for our MCP model. The probability for an atom falling inside a channel to ionize a first electron, and for this electron not to escape the channel also limits the quantum efficiency. Low quantum efficiencies are particularly problematic for detecting correlations between particles since there are as many powers of η_{MCP} as there are particles between which correlations are computed. The measurement of this quantum efficiency for our MCP, presented in Section 1.4, yields $\eta_{\mathrm{MCP}} = 53(2)\%$.

The detection range of the MCP is limited by its 8 cm diameter, which cuts into the transverse velocity distribution of the released cloud. This is even more true with a TOF as long as ours, and is the trade-off for our excellent momentum resolution. This constraint does not affect the vertical detection range and is not a problem when measuring BECs, which are narrow structures even after the TOF. However, it does limit the observation of lattice gases to the first Brillouin zone and becomes a real challenge for measuring the high-momentum tails of 1D Bose gases [74].

Saturation of the detection chain occurs in three different forms. The first is the local saturation of the MCP itself when working with high atomic flux. This effect arises from the time it takes for a micrometer channel to replenish its electrons after an avalanche process. If another $^4He^*$ atom enters the channel in the meantime, the amplification of the ionized electron may be too low for the resulting pulses to be detected by the electronics. This saturation is well known when working with MCPs [28, 75], and a previous investigation in our team [48, 49, 73] concluded that it occurs with our MCP for an atomic flux of the order of 250×10^3 atoms/cm^2/s. This threshold is reached when working with BECs or lattice superfluids. To study the number of atoms in the densest parts of these clouds, it is necessary to artificially reduce the atomic flux on the detector (see section 1.4). The second type of saturation comes from the electronics of the detection chain. More precisely, the TDC contains a multiplexer working at 16.4 MHz to transmit the arrival times of the pulses to the computer, which limits the detection of events to 4.1 MHz per channel. The final saturation effect comes from the reconstruction algorithm, which has difficulty identifying the correct time quadruplets when the atomic flux is high. This mixing of arrival times between different detection events is indicated by a "saturation cross" in the plane $k_z = 0$ of the momentum distributions (see Figure 1.13). Indeed, one can show [48] that the criteria used for the pulse assignment are not error-proof and can lead, for high fluxes, to erroneously reconstructed atoms for which the arrival times have been mixed. This mixing artificially adds atoms on the $\pm 45°$ directions of the MCP images (which do not coincide with the $+45$ and -45 lattice directions), hence the saturation cross. According to the constructor, a solution to this third type of saturation is provided by working with hexagonal delay lines that would lead to the emission of six pulses for each detection event. This higher number of pulses per atom results in lifting the uncertainty of the pulses assignment.

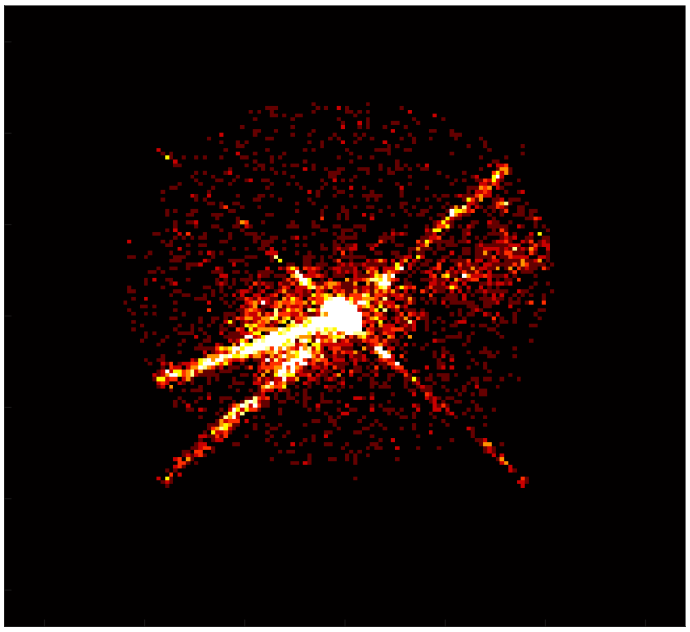

Figure 1.13: **Saturation cross on the MCPs.** Time-integrated top view of the atom's impacts on the MCP surface, where one dot represents each detected atom. The saturation cross is made up of erroneous atoms reconstructed along the $\pm 45°$ axis of the image. The almost horizontal line corresponds to real atoms trapped inside an arm of the ODT, that are released during optical evaporation.

1.4 Implementing a two-photon Raman transfer

The fact that condensation is reached in the $m_J = 1$ sublevel of the $2\,^3S_1$ excited state is problematic for our detection after a long TOF because this sublevel is sensitive to the magnetic field. Therefore, any residual magnetic gradient during during the 43 cm TOF deviates the atoms and destroys the correspondence between the measured spatial distribution and the momentum distribution in the trap. Fortunately, this effect is circumvented by transferring the atoms to the $m_J = 0$ sublevel at the beginning of the TOF. For the first months of my Ph.D., this transfer was done by splitting the sublevels of the $2\,^3S_1$ state with a magnetic bias and addressing the resulting Zeeman shift $\Delta E \simeq h \times 13$ MHz between the $m_J = 0$ and $m_J = 1$ sublevels with a radio-frequency (RF) wave. Although easy to implement, such a technique has a fundamental limitation: the RF wave is also resonant with the $m_J = 0 \rightarrow m_J = -1$ transition, bounding the maximum transfer to the $m_J = 0$ state to 50% of the condensed atoms. This barrier dramatically limits the overall efficiency of our detection chain, as it adds a factor 1/2 to the already low MCP's detection efficiency. This effect is not too problematic if one is only interested in measuring the momentum occupation average, namely the momentum density. This is actually the case for the data presented in the next chapter, for which the efficiency of the RF transfer has even been lowered to avoid saturating the MCPs. However, one of the strengths of our experiment is the ability to measure momentum correlations between individual particles. Because such measurements rely on the joint detection of several atoms, they are more affected by the detection efficiency the higher the order of the correlations. To overcome this issue, we replaced the RF transfer by a two-photon Raman transfer that allows keeping 100% of the condensed atoms. This improvement is at the origin of the experimental results presented in Chapters 3 and 4. This section summarizes the implementation of the Raman transfer, whose first use was to calibrate precisely the MCP's detection efficiency.

1.4.1 Brief description

The comparison between the RF and Raman transfer configurations is shown in Figure 1.14. In both cases, the magnetic sublevels of the $2\,^3S_1$ state are split by a Zeeman shift ΔE. While the condensed and detected states are directly coupled in the RF case, the optical transfer relies on a two-photon process addressing the intermediate $|2\,^3P_0\ ,\ m_J = 0\rangle$ state. More specifically, a Pump beam, σ^- polarized, couples the $|2\,^3S_1\ ,\ m_J = 1\rangle$ and $|2\,^3P_0\ ,\ m_J = 0\rangle$ states, while a Stokes beam, π polarized, couples the $|2\,^3P_0\ ,\ m_J = 0\rangle$ and $|2\,^3S_1\ ,\ m_J = 0\rangle$ states. Absorption of a Pump photon followed by stimulated emission into the Stokes beam allows the transfer of atoms from the condensed state to the detected one. In the experiment, the beams are co-propagating to avoid any simultaneous transfer of momentum that would affect the reconstruction of the in-trap momentum distributions. This co-propagation is achieved by using a single polarization-maintaining optical fiber to send both beams onto the atoms. The beam's polarizations are set to be linear and orthogonal. At the exit of the fiber, a half-wave plate allows to control the polarization orientation of the beams. The Stokes π-polarization is obtained by aligning its linear polarization with the quantization axis of the magnetic field, defined along the x-axis. In contrast, the Pump beam's linear polarization splits into a σ^- and a σ^+ components. The former is used for the transfer, while the latter does not interact with the atoms because there is no sublevel of the $2\,^3P_0$ state to which couple them. This means that half the power of the Pump is useless, and so twice as much power has to be put on the Pump

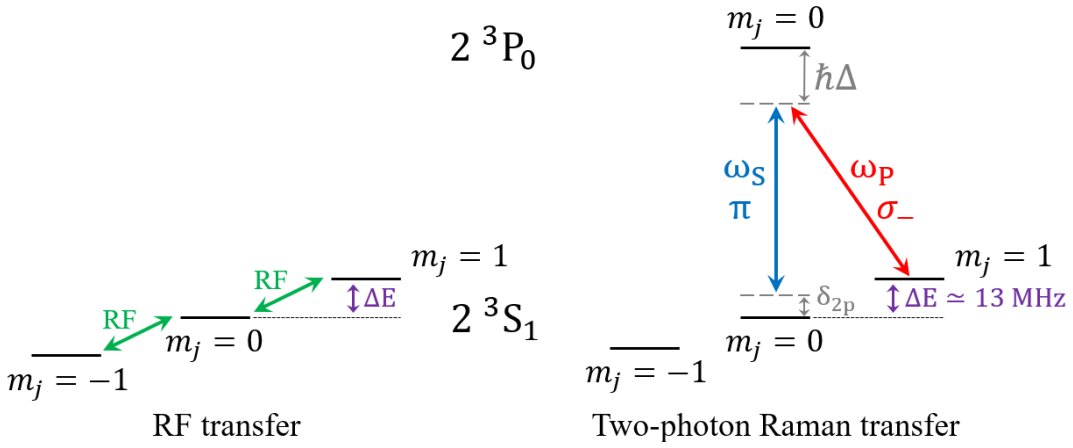

Figure 1.14: **RF transfer and two-photon Raman transfer configurations.** Rf transfer addresses directly the transition between the $|2\,^3S_1\ ,\ m_J = 0\rangle$ and $|2\,^3S_1\ ,\ m_J = 1\rangle$ states, and is limited to 50% as the $|2\,^3S_1\ ,\ m_J = -1\rangle$ state can also be populated. Conversely, a two-photon Raman transfer relies on a Λ-configuration in which only the condensed and detected states could be coupled, leading to the possibility of a 100% transfer (see text).

beam than on the Stokes one to reach a symmetrical configuration.

To transfer the atoms from the $m_J = 1$ to the $m_J = 0$ sublevel of the $2\,^3S_1$ state, one must satisfy the conditions of *(i)* large one-photon detuning $\Delta \gg \Gamma$ to avoid one-photon absorption towards the intermediate state, and *(ii)* two-photon resonance $\delta_{2p} = 0$ so that the energy difference between both beams matches the Zeeman shift ΔE. To reach large Δ, a first double-pass AOM (originally intended for saturated absorption spectroscopy) applies a $2 \times (-200)$ MHz detuning to the $2\,^3S_1 \rightarrow 2\,^3P_0$ transition at the output of an External-Cavity Diode laser [76]. This light is then split into two beams, the Pump and Stokes ones, which both possess their own double-pass AOM. The Pump AOM adds an additional and fixed $2\times(-200)$ MHz detuning, while that of the Stokes adds a controllable detuning of roughly $2\times(-193.5)$ MHz. These settings fulfill the conditions *(i)* and *(ii)* since they correspond to $|\Delta| = 800$ MHz and $\delta_{2p} = \nu_{\text{Stokes}} - \nu_{\text{Pump}} = 13$ MHz. The large value of Δ, permitted by the 29.9 GHz separation between the $2\,^3P_0$ and $2\,^3P_1$ states, allows to eliminate adiabatically the intermediate $2\,^3P_0$ state. The three-level Λ-configuration becomes equivalent to an effective two-level system driven by the effective Hamiltonian:

$$\hat{H}_{\text{eff}} = \begin{pmatrix} 0 & \Omega_{2p} \\ \Omega_{2p} & -\delta' \end{pmatrix} \tag{1.20}$$

The two-photon Rabi frequency and detuning are expressed as $\Omega_{\text{eff}} = \Omega_S\Omega_P/2|\Delta|$ and $\delta' = \delta_{2p} - (\Omega_S^2 - \Omega_P^2)/4\Delta$. Provided that the optical powers of the Pump and Stokes beams are equal (symmetric configuration), the lightshifts $\Omega_{S/P}^2/4\Delta$ cancel out, and the detuning is only given by δ_{2p}. The unitary dynamics of an atom under such Hamiltonian is well known [77]: the atom performs Rabi oscillations between states $|2\,^3S_1\ ,\ m_J = 0\rangle$ and $|2\,^3S_1\ ,\ m_J = 1\rangle$, at an effective Rabi frequency:

$$\Omega_{\text{eff}} = \sqrt{\frac{\Omega_S^2\Omega_P^2}{4\Delta^2} + \delta_{2p}^2} \tag{1.21}$$

The maximum transferred efficiency is given by the ratio $\Omega_{2p}^2/\Omega_{\text{eff}}^2$, which means that 100%

transfer can be achieved when the two-photon resonance condition $\delta_{2p} = 0$ is met and the pulse duration is π/Ω_{2p} (π-pulse).

1.4.2 Experimental calibration

The two-photon Raman transfer must be carefully implemented. The first step consists in setting the beams' alignment onto the atoms. By sending the Pump beam alone onto a BEC, in a configuration that maximizes the one-photon absorption (small $|\Delta|$, high optical power), the amount of losses on absorption images informs us of how good the alignment is. The latter is optimized by maximizing the losses while decreasing the optical power in the Pump beam from a few mW to tens of µW. The orientation of the half-wave plate at the output of the Raman fiber is calibrated in the same way. After that, one can check that sending the Stokes beam alone on the condensed atoms has no effect. This is due to the π-polarization of the beam, which cannot couple the $|2\,^3\mathrm{S}_1\ ,\ m_J = 1\rangle$ and $|2\,^3\mathrm{P}_0\ ,\ m_J = 0\rangle$ states. At this stage, setting $|\Delta| = 800$ MHz and twice as much power in the Pump beam than in the Stokes one generally allows imaging partially a BEC on the MCP by performing a preliminary two-photon Raman transfer. Naturally, the parameters δ_{2p} and Ω_{eff} have still to be optimized. This second part is more like a daily calibration, which must be repeated before taking any data.

This calibration starts by measuring the Raman resonance frequency corresponding to the condition $\delta_{2p} = 0$. To do that, the optical power is reduced to 30/60 µW for the Stokes/Pump beams before the Raman fiber to achieve slow Rabi oscillations of ~ 200 µs period. These settings allow us to use rather long pulse durations of ~ 50 µs to increase the energy resolution, while staying at the beginning of the first Rabi oscillation. Note that the pulse duration cannot be extended much further as the transfer would then be sensitive to magnetic field fluctuations. To locate the two-photon resonance, the Stokes AOM detuning is varied around -387 MHz. Two things happen when approaching the resonance frequency: the transfer efficiency increases $\left(\Omega_{2p}^2/\Omega_{\mathrm{eff}}^2 \to 1\right)$ and the Rabi oscillations become slower ($\Omega_{\mathrm{eff}} \searrow$). Both effects act in opposite ways on the transferred atom number, but the first one dominates and the transferred atom number is maximum at the resonance. A Lorentzian fit provides the Stokes AOM frequency corresponding to the two-photon resonance condition $\delta_{2p} = 0$. The second part of the calibration procedure is to set the π-pulse duration to $\Delta t \sim 10$ µs. To do this, Rabi oscillations are measured for different optical powers at the input of the Raman fiber until the period of the oscillations reaches the desired value of 20 µs. The π-pulse duration is chosen as small as possible (given the time resolution of our experimental sequencer) for two reasons. One is simply to be less sensitive to magnetic field fluctuations. The other one results from the presence of a residual magnetic gradient of 0.17 G/cm in our experiment, affecting the atoms in the $m_J = 1$ sublevel during the TOF. For long pulse durations, the gas expands sufficiently that this magnetic gradient induces different Zeeman shifts between different parts of the atomic cloud, preventing the transfer from being resonant with the whole cloud at the same time. Finally, a simple observable to verify that the transfer is properly calibrated is to detect twice as many atoms on the MCP as with the RF transfer.

1.4.3 Measurement of the MCP detection efficiency

The first use of the two-photon Raman transfer was to quantify the MCPs' quantum efficiency η_{MCP}, defined as the ratio between the number of atoms detected and the actual number of atoms falling onto the detector. As mentioned in Section 1.3.4, this ratio is not limited in our case by a poor open-to-air ratio, as ours reaches 90%. What is left are the probabilities for an initial $^4\mathrm{He}^*$ atom to ionize the first electron and for this electron not to escape the channel. This last probability is about 1/2 and constitutes a higher bound for η_{MCP}. Still, we expect a larger value than those typically reported for MCPs with lower open-to-air ratios. For instance, a quantum efficiency of $25 \pm 15\%$ was reported in [78] for a 60% open-to-air ratio.

The measurement of η_{MCP} with the RF transfer can only be approximate. Indeed, the limited RF power implies relatively slow Rabi frequencies ≤ 8 kHz. Consequently, the maximum 50% transfer achievable requires long pulse durations ~ 100 µs, for which the resonance condition becomes sensitive to magnetic field fluctuations. To avoid large shot-to-shot fluctuations of the transferred atom number, we used to work with shorter pulses for which the transfer efficiency ($< 50\%$) was never known exactly. The implementation of a two-photon Raman scheme makes it possible to circumvent this obstacle because the optical power available to us leads to Rabi frequencies of ~ 100 kHz, which are sufficiently large to perform tens of Rabi oscillations in a few tens of microseconds. From these Rabi oscillations, we can access the MCP detection efficiency η_{MCP} via the formula:

$$N_{\mathrm{MCP}} = N_{\mathrm{BEC}} \left(\frac{\Omega_{2\mathrm{p}}}{\Omega_{\mathrm{eff}}}\right)^2 \sin^2\left(\frac{\Omega_{\mathrm{eff}}\Delta t}{2}\right) \eta_{\mathrm{MCP}} \tag{1.22}$$

$(\Omega_{2\mathrm{p}}/\Omega_{\mathrm{eff}})^2 \sin^2(\Omega_{\mathrm{eff}}\Delta t/2)$ represents the fraction of the initial BEC atom number N_{BEC} that is transferred to the $|2\,^3\mathrm{S}_1\ ,\ m_J = 0\rangle$ state by the Raman pulse, whose duration Δt sets the position on the Rabi oscillation. η_{MCP} relates this number of atoms reaching the detector to the number actually detected N_{MCP}. For a π-pulse, the two-photon Raman transfer is maximal, and η_{MCP} is obtained from:

$$N_{\mathrm{MCP}}^{\mathrm{max}} = N_{\mathrm{BEC}} \left(\frac{\Omega_{2\mathrm{p}}}{\Omega_{\mathrm{eff}}}\right)^2 \eta_{\mathrm{MCP}} \tag{1.23}$$

Equation 1.23 does not account for the effect of saturation, which is hardly measurable. As a consequence, the two-photon resonance condition cannot be met in the measurement of η_{MCP} as the resulting atomic flux on the MCP would induce saturation and falsify N_{MCP}^{max}. The trick is to perform Rabi oscillations with off-resonance Raman transfers, where large two-photon detunings $\delta_{2\mathrm{p}}$ ensure low transfer efficiencies and prevent saturating the detector. Knowing the value of $\delta_{2\mathrm{p}}$, the measurement of Ω_{eff} yields the two-photon Rabi frequency $\Omega_{2\mathrm{p}} = \sqrt{\Omega_{\mathrm{eff}}^2 - \delta_{2\mathrm{p}}^2}$ while $N_{\mathrm{MCP}}^{\mathrm{max}}$ is obtained from the maximum transfer of the Rabi oscillation. A separated calibration of N_{BEC} with absorption imaging finally gives η_{MCP}. This experimental procedure relies on the precise knowledge of the two-photon detunings and, thus, of the two-photon resonance frequency. As aforementioned, the latter is routinely estimated from the maximum transferred atom number measured when scanning the Stokes beam detuning. However, a more accurate (and time-consuming) estimate can be obtained from Rabi oscillations performed at fixed optical power ($\Omega_{2\mathrm{p}}$ constant) and various Stokes beam detunings $\Delta\nu$. Fitting the measured Ω_{eff} with the scaling of Equation 1.21 allows to extract $\delta_{2\mathrm{p}}$ from the position of the minimum, as shown

in Figure 1.15 (a). This preliminary calibration is followed by the off-resonance Rabi oscillations. For the latter, initial BECs of $N_{\mathrm{BEC}} = 2 \times 10^5$ atoms are transferred onto the $m_J = 0$ state with a two-photon Raman transfer of fixed optical power ($\Omega_{2\mathrm{p}} = 20$ kHz) and large two-photon detunings ($\delta_{2\mathrm{p}} \in [300; 1000]$ kHz). Figure 1.15 (b) summarizes the results: the maximum atom number transferred $N_{\mathrm{MCP}}^{\mathrm{max}}$ for each detuning is plotted versus all the other terms of Equation 1.23 except η_{MCP}. The expected linear scaling is found, whose slope is fitted to obtain the MCPs' quantum efficiency $\eta_{\mathrm{MCP}} = 53(2)\%$, where the error denotes the fit uncertainty. This value is consistent with the fact that the quantum efficiency should mainly be limited in our case by the 1/2 probability for the first ionized electron to escape from the micrometer channel.

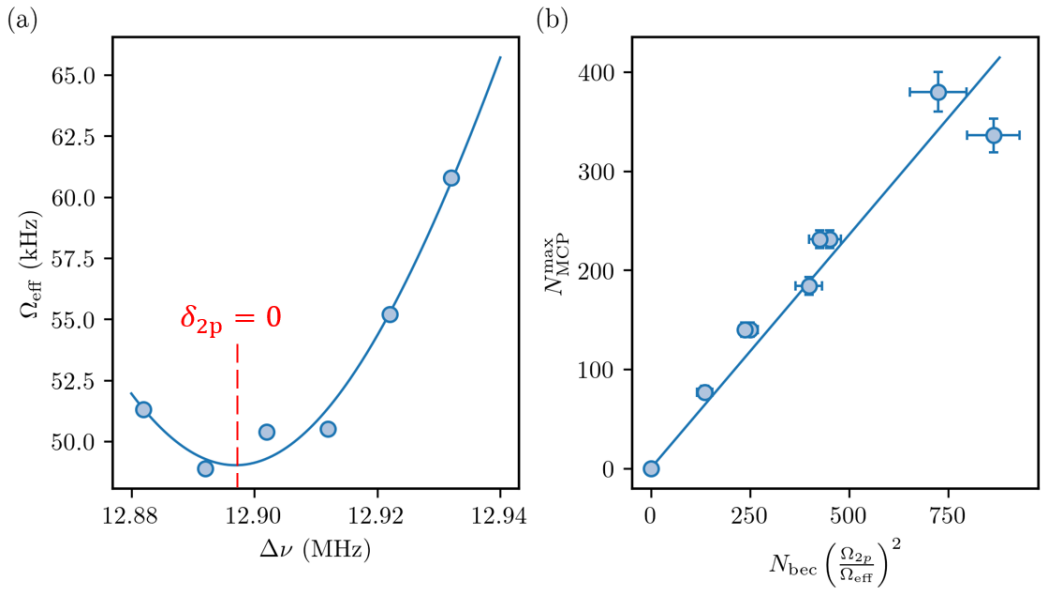

Figure 1.15: **Measurement of the MCP's quantum efficiency.** (a) The two-photon resonance frequency is extracted using the scaling of Equation 1.21 and the measured Ω_{eff} at various Stokes beam frequencies. (b) Maximum atom number transferred with off-resonance Rabi oscillations versus $N_{\mathrm{BEC}} (\Omega_{2\mathrm{p}}/\Omega_{\mathrm{eff}})^2$. According to Equation 1.23, the slope of this curve corresponds to the MCPs' detection efficiency. A linear fit yields $\eta_{\mathrm{MCP}} = 53(2)\%$.

1.4.4 Improvements of the Raman transfer

The two-photon Raman transfer has received several improvements after its first implementation, mainly to enhance its stability and repeatability. They are listed here to conclude this section.

The first change was to replace the homemade External-Cavity Diode (ECD) laser with a mono-mode fiber laser from NKT Photonics that we had at our disposal. This choice originated from the slow drift of the ECL laser wavelength on the time scale of tens of minutes, illustrated in Figure 1.16. This drift was problematic as, for a long period, the Raman transfer had to be done without a spectroscopy cell because it was under repair. Therefore, we could not perform saturated absorption to lock the laser wavelength on the transition $2\,^3\mathrm{S}_1 \rightarrow 2\,^3\mathrm{P}_2$, and had to adjust it manually several times a day. On the contrary, NKT's laser does not drift, which makes it more stable in the long term. Note

that the early fast decrease of the ECD laser wavelength in a few tens of seconds simply corresponds to the laser needing some time to stabilize time when switched on. After already two hours, the wavelength drift corresponds to a frequency shift of ~ 180 MHz, which affects the one-photon resonance condition of the Raman transfer and makes Ω_{2p} decreased by $\sim 22\%$. Consequently, the π-pulse duration changes, and the transferred atom number decreases over time.

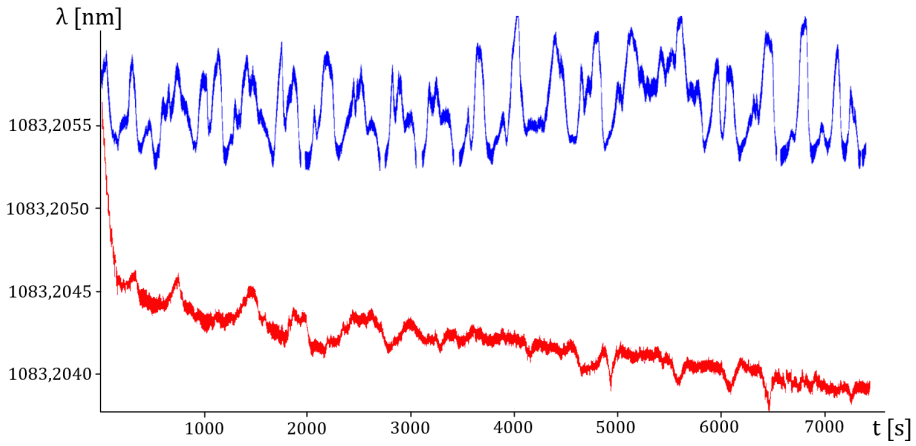

Figure 1.16: **Wavelength stability of the Raman lasers.** The wavelength of the homemade ECD laser (red) and of the commercial NKT model (blue) is recorded for two hours. The slow drift of the ECD laser is problematic for the stability of the two-photon Raman transfer (see text).

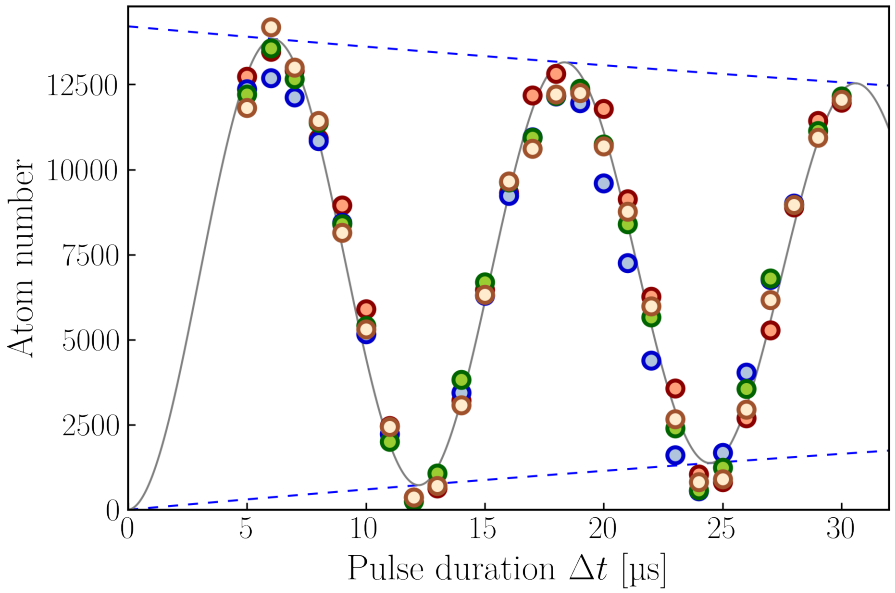

Figure 1.17: **Clean Rabi oscillations.** We repeated the measurement of a Rabi oscillation four times consecutively, each corresponding to a given color. The fact that all points can be placed on a single curve illustrates the stability of the two-photon resonance frequency after replacing the RF drivers.

At some point, significant variations in the transferred atom number made us realize that the two-photon resonance frequency was shifting through the day by several tens

of kilohertz, which is large enough to get strongly out-of-resonance. To solve this issue, we first upgraded the analog card transmitting our sequencer's voltage command to the power supply of the coils shifting the $m_J = 1$ sublevel during the transfer. The idea was to see whether the improved 16-bit encoding of the novel NI PXI-6738 card (12-bit for the old NI PXI-6723 model) could suppress possible magnetic field fluctuations at the origin of the two-photon resonance instability. Indeed, the previous 12-bit encoding of the voltage command setting the $\sim$ 200 MHz detuning of the Stokes AOM could induce relative fluctuations of $\sim 10^{-4}$. Those would result in $\sim$ 40 kHz fluctuations of the Stokes frequency, which agrees with the order of magnitude of the shifts observed on the two-photon resonance condition. On the other hand, a 16-bit encoding would only induce fluctuations of a few kilohertz, to which the two-photon Raman transfer is insensitive. However, the problem persisted after this upgrade. Then, we decided to improve the stability of the Pump/Stokes frequencies by replacing the homemade RF drivers of the AOMs with a more stable arbitrary waveform generator (SDG6022X model from SIGLENT). This choice solved the stability issue, and no shift of the two-photon resonance has been observed since then. The resulting Rabi oscillations are reproducible, as reflected in Figure 1.17 where stable Rabi oscillations were measured four times in a row. These measurements are fitted by a damped Rabi oscillation function (solid gray line) of the form $(N_{\max}/2)\,[1 - \cos(\Omega_{\text{eff}}\,\Delta t)\exp(-\Delta t/\tau)]$, yielding an effective Rabi frequency $\Omega_{\text{eff}} \simeq 80$ kHz and a damping time $\tau \simeq 115$ µs. This damping, illustrated by the dashed blue lines, is attributed to some residual misalignment of the Raman beams. Indeed, such a defect leads to a non-homogeneous intensity profile seen by the atoms, resulting in a mixing of Rabi oscillations at different frequencies.

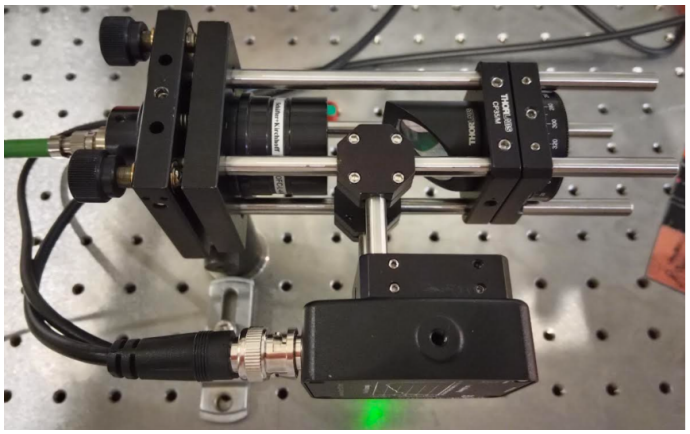

Figure 1.18: **Cage mount of the Raman collimator.** From left to right: the Raman fiber is inserted into a large diameter collimator, followed by a beam sampler reflecting part of the beam onto a photodiode (at the bottom of the image), and finally, a half-wave plate setting the orientation of the polarization axis.

Finally, a previous study of Tan's Contact [79] in 1D Bose gases was limited by the 50% RF transfer efficiency [74]. One of our mid-term objectives is to renew this investigation with the higher statistics offered by the Raman transfer. However, the experimental procedure requires a $\sim$ 15 ms before transferring the atoms to the $|2\,^3\mathrm{S}_1\,,\ m_J = 0\rangle$ state. In the meantime, the $\sim$ 4 mm cloud expansion prevents transferring all the atoms with the Raman transfer because of the $1/e$ beam size of $\sim$ 1.7 mm. This future investigation motivated us to replace the Raman collimator with a larger model (60FC-L-4-M60L-37 from Schäfter+Kirchhoff) whose 24 mm clear aperture should increase the beam size by

a factor ~ 5. We took this opportunity to mount properly all the optical components at the output of the Raman fiber into a cage (see Figure 1.18). The latter contains the new collimator, followed by a beam sampler at 45° reflecting $1\% - 10\%$ (depending on the polarization) of the incident light on a photodiode, and finally the half-wave plate used to orientate the Pump and Stokes polarization axis just before the science chamber. This implementation of the different elements is more robust and limits the risks of accidental misalignment of the beam. In addition, the screws of the collimator mount makes the fine tuning of the alignment easier, and the added photodiode allows us to infer from its voltage the total Raman power sent on the atoms. Note that the larger beam size limits the Rabi frequencies and typically prevents doing π-pulse in less than ~ 100 µs with the 25 mW of the NKT laser. To spare an amplifier, we decided to switch back to the ECD laser whose ~ 170 mW enables 10 µs π-pulses even with the larger collimator. The stability of the Rabi oscillations illustrated in Figure 1.17 was also checked with this new collimator [80].

1.5 Ballistic expansion of interacting lattice gases

As explained in Section 1.3, one of the specificities of our experiment is to combine MCPs and delay lines to detect atomic distributions after TOF with both exquisite resolution and single-atom sensitivity. Another feature of our experiment is to use optical lattices to simulate the Bose-Hubbard Hamiltonian and explore the richness of its associated phase diagram (see Chapter 2). Indeed, our original electronic detection provides new information on the momentum properties of lattice bosons compared to what can be accessed via optical imaging. A prerequisite is therefore to relate the spatial distribution recorded after TOF to the momentum distribution in the trap. Ideally, this is achieved thanks to the ballistic relationship of Equation 1.18. Two conditions are required for this equation to be valid: no interactions should deform the momentum distribution during the TOF, which, in addition, must be long enough for the cloud to reach the far-field expansion regime. The first condition is generally not met when considering a BEC released from a harmonic trap. In this case, the cloud expansion is driven by the mean-field repulsion energy, which distorts the momentum distribution into a so-called parabolic Thomas-Fermi profile [81]. One possible route to avoid the effect of the mean-field potential during the TOF is to switch off interactions using Feshbach resonances [82]. This is however impossible in the case of ^{4}He* for which no Feshbach resonance is accessible. Fortunately, we shall see in the second part of this Section that accessing the in-trap momentum distribution is possible when considering the expansion from an optical lattice. Before that, we briefly describe how such a lattice is implemented in our experiment.

1.5.1 3D Optical lattice

An optical lattice refers to a periodic potential obtained with a standing-wave laser light far-detuned from any atomic transition. Similarly to an optical dipole trap, atoms are either trapped at the maxima or at the minima of the light intensity depending on the sign of the detuning. The simplest implementation of an optical lattice consists in retro-reflecting a laser beam. The resulting interference pattern modulates spatially the light intensity and consequently the potential. This concept is easily extended to higher dimensions by adding retro-reflected beams along other directions of space. To avoid interference effects

between the different lattice beams, the latter are generally detuned from each others by tens of MHz using AOMs. Then, the atoms only feel the sum of the time-average lattice potentials along each lattice axis, which for a 3D cubic lattice writes:

$$V(\boldsymbol{r}) = V_0 \left(\sin^2\left(\frac{k_d}{2}x\right) + \sin^2\left(\frac{k_d}{2}y\right) + \sin^2\left(\frac{k_d}{2}z\right) \right) + \frac{m}{2}\omega_{\text{ext}}^2 r^2 \tag{1.24}$$

The lattice wave vector $k_d = 2\pi/d$ depends on the lattice spacing $d = \lambda_L/2$. V_0 is the lattice potential and is usually expressed as $V_0 = s\,E_r$, with $E_r = h^2/8md^2$ the recoil energy and s the dimensionless lattice depth. This potential varies proportionally to the optical power of the lattice beams and is then easily tuned experimentally. Finally, the second term in Equation 1.24 describes the residual harmonic confinement induced by the Gaussian intensity profile of the lattice beams.

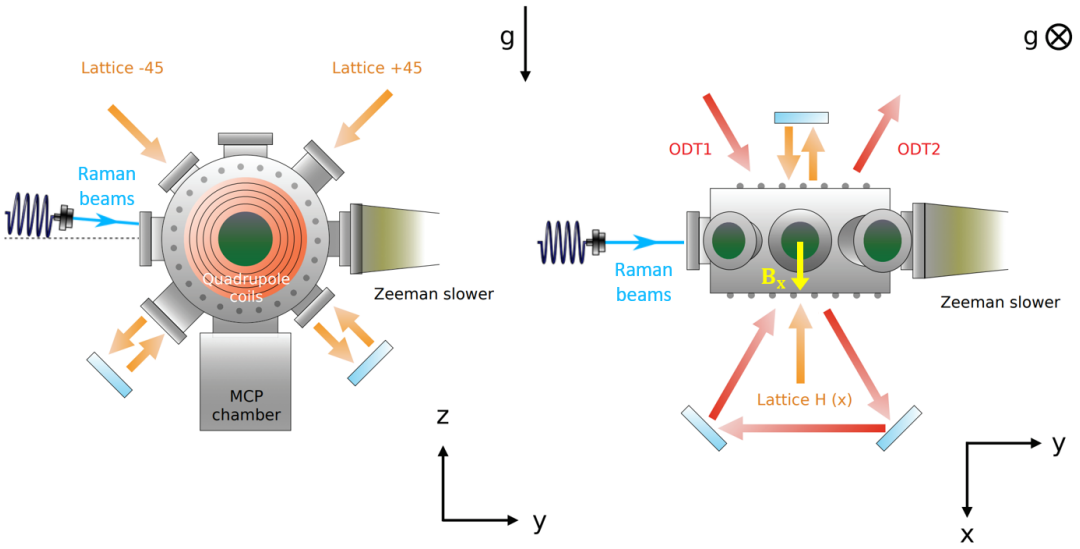

Figure 1.19: **Scheme of the ODT and lattice beams around the science chamber.** The ODT1 beam is recycled into ODT2, after refocusing it and shifting its frequency with an AOM. The names of the lattice beams originate from their orientations around the science chamber. Also represented are the co-propagating Raman beams, for which the quantization axis is set by two coils in Helmoltz configuration producing a magnetic bias along the x-axis (see Section 1.4).

Such a 3D cubic lattice is implemented in our experiment with far red-detuned laser light at $\lambda_L = 1550$ nm. An initial 15 W beam, produced by an Erbium-doped fiber laser (Keopsys), is split into three components which are retro-reflected and intersect at the center of the science chamber. One of the directions is along the x axis and is labeled H. The two other orthogonal directions belong to the yz plane and form an angle of $\pm 45°$ with the y axis, hence their names $+45$ and -45. The lattice beams have a waist of ~ 150 µm and their detunings are respectively $(93, 70, -80)$ MHz for $(H, +45, -45)$. Their orientations around the science chamber are schematically represented in Figure 1.19. To keep the coherence along the ~ 1 m retro-reflection paths, the laser has a narrow linewidth of ~ 40 kHz. Each lattice beam has its own PID controller to lock its amplitude to the desired value, and a photodiode to monitor the beam intensity for the feedback loop. Finally, the Gaussian intensity profiles of the lattice beams adds an external confinement whose frequency depends on the beam waists and intensities. In our experiment, this trapping frequency is expressed as $\omega_{\text{ext}} = 2\pi \times 140 \times \sqrt{s}$ and corresponds typically to few hundred Hertz.

1.5.2 Neglecting mean-field effects and two-body collisions during the TOF

At the mean-field level, atomic interactions are quantified by the interaction energy $U_{\text{int}} = gn$, with n the atomic density and $g = 4\pi\hbar^2 a_s/m$ the coupling constant. The latter depends on the atom mass m and scattering length a_s, which correspond respectively to $m = 4\,u$ and $a_s = 142\,a_0$ for $^4\text{He}^*$ atoms. With our typical experimental numbers, the interaction energy of a BEC in the harmonic optical trap corresponds to $U_{\text{int}}/h \sim 10^3$ Hz. In contrast, the ODT average trapping frequency after the evaporation ramps is only $\bar{\omega} \sim 2\pi \times 300$ Hz, explaining why the expansion from the ODT is driven by the repulsive interaction energy rather than by the kinetic energy. The situation is quite different in the optical lattice, where each lattice site is approximated by a harmonic trap of frequency $\omega_L/2\pi \sim 10^5 - 10^6$ Hz. This energy scale greatly exceeds the mean-field interaction energy, even though the latter is increased compared to the ODT because of the tighter confinement. As a consequence, the early stage of the expansion from the lattice is ballistic. Later during the expansion, another mean-field interaction may kick in when the atomic wavefunctions between different lattice sites overlap. This effect occurs when the spatial extent of the wavefunctions is of the order of the lattice spacing d. By that time, the density has decreased by a factor $(x_{\text{HO}}/d)^3 \sim 10^2$ (for $s = 10$), where x_{HO} is the harmonic length associated with a single lattice site. Therefore, this mean-field interaction can be neglected provided that the initial density is not too high [83]. Finally, interaction energy induces a dephasing between the wavefunctions of lattice sites whose filling differ [84]. The consequence of this dephasing is a reduction of the visibility of the interference pattern after TOF, which can be drastic in the 1D case [85]. However, this effect is far less important in the 3D case ($< 5\%$) [84], provided again that the density is not too high. As shown below, this condition corresponds for us to BECs of a few thousand atoms. This small atom number combined with the tight harmonic confinement at each lattice site and the low atomic mass of the Helium atoms means that the Thomas-Fermi parameter is less than one in the lattice, which is another way of understanding why mean-field effects are negligible during the expansion.

Beyond mean-field interactions, such as two-body collisions, can also affect the early stage of a TOF expansion from a shallow optical lattice. As formally explained in the next chapter, a low-amplitude optical grating behaves like a grating for the coherent matter wave that is the BEC. Consequently, the atomic distributions after the TOF exhibit sharp diffraction peaks whose momentum periodicity, set by k_d, reflects that of the lattice. Elastic collisions during the separation of these different BEC copies result in the presence of scattering halos between the diffraction peaks [86], similar to when two BECs collide [87–89]. Our team has conducted a thorough investigation of this effect in 2020 [90], which is described in the thesis manuscripts of Cécile Carcy [49] and Antoine Ténart [74]. This work concluded that the probability for such collisions to occur during the TOF is only $\sim 10^{-3}$ when considering experimentally relevant atom numbers ($N_{\text{BEC}} = 5 \times 10^3$) and shallow optical lattices ($s = 5$). Therefore, the similar experimental conditions used in this manuscript allow us to safely neglect these collisions.

It is now clearer why the momentum distribution should not be affected by interactions during the TOF. However, the mapping between the momentum and spatial distributions via the ballistic equation 1.18 is only correct under the assumption that the expanding cloud has reached the far-field regime. This condition is equivalent to the Fraunhofer regime in optics and ensures that all the momentum features have had enough time to fully develop. For a trapped system of size L, this condition is fulfilled after an expansion

time [91, 92]:

$$t_{\mathrm{FF}} \simeq \frac{mL^2}{2\hbar} \tag{1.25}$$

Our typical BECs occupy ~ 50 lattice sites which corresponds to a trapped size $L \simeq 39$ µm, and the corresponding far-field time is $t_{\mathrm{FF}} \simeq 50$ ms. Therefore, our experiment's 297 ms TOF is more than enough to satisfy the far-field condition. The measured atomic distribution should then, in principle, map accurately onto the momentum distribution. This assertion was verified experimentally using a comparison with ab-initio Quantum Monte-Carlo (QMC) simulations [93]. QMC algorithms are the only exact numerical approach able to simulate the ab-initio momentum density of our system, provided that the atom number is not too large. These simulations were performed by Tommaso Roscilde (ENS Lyon) using all our experimental parameters (atom number, external trapping frequency, lattice depth) except the temperature. The latter is chosen to minimize the mismatch between numerical and experimental data. An example of this comparison is shown in Figure 1.20 for a shallow optical lattice. The excellent agreement over more than three decades in density confirms that our experiment allows us to measure the in-trap momentum distribution of lattice bosons. In particular, the fact that the experimental diffraction peaks are not larger than the simulated ones confirms that the cloud is detected in the far-field regime of expansion, where even the narrowest features of the momentum distribution are fully developed.

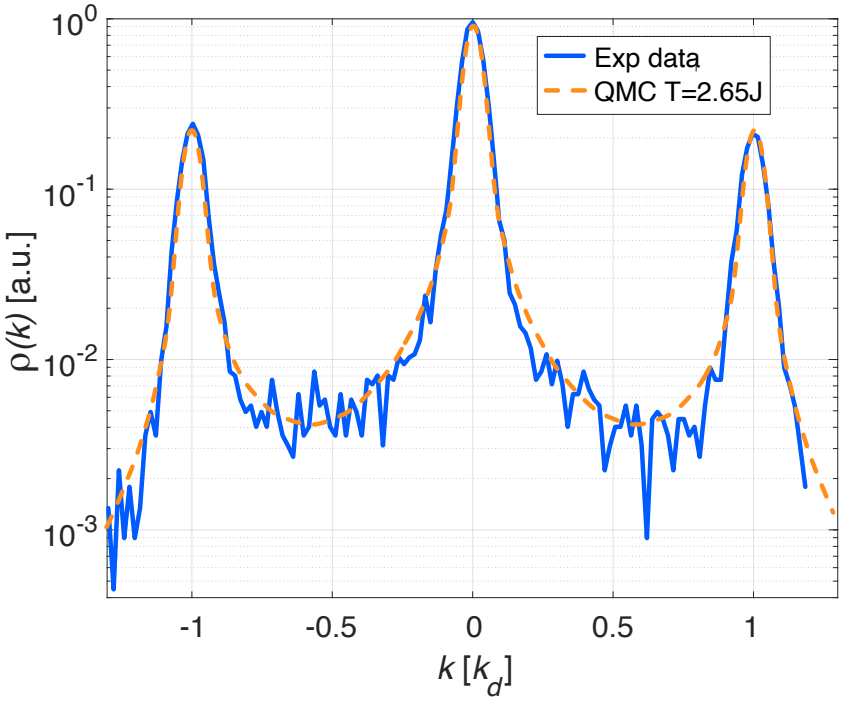

Figure 1.20: **Comparison between the measured density after TOF and ab-initio QMC simulations of the in-trap momentum density.** Temperature is the only adjustable parameter in the simulations and is chosen to minimize the discrepancies between both curves. It is expressed in units of the Bose-Hubbard parameter J, which will be defined in the next chapter. The BEC atom number for these data is only $N_{\mathrm{BEC}} = 3000$ atoms, which explains the noise around $k = 0.5\ k_d$ where the density level is the lowest.

1.6 Conclusion

This first chapter has presented our Helium-4 experiment, which was slightly improved during this thesis to produce BECs of ^{4}He* atoms every ~ 4 s instead of every 6.8 s. This gain has brought us close to the current state-of-the-art cycle duration of 3.3 s, obtained with an innovative experimental setup recently reported by the group of Canberra [38].

A TOF is performed to access the momentum space, after which the clouds are detected electronically by Micro-Channel Plates and delay lines. The 297 ms TOF duration combined with the $t_0 = 120$ ps coding step of the electronic chain allow the detection of individual ^{4}He* atoms with an extreme momentum resolution. In addition, the TOF duration is far superior to the far-field condition $t_{\mathrm{FF}} \simeq 50$ ms for Helium, required for a correct mapping between the spatial and the momentum distributions. To avoid residual magnetic fields affecting the momentum distributions during such a long TOF, the atoms are transferred from the condensed state $|2\,^3\!1_1, m_J = 1\rangle$ to the detected state $|2\,^3\!1_1, m_J = 0\rangle$ at the beginning of the expansion. During this thesis, we replaced the old RF transfer by a two-photon Raman transfer to gain a factor of two on the statistics of the detected distributions.

Considering BECs of moderate atom number released from an optical lattice, both mean-field and beyond mean-field interaction processes are negligible during the expansion. The measured far-field spatial distribution then reproduces the in-trap momentum distribution via the ballistic formula, which has been verified experimentally by benchmarking our setup with ab-initio QMC simulations. Therefore, our experiment is designed to investigate the physics of lattice bosons in momentum space, with a renewed approach relying on the single-atom sensitivity offered by the electronic detection. In particular, the capabilities to detect dilute signals without line-of-sight integration or to compute momentum correlations between individual atoms are crucial for the work presented in this manuscript.

Chapter 2

2. Average mode occupancy $\rho(k)$: study of the low-entropy Mott transition

Mott insulators initially referred to a particular class of semiconductors and insulators predicted by the band theory to conduct electricity. Following their discovery in 1937 by Boer and Verwey [94], Peierls intuited that their insulating behavior could result from the strong Coulomb repulsion between the electrons [95]. Mott's pioneering work [96–98] confirmed this explanation and gave his name to these insulators. In the past decades, numerous theoretical advances have provided a better understanding of these materials [99]. In particular, Hubbard's celebrated model [100–102] was the first theoretical framework to describe the transition between the Mott insulator and metal phases. However, the complexity of this model as the number of electrons increases makes it difficult to solve numerically for only a few dozen electrons. Therefore, its investigation turned towards experimental approaches.

Cold atoms are a versatile platform for implementing the Hubbard model, where atoms loaded inside the periodic potential of an optical lattice simulate the electrons of a crystalline structure. The idea of using cold atoms as quantum simulators of the Bose-Hubbard model was suggested by P. Zoller's group in 1998 [20] and realized experimentally in the group of I. Bloch in 2002 [19]. It was followed by the implementation of the Fermi-Hubbard model in the groups of T. Esslinger and I. Bloch in 2008 [103, 104]. Cold atoms platforms offer precise control of the parameters driving the transition towards a Mott insulating phase and unique detection methods, which have provided numerous breakthroughs in understanding Hubbard physics in the past twenty years. Of course, grey areas remain, and among them, the critical region of the phase diagram above the $T = 0$ superfluid-to-Mott transition which is still largely unexplored. Investigating this critical region is precisely the aim of this chapter. This study is based on the measurement of momentum densities resolved at the individual atom level, as permitted by the detection of $^4\mathrm{He}^*$ atoms.

The chapter is divided into five sections. Section 2.1 presents the transition from a continuous description of lattice bosons with the band Hamiltonian to a discrete description in terms of lattice sites with the three-dimensional (3D) Bose-Hubbard (BH) Hamiltonian. Section 2.2 describes the main regions of the $T = 0$ phase diagram, namely the superfluid and Mott insulator limits, as well as the interactions-induced quantum phase transition between both regimes. Section 2.3 recalls some experimental aspects and limitations of

implementing the Bose-Hubbard model with cold atoms platforms to keep them in mind during the presentation of our experimental results, which is done in the last two sections. The adiabatic preparation of equilibrium states of the 3D BH model is demonstrated in Section 2.4, while Section 2.5 focuses on revealing critical properties of the transition.

2.1 Bose-Hubbard model

This section describes homogeneous ultracold bosons loaded in a 3D optical lattice, implementing the celebrated 3D BH model. For the sake of simplicity, the lattice potential is assumed to be flat so that it does not induce any external confinement. The consequences of external trapping are considered later in this chapter, along with the finite size and finite temperature effects. Extensive literature exists on this topic, and the reader is referred to *e.g.* [105, 106] for more exhaustive information.

2.1.1 The band Hamiltonian

We consider a 3D optical lattice, with cubic symmetry and lattice spacing d similar to that of our experiment, whose periodic potential writes:

$$V(\boldsymbol{r}) = V_0 \left(\sin^2\left(\frac{k_d}{2}x\right) + \sin^2\left(\frac{k_d}{2}y\right) + \sin^2\left(\frac{k_d}{2}z\right) \right) \tag{2.1}$$

The Hamiltonian describing a system of N ultracold bosons trapped inside this lattice is expressed as:

$$\hat{H} = \sum_{i=1}^{N} \frac{\boldsymbol{p}_i^2}{2m} + \sum_{i}^{N} V(\boldsymbol{r}_i) + \sum_{i}^{N}\sum_{j>i}^{N} U_{\text{int}}(\boldsymbol{r}_i, \boldsymbol{r}_j) \tag{2.2}$$

The first two terms are often referred to as the band Hamiltonian and describe the behavior of ideal bosons in the 3D lattice. In this non-interacting case, the Bloch theorem states that eigenfunctions are a product of a plane wave with a periodic function whose periodicity reflects that of the lattice [107]. The band Hamiltonian being separable, we can restrict ourselves to the 1D case and express the Bloch's functions as:

$$\psi_q(x) = e^{iqx} u_q(x) \tag{2.3}$$

with $q \in \mathbb{R}$ the quasi-momentum. Injecting Equation 2.3 into the eigenvalue equation gives:

$$\left[\frac{(p_x + \hbar q)^2}{2m} + V_0 \sin^2\left(\frac{k_d}{2}x\right) \right] u_q(x) = E(q) u_q(x) \tag{2.4}$$

This equation can be solved numerically to obtain the band energies $E_n(q)$ (indexed by n so that $E_0(q) < E_1(q) < \cdots$) and the corresponding $u_{n,q}(x)$. Due to the periodicity of the functions $u_{n,q}(x)$, the quasi-momentum can be restricted to the first Brillouin zone $q \in [-\frac{k_d}{2}; \frac{k_d}{2}]$.

As represented in Figure 2.1, a specificity of the energy band is that they separate from each other and flatten out as the lattice potential increases. Consequently, the effective mass m^*, defined from the curvature of the energy bands as:

$$\frac{1}{m^*} = \frac{1}{\hbar^2} \frac{\mathrm{d}^2 E_n(q)}{\mathrm{d}\, q^2} \tag{2.5}$$

increases with the lattice potential. This quantity describes how the lattice affects an isolated wave packet. Indeed, the bottom of the lowest energy (or fundamental) band is well approximated by a parabolic function:

$$E_0(q) \simeq \frac{\hbar^2 q^2}{2m^*} \tag{2.6}$$

which is identical to the dispersion relation of free particles considering the normalization of the mass $m \to m^*$. In the 3D case, a gap between the fundamental and the first excited band appears for $V_0 \simeq 2.2\, E_r$. For such lattice potential and at unit filling, a BEC only populates the fundamental band $E_0(q)$ of the lattice. As both conditions are fulfilled throughout this manuscript, the index n is dropped in the following.

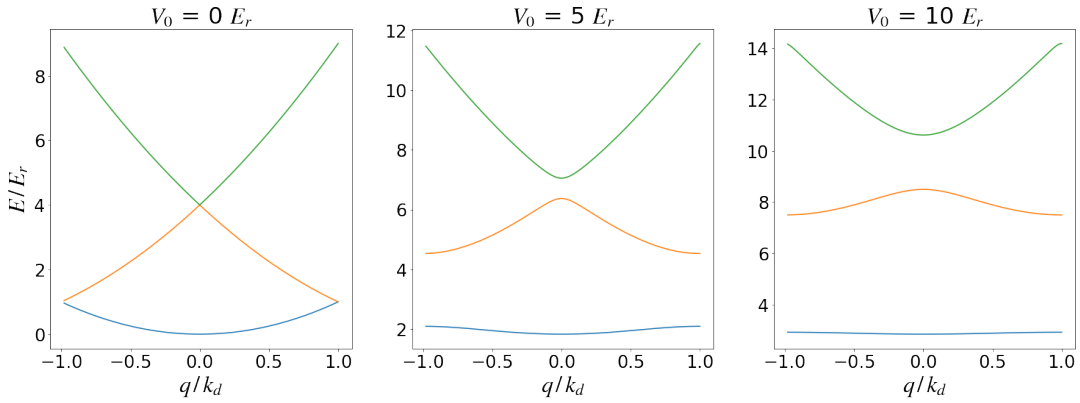

Figure 2.1: **First three energy bands at various lattice amplitudes.** The energy bands $E_n(q)$ for $n \in [0, 1, 2]$ are plotted versus the quasi-momentum in the first Brillouin zone.

2.1.2 The Bose-Hubbard Hamiltonian

The Bloch functions are delocalized over the entire momentum space. As we shall see, it is convenient to work in the basis of the Wannier functions [108], which are all the more localized on the lattice sites the higher the lattice potential. They are expressed in terms of the Bloch functions as:

$$w_j(x) = \sqrt{\frac{d}{2\pi}} \int_{1\mathrm{BZ}} \psi_q(x) e^{-ijqd} dq\,, \quad j \in \mathbb{Z} \tag{2.7}$$

where the index 1BZ refers to an integration over the first Brillouin zone. Wannier function verifies the relation $w_0(x - jd) = w_j(x)$, and can be interpreted as the wavefunction of a particle located on site j. After inverting Equation 2.7, the delocalized Bloch functions write as a sum of localized functions on the different lattice sites:

$$\psi_q(x) = \sqrt{\frac{d}{2\pi}} \sum_j w_j(x) e^{-ijqd} \tag{2.8}$$

Re-writing the band Hamiltonian in the Wannier basis makes the description of non-interacting lattice bosons more intuitive. In the second quantization formalism, the band Hamiltonian expression is:

$$H_{\mathrm{band}} = \int_{1\mathrm{BZ}} E(q) \hat{c}_q^\dagger \hat{c}_q \, dq \tag{2.9}$$

where the operator $\hat{c}_q$ (*resp.* $\hat{c}_q^\dagger$) annihilates (*resp.* creates) a particle in the Bloch function $\psi_q(x)$. Introducing the corresponding operators $\hat{b}_j$, $\hat{b}_j^\dagger$ for the Wannier functions, one can repeat the change of variables of Equation 2.7:

$$\hat{c}_q^\dagger = \sqrt{\frac{d}{2\pi}} \sum_j \hat{b}_j^\dagger e^{-ijqd} \tag{2.10}$$

and re-write the band Hamiltonian of Equation 2.9 with these new operators:

$$\hat{H}_{\text{band}} = \sum_{j,j'} J(j'-j) \hat{b}_j^\dagger \hat{b}_{j'} \tag{2.11}$$

Under this form, the physics behind $\hat{H}_{\text{band}}$ is easy to grasp: the term $\hat{b}_j^\dagger \hat{b}_{j'}$ describes hops of the particles between two different lattice sites j' and j with the tunnelling energy $J(j'-j)$ given by:

$$J(j'-j) = \frac{d}{2\pi} \int_{1\text{BZ}} e^{i(j'-j)qd} E(q)\, dq \tag{2.12}$$

This amplitude decreases the further away the sites are, and also the higher the lattice potential. In the tight-binding regime, reached for $V_0 \geq 5E_r$ [106], only the tunnelling processes between adjacent lattice sites are non-negligible. The tunnelling energy is equal for all these processes and is usually written as $J = -J(1)$ ($J > 0$). The expression of the band Hamiltonian finally simplifies into:

$$\hat{H}_{\text{band}} = -J \sum_{\langle i,j \rangle} \hat{b}_i^\dagger \hat{b}_j \tag{2.13}$$

where the notation $\langle i,j \rangle$ refers to all the pairs of adjacent lattice sites i and j. This expression is identical for the 3D lattice, and corresponds to the non-interacting part of 3D the BH model.

The interaction part of Hamiltonian 2.2 can be treated similarly, and its expression in second quantization is:

$$\hat{H}_{\text{int}} = \frac{1}{2} \iint U_{\text{int}}(x,x') \hat{\Psi}^\dagger(x) \hat{\Psi}^\dagger(x') \hat{\Psi}(x') \hat{\Psi}(x')\, dx\, dx' \tag{2.14}$$

with $\hat{\Psi}(x)$ the operator destroying a particle at position x:

$$\hat{\Psi}(x) = \sum_j w_j(x) \hat{b}_j = \sum_j w_0(x - x_j) \hat{b}_j \tag{2.15}$$

The particles are assumed to interact via two-body contact interactions $U_{\text{int}}(x_1, x_2) = g\delta(x_1 - x_2)$, with $g = 4\pi\hbar^2 a_s/m$ the coupling constant and a_s the scattering length. In this case, Equation 2.14 becomes:

$$\hat{H}_{\text{int}} = \frac{g}{2} \sum_{j_1} \sum_{j_2} \sum_{j_3} \sum_{j_4} \hat{b}_{j_4}^\dagger \hat{b}_{j_3}^\dagger \hat{b}_{j_2} \hat{b}_{j_1} \int w_{j_4}^*(x) w_{j_3}^*(x) w_{j_2}(x) w_{j_1}(x) dx \tag{2.16}$$

Within the tight-binding regime, the overlap between the different Wannier functions in this equation is non-negligible only when considering two particles on the same site, meaning $j_1 = j_2 = j_3 = j_4$. With this simplification, the interaction Hamiltonian becomes:

$$\hat{H}_{\text{int}} = \frac{U_{1\text{D}}}{2} \sum_j \hat{n}_j(\hat{n}_j - 1) \tag{2.17}$$

with $\hat{n}_j = \hat{b}_j^\dagger \hat{b}_j$ the atom number on site j, and $U_{1D} = g \int |w_0(x)|^4 dx$ the on-site interaction energy. The latter is easily generalized to the 3D case : $U = g \left(\int |w_0(x)|^4 dx \right)^3$. Then again, the interpretation of the interaction Hamiltonian in the Wannier basis is intuitive: the total energy is simply obtained by summing the interaction energy U of all atom pairs located inside a same lattice site j.

Combining Equation 2.13 with Equation 2.17 yields the celebrated 3D BH Hamiltonian:

$$\hat{H}_{\mathrm{BH}} = -J \sum_{\langle i,j \rangle} \hat{b}_i^\dagger \hat{b}_j + \frac{U}{2} \sum_j \hat{n}_j (\hat{n}_j - 1) \tag{2.18}$$

which describes the behavior of ultracold bosons loaded inside the fundamental band of an optical lattice. The next section describes how the many-body ground state of this Hamiltonian evolves depending on the ratio $u = U/J$.

2.2 The superfluid-to-Mott transition

This section begins by treating the two limiting cases $U/J \to 0$ and $U/J \to \infty$ as they are analytically solvable. We consider a homogeneous gas of N bosons loaded inside the fundamental band of a lattice of M sites, and assume the filling to be commensurate, meaning that $\bar{n} = N/M$ is an integer.

2.2.1 Analytical cases : the limits $U/J \to 0$ and $U/J \to \infty$

In the non-interacting limit, the ground state of the system writes as the N product of the single particle ground state. According to the previous section, the latter corresponds to the Bloch function at quasi-momentum $\boldsymbol{q} = \mathbf{0}$. Including the normalization factor in a lattice with M sites, the ground state of the system is:

$$|\Psi_0\rangle_{\mathrm{SF}} = \frac{1}{\sqrt{N!}} \left(\hat{c}_{\boldsymbol{q}=\mathbf{0}}^\dagger \right)^N |0\rangle = \frac{1}{\sqrt{N!}} \left(\frac{1}{\sqrt{M}} \sum_{j=1}^{M} \hat{b}_j^\dagger \right)^N |0\rangle \tag{2.19}$$

For such a state, it can be shown [106] that the probability distribution to find n_j atoms at site j in the thermodynamic limit ($N, M \to \infty$ and $N/M = \bar{n}$) is Poissonian:

$$p(n_j) \approx e^{-\bar{n}} \frac{\bar{n}^{n_j}}{n_j!} \tag{2.20}$$

One would have obtained a similar distribution for a coherent state with a mean atom number N:

$$|\Psi_{\mathrm{coh}}\rangle = \mathcal{N} e^{\sqrt{N}\, \hat{c}_{\boldsymbol{q}=\mathbf{0}}^\dagger} |0\rangle \tag{2.21}$$

Due to the relationship between $\hat{c}_{\boldsymbol{q}=\mathbf{0}}^\dagger$ and $\hat{b}_j^\dagger$, the coherent state $|\Psi_{\mathrm{coh}}\rangle$ can be written as a product of local ones $|\alpha_j\rangle_j$ at each lattice site j:

$$|\Psi_{\mathrm{coh}}\rangle = \mathcal{N} e^{\sqrt{N}\, \hat{c}_{\boldsymbol{q}=\mathbf{0}}^\dagger} |0\rangle = \mathcal{N} \prod_{j=1}^{M} e^{\sqrt{\bar{n}}\, \hat{b}_j^\dagger} |0\rangle = \prod_{j=1}^{M} \mathcal{N}_j \sum_{n_j=0}^{\infty} \frac{\alpha_j^{n_j}}{\sqrt{n_j!}} |n_j\rangle_j = \prod_{j=1}^{M} |\alpha_j\rangle_j \tag{2.22}$$

The amplitudes and normalization factors of each local coherent state are respectively $\alpha_j = \sqrt{\bar{n}}$ and $\mathcal{N}_j = e^{-|\alpha_j|^2/2}$. In a good approximation, the predictions made for $|\Psi_0\rangle_{\mathrm{SF}}$ and $|\Psi_{\mathrm{coh}}\rangle$ are the same, and one may choose to work with the latter which is easier to manipulate. In particular, the computation of the first order correlation function $G^{(1)}(i,j) = \langle \hat{b}_i^\dagger \hat{b}_j \rangle$ between two sites i and j is straightforward:

$$G^{(1)}(i,j) = \langle \Psi_{\mathrm{coh}} | \hat{b}_i^\dagger \hat{b}_j | \Psi_{\mathrm{coh}} \rangle = \alpha_i^* \alpha_j = \bar{n} \tag{2.23}$$

The result is independent of the separation between the lattice sites, indicating off-diagonal long range order for the ground state of the system. This $U/J \to 0$ limit [1] is called the superfluid regime.

In the opposite limit where the on-site interaction U diverges and the tunnelling energy J is small, the Hamiltonian reduces to:

$$\hat{H}_{\mathrm{BH}} \simeq \frac{U}{2} \sum_j \hat{n}_j (\hat{n}_j - 1) \tag{2.24}$$

which is diagonal in the Fock states basis. Consequently, the ground state writes:

$$|\Psi_0\rangle_{\mathrm{MI}} = \frac{1}{\sqrt{N!}} \prod_{j=1}^{M} \left(\hat{b}_j^\dagger \right)^{\bar{n}} |0\rangle \tag{2.25}$$

and is called a Mott insulator state [109]. Due to the vanishing tunnelling, the atoms are localized on the lattice sites, that evolve independently from each other. To minimize the interaction energy, each site must then contain as fewer atoms as possible. This ground state configuration is reached when each site contains exactly $\bar{n} = N/M$ atoms. The fluctuations of the phase are then maximal, and no off-diagonal long range order exists. Indeed, the first order correlation function is now zero when considered between different lattice sites:

$$G^{(1)}(i,j) = {}_{\mathrm{MI}}\langle \Psi_0 | \hat{b}_i^\dagger \hat{b}_j | \Psi_0 \rangle_{\mathrm{MI}} = \delta_{i,j} \bar{n} \tag{2.26}$$

Consequently, the system is incoherent in the Mott insulator limit $U/J \to 0$. The transition between both regimes is called the superfluid-to-Mott transition [109], and we now recall some of its characteristics.

2.2.2 A continuous quantum phase transition in 3D

The superfluid-to-Mott transition is a quantum phase transition: it occurs at $T = 0$ in the many-body ground state due to the competition between two energy scales rooted inside the system's Hamiltonian. Those are the on-site interaction U and the tunnelling energy J, and the transition is consequently driven by the dimensionless interaction parameter $u = U/J$.

The superfluid-to-Mott phase transition is a continuous (or second-order) phase transition [110, 111]. Such transitions are characterized by an order parameter whose value is non-zero in the ordered phase and zero in the disordered phase. At the transition (or critical) point, where the order parameter cancels out, its fluctuations become long-ranged in time and space, with a diverging decay time τ_c:

$$\tau_c \propto \xi^z \propto |t|^{-\nu z} \tag{2.27}$$

[1] The case $U = 0$ is excluded as it corresponds to an ideal BEC, which is not superfluid.

and a diverging correlation length ξ:

$$\xi \propto |t|^{-\nu} \tag{2.28}$$

In these equations, t is some dimensionless distance from the transition point. Note that the divergence of τ_c on approaching the transition point implies a vanishing energy scale of the fluctuations above the ground state. This feature is illustrated in the Bose-Hubbard Hamiltonian by the transition from gapped particle-holes excitations in the Mott phase to the gapless Bogoliubov excitation spectrum in the superfluid phase. Due to the divergences in Equations 2.27 and 2.28, all observables near the transition point scale as power laws with a given set of exponents. This phenomenon is known as criticality. An even more intriguing feature of continuous phase transition is universality. Due to the diverging correlation length, the microscopic details of the Hamiltonian are irrelevant at the transition point. Consequently, all the phase transitions belonging to the same universality class share the same critical exponents, which can thus be observed in totally different systems. In particular, the superfluid-to-Mott phase transition belongs to the 3D XY universality class [112], characterized by short-range interactions, $O(2)$ symmetry, and a two-component order parameter. In 3D, the latter corresponds to the BEC wavefunction whose modulus square, the condensed fraction, takes a non-zero value in the superfluid (ordered) phase and cancels out as soon as the system enters the Mott insulating (disordered) phase [106].

2.2.3 Numerical approaches to tackle the Bose-Hubbard model

The complexity of the BH model away from the aforementioned limiting case lies in the Hamiltonian of Equation 2.24 not being diagonal in either the Bloch or the Fock states basis. It must then be addressed via numerical approaches, which are either approximate or exact.

Mean-field theories, such as the Gross-Pitaevskii equation, neglect particle correlations in position space. Consequently, they are not suited to describe the superfluid-to-Mott transition because they give an approximate account of interactions, despite their critical role in driving the system's evolution. Even the next order Bogoliubov approach (see Chapter 4 for more details) fails to predict the presence of a transition in the 2D and 3D cases [113]. On the Mott insulator side, the strong-coupling approximation allows to treat interactions exactly while approximating the kinetic energy. Many approaches exist depending on the level of approximation. At the mean-field level, the tunnelling energy J can be treated as a perturbation [109] or with a site-decoupling approach [113, 114]. More sophisticated methods also exist, such as the strong coupling expansion [115, 116].

All these approaches qualitatively transcribe the phase diagram of the homogeneous BH model at zero temperature. The latter is plotted in Figure 2.2, where the filling $\bar{n}$ (and thus the chemical potential μ) is allowed to vary. As $\bar{n}$ is independent of the dimensionless interaction in the homogeneous case, the system must follow iso-filling lines on varying U/J. Only when the filling is commensurate ($\langle N \rangle = 1, 2, 3$ in the figure) can the system reach a Mott insulating phase. In this case, and as long as J is sufficiently large, tunnelling always compensates for the energy cost of having two or more atoms on the same lattice site. On decreasing J, there comes the point where the total energy becomes dominated by the interaction energy, which is minimized by having exactly $\bar{n}$ atoms per site. The system then enters a Mott insulating phase, at a critical ratio $(J/U)_c$ that decreases with

the filling $\bar{n}$. In the incommensurate case, though, the excess atoms must be delocalized over the entire lattice to minimize the interaction energy, and superfluid properties are conserved down to the lowest values of J.

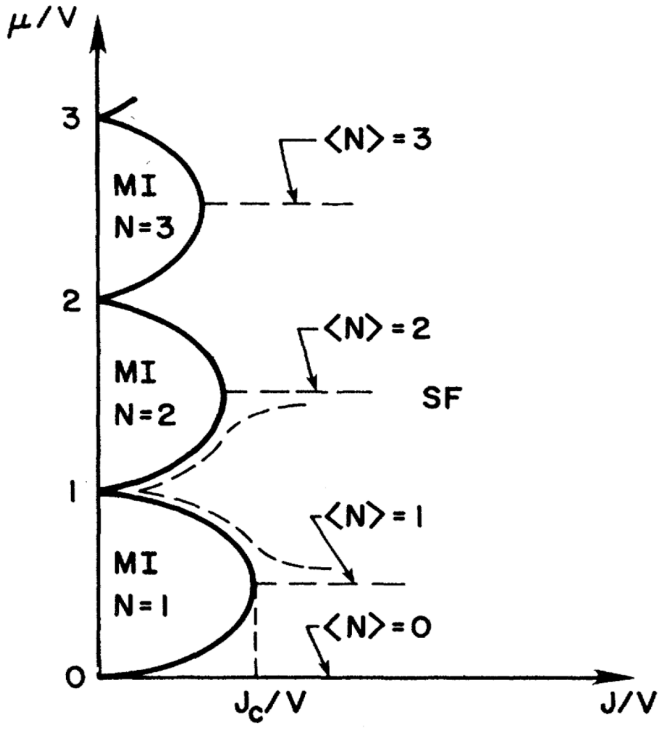

Figure 2.2: **Zero-temperature phase diagram of the homogeneous BH model, from [109].** The filling is noted $\langle N \rangle$, and the dashed lines are iso-filling lines. A superfluid-to-Mott transition only occurs for commensurate filling (horizontal dashed lines).

Another kind of approximate method to assess the BH Hamiltonian is the mean-field variational Gutzwiller approach [20, 117–119], in which the many-body ground state is found by minimizing the free energy starting from the Gutzwiller ansatz:

$$|\Psi_G\rangle = \prod_{j=1}^{M} |\phi_j\rangle = \prod_{j=1}^{M} \sum_{n_j=0}^{\infty} f_j(n_j)|n_j\rangle_j \tag{2.29}$$

The latter consists in writing the many-body ground state in product form of on-site wavefunctions $|\phi_j\rangle$ developed in the Fock states basis. The amplitudes $f_j(n_j)$ are the coefficients to be optimized while verifying the normalization condition $\sum_{n_j}^{\infty} |f_j(n_j)|^2 = 1$. Interestingly, this description is exact in the two limiting cases of the phase diagram:

- $U/J \to 0$: the superfluid state $|\Psi_0\rangle_{\mathrm{SF}}$ of Equation 2.19 is a coherent state, and is retrieved from the Gutzwiller ansatz for $f_j(n_j) = \mathcal{N}_j \frac{\alpha_j^{n_j}}{\sqrt{n_j!}}$
- $U/J \to \infty$: the Mott insulator state $|\Psi_0\rangle_{\mathrm{MI}}$ of Equation 3.8 is already a Fock state with $\bar{n}$ atom per site, so $f_j(n_j) = \delta_{n_j,\bar{n}}$

Despite working poorly close to the quantum critical point, this method provides accurate predictions in both the superfluid and Mott insulating limits. In particular, it can be

used to estimate the ground state density profile and the condensed fraction, even in the presence of an external trapping potential (see Chapter 4).

Quantum Monte Carlo (QMC) algorithms are the only ones able to solve exactly the 3D BH model. They are based on a stochastic estimation of the partition function, from an ensemble of space-time configurations (world-lines) in its path-integral representation (see *e.g.* [120]). They were used soon after the seminal paper of M. P. Fisher *et al.* [109] to characterize the BH model [121–125], particularly its $(\mu/U, J/U)$ phase diagram, for which they predicted the positions of the quantum critical points and also critical exponents.

All these approaches provide approximate/exact predictions for the superfluid-to-Mott transition that can be confronted with experiments. In this chapter, we focus on the critical ratio $(U/J)_c$ and the critical exponents in the 3D case, for which theoretical computations give quite different results. For the BH model with unit filling $\bar{n} = 1$, all mean-field theories predict a quantum critical point at $(U/J) = 5.8\,z$, with z the number of nearest neighbors. In 3D, $z = 6$ and the mean-field prediction is consequently $(U/J)_c^{\mathrm{MF}} = 34.8$. This value is quite larger the exact QMC estimate $(U/J)_c^{\mathrm{QMC}} = 29.34$ [126]. Surprisingly, the critical ratios found in several experiments were consistent with [19, 127–129] (or indistinguishable from [130]) the mean-field prediction rather than the QMC simulations. In addition, critical exponents of the 3D BH model have never been observed so far, further questioning the capacity of quantum gas experiments to study the critical region. To provide some first explanations, the next section reminds practical aspects of investigating the Bose-Hubbard model with cold atoms.

2.3 Investigating the Mott transition with ultracold atoms

In the first implementation of the BH model with lattice bosons [19], the transition from a superfluid to a Mott insulating phase was signaled by the opening of a gap in the excitation spectrum and the loss of off-diagonal long range order. Different signatures of the transition were then reported by other teams, such as kinks in the visibility of the interference pattern [83, 128] and in the width of the momentum density [130], as well as the breakdown of superfluid currents [127]. The work of [19] opened the field of quantum simulation of the BH model with cold atoms, which is still very active today. Our experiment belongs to this line of research. More specifically, our original detection of individual atoms in momentum space allows us to shed new light on the superfluid-to-Mott transition, in addition to what can be known from optical imaging. Our experimental results are detailed in the last two sections of this chapter. Here we first consider some practical aspects of studying the BH model with cold atoms and the possible limitations of an actual experiment compared to the ideal case considered so far.

2.3.1 Experimental control of U/J

On top of implementing the BH Hamiltonian, bosons in optical lattice offer complete control over the dimensionless interaction $u = U/J$ via the lattice potential V_0. Indeed, the latter is directly proportional to the lattice beam power and can be tuned from zero to a few tens of the recoil energy. The variations of the BH parameters U and J over this range are plotted on the left side of Figure 2.3 for our experimental parameters. The

on-site interaction energy $U = g\left(\int |w_0(x)|^4 dx\right)^3$ increases due to the tightening of the Wannier functions with the increasing lattice potential. At the same time, the tunnelling energy J is exponentially suppressed because of the potential barrier getting higher. Both effects allow to vary the dimensionless interaction over several orders of magnitude (right side of Figure 2.3), from the superfluid regime to deep into the Mott insulating phase.

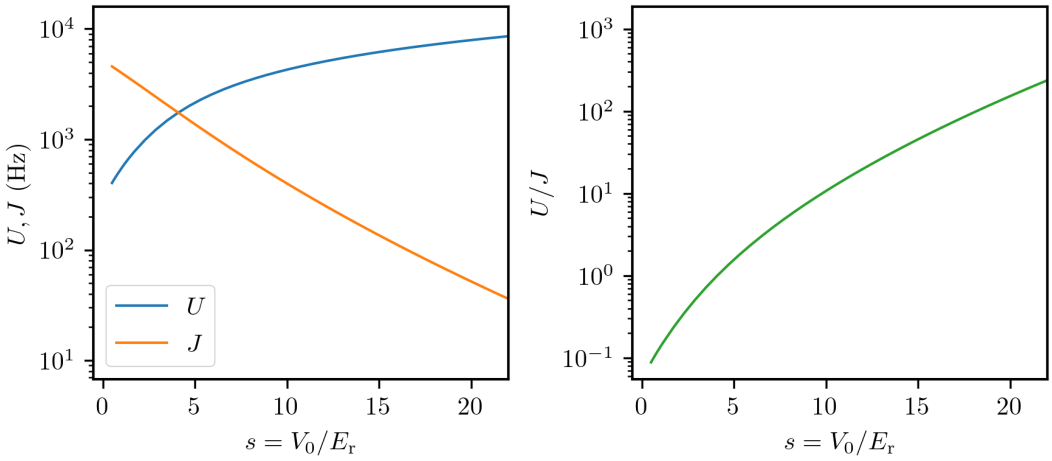

Figure 2.3: **Numerical values of U, J, and U/J versus the lattice depth for Helium atoms and $d = 775$ nm.** (Left) The on-site interaction U increases smoothly with the lattice depth, while the tunnelling energy J is exponentially suppressed. (Right) Both effects result in an exponential increase of the dimensionless interaction $u = U/J$ with the lattice potential.

2.3.2 Calibration of the lattice depth

As the ratio U/J is extremely sensitive to the lattice potential V_0, the latter must be finely calibrated to reach a desired U/J value. Such a calibration is performed via parametric excitation of the atoms from the fundamental band of the lattice to the second one [131, 132]. This is achieved via the experimental procedure represented in Figure 2.4. The atoms are loaded from the ODT to the optical lattice, for which two beams are increased up to $s = 7$ and the third one to $s = 10$. The lattice amplitude of this last beam is then modulated for a time $t_{\text{mod}} = 20\,ms$ at a frequency f_{mod}. To do so, the voltage command of the AOM driver for this beam is modulated at the frequency f_{mod}. Because the driver is linear, this modulation is printed on the AOM output power, which is proportional to the lattice amplitude. When the resonance condition is met, namely $f_{\text{mod}} = 2 \times f_{\text{res}}$ with $f_{\text{res}} = \left(E_2(q = 0) - E_0(q = 0)\right)/h$, atoms are parametrically excited from the zeroth to the second energy band of the lattice. These atoms are lost when loading back the gas from the optical lattice to a low-depth ODT. Therefore, monitoring with absorption imaging the losses of the atom number while tuning the modulation frequency allows us to pinpoint the resonance (see left panel of Figure 2.5). From the energy band calculations, the dependency of f_{res} on s is known, allowing the latter to be derived from the measurement of the former (right panel of Figure 2.5). As shown in this figure, the uncertainties in the fitted resonant frequency and lattice depth are less than the percent level. Due to the linear relationship between the AOM driver voltage command and the lattice depth, it is sufficient to divide the old calibration factor by the measured lattice depth to update it.

This calibration method is then repeated for the other two beams to calibrate all three axis of the optical lattice.

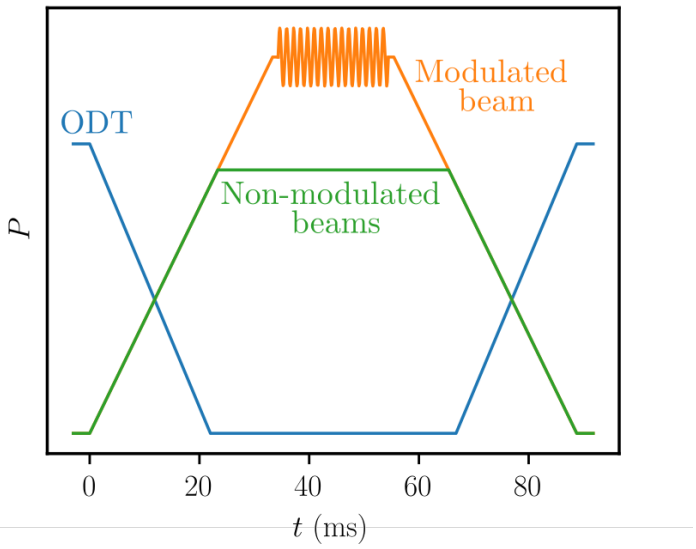

Figure 2.4: **Scheme of the lattice calibration sequence.** The ODT is ramped down while the lattice beams are ramped up, with one beam being set to a higher amplitude than the other two. The amplitude of this beam is modulated for a time t_{mod} and at a frequency f_{mod}, which is tuned to find the parametric heating resonance frequency. For each f_{mod} value, the cloud is transferred back into the ODT and the fraction of excited (lost) atoms is measured with absorption imaging.

2.3.3 Finite temperature effect

An experimental implementation of the BH model necessarily occurs at finite temperature. The corresponding phase diagram for the homogeneous system, which depends now on the dimensionless ratios U/J and T/J, is plotted in Figure 2.6. The $T = 0$ (quantum) phase transition between a superfluid and a Mott insulator is represented by the x-axis, both phases being separated by the quantum critical point. A third phase, called the normal gas, appears at higher temperatures. By increasing the temperature from the superfluid side, the gas undergoes a classical superfluid-to-normal phase transition, similar to the Bose-Einstein condensation transition. It is classical in the sense that it is driven by thermal fluctuations, characterized by the reduced temperature T/J. On the Mott insulator side, there is no transition but a smooth crossover to the normal phase. On increasing the temperature, the Mott plateau is progressively nibbled away by the particle-hole excitations that occur on its edges, until the "melting" temperature $T^* \sim 0.2\,U k_B$ is reached where the remaining Mott plateau vanishes [133].

Of particular interest is the quantum critical region of the phase diagram, above the quantum critical point, where critical properties of the $T = 0$ phase transition should be accessible despite being at finite temperature [111]. The reason for that can be understood in terms of energy scales. From the characteristic decay time of the order parameter fluctuations (Equation 2.27), a characteristic energy scale can be deduced whose behavior

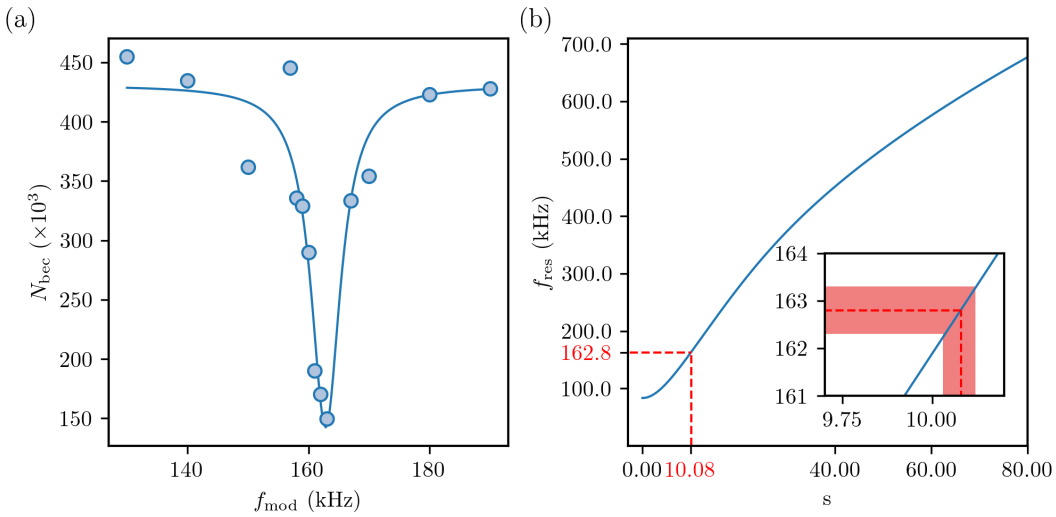

Figure 2.5: **Calibration of the lattice depth from the parametric heating process.** Left: Typical resonance curve for the modulation frequency. The atom number is obtained from absorption imaging and the resonance is fitted with a Lorenztian curve (solid line). This measurement gives here $f_{\text{res}} = 162.8(5)$ kHz. Right: Derivation of the lattice depth s from its calculated dependency with the resonance frequency. The result here is $s = 10.08(5)$. The uncertainty on the lattice depth comes from the fitting error on the resonance frequency (see red shaded area in the inset).

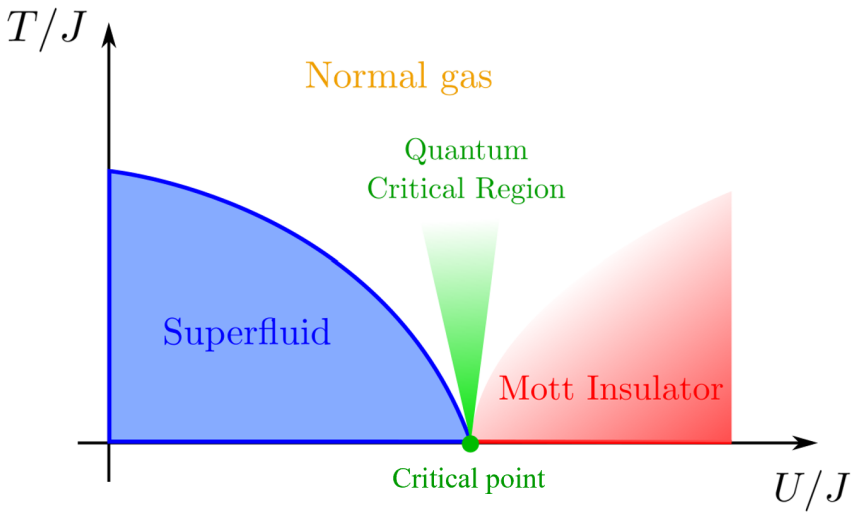

Figure 2.6: **Schematic phase diagram of the BH model at finite-temperature.** The position on this phase diagram depends on the ratio T/J and U/J that quantify the effect of temperature and interactions, respectively. At $T = 0$, the superfluid-to-Mott transition is retrieved, with the quantum critical point separating both phases. At finite temperatures, these two regimes are separated by a normal phase whose part just above the quantum critical point is referred to as the quantum critical region (see text).

on approaching the transition follows the critical scaling:

$$\hbar\omega_c \propto |t|^{\nu z} \tag{2.30}$$

A general rule is that quantum mechanics affect the transition as long as this energy scale is larger than the temperature, while a purely classical description of the order parameter fluctuations can be applied in the case $\hbar\omega_c \ll k_B T$. Therefore, the boundaries of the critical quantum region are set by the inequality $\hbar\omega_c > k_B T$. Within this region, the system "looks critical", but is driven away from criticality by thermal fluctuations. Although the superfluid and Mott insulating phases can be observed experimentally, the temperature achieved may be too high to reveal the critical properties of quantum phase transition.

2.3.4 The paradigm of adiabatic state preparation

The need for a low temperature to access the physics of the quantum critical point is now clearer. To carry out this study with cold atoms, experimentalists start from a state of non-zero entropy, namely a BEC at finite temperature. The transformation of the system's Hamiltonian from this initial state to the desired equilibrium state of the BH model must then be adiabatic. In other words, both the loading into the lattice and the ramping up of the lattice potential to the desired u must not create excitations.

The evolution of a system during an external driving of its Hamiltonian is called adiabatic as long as the system's state remains close to the instantaneous time-dependent eigenstate of the Hamiltonian. The adiabatic theorem [134] states that this condition can always be fulfilled for a pure state if the driving rate is chosen sufficiently small. The extension of this notion to quantum systems prepared at finite temperature has only started to be addressed theoretically [135]. On the experimental side, adiabaticity of the loading process has been a central preoccupation since the early investigations of the BH model with cold atoms. This issue has been studied in the superfluid regime ($u \leq u_c$) with indirect signatures of non-adiabaticity, such as observing an increased fraction of atoms populating the higher energy bands of the lattice [136], or a degraded visibility of the interference pattern in the superfluid regime [137]. A direct measurement of the entropy is hardly achievable with cold atom, preventing such mixed-state adiabaticity from being certified quantitatively. Moreover, it is still an open question to which extent the latter is fulfilled on crossing a quantum phase transition.

2.3.5 Effect of an external confinement

In actual experiments, optical lattices are usually generated by the counter-propagation of focused laser beams. Due to their Gaussian shape, the average intensity profile of the interference pattern is not flat, which induces a weak external confinement on the atoms:

$$V_{\text{ext}}(\boldsymbol{r}) = \frac{1}{2} m\omega_{\text{ext}}^2 \boldsymbol{r} \tag{2.31}$$

This confinement increases with the intensity of the lattice beams, and is given in our case by $\omega_{\text{ext}} = 2\pi \times 140\sqrt{s}$ Hz. Such a frequency corresponds typically to a few hundred Hertz, which is low enough for the Local Density Approximation [139] to apply. The latter allows for a numerical resolution of the inhomogeneous BH model by replacing the chemical potential μ with an effective one[2]:

$$\mu_{\text{eff}}(\boldsymbol{r}) = \mu - V_{\text{ext}}(\boldsymbol{r}) \tag{2.32}$$

[2] A failure of this approximation can be observed near the quantum critical point [120]

The effective chemical potential is maximum at the trap center and decreases to zero on approaching the edges of the system. The filling $\bar{n}$ follows a similar behavior, which dramatically changes the many-body ground state. For sufficiently low U/J ratios, the system remains in the superfluid phase for any filling, as represented by a green arrow in Figure 2.7 (a). As U/J increases, there comes the point where the filling at the center of the trap reaches exactly one, and a Mott plateau appears there while the rest of the cloud remains superfluid. The unitary filling at the trap's center is preserved as U/J keeps increasing due to the incompressibility of the Mott phase. It is then the size of the Mott region that grows bigger as more and more sites fulfill the $\bar{n} = 1$ condition until a second Mott plateau appears at the center of the trap when the filling there reaches $\bar{n} = 2$ (yellow arrow in Figure 2.7 (a) and (b)). The system's ground state then consists of a stack of Mott shells, with superfluid shells between them (see Figure 2.7 (b)). At finite temperature, this wedding cake structure is expected to survive, with normal gas separating the Mott shells. The resulting "wedding cake" structure was first observed with a quantum gas microscope, permitting to reveal the onset of each Mott plateau (see Figure 2.7 (c)). In the remaining of this chapter, the system is said to be in the Mott insulating

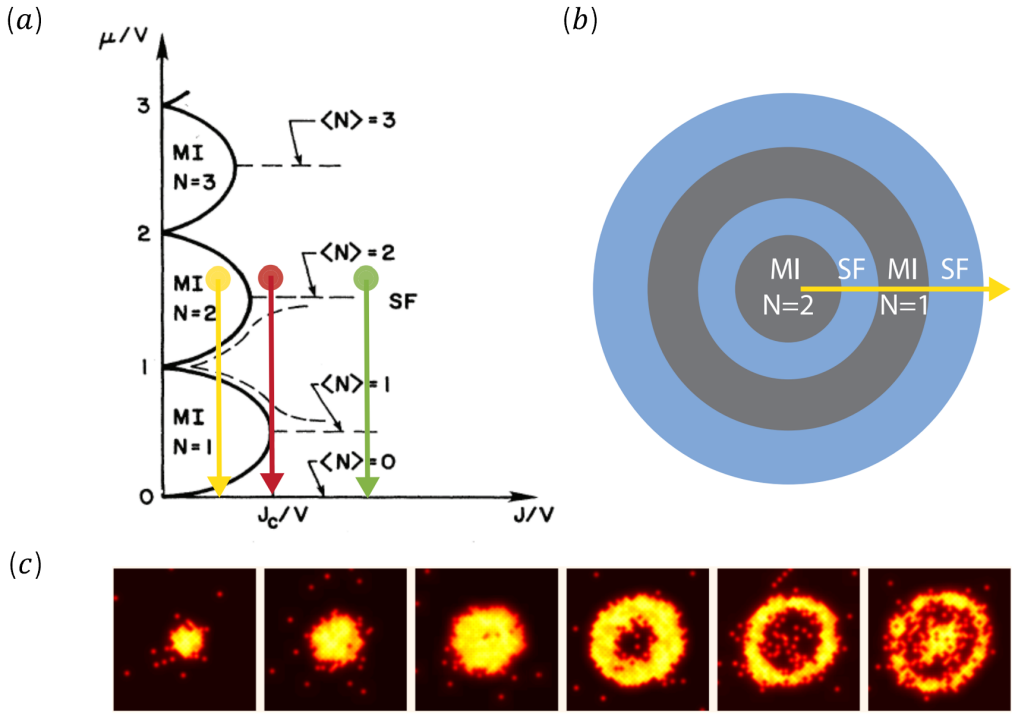

Figure 2.7: **Wedding-cake structure of the inhomogeneous system.** (a) Depending on the ratio U/J, the many-body ground state of the inhomogeneous system may correspond to: a superfluid phase (green arrow), a Mott insulating phase with $\bar{n} = 1$ at the trap's center surrounded by a superfluid shell (red arrow), an alternation of superfluid and Mott insulating phase with an increasing filling as one gets closer to the trap's center (yellow arrow). (b) Scheme of the wedding-cake structure corresponding to the yellow arrow of (a). (c) Experimental observation of the Mott insulating phases with a quantum microscope experiment. The imaging technique used here reveal the presence of atoms trapped inside individual lattice site, as long as the atom number is odd. The ratio U/J is increased from left to right, resulting in successive observation of the $\bar{n} = 1$, $\bar{n} = 2$, and $\bar{n} = 3$ Mott insulating phases at the trap's center. Taken from [138].

phase as soon as a Mott plateau exists.

In conclusion, the physics of the system gets richer in the presence of external confinement. The latter can even be an asset from an experimental point of view, as it makes the constraint on the atom number less stringent than in the homogeneous case to observe the formation of a Mott plateau. The coexistence of different phases also allows for the distribution of the entropy into the superfluid part as U/J increases, preventing the system from heating up due to the gapped energy spectrum of the Mott insulator phase. However, the system no longer exhibits a proper phase transition due to the reminiscence of superfluid or normal parts way beyond the formation of a Mott plateau. This effect might very well prevent the investigation of the quantum critical point and critical properties compared to the homogeneous case.

2.4 Certifying the adiabatic state preparation near the Mott transition

This section presents our work [29] to validate the mixed-state adiabaticity mentioned earlier in Section 2.3.4. This result was obtained thanks to a thermometry developed in collaboration with Tommaso Roscilde from the ENS Lyon, and based on the comparison of our experimental momentum densities with exact QMC simulations. Before presenting this thermometry, this section begins with a description of the experimental ramps used to increase the lattice potential.

2.4.1 Description of the lattice ramps

The experimental sequence used to load the optical lattice from the ODT is schematically represented in Figure 2.8. The optical power of the ODT is decreased linearly in a time t_{down} while the lattice power is increased linearly after a delay time t_{delay}. The linear increase of the lattice power translates into an exponential growth of the dimensionless interaction $u = U/J$. The rate at which the lattice is ramped up is fixed whatever the final value of u, meaning that the ramps used for two different final depths are identical up to the smallest of the two depths.

The ramp parameters were optimized by minimizing the atom losses and the heating when loading a BEC from the ODT into the lattice and then back into the ODT. Indeed, a similar BEC than the initial one is expected if the ramps are adiabatic. In practice, the percentage of losses is never less than 15% due to the imperfect overlap between the ODT and the lattice. The optimum parameters were found to be $t_{\text{down}} = 22$ ms, $t_{\text{delay}} = 0$ ms and $0.3E_r/ms$ for the rate at which the power increases. As any discontinuity in the ramps can lead to non-adiabaticity, they usually have a s-shape with smooth variations at the beginning and the end. However, no improvement was found between an s-shape and a linear one [49], so we kept the linear ramps as they ensure a identical increase of the lattice potential between different s values . For all the datasets used in this manuscript, the linear rate of $0.3E_r/ms$ implies that the ramp duration is at least 18 ms. The limiting (longest) time scales in our system are associated with the smallest energy scales, namely the tunnelling energy J and the external trapping confinement $\hbar\omega_{\text{ext}}$. For the lattice depths used in this manuscript, both are below 10 ms, which ensures that the driving rate of the Hamiltonian is indeed slower than any other time scale in the system. Minimizing

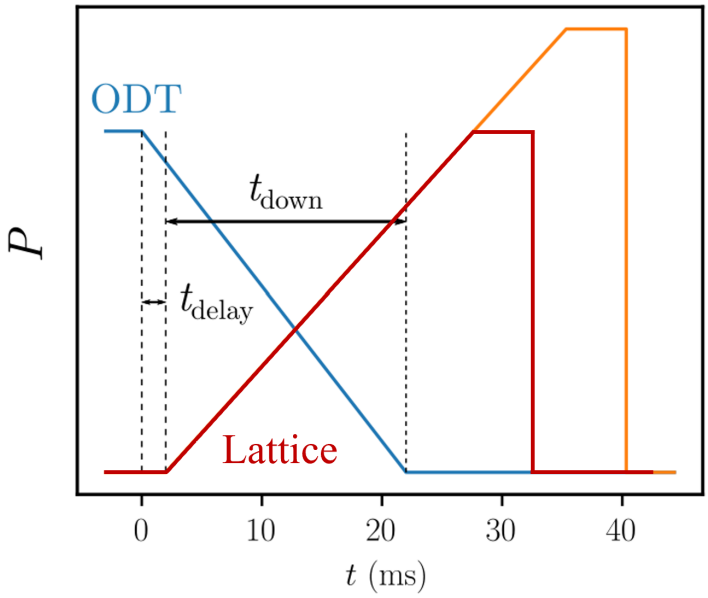

Figure 2.8: **Scheme of the experimental sequence used for loading the lattice.** The power of the optical dipole trap decreases as the lattice amplitude is ramped up. The loading parameters t_{down}, t_{delay}, and the loading rate were optimized experimentally.

the losses in this ramping up and down of the lattice is certainly handy to check routinely that the ramps do not induce heating but does not constitute a quantitative certification of adiabaticity. The latter requires the knowledge of the gas's temperature and entropy, which can be accessed from a comparison with ab-initio QMC calculations.

2.4.2 Thermometry of lattice bosons using ab-initio QMC simulations

Without any analytical prediction for the trapped 3D BH model, the gas temperature cannot be estimated from the momentum density measurement alone. A viable route for assessing the adiabaticity of the state preparation comes from a quantitative comparison with ab-initio calculations [140]. To this aim, we record 3D momentum distributions of lattice gases after a time of flight, whose average yields the 3D momentum density $\rho_{\text{exp}}(\boldsymbol{k})$. The latter can directly be compared with the ab-initio QMC estimate $\rho_{\text{QMC}}(\boldsymbol{k})$ calculated in the trap. Our single atom sensitivity allows us to work with low atom number BECs of $N_{\text{BEC}} = 3.0(5) \times 10^3$, which are numerically accessible for the QMC simulations. The calculations are performed by Tommaso Roscilde [141] using a Stochastic Series Expansions in the canonical ensemble. They account for the specificities of our experiment, such as the atom number, the external trapping frequency, or the lattice amplitude, leaving T the only adjustable parameter.

The agreement between the experimental and simulated momentum densities is illustrated in Figure 2.9 for a dimensionless interactions $u = 30$. The quantities plotted are normalized momentum density cuts of the experimental density $\tilde{\rho}_{\text{exp}}(k) = \rho_{\text{exp}}(k, 0, 0)/\rho_{\text{exp}}(\mathbf{0})$ and simulated ones $\tilde{\rho}_{\text{QMC}}(k; T) = \rho_{\text{QMC}}(k, 0, 0; T)/\rho_{\text{QMC}}(\mathbf{0}; T)$ for the first Brillouin zone. The simulated densities shown in the figure correspond to the reduced temperatures $T_J \equiv T/J = 2.2$, 2.4, and 2.6. The agreement between $\tilde{\rho}_{\text{exp}}(k)$ and $\tilde{\rho}_{\text{QMC}}(k; T)$ is optimum

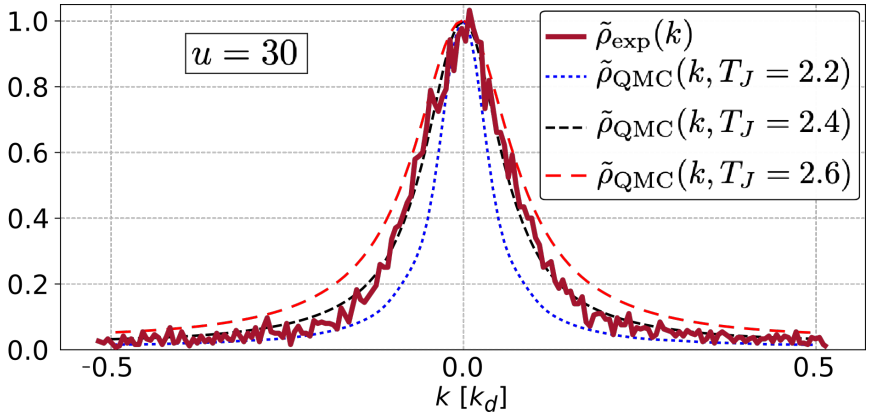

Figure 2.9: **Comparison between experimental and numerical momentum densities.** The normalized density cut of the experimental density $\rho_{\rm exp}(\boldsymbol{k})$ is compared with ab-initio QMC simulations $\rho_{\rm QMC}(\boldsymbol{k})$ at various temperatures T and fixed atom number $N = 3000$. The experimental temperature is the only adjustable parameter in the simulations and is found from the optimum matching between the real and simulated data. This thermometry yields here $T_J = 2.4(2)$ at $u = 30$.

for the reduced temperature $T_J = 2.4$ (the temperature resolution of the simulations is 0.2 T_J). In the case where the system is close to the superfluid-to-normal transition, such as in Figure 2.9, the momentum density is extremely sensitive to temperature changes, and the identification of the best temperature to match $\tilde{\rho}_{\rm exp}(k)$ and $\tilde{\rho}_{\rm QMC}(k;T)$ is excellent. However, a quantitative estimate of this agreement is handy for the remaining part of the phase diagram where variations of the momentum density with temperature are more subtle.

The goodness of the matching between experimental and numerical densities is measured via the reduced chi-square parameter:

$$\chi_r^2(T) = \frac{1}{N_p} \sum_{j=1}^{N_p} \frac{\left(\tilde{\rho}_{\rm exp}(k_j) - \tilde{\rho}_{\rm QMC}(k_j;T)\right)^2}{\sigma_{\rm exp}(k_j)^2} \tag{2.33}$$

where the first Brillouin zone has been discretized with a uniform mesh of $N_p = 120$ points, and $\sigma_{\rm exp}(k_j) = \sqrt{\tilde{\rho}_{\rm exp}(k_j)/M}$ is the error estimate on the experimental density from the finite sample of M experimental realizations (assuming Poissonian statistics). The chi-square parameter is plotted in Figure 2.10 for all the numerical densities at various temperatures. This parameter shows a clear minimum with temperature, with a minimum value $\chi_r^2(T = 2.4J) = 3.6 \pm 3.0$ compatible with unity. The exact position of the minimum can be obtained from a parabolic fit, giving $T_J = 2.36(3)$ at $u = 30$. Outside of the region near the superfluid-to-normal transition, this method generally overlooks the uncertainty induced by the shot-to-shot fluctuations of the atom number within the range $[2500 - 3500]$ (see discussion below). To be more realistic, we rather choose as error bars the temperature interval over which distinct $\chi_r^2(T)$ are observed, giving here $T_J = 2.4(2)$. This procedure is finally extended to any u across the Mott transition. One comment here is that such agreement is not given: it assumes that *(i)* the experiment produces equilibrium states of the BH model and *(ii)* that the temperature is well-defined despite shot-to-shot fluctuations of the atom number. Both hypotheses can only be checked *a posteriori* by finding a convincing agreement between the experimental and numerical

data. The second hypothesis was tested thoroughly by additional simulations carried out at different atom numbers, the results of which are plotted in Figure 2.11.

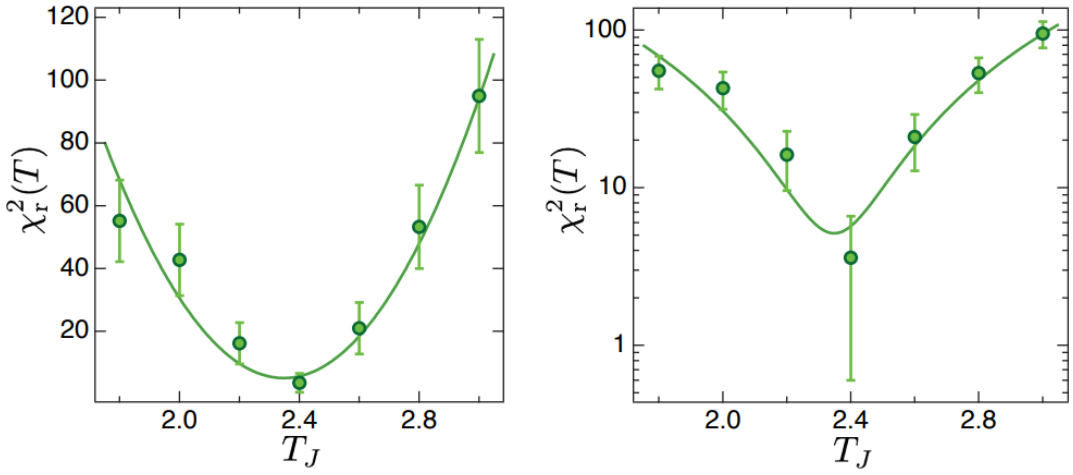

Figure 2.10: **Chi-square parameter for all simulated data at $u = 30$.** The parameter $\chi^2_r(T)$ (see text) exhibits a clear maximum in linear (left) and semilog (right) scale. A parabolic fit (solid line) yields $T_J = 2.36(3)$ for the estimated optimum temperature.

Each of the four subplots contains the numerical simulations for a fixed u, starting from the superfluid phase, then to the vicinity of the superfluid-to-normal transition, and finally deep into the Mott insulating phase. Contrary to Figure 2.9, the simulations are carried out at various atom numbers within the experimental range $[2500 - 3500]$ of the post-selected datasets. All densities corresponding to the same temperature but different atom numbers are plotted in the same color. The goal of these additional calculations is to estimate the effect of shot-to-shot fluctuations of the atom number on the estimated temperature. Namely, if the density range allowed by the fluctuations of N exceeds that given by the fluctuations of T, then the densities $\tilde{\rho}_{\mathrm{QMC}}(k; N = 3000; T)$ and $\tilde{\rho}_{\mathrm{QMC}}(k, N' \in [2500; 3500], T + \Delta T)$ overlap and the minimum uncertainty on the temperature $\Delta T_{min} = 0.2\,J$ is underestimated. Figure 2.11 shows that the effect of atom number fluctuations is quite different between the different phases. Deep into the superfluid regime ($u = 10.5$), small variations of T_J far from the critical temperature only slightly affect the shape of the density. Conversely, variations of the atom number at these temperatures have a greater impact. On adding atoms in the system, a given fraction populates the peak at $k = 0$, while the other ones spread uniformly over the remaining modes. Due to the normalization by the height of the $k = 0$ peak (increasing with N), the density tails are suppressed as N increases. Consequently, the overlap between numerical densities separated by $0.2\ J$ is significant, and a clear separation is only found for a lower temperature resolution $\Delta T = 0.4\,J$. This lower resolution is compatible with the experimental error bars given by the non-overlapping condition between the different $\chi^2_r(T)$ at fixed $N = 3000$.

Deep into the Mott insulator regime ($u = 60$), the experimental temperatures T_J are lower than the energy gap for the Mott plateau at the trap center. Therefore, the extra particles mainly populate the momentum density wings. As a consequence, the normalization to the $k = 0$ peak height becomes insensitive with the atom number, and the wings of $\tilde{\rho}_{\mathrm{QMC}}(k; N; T)$ increase with N contrary to the superfluid case. Experimental temperatures are also much higher than the critical temperature for the superfluid-to-normal transition. Therefore, temperature steps of $0.2\,J$ only weakly affect the momentum den-

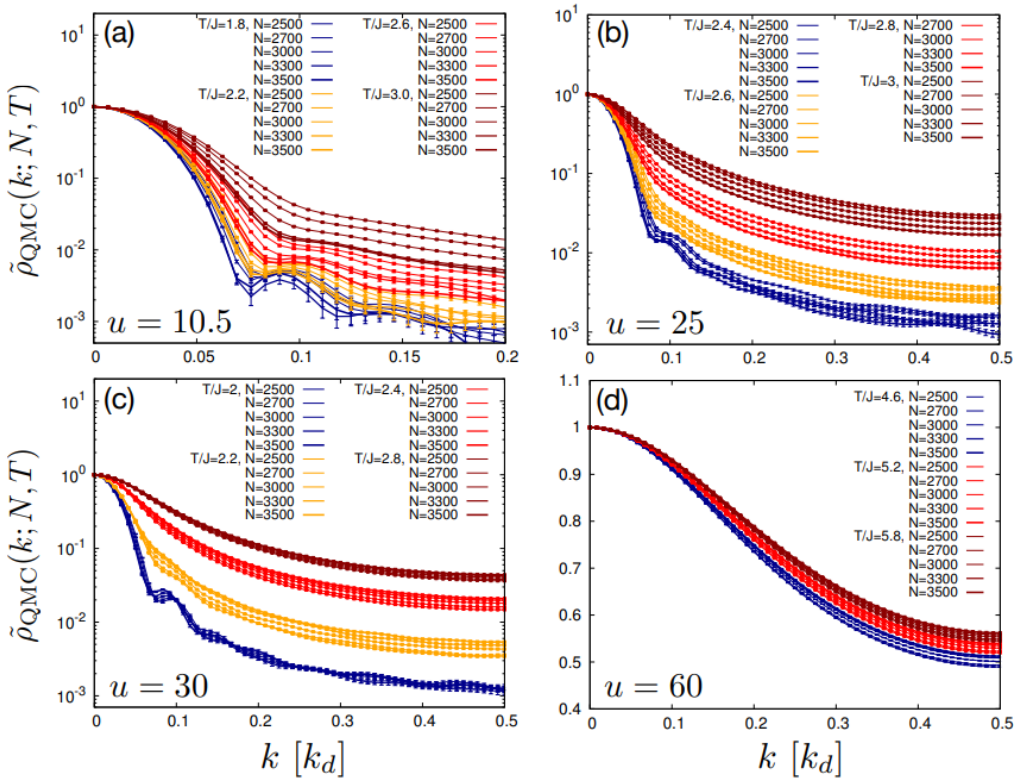

Figure 2.11: **Effects of atom number fluctuations on the thermometry.** Additional QMC simulations are provided in different regions of the phase diagram for experimentally relevant temperature and atom number ranges. These simulations estimate the reliability of the 0.2 J temperature resolution at fixed $N = 3000$, considering the uncertainty given by the shot-to-shot atom number fluctuations in the experiment (see text).

sities. Overall, the dependency of $\tilde{\rho}_{\mathrm{QMC}}(k; N; T)$ with T is much smoother than with N, and the minimum temperature resolution to distinguish between different atom numbers is larger now, about $0.6\,J$. The experimental temperature uncertainty based on the distinction between different $\chi^2_r(T)$ is however much larger than this minimum temperature resolution.

In the vicinity of the superfluid-to-normal transition ($u = 25$ and $u = 30$), the extreme sensitivity of the momentum density with temperature makes the curves at different atom numbers discernible even at the lowest temperature resolution of 0.2 J. Moreover, the opposite scalings of $\tilde{\rho}_{\mathrm{QMC}}(k; N; T)$ with N in the superfluid and Mott insulator regimes cancel out near the transition, reducing the effect of N on the densities further. Therefore, the temperature resolution of the simulations is *a priori* meaningful near the transition and, in practice, is the one found to correctly estimate the uncertainty on the experimental $\chi^2_r(T)$ (see Figure 2.10).

In conclusion, experimentally allowed atom number fluctuations impose a larger temperature uncertainty than the $0.2\,J$ resolution of the simulations in the limiting cases of the phase diagram. However, the error bars in these regions are dominated by the experimental ones, estimated via the comparison between $\tilde{\rho}_{\mathrm{exp}}(k)$ and $\tilde{\rho}_{\mathrm{QMC}}(k; N = 3000; T)$. Therefore, we conclude that the simulations of the 3D BH model in the canonical ensemble reproduce the experiment well, considering the experimental uncertainties. This

statement is even more true near the superfluid-to-normal transition, where the effect of atom number fluctuations is found to be negligible compared with temperature fluctuations of $0.2\,J$. In this case, the minimum uncertainty achievable obtained from the fit of $\chi^2_r(T)$ is meaningful. As a concluding remark, Figure 2.11 illustrates that the quantitative comparison between experimental and numerical data requires a precise detection of the low-density wings of $\tilde{\rho}_{\mathrm{exp}}(k)$ for only $N_{\mathrm{BEC}} = 3000$. Such extreme sensitivity can only be achieved thanks to the Multi-Channel-Plate detector.

2.4.3 Adiabatic state preparation across the superfluid-to-Mott transition

To investigate the adiabaticity of the lattice ramps, we recorded 3D momentum densities for lattice bosons prepared at various interaction parameter u, spanning the entire phase diagram from the superfluid regime ($u = 5$) to deep into the Mott insulating phase ($u = 92$). The lowest interaction parameter already corresponds to a lattice potential $V_0 = 7.75\,E_r$, ensuring that the energy bands are well separated and that the tight binding approximation is valid. The target atom number for the initial BEC is $N_{\mathrm{BEC}} = 3000$, and for each u, about $M \sim 600$ experimental densities satisfy the post-selection criterion that the atom number must fall within the window $[2500 - 3500]$. This atom number ensures a filling $\bar{n} \leq 1$ at the trap center. Our thermometry is applied to each data set and the resulting experimental temperatures are plotted in Figure 2.12.

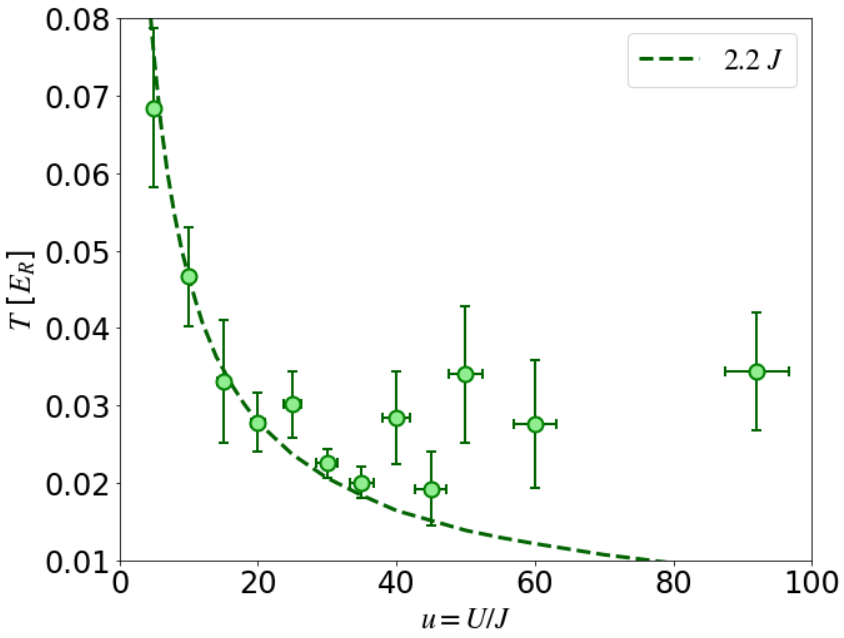

Figure 2.12: **Experimental temperatures across the superfluid-to-Mott transition.** The temperatures and their vertical error bars are extracted via the thermometry based on comparison with ab-initio QMC simulations for the 3D momentum density (see Section 2.4.2). Horizontal error bars represents the uncertainty on the final lattice depth calibrated with parametric heating (see Section 2.3.2). The dashed-line corresponds to the energy $2.2\,J$ expressed in units of the recoil energy, which best matches the experimental date in the range $u = 5 - 20$.

The variations of T with the interaction parameter u are now discussed. In the super-

fluid regime, the exponential decrease in temperature is known as adiabatic cooling [142]. This phenomenon is due to the decrease in the speed of sound $c = \sqrt{U/m^*} \propto \sqrt{UJ}$ as the lattice potential increases. As this happens, the number of thermally populated excited states increases if the temperature remains constant. The adiabaticity of the loading then dictates that the temperature must decrease in proportion to the width $\sim J$ of the energy band to maintain a constant entropy when driving the Hamiltonian. This proportionality between T and J is illustrated by the experimental temperatures in the superfluid regime (see Figure 2.12). The energy spectrum changes dramatically when the Mott transition is crossed, as a gap $\Delta \sim U$ gradually opens. The temperature must then increase with the depth of the lattice to conserve the entropy, which is referred to as adiabatic heating. In the experimental data, such increase of T when going deeper in the Mott insulator regime is observed (comparing the temperatures at $u = 30$, 35 with those at larger u) but barely resolved by the error bars.

To quantitatively assess the adiabaticity of the ramps, our experimental temperatures need be compared with the isentropic lines of the BH phase diagram. Tommaso Roscilde has provided us with the full entropy map (in false color in Figure 2.13) of the trapped 3D BH model at fixed atom number $N = 3000$ for our experimentally relevant temperature and interaction ranges. This map is accessible because the average energy per particle,

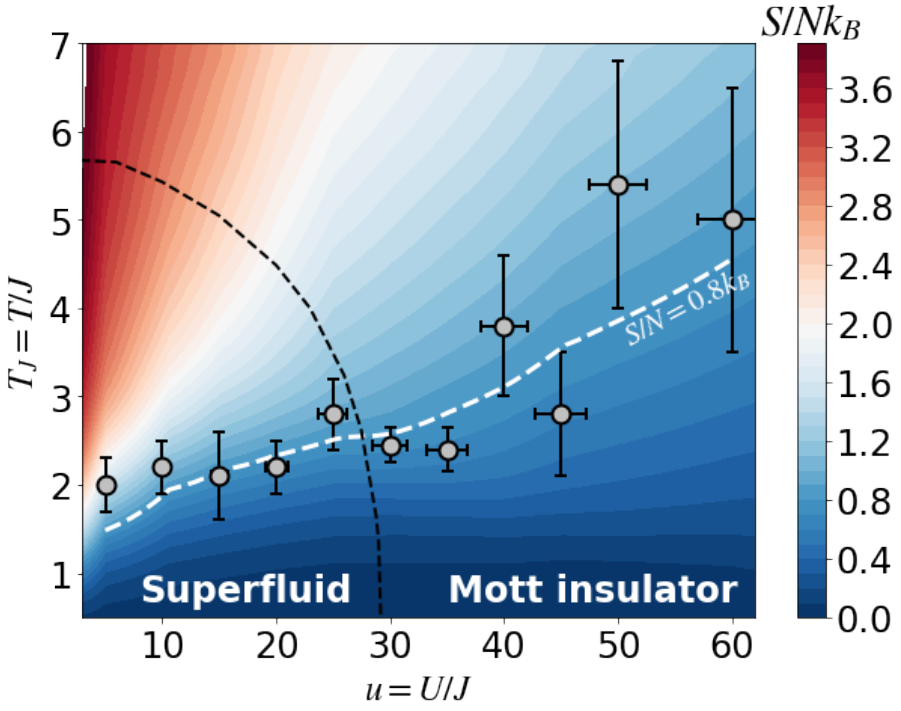

Figure 2.13: **Comparison between experimental temperatures and isentropic curves over the phase diagram.** The entropy map of 3D trapped lattice bosons extracted from the QMC data (see text) is plotted in false color, together with the experimental temperatures expressed in units of J. All experimental points (except the one at $u = 5$) are compatible with isentropic lines spanning the range $S/N = 0.8(1)\,k_B$, confirming the adiabatic state preparation over the entire phase diagram. The black dashed line shows the QMC critical temperatures for the homogeneous 3D BH model with $\bar{n} = 1$ [126], shown as a reference.

$e(T)$, can also be calculated from the QMC simulations for our experiment's moderate atom numbers and system sizes. A high-order polynomial fit of $e(T)$ provides a smooth interpolation of the numerical data, $e_{\mathrm{fit}}(T)$, from which the entropy per particle is derived [29]:

$$\frac{S(T)}{N} = \int_0^T \frac{d\theta}{\theta} \frac{de_{\mathrm{fit}}(\theta)}{d\theta} \tag{2.34}$$

Figure 2.13 also contains our experimental temperatures expressed in units of J. The main observation is that all the experimental temperatures (except the one at $u = 5$)[3] are compatible with isentropic curves spanning the range $S/N = 0.8(1)\, k_B$. This finding validates the picture that tuning the lattice potential produces a sequence of thermal equilibrium states in which the entropy is conserved, thus certifying the experimental adiabatic preparation of equilibrium states of the trapped 3D BH Hamiltonian. It also confirms mixed-state adiabaticity's robustness on crossing the low-entropy Mott transition.

In addition, the entropy per particle of the initial BECs inside the ODT was measured, to be compared with that of the lattice gas over the phase diagram. In a harmonic trap, the condensed fraction f_c is linked with the entropy per particle S_0 via the formula [143]:

$$\frac{S_0}{N\, k_B} = \frac{4\, g_4(1)}{\eta(3)}(1 - f_c) \tag{2.35}$$

with $g_4(1) \sim 1.082$ and $\eta(3) \simeq 1.2026$. The condensed fraction is estimated by a bi-modal fit of the momentum density to quantify its condensed and depleted components. The

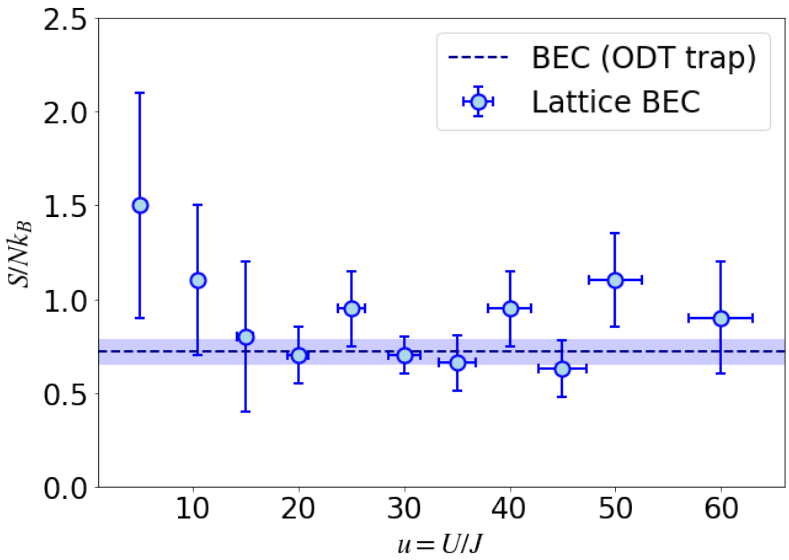

Figure 2.14: **Entropy per particle of lattice bosons at various u.** The entropy per particle for each data set is extracted from the experimental temperatures in Figure 2.13. Almost all points are compatible with the entropy per particle of the initial BEC $S_0/N = 0.72(7)\, k_B$ (dashed blue line and blue shaded area).

[3] Our thermometry is mostly sensitive to the dilute tails of the momentum density, whose amplitude deep into the superfluid regime can be four orders of magnitude smaller than the peak density at $\boldsymbol{k} = \boldsymbol{0}$. Then, the background counts may contribute to these tails, resulting in an over-estimation of the temperature. This effect, which rapidly disappears as the depletion level increases, is a possible explanation for the discrepancy between the experimental temperature and the $S/N = 0.8\, k_d$ entropy curve at $U/J = 5$.

use of Equation 2.35, valid for non-interacting bosons, is justified in our experiment by the different energy scales of the temperature $k_B\,T \simeq h \times 2380$ Hz and chemical potential $\mu \simeq h \times 350$ Hz. Equation 2.35 yields an initial entropy per particle of $S_0/N = 0.72(7)k_B$. As illustrated in Figure 2.14, this value is compatible with the ones in the lattice for almost all interaction parameters u. This additional measurement shows that the loading from the optical dipole trap to the lattice is adiabatic as well.

2.4.4 Saturation of the Cramér-Rao bound for the thermometry

As concluding remarks, this section comments on the experimental temperature error bars in Figure 2.13, namely the resolution of our thermometry over the entire phase diagram. As discussed in the previous section, the latter encompasses the effect of atom number fluctuations and seems to work best near the superfluid-to-normal transition, where the momentum density is the most sensitive to temperature variations. A quantitative evaluation of the temperature resolution is possible by considering the theoretical Cramér-Rao bound [144]. When applied to our thermometry, this limit states that the experimental temperature uncertainty δT_J from M momentum distributions is bounded by:

$$(\delta T_J)_{\min} = \frac{1}{\sqrt{I(T)\,M}} \tag{2.36}$$

with $I(T)$ the Fisher information [145] associated with temperature. Generally speaking, the latter quantifies the variations of an observable according to a given parameter. The more sensitive the observable, the larger the Fisher information and the smaller the Cramér-Rao uncertainty bound. For our thermometry, the Fisher information captures the sensitivity of the simulated momentum densities with temperature variations:

$$I(T) = \sum_k \frac{\tilde{\rho}_{\mathrm{QMC}}(k;T)}{\mathcal{N}_T}\left[\frac{\partial \log(\tilde{\rho}_{\mathrm{QMC}}(k;T)/\mathcal{N}_T)}{\partial T_J}\right]^2 \tag{2.37}$$

where $\mathcal{N}_T$ is the normalization of $\tilde{\rho}_{\mathrm{QMC}}(k;T)$ when summed over k. In the simulations, k forms a discrete grid with a momentum spacing $\Delta k < 10^{-2}k_d$ fine enough to resolve the features of the momentum density. The Fisher information is computed from the QMC data at fixed $N = 3000$, by approximating the derivative of the logarithm in Equation 2.37 with the finite difference:

$$\frac{\partial \log(\tilde{\rho}_{\mathrm{QMC}}(k;T)/\mathcal{N}_T)}{\partial T_J} \simeq \frac{1}{\Delta T}\log\left(\frac{\tilde{\rho}_{\mathrm{QMC}}(k;T+\Delta T)}{\tilde{\rho}_{\mathrm{QMC}}(k;T)}\frac{\mathcal{N}_T}{\mathcal{N}_{T+\Delta T}}\right) \tag{2.38}$$

where $\Delta T = 0.1\,J$.

Figure 2.15 shows in false color the values of the Fisher information over the entire phase diagram. Our experimental temperatures are shown for reference. The Fisher information exhibits a dramatic excursion over four orders of magnitude, which confirms the potential of a thermometry based on the measurement of the momentum density. The peak values are reached at the superfluid-to-normal transition, whose location in the phase diagram is discussed in detail in the next section. The lowest Fisher information is found deep into the Mott insulator regime, where thermal effects weakly affect the momentum density at our experimental temperatures. Conversely, little information on T can be obtained from the knowledge of $\tilde{\rho}_{\mathrm{QMC}}(k;T)$ in this region. A first comment is that the size of the experimental error bars varies accordingly with the values of Fisher

information. Secondly, the Cramér-Rao bound can now be estimated from the values of the Fisher information. The latter are *(i)* $I(T) \sim 0.1$ in the superfluid regime, *(i)* $I(T) \sim 10^{-3}$ in the Mott insulator regime, and *(iii)* $I(T) \sim 7$ at the superfluid-to-normal transition. They correspond respectively to the Cramér-Rao bounds *(i)* $(\delta T_J)_{\min} \sim 0.4$, *(ii)* $(\delta T_J)_{\min} \sim 1.3$, and *(iii)* $(\delta T_J)_{\min} \sim 0.02$. On the experimental side, the error bars in the superfluid and Mott insulator regimes are respectively $\delta T_J \sim 0.3$ and $\delta T_J \sim 1.5$, and therefore fully agree with the Cramér-Rao limit. This is also true near the superfluid-to-normal transition, where the fitting procedure of $\chi^2_r(T)$ yields $\delta T_J \sim 0.03$. As it nearly saturates the Cramér-Rao bound over the entire phase diagram, our thermometry thus fully exploits the information contained within the momentum density.

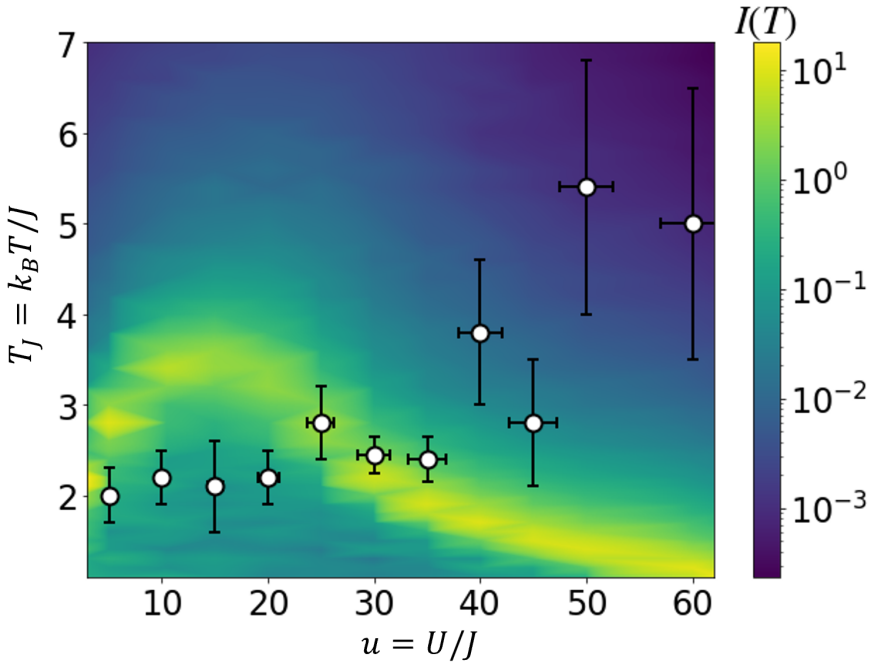

Figure 2.15: **Fisher information $I(T)$ for the temperature estimation from the simulated momentum densities.** The values of $I(T)$, plotted in false color, reflect the sensitivity of $\tilde{\rho}_{\mathrm{QMC}}(k;T)$ with variations of T and, conversely, the potential accuracy of a thermometry based on $\tilde{\rho}_{\mathrm{QMC}}(k;T)$. The Fisher information is minimum deep in the Mott insulator phase, while it is four orders of magnitude larger at the superfluid-to-normal transition. The evolution of $I(T)$ is consistent with the experimental error bars of the temperature estimates.

2.5 Study of the low-entropy Mott transition

Having certified the adiabatic preparation of the 3D BH Hamiltonian equilibrium states, the next step is the study of the critical region above the quantum critical point. Let us recall that the precise location of the superfluid-to-Mott transition with experiments has remained challenging so far. Many experiments [19, 127–129] have reported values of the unit-filling critical interaction $u_c^{(\bar{n}=1)}$ closer to the mean-field prediction at zero temperature, $u_c^{\mathrm{MF}} \simeq 34.8$, rather than the exact QMC values [126] at zero $\left(u_c^{\mathrm{QMC}} \simeq 29.3\right)$ and non-zero temperatures (black dashed line in Figure 2.13). The critical exponents have

not yet been measured either, in particular due to inhomogeneity and finite-size effects in the experimental implementations. Here this investigation is renewed with a novel approach that combines, as in the previous section, our original detection method with the QMC simulations performed by Tommaso Roscilde [30].

2.5.1 Phase-diagram of the trapped 3D Bose-Hubbard model

In principle, the low-entropy Mott transition can be monitored via the measurement of the condensed fraction f_c. Similarly to the case of a harmonically trapped BEC, the momentum density of lattice bosons loaded inside a shallow optical lattice exhibits a clear double structure (a condensate and a pedestal), from which f_c can be reliably accessed. This technique has already allowed us to investigate the condensation transition at $u \simeq 10$ [146]. However, such a distinction becomes blurred at stronger interactions, particularly near the Mott transition where f_c is so small that the condensed and non-condensed components in the momentum density can hardly be identified. A different approach is used here to circumvent this difficulty. Rather than the condensed fraction, we record the maximum density at the center of the Brillouin zone $\rho_0 = \rho(\boldsymbol{k} = \boldsymbol{0})$. This quantity corresponds to the mean atom number inside a small 3D momentum volume $V_k = (k_d/30)^3$ centered on $\boldsymbol{k} = \boldsymbol{0}$, and is only accessible through our single-atom resolved detection in 3D. In particular, it is beyond the reach of absorption imaging techniques where the integration along the camera line of sight provides integrated 2D momentum densities. As the condensate mode is strongly peaked around $k = 0$, ρ_0 is intimately connected with the condensed fraction [147], and is measured directly without depending on a fit of the momentum density. The experimental variation of ρ_0 across the transition are discussed in the next section. To better understand this result, it is insightful to first have a look at the QMC values of ρ_0 across the entire phase diagram.

Figure 2.16 shows the variations with U/J of $\tilde{\rho}_{\mathrm{QMC}}(k;T)$, for $N = 3000$ atoms and experimentally relevant temperatures. The onset of a superfluid regime corresponds to $\rho_0 \gtrsim 10$ atoms/V_k (white line in Figure 2.16) and is consistent with the region of the phase diagram where the Fisher information is maximum (yellow line in Figure 2.13). The condition $\rho_0 \simeq 10$ atoms/V_k represents a line of critical temperatures for our trapped system, which differs significantly from the QMC prediction for the homogeneous case with $\bar{n} = 1$ (black dashed line in Figure 2.16). The discrepancy below $u \sim 26$, where the critical temperatures of the homogeneous system are systematically higher than for the trapped case, comes from the choice of the total atom number. Based on previous QMC simulations, the latter was chosen to have $\bar{n} \sim 1$ at the trap center for $u \sim 30$. The weaker external confinement at lower U/J imposes a density $n < 1$ at the trap center, explaining why the temperature extent of the superfluid phase is smaller in our trapped system than for the homogeneous one. Similarly, the slight increase of the line of critical temperatures below $u \sim 15$ results from the growth of n with the lattice beams intensity in this regime. Above $u \sim 26$, the contrasting behaviors between the homogeneous and trapped systems result from the coexistence of several phases in the trap. At sufficiently low temperatures, the halo surrounding the Mott insulator core is superfluid and keeps the value of ρ_0 high, despite the Mott atoms disappearing from the condensate peak. As $u \to \infty$, the superfluid shell shrinks to a thin spherical corona where the atoms reproduce the physics of 2D hardcore bosons at half-filling, for which the critical temperature is given by $T_c = 0.785\, J/k_B$ [148].

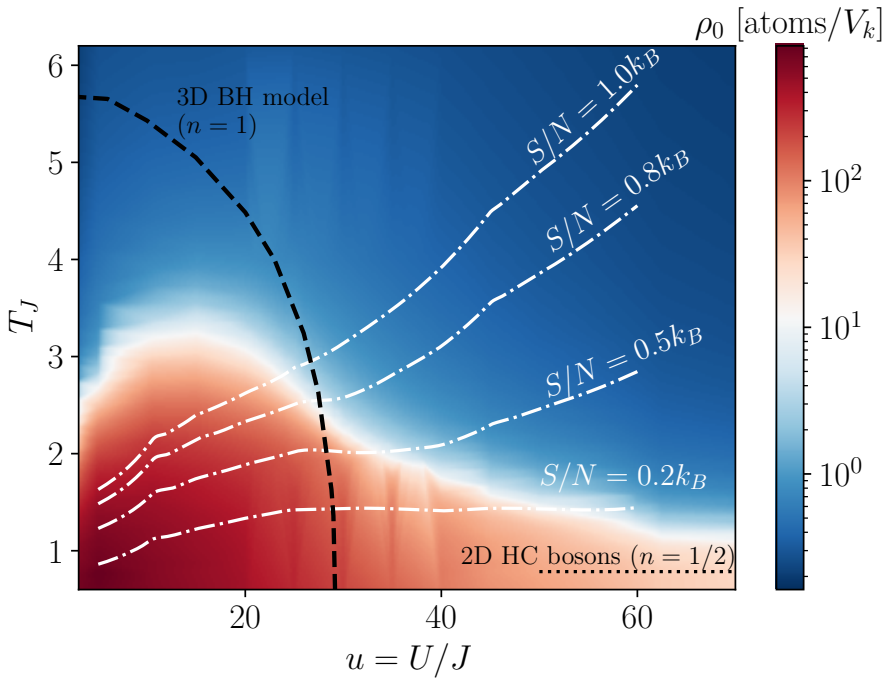

Figure 2.16: **Phase diagram of 3D lattice bosons in a trap.** The maximum momentum density ρ_0 is plotted in false color for all u and T_J. ρ_0 corresponds to the atom number inside a volume $V_k = (k_d/30)^3$ centered on $\boldsymbol{k} = \mathbf{0}$, and is extracted from the simulated momentum densities $\tilde{\rho}_{\mathrm{QMC}}(k;T)$ at $N = 3000$. The black dashed line represents the line of critical temperatures for the homogeneous 3D BH model with $\bar{n} = 1$ [126]. The white dashed-dotted lines depict isentropic trajectories computed for our experimental parameters (see Equation 2.34). The black dotted line indicates the critical temperature $k_B T = 0.785\,J$ for 2D hard-core (HC) bosons at half filling $\bar{n} = 1/2$ [148].

Of particular interest to us is the isentropic line $S/N = 0.8\,k_B$ describing the trajectory of our experiment in the phase diagram. According to the QMC data simulating our trapped system (false color), our experiment should cross the superfluid-to-normal transition at a temperature $T_{\mathrm{exp}} \simeq 2.6\,J/k_B$ for which the interaction strength $u_c(T_{\mathrm{exp}})$ is close to the bulk value for the $T = 0$ Mott transition $u_c^{\mathrm{QMC}} = 29.34$. Therefore, the transition probed experimentally is located in the quantum critical region of the phase diagram, possibly affected by the presence of the quantum critical point just below. In addition, the fact that $u_c(T_{\mathrm{exp}}) < u_c^{\mathrm{QMC}}$ ensures that the cloud is fully normal when a Mott core starts forming at the trap center. For these reasons, we refer to the transition probed experimentally as a *low-entropy* Mott transition, although we expect it to exhibit critical properties of the finite-temperature superfluid-to-normal transition. This conclusion is not generic and results from a careful choice of the atom number given our experiment's temperature regime and trapping frequencies.

2.5.2 Experimental determination of the Mott transition and of the critical exponent

Figure 2.17 shows the variations of the measured ρ_0 versus the interaction strength u. The error bars, induced by the shot noise, are rather large because of the low (5%) detection efficiency used here to avoid saturating the ^{4}He* detector. In agreement with the

homogeneous case, ρ_0 exhibits a sharp decrease in the range $u \in [5-25]$ where it seems unaffected by our system's inhomogeneity and finite size. However, both effects mask the sharp variations of ρ_0 in the region $u \in]25-35]$, where a slowly-decaying tail is observed. Consequently, only the region $u \in [5-25]$ is used to derive the critical ratio u_c of the bulk system (blue shaded area in Figure 2.17). The variations of ρ_0 are fitted with the critical scaling expected for the homogeneous system near the transition:

$$\rho_0^{\text{fit}}(u) = \rho_0^{u=0}\left[1 - \frac{u}{u_c}\right]^{2\beta} \tag{2.39}$$

where $\rho_0^{u=0}$ and u_c are chosen as fitting parameters. The critical exponent is fixed to its theoretical value for the 3D XY universality class $\beta = 0.3485$ [112].

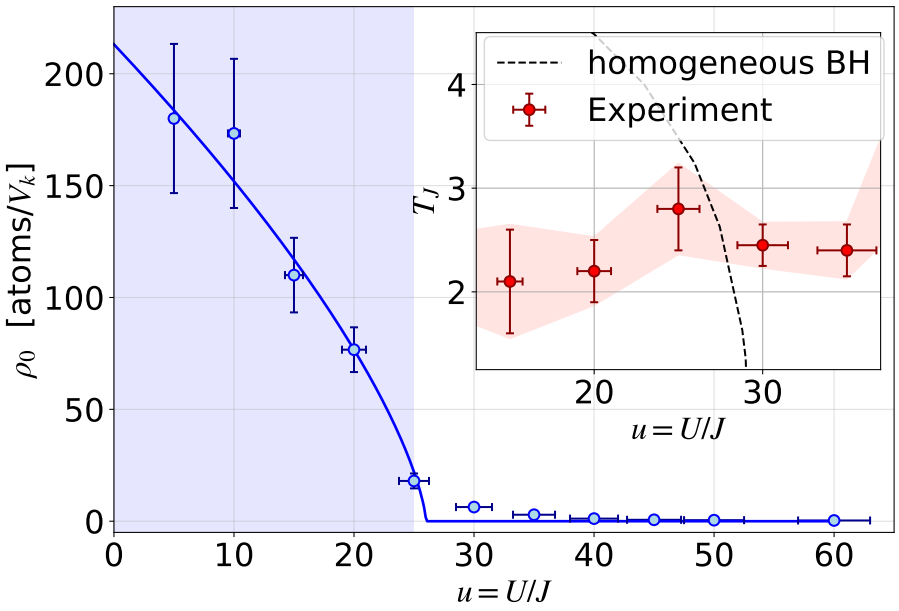

Figure 2.17: **Location of the Mott transition.** The experimental values of ρ_0 below $u \leq 25$ (blue shaded area) are fitted with the critical scaling expected for the 3D XY universality class (solid blue line). The fitted function matches well with the experimental data, and returns $\rho_0 = 215(15)$ atoms/V_k and $u_c = 26(1)$. Inset: the line of critical temperatures for the homogeneous 3D BH model with $\bar{n} = 1$ (black dashed line) is superimposed with the experimental temperatures. The intersection between both curves yields $u_c = 27(1)$, in good agreement with the value derived from the critical scaling of ρ_0.

The agreement between Equation 2.39 and the experimental data in Figure 2.17 confirms the experimental observation of a critical scaling, with the expected critical exponent for a homogeneous system belonging to the 3D XY universality class. Surprisingly, the critical scaling manifests itself in a broad range of interactions, even well below the transition. The fitted parameters are $\rho_0 = 215(15)$ atoms/V_k and $u_c = 26(1)$. As expected, this critical interaction is compatible with the QMC prediction for our trapped system at the temperature of our experiment (false color in Figure 2.16). In addition, the inset of Figure 2.17 shows the intersection between the line of critical temperatures for the homogeneous 3D BH model with $\bar{n} = 1$ (black dashed line in Figure 2.16) and our experimental temperatures. This analysis yields a critical interaction $u_c = 27(1)$ compatible with the one measured experimentally. In contrast to what was reported in other experiments, both results clearly differ from the zero-temperature mean-field prediction $u_c^{\text{MF}} \simeq 34.8$.

Their compatibility confirms the ability of our experiment to reveal the physics of the bulk system, which again stems from an appropriate choice of the atom number to have $\bar{n} = 1$ around $u \sim u_c$ given our experimental conditions.

It may seem surprising to observe the criticality of the homogeneous system at $T = 0$ in our experiment, especially over such a wide range of interactions u. This feature may be explained by the condensate mimicking a homogeneous system due to the flatness of the harmonic potential at the trap's center. Interestingly, this finding is supported by a similar observation for the QMC data. Indeed, The variations of the simulated ρ_0 along different isotherms around T_{exp} are all compatible with the critical scaling of the 3D XY universality class (see the left panel of Figure 2.18). As with the experimental data, the tail of the simulated ρ_0 is excluded from the analysis in order to probe the physics of the homogeneous system. Furthermore, the left panel of the figure illustrates that the critical exponent of the theoretical and experimental data clearly differs from the mean-field criticality $\beta^{\text{MF}} = 1/2$. Note that even though the experiment follows an isentropic trajectory in the phase diagram, the temperature remains close to T_{exp} for $u \leq 40$ so that a comparison with the QMC data along isotherms is meaningful in this region. However, the contribution of the cloud shell affects the fitted value of u_c for both isotherms at the lowest temperatures. In particular, the value at $T_J = 2.2$, $u_c \simeq 31$, exceeds the largest critical ratio $u_c^{\text{QMC}} \simeq 29.3$ of the homogeneous case.

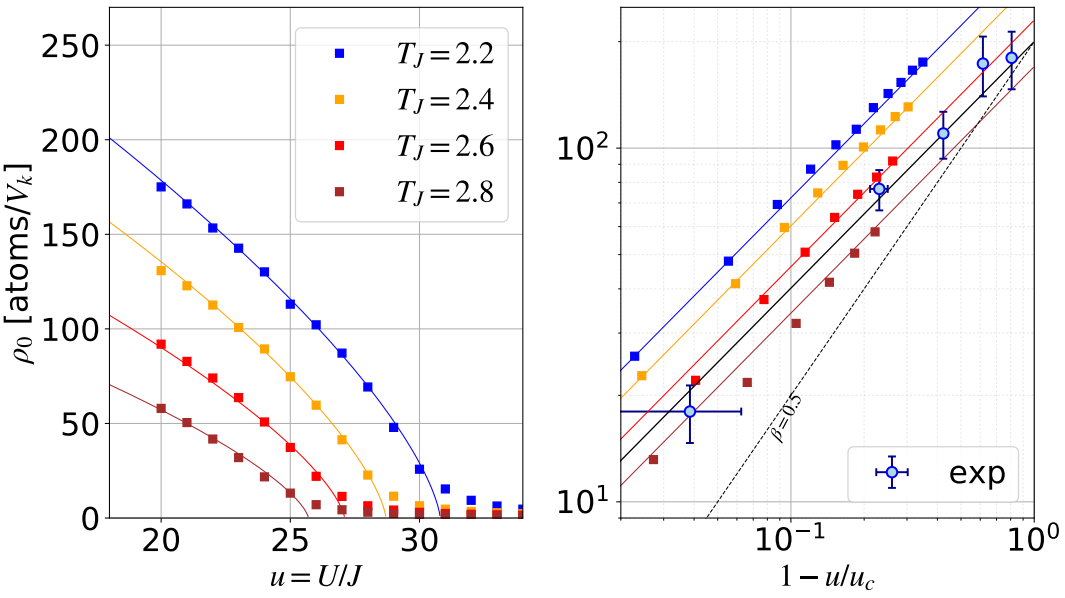

Figure 2.18: **Criticality of ρ_0 from the QMC and experimental data.** Left: simulated values of ρ_0 along relevant isotherms and near the transition. The solid lines are fitting functions of the form 2.39, whose agreement with the data confirms the presence of the 3D XY criticality. Right: QMC data and experimental points plotted in log-log scale versus $1 - u/u_c$, so that the superfluid region is on the right side and the transition is on the left side. Theoretical and experimental data are inconsistent with the mean-field critical exponent $\beta^{\text{MF}} = 1/2$.

2.5.3 Phase coherence properties on the Mott insulator side

As aforementioned in Section 2.2.2, the in-trap correlation length ξ of a homogeneous system diverges on approaching the transition from the Mott insulator side:

$$\xi \propto |t|^{-\nu} \tag{2.40}$$

with $\nu \simeq 0.671$ for the 3D XY universality class [112]. The central peak width of the interference pattern is inversely proportional to ξ and therefore provides information on the in-trap coherence properties of system [130, 149, 150]. To investigate the divergence of the correlation length, the half width at half maximum (HWHM) δk of the central peak is extracted from the momentum densities. The left panel of Figure 2.19 shows a log-log plot of $1/\delta k \propto \xi$ versus the distance from the transition $u/u_c - 1$. On approaching the transition from right to left, $1/\delta k$ increases with a scaling compatible with an algebraic one. However, the points scattering is significant and may be explained by the temperature scattering in Figure 2.13 (the colder temperatures corresponding to smaller δk). As a consequence, our data cannot distinguish between the 3D XY criticality and the mean-field one $\left(\nu^{\mathrm{MF}} = 1/2\right)$. Indeed, fitting the data with $\xi_0(u/u_c - 1)^\nu$ using ξ_0 and ν as fitting parameters yields $\nu = 0.6(1)$. Similarly to the previous section, the behavior of the QMC data can also be examined. The inverse widths $1/\delta k$ extracted from the simulated momentum densities are plotted in the right panel of Figure 2.19, along the same isotherms as before. Comparing these isotherms with the isentropic trajectory $S/N = 0.8\,k_B$ followed by the experiment is more questionable on the Mott insulator side. Nevertheless, the

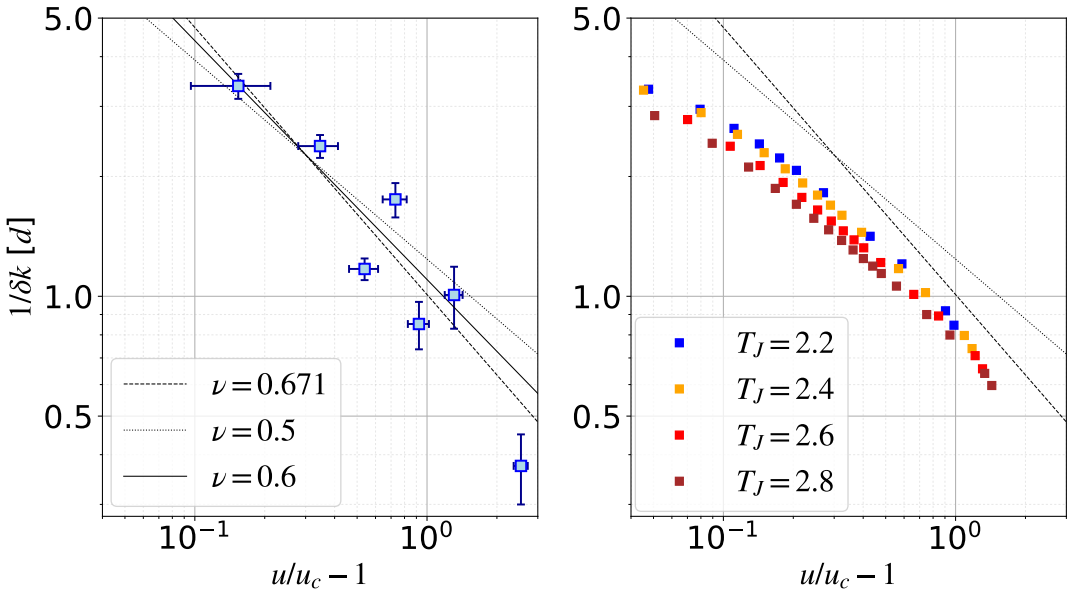

Figure 2.19: **Criticality of the correlation length on the Mott insulator side of the transition.** Left: log-log plot of the inverse HWHM $1/\delta k$ in units of the lattice spacing d versus the distance from the transition. The solid black line is a fit of the data with the function $\xi_0(u/u_c - 1)^\nu$, yielding $\nu = 0.6(1)$. The point on the far right ($u = 92$) is not used for the fit. The black dotted (*resp.* dashed) line is a fit of ξ_0 using the same fitting function and the critical exponent of the 3D XY (*resp.* mean-field) value. Right: same plot for the QMC data along isotherms close to the experimental temperature. The critical scaling observed seems rather compatible with the mean-field exponent $\nu = 1/2$.

QMC data still exhibit a critical scaling, but one seemingly compatible with the mean-field exponent. This last observation leads us to the conclusion that trapping effects are too strong to observe the bulk critical behavior of the correlation length, and consequently of $1/\delta k$, on the Mott insulator side of the transition. This can be interpreted by the fact that the phase coherence in the Mott regime first increases on approaching the transition in the normal outer shells, which are located at positions where the trap is strongly non-homogeneous.

2.6 Conclusion

In this chapter, we have renewed the investigation of the *low-entropy* Mott transition with cold atoms, with an original approach combining our measured 3D momentum densities at various interactions with ab-initio QMC calculations performed by Tommaso Roscilde at ENS Lyon [29, 30]. Such a comparison is possible thanks to our single-atom resolved detection of ^{4}He* atoms, which allows us to work at low atoms numbers for which numerical simulations are still accessible.

Minimizing the discrepancies between our experimental densities and the simulations performed at various temperatures provides a unique thermometry for the lattice gases. Computing the Fisher information associated with this thermometry confirms that it almost reaches the maximum accuracy allowed by the Cramér-Rao limit, which includes the regime close to the superfluid-to-normal transition where the temperature is the most accurately estimated. Building on this technique and on the first unbiased calculation of an entropy map for the 3D BH model, we experimentally certified the adiabatic preparation of finite entropy states over the whole phase diagram at a constant entropy per particle $S/N = 0.8\,k_B$. The latter is compatible with that of the initial BEC. This mixed-state adiabaticity appears to be a robust property, unaffected by the superfluid phase's gapless energy spectrum or the crossing of a finite-temperature phase transition. This feature differs greatly from experimental platforms manipulating nearly zero-entropy states (such as trapped ions, Rydberg atoms, or quantum circuits) in which systematic deviations to adiabaticity are observed upon crossing a quantum phase transition due to the disappearance of the energy gap [150, 151].

The adiabatic preparation of equilibrium states of the 3D Bose-Hubbard model paved the way for the study of the quantum critical region above the quantum critical point of the phase diagram. In principle, finite-temperature superfluid-to-normal transitions occurring sufficiently close to the quantum critical point should exhibit the critical properties of the $T = 0$ Mott transition. However, the temperature range of the quantum critical region is unknown, and critical properties of homogeneous systems are difficult to measure due to trapping and finite-size effects. Our detection of the full 3D momentum density allows us to access $\rho_0 = \rho(\boldsymbol{k} = \boldsymbol{0})$ without suffering from line-of-sight integration present in absorption images, which partially circumvents these limitations. The strong suppression of ρ_0 on the superfluid side of the transition yields a critical interaction $u_c = 26(1)$ consistent with the QMC prediction for the uniform 3D BH model at unit filling and finite temperature. This compatibility originates from our careful choice of the atom number to reach a unit filling close to the transition point. Such a strong dependence on the experimental conditions limits the relevance of using a trapped system to locate the transition in the homogeneous case, as illustrated by the mean-field compatible values reported in experiments where the

filling was greater than one [19, 128]. For both the experimental and theoretical data, the decay of ρ_0 is compatible with the critical exponent of the 3D XY universality class, to which the $T = 0$ superfluid-to-Mott transition belongs. To our knowledge, this is the first time this critical scaling has been observed experimentally. Here again, this finding strongly depends on the experimental conditions. In particular:

- QMC data showed that the persistence of a superfluid shell at (significantly) lower entropies than ours would have prevented the observation of the transition,
- The measured width of the central peak does not allow for distinguishing between the 3D XY and the mean-field criticality, whereas QMC data seem consistent with a mean-field exponent. Both results suggest that the trap's presence masks the criticality of the bulk system for the correlation length.

To overcome these obstacles, one could work with box-like potentials [152] to experimentally implement the homogeneous 3D BH model. However, the unitary filling condition achieved naturally in our case (at the center of the trap) by the harmonic confinement would then be difficult to fulfill. An alternative approach would be to selectively probe the coherence properties at the center of the trap [153] to minimize the effect of the surrounding superfluid shell.

Chapter 3

3. Local N-body correlations : Full Counting Statistics and high-order moments of interacting lattice bosons

The previous chapter presented our exploration of the low-entropy Mott transition and its critical properties based on the measurement of the 3D momentum density, as offered by our original electronic detection. This study has focused on the average mode occupancy $\rho(\boldsymbol{k}) = \langle \hat{a}^\dagger(\boldsymbol{k})\hat{a}(\boldsymbol{k})\rangle$. In quantum mechanics, the fluctuations of an observable are known to contain a wealth of information unavailable to the mean value. The noise analysis is thus central in many fields, such as quantum electronics [154], quantum optics [155], or quantum gases [156–158].

In this chapter, we extensively investigate the statistics of the occupation number fluctuations in 3D lattice gases detected after a long free-fall expansion. This study takes advantage of the single-atom-resolved detection in the far-field regime to reveal the many-body coherence of the systems under study. To this aim, we measure the Full Counting Statistics (FCS) and high-order moments of the momentum occupation number beyond the mean and variance [31]. The novelty of our approach is to consider interacting atomic gases, for which an optical lattice enhances interactions. We focus on two iconic states of lattice bosons, Bose superfluids and Mott insulators, which we characterize from their statistical properties measured with unrivaled precision.

This chapter is divided into three sections. The first two present our measurements of the FCS and high-order moments up to $n = 6$ in the BEC mode ($\boldsymbol{k} = \boldsymbol{0}$) of Bose superfluids and Mott insulators. Section three is dedicated to understanding the deviations to the prediction for a coherent state observed for the BEC.

3.1 Full counting statistics

A powerful tool to thoroughly investigate the fluctuations of an observable is the Full Counting Statistics (FCS), which consists in counting the number of particles detected in a given time and/or space interval. This technique was first implemented in quantum optics and mesoscopic conductors [159] thanks to the early development of single-particle-resolved probes for photons and electrons. Following the advent of quantum simulations

with cold atoms, the FCS was applied to the study of Rydberg atoms [160–162] and non-interacting atomic gases [26, 163]. Many theoretical studies have demonstrated the capabilities of the FCS to explore quantum phase transitions [164–166], universality [167, 168], entanglement properties [169], or out-of-equilibrium dynamics [170]. The FCS is also promising from a quantum information perspective, as it can probe the diagonal part of the many-body density matrix and, therefore, identify quantum states with large numbers of particles without resorting to a consuming quantum state tomography [171]. In addition, recent works [172, 173] have also shown that applying random unitary transformations on a system before measuring the FCS would allow access to the non-diagonal correlators. All these reasons call for further developments of experimental approaches to access the FCS in quantum simulators.

In this work, the FCS is characterized by measuring the probability distribution of the atom number N_Ω falling inside a small voxel of volume V_Ω in momentum space, for either Bose superfluids or Mott insulators. What "small" refers to will be discussed in detail in the presentation of the analysis procedure. First, we remind what is the expected FCS in the two limiting regimes of the Bose-Hubbard phase diagram.

3.1.1 Poisson and thermal FCS

The Bose-Einstein condensed phase is characterized by a complex order parameter, the condensate wavefunction, whose arbitrary choice of phase when crossing the transition point corresponds to a breaking of the gauge symmetry [143]. This well-defined phase enables to describe an ideal BEC at zero temperature by a coherent state, in which all the particles have condensed into the single-particle ground state. Such a coherent state $|\alpha\rangle$ can be written in the Fock state basis $|n\rangle$ as follows:

$$|\alpha\rangle = e^{-|\alpha|^2/2} \sum_n \frac{\alpha^n}{\sqrt{n!}} |n\rangle \tag{3.1}$$

This decomposition yields a Poissonian probability distribution for the occupation number:

$$P(n) = |\langle n|\alpha\rangle|^2 = e^{-|\alpha|^2} \frac{|\alpha|^2}{n!} \tag{3.2}$$

which is entirely defined by the mean atom number $|\alpha|^2$. Of course, BECs produced experimentally are neither ideal nor zero temperature. Therefore, there is no guarantee that a Poisson FCS is found when studying the BEC mode ($\boldsymbol{k} = \mathbf{0}$) of Bose superfluids. More generally, pure states cannot even be prepared experimentally, strictly speaking, due to the inevitable coupling with the environment. To what extent a pure-state description correctly describes the result of an experiment remains an open question that is of particular interest for the development of experimental platforms for quantum technologies.

Similarly, this concern also applies to the other side of the BH phase diagram. Uniform Mott insulators at zero temperature are described by Fock states in the in-trap position basis (see Equation 3.8 in Chapter 2). In the momentum basis, which is the one probed after the TOF, a Mott insulator exhibits thermal-like statistics [92, 174, 175]. This property can be understood intuitively from the fact that the different lattice site behave as a discrete series of uncorrelated emitters in the limit of zero tunnelling ($J \to 0$), which is analogous to a thermal gas with a correlation length shorter than the lattice spacing. Therefore, the

FCS for a Mott insulator should be characterized by the geometric probability distribution associated with a thermal distribution:

$$P(n) = \frac{\bar{n}^n}{(\bar{n}+1)^{n+1}} \tag{3.3}$$

We comment here that the imperfect detection efficiency of our detector ($\eta_{\mathrm{MCP}} < 1$) does not prevent in practice the observation of the probability distributions 3.2 and 3.3. Indeed, one sees that replacing $|\alpha|^2$ by $\eta_{\mathrm{MCP}}|\alpha|^2$ in Equation 3.2 (*resp.* $\bar{n}$ by $\eta_{\mathrm{MCP}}\bar{n}$ in Equation 3.3) still yield a Poisson (*resp.* geometrical) distribution. This property is in fact generic to Gaussian states [155].

3.1.2 Experimental constraints on the volume probed for the FCS

A first necessary condition to measure the FCS associated with a given quantum state is to count the atoms in a smaller volume than that of the state itself. This condition enables bypassing the thermodynamical constraints on macroscopic quantities (the atom number here that has small fluctuations) of quantum states prepared at equilibrium. To illustrate that, let us consider the simplified case where the experiment repeatedly produces ideal BECs with a strictly constant atom number at zero temperature. After the expansion, the condensed atoms occupy a momentum volume $V_{\mathrm{BEC}} \simeq (1.6/L)^3$ [176] roughly set by the inverse of the in-trap spatial size L. In this volume, the atom number detected between different experimental realizations is constant as the experiment reproduces the canonical ensemble [177]. To measure the fluctuations associated with a coherent state, one must somehow mimic the grand canonical ensemble and let the atom number fluctuate [178]. This is achieved by probing a volume V_Ω much smaller than V_{BEC}, in which the atom number N_Ω can fluctuate thanks to the remaining cloud acting as a reservoir.

A second constraint for accessing the FCS is illustrated in Figure 3.1 (right panel) and consists in probing a volume equal to or smaller than that of a single mode in the momentum space. This volume corresponds to $(2\pi/L)^3$ and is referred to as the correlation volume V_c in the following of this chapter for a reason that will become clear in Section 3.2.2. When considering the condensate mode of Bose superfluids, the condition $V_\Omega \lesssim V_c$ is automatically fulfilled by the previous one $V_\Omega \ll V_{\mathrm{BEC}}$. On the other hand, Mott insulators are large and dilute clouds in the momentum space, whose volumes V_{Mott} exceed the first Brillouin zone. Therefore, the condition $V_\Omega \lesssim V_c$ is even more stringent than $V_\Omega \ll V_{\mathrm{Mott}}$. Consequently, the statistics within V_Ω is greatly limited in the case of Mott insulators compared to the condensate mode of Bose superfluids, and imposes two different analysis procedures to extract the FCS of both systems.

3.1.3 Analysis procedures and experimental results

Our investigation starts by recording around $N_{\mathrm{runs}} \simeq 2000$ momentum distributions of Bose superfluids and Mott insulators. The former corresponds to $U/J = 5$ and $N = 5(1) \times 10^3$, and the later to $U/J = 76$ and $N = 7(2) \times 10^3$. Both data sets were taken with the Raman transfer so that the overall detection efficiency η is only limited by that of the MCPs $\eta_{\mathrm{MCP}} = 53(2)\%$. This is a fundamental improvement compared to previous works done in our team [146, 174] or in Australia [1], for which $\eta < 15\%$. Indeed, a large detection efficiency is obviously necessary to extend the probability distribution to large

atom numbers and to reach high-order moments. This is all the more true since these measurements require probing the gases in small momentum-space volumes V_Ω after a long TOF of 297 ms (see Figure 3.1).

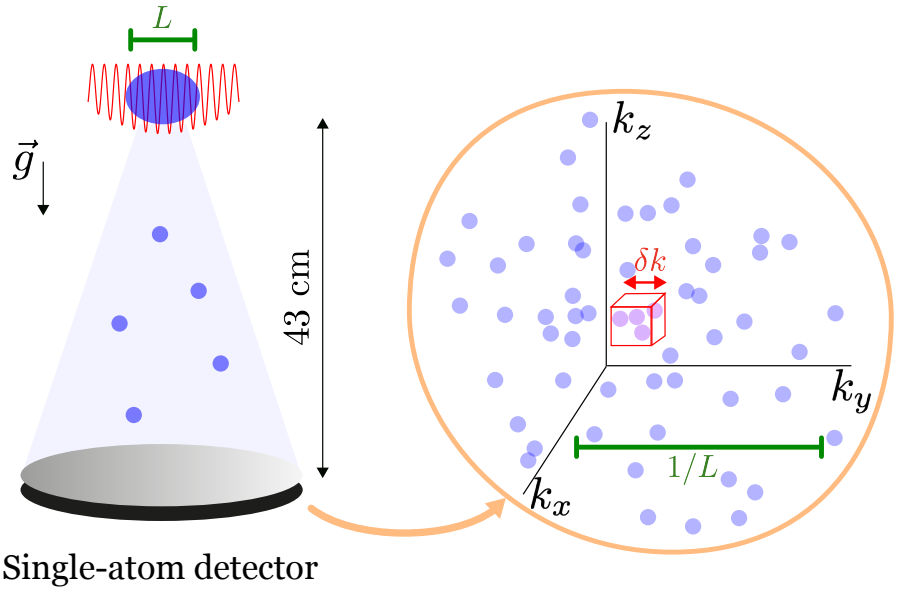

Figure 3.1: **Sketch of the experimental procedure.** Interacting quantum gases of ^{4}He* atoms undergo a free-fall expansion from a 3D optical lattice. The detection by the MCPs yields the 3D single-atom resolved momentum distributions, from which the probability distribution $P(N_\Omega)$ is extracted. To properly reveal the statistical properties of N_Ω, the volume probed $V_\Omega \sim \delta k^3$ must be equal to or smaller than that of a single mode $V_c = (2\pi/L)^3$.

The procedure for extracting $P(N_\Omega)$ differs between a Mott insulator and the BEC mode of a Bose superfluid, as the former is a dilute cloud spread over the entire first Brillouin zone while the latter is highly peaked at $\boldsymbol{k} = \boldsymbol{0}$. For a Mott insulator, the entire first Brillouin zone is binned with cubic voxels of side $\delta k = 6 \times 10^{-2}\ k_d$ corresponding to $V_\Omega = 0.9\, V_c$. The probability distributions of all the voxels V_Ω are then averaged to obtain that of a Mott insulator with better statistics. On the other hand, the condensed atoms of lattice superfluids probed in the far-field regime of expansion are located inside narrow diffraction peaks of width $\Delta k \sim 15 \times 10^{-2}\ k_d$ [32]. Therefore, these peaks are very dense and contain enough atoms to probe the statistics of the BEC mode with a single voxel smaller than $(\Delta k)^3$. In practice, we use a spherical voxel S_Ω of radius $\delta k = 0.025\, k_d \ll \Delta k$ centered on $\boldsymbol{k} = \boldsymbol{0}$. The resulting probability distributions of Mott insulators and Bose superfluids are plotted in Figure 3.2.

In both cases, the experimental data are compared with the Poisson and geometric distributions of Equations 3.2 and 3.3 associated with the average atom number $\langle N_\Omega \rangle$ measured in the experiment. For Mott insulators, $\langle N_\Omega \rangle = 0.46(5)$, and an excellent agreement is found with the corresponding geometric distribution expected for a thermal state. Therefore, the momentum FCS of a Mott insulator is identical to that of a statistical mixture of thermal bosons. On the other hand, the BEC data exhibits a very contrasted probability distribution which matches well (but not perfectly) with the Poisson law at the measured $\langle N_\Omega \rangle = 5.3(2)$. As expected, the different statistical properties of BECs and Mott insulators are clearly reflected by their FCS, which are consistent with those

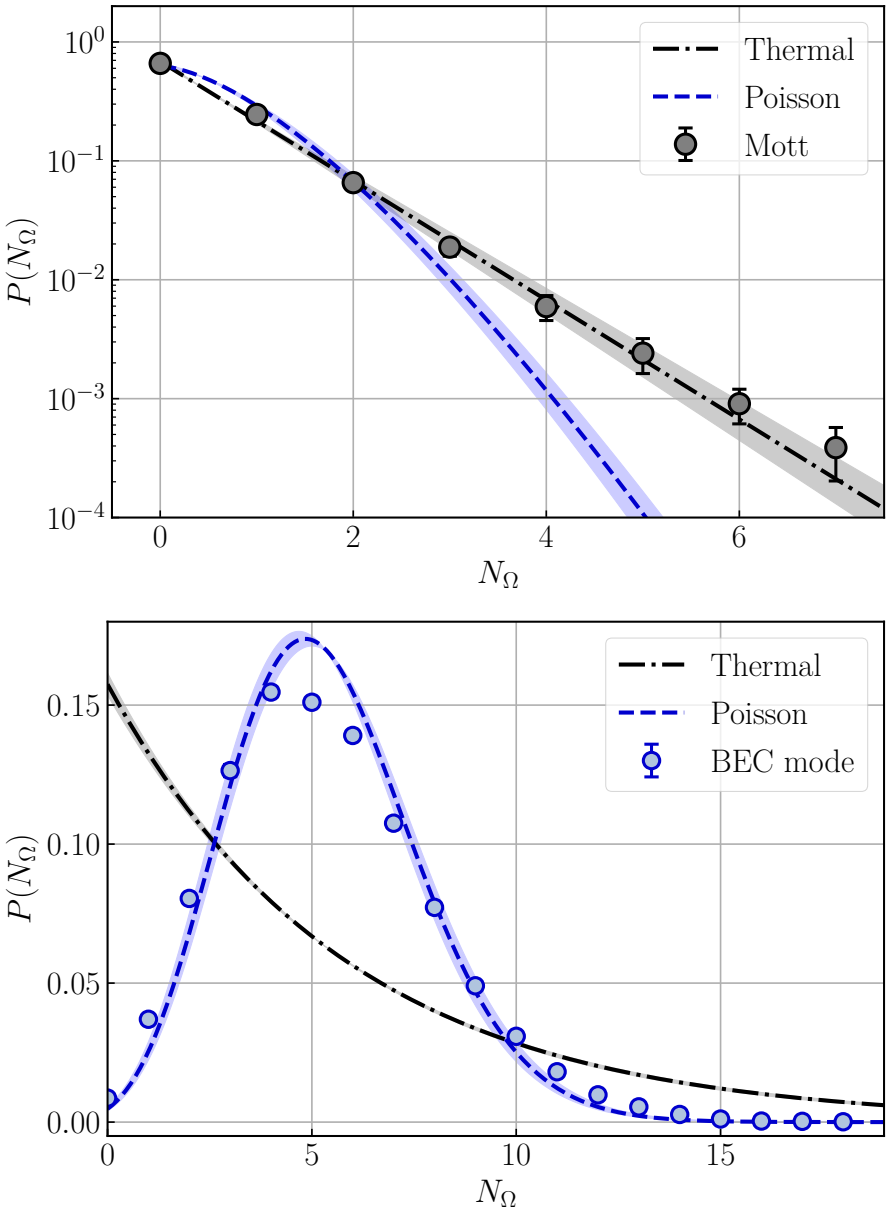

Figure 3.2: **Full Counting Statistics $P(N_\Omega)$ of BECs and Mott insulators.** The error bars on the experimental points correspond to the statistical uncertainty (standard deviation) estimated via the bootstrapping method. The experimental data are compared with the expectations for a thermal and coherent state, respectively a geometric law (dashed-dotted black line) and a Poisson law (dashed blue line). Both predictions are entirely defined, without any adjustable parameter, from the measured average atom number: $\langle N_\Omega \rangle = 0.46(5)$ in the Mott case (top panel) and $\langle N_\Omega \rangle = 5.3(2)$ in the BEC case (bottom panel). The uncertainty on these curves (shaded areas) reflects that on the measured $\langle N_\Omega \rangle$.

expected for coherent and thermal states. The origin of the discrepancies between the BEC data and the Poisson distribution will actually become clear when studying the high-order moments. Before that, the next section illustrates the importance of the criterion $V_\Omega \lesssim V_c$ to reveal the thermal statistics of Mott insulators.

3.1.4 Increasing V_Ω when computing the FCS of Mott insulators

In Figure 3.3, we test varying the voxel volume $V_\Omega = \delta k^3$ compared to V_c in the computation of $P(N_\Omega)$ for Mott insulators. The black data points correspond to the voxel size used in the previous section ($\delta k = 6 \times 10^{-2}\, k_d$) for which $V_\Omega = 0.9\, V_c$ and the FCS is correctly fitted by a geometric law. As V_Ω is increased, $P(N_\Omega)$ keeps deviating from the geometric distribution (dashed-dotted lines) associated with the correspondingly increasing average atom number $\langle N_\Omega \rangle$. Because Equation 3.3 concerns a single mode with thermal statistics, its failing to describe the data at larger volumes V_Ω suggests to describe the statistical properties of N_Ω by accounting for the contributions of several modes. As derived in [179], the probability distribution resulting from the contribution of M independent modes with thermal statistics and average occupation $\langle N \rangle$ is a multimode thermal distribution:

$$P_M(N) = \frac{(\langle N \rangle + M - 1)!}{\langle N \rangle!\,(M-1)!} \frac{(\langle N \rangle / M)^N}{(1 + \langle N \rangle / M)^{N+M}} \tag{3.4}$$

Naturally, the single-mode case $M = 1$ returns the geometric distribution of Equation 3.3. As shown in Figure 3.3, the predictions $P_M(N)$ (solid lines) are in perfect agreement with the experimental data when $V_\Omega > V_c$. Those predictions do not rely on any adjustable

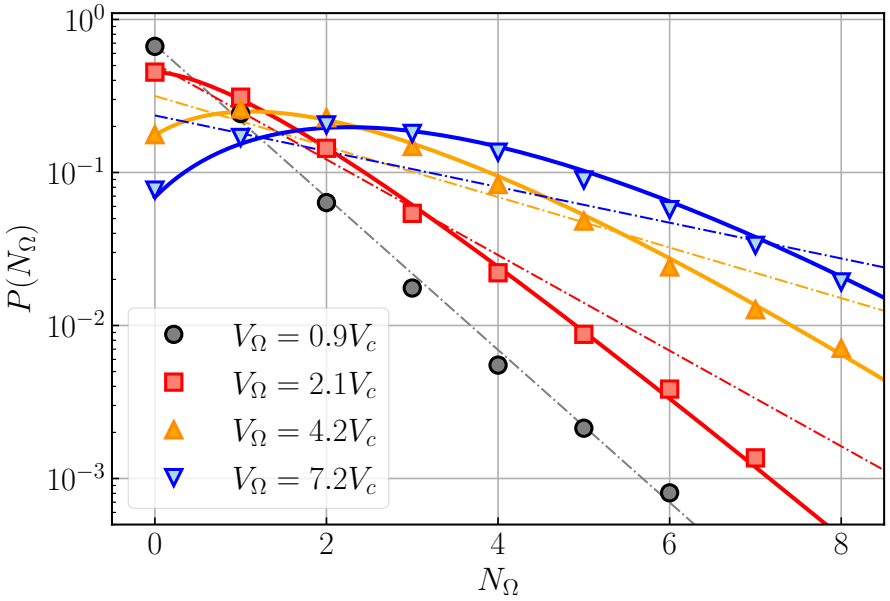

Figure 3.3: **Full counting statistics $P(N_\Omega)$ of Mott insulators for different V_Ω.** Predictions of Equation 3.3 for a thermal distribution are indicated as dashed-dotted lines, while the multimode thermal predictions of Equation 3.4 correspond to the solid lines. These multimode thermal scalings only depend on $\langle N_\Omega \rangle$ and on the chosen ratio $M = V_\Omega / V_c$ corresponding to the number of independent modes per voxel. As expected, they are found to correctly fit the data when $V_\Omega > V_c$.

parameters: they are entirely defined by the average atom number $\langle N_\Omega \rangle$ and the number of modes per voxel $M = V_\Omega/V_c$. These results allow us to conclude that the condition $V_\Omega \lesssim V_c$ is sufficient to retrieve the thermal statistics associated with Mott insulators. In particular, the more stringent requirement $V_\Omega \ll V_c$ (which we verified was also leading to thermal FCS) is unnecessary here.

3.2 High-order moments

As an alternative to measuring the FCS, the validity of a pure-state description of Bose superfluids and Mott insulators can be assessed by looking at the maximum order of correlations at which the correlation amplitude in these systems is compatible with that expected for a pure state. This idea stems from R. Glauber's characterization of light fields through their photon correlations at any order [180, 181]. As for the case of light propagation, the many-body coherence of atomic gases is accessed in the far-field regime of expansion, where momentum correlations reflect multi-particle interferences [182].

In quantum gases, momentum correlations up to the second order have been measured with single-atom-resolved detection in non-interacting and non-degenerate bosonic [28, 183] and fermionic systems [44, 184], BECs [1], interacting lattice bosons [32, 146, 174] (by our team), and interacting fermions [185]. The only extensions of such measurements to higher-order correlations were performed several years ago by the Australian ^{4}He* team with BECs [1] (up to the third order), and non-interacting bosons [183] (up to the sixth order). For Gaussian states, high-order correlations factorize into lower-order ones and do not bring additional information. On the contrary, signatures of non-Gaussianity in strongly-correlated systems should precisely be contained within high-order correlations, as recently suggested [186–188]. This motivates the following investigation of high-order correlations in strongly-interacting lattice Bose gases for both Bose superfluids and Mott insulators. This starting point will open the way towards similar measurements in more strongly-correlated systems close to the superfluid-to-Mott transition.

3.2.1 Many-body coherence of Bose superfluids and Mott insulators

According to R. Glauber [180], the definition of the nth-order coherence of a light field relies on that of the joint probability for detecting n photons at a given set of position and time coordinates $x_j = (r_j, t_j)$, noted $G^{(n)}(x_1, \dots, x_n)$. More conveniently, the notion of coherence is quantified via the normalized correlation function:

$$g^{(n)}(x_1, \dots, x_n) = \frac{G^{(n)}(x_1, \dots, x_n)}{\prod_{j=1}^{n} G^{(1)}(x_j)} \tag{3.5}$$

Coherent light fields, such as lasers, are defined by a perfect coherence at any order $g^{(n)}(x_1, \dots, x_n) = 1$ and for any set of coordinates $(x_1, \dots, x_n)$. On the other hand, looking at simultaneous and localized detection events $x_1 = \dots = x_n \equiv x$ with incoherent (or chaotic) light fields yields the very different result $g^{(n)}(x, \dots, x) = n!$ [181]. This scaling is notably valid for thermal light, with the most famous example of the Hanbury-Brown and Twiss experiment [189]. The latter, which actually motivated the work of R. Glauber on the nth-order coherence, is discussed in the next section.

Glauber's predictions for the amplitude of the normalized correlation functions are readily transposed to the momentum space [180], where the notation $g^{(n)}(0)$ refers to $g^{(n)}(\boldsymbol{k},\ldots,\boldsymbol{k})$. Expressing $g^{(n)}(0)$ in terms of the operators $\hat{a}(\boldsymbol{k})$ and $\hat{a}^\dagger(\boldsymbol{k})$ (second quantization), Glauber's predictions are easily derived from the bosonic commutation rules $\left[\hat{a}(\boldsymbol{k}),\hat{a}^\dagger(\boldsymbol{k'})\right] = \delta_{\boldsymbol{k},\boldsymbol{k'}}$. As an example, the amplitude of the second-order correlations writes:

$$\begin{aligned} g^{(2)}(0) &= \frac{\langle \hat{a}^\dagger(\boldsymbol{k})\hat{a}^\dagger(\boldsymbol{k})\hat{a}(\boldsymbol{k})\hat{a}(\boldsymbol{k})\rangle}{\langle \hat{a}^\dagger(\boldsymbol{k})\hat{a}(\boldsymbol{k})\rangle^2} \\ &= \frac{\langle \hat{a}^\dagger(\boldsymbol{k})\left(\hat{a}(\boldsymbol{k})\hat{a}^\dagger(\boldsymbol{k})-1\right)\hat{a}(\boldsymbol{k})\rangle}{\langle \hat{a}^\dagger(\boldsymbol{k})\hat{a}(\boldsymbol{k})\rangle^2} \\ &= \frac{\langle \hat{N}(\hat{N}-1)\rangle}{\langle \hat{N}\rangle^2} \\ &= \frac{\langle \hat{N}^2\rangle - \langle \hat{N}\rangle}{\langle \hat{N}\rangle^2} \\ &= 1 + \frac{\sigma_N^2 - \langle \hat{N}\rangle}{\langle N\rangle^2} \end{aligned} \tag{3.6}$$

with $\sigma_N^2 = \langle \hat{N}^2\rangle - \langle \hat{N}\rangle^2$ the variance of the number of particles N. Therefore, one finds that the correlation amplitude depends on the state statistics. For a coherent state, the Poissonian probability distribution function implies $\sigma_N^2 = \langle \hat{N}\rangle$ and one retrieves $g^{(2)}(0) = 1$. On the other hand, the geometric probability distribution of the atom number for thermal sources yields $\sigma_N^2 = \langle \hat{N}\rangle^2 + \langle \hat{N}\rangle$, which leads to the bosonic bunching effect $g^{(2)}(0) = 2$.

As shown in the previous section, Mott insulators exhibit the probability distributions of thermal states. This finding is consistent with a previous work [174] in which our team measured $g^{(2)}(0) = 2$ for Mott insulators. Using correlation functions, the fact that Mott insulators should exhibit thermal statistics in momentum space can be expressed explicitly. To this aim, one uses the decomposition of the momentum space operator and of the ground state wave function of a Mott insulator into the basis of Wannier functions:

$$\hat{a}(\boldsymbol{k}) = \frac{1}{\sqrt{V}} \sum_{j=1}^{N_{\text{site}}} e^{i\boldsymbol{k}.\boldsymbol{r_j}} \hat{b}_j \tag{3.7}$$

$$|\Psi_0\rangle_{\text{MI}} = \frac{1}{\sqrt{N!}} \prod_{j=1}^{N_{\text{sites}}} \left(\hat{b}_j^\dagger\right)^{\bar{n}} |0\rangle \tag{3.8}$$

where the operators $\hat{b}_j^\dagger, \hat{b}_j$ create/annihilate an atom in the Wannier function localized on site j. From these expressions, the calculations of the second-order correlation function $g^{(2)}(0)$ for a perfect Mott insulator ($J = 0$) yields correlations of the type $\langle \hat{b}_i^\dagger \hat{b}_j^\dagger \hat{b}_k \hat{b}_l\rangle$, which decomposes into:

$$\langle \hat{b}_i^\dagger \hat{b}_j^\dagger \hat{b}_k \hat{b}_l\rangle = \bar{n}^2\left(\delta_{i,k} + \delta_{j,l}\right) - \bar{n}\,\delta_{i,j,k,l} \tag{3.9}$$

where $\bar{n}$ denotes the lattice filling. Both first terms correspond to a double sum over the lattice sites ($\propto N_{\text{site}}^2$), while the last term only correspond to a single sum ($\propto N_{\text{site}}$). Therefore, this last term becomes negligible when the number of occupied sites is large. Because this condition is fulfilled experimentally ($N_{\text{sites}} \sim 40^3$), and as $\langle \hat{a}^\dagger(\boldsymbol{k})\hat{a}(\boldsymbol{k})\rangle^2 = \bar{n}^2$, one retrieves the bunching amplitude $g^{(2)}(0) = 2$ associated with a thermal state. This

reasoning can be extended to any order $n > 2$, explaining why the many-body coherence properties of Mott insulators and thermal states are similar in momentum space up to negligible terms. In particular, one expects $g^{(n)}(0) = n!$ for any order n.

3.2.2 Condition for measuring fully-contrasted correlation amplitudes

Another fundamental quantity of correlation functions is the correlation length l_c associated with the decay of the correlation amplitude. When correlations are measured in the far-field regime, l_c represents the typical momentum separation between uncorrelated components of the system and is inversely proportional to the source size. The most famous illustration of this property dates back to the first observation of the bosonic bunching effect in 1956. In their landmark experiment [189], Hanbury-Brown and Twiss used two photon detectors at positions $\boldsymbol{r_1}$ and $\boldsymbol{r_2}$ to collect the photons of the star Sirius. A star being an incoherent light source, the photons emitted are associated with thermal statistics, and a bunching peak was observed by Hanbury-Brown and Twiss when placing the two detectors at the same position $\boldsymbol{r_1} = \boldsymbol{r_2}$. In this experiment, the decay of the bunching amplitude when increasing the detectors separation $|\boldsymbol{r_1} - \boldsymbol{r_2}|$ was used to obtain l_c, from which Hanbury-Brown and Twiss deduced the angular size of the star.

An important consequence of the (finite) correlation length of systems with thermal statistics is that fully-contrasted correlation amplitudes $g^{(n)}(0) = n!$ can only be measured inside volumes smaller than the one set by l_c. Otherwise, uncorrelated atoms are mixed together, resulting in a reduction/suppression of the correlation amplitude. This effect was clearly observed in a previous investigation of the third-order momentum correlations of Mott insulators done by our team in 2019 [174]. The correlation length reported at the time for Mott insulators with similar atom numbers to ours was $l_c \simeq 3 \times 10^{-2}$. This value, defined as the $1/e^2$ width of the Bell-shaped bunching peak, was compatible with the prediction $2\pi/L$ for an in-trap size L. Therefore, the volume $V_c = (2\pi/L)^3$ can be identified in a relatively good approximation to the one set by the correlation length[1], hence his name. Consequently, the condition $\delta k \ll l_c$ for measuring fully-contrasted correlation amplitudes translates into $V_\Omega \ll V_c$, which is more stringent than in the case of the FCS.

3.2.3 Experimental procedure

In quantum optics, the high-order moments of the photon number are also called the factorial moments because of the relationship [190, 191]:

$$g^{(n)}(0) \equiv \frac{\langle \hat{N}^{(n)} \rangle}{\langle \hat{N} \rangle^n} = \frac{\langle : \hat{N}^n : \rangle}{\langle \hat{N} \rangle^n} = \frac{\langle \hat{N}(\hat{N}-1)\dots(\hat{N}-n+1) \rangle}{\langle \hat{N} \rangle^n} \tag{3.10}$$

which appeared already for the second-order correlation function in Equation 3.6. This relationship results from the normal operator ordering $\langle : \hat{N}^n : \rangle = \langle (\hat{a}^\dagger)^n \, \hat{a}^n \rangle$, reflecting the fact that a detected photon is necessarily destroyed and ensuring that the numerator of Equation 3.10 is zero for the vacuum state. Interestingly, our detector of $^4\mathrm{He}^*$ atoms works similarly since each atom detected is destroyed from the metastable state (the atom returns to the ground state $1\,^1\mathrm{S}_0$). Transposing the result of quantum optics, we compute

[1] This would not be true quantitatively if l_c were defined as a RMS width.

the amplitude of the normalized correlation functions $g^{(n)}(0)$ at any order:

$$g^{(n)}(0) = \frac{\langle N_\Omega(N_\Omega - 1)\dots(N_\Omega - n + 1)\rangle}{\langle N_\Omega\rangle^n} \tag{3.11}$$

from the atom number N_Ω detected in the volume Ω_k for each momentum distribution. This atom number yields the factorial moment $N_\Omega(N_\Omega - 1)\dots(N_\Omega - n + 1)$, whose statistical average $\langle . \rangle$ over the $N_{\text{runs}} \sim 2000$ experimental distributions gives the numerator of Equation 3.11. Note that this computation method, that we implemented recently, speeds up the computation of (local) correlations at fixed momentum $\boldsymbol{k}$ compared to our "traditional" algorithm used in [146, 174]. However, it cannot compute the correlations at opposite momenta, which are the object of focus of the next chapter. The algorithm used for the measurement of these $\boldsymbol{k}$/-$\boldsymbol{k}$ correlations will be described in the next chapter.

For Bose superfluids, the atom number N_Ω is the one detected inside the same sphere S_Ω located on $\boldsymbol{k} = \boldsymbol{0}$ than for the measurement of the FCS. Indeed, the relatively large average atom number in the volume S_Ω ($\langle N_\Omega\rangle = 5.3(2)$) allows us to compute accurately the factorial moments. On the contrary, the voxel size used to compute the correlation function of Mott insulators has to be reduced compared to that of the FCS case to fulfill the condition $\delta k \ll l_c$ and obtain well-contrasted correlation amplitudes. This necessity further reduces the already low statistics inside the voxels of Mott insulators, which, as a reminder, are dilute clouds with momentum extents exceeding that of the first Brillouin zone. To circumvent this issue, the statistical properties of Mott insulators are accessed by binning the momentum space with anisotropic voxels of volume $V_\Omega = \delta k \times \delta k_\perp^2$. The transverse size is chosen larger than the correlation length, $\delta k_\perp > l_c > \delta k$, to increase the statistics inside the voxels. The resulting atom number is noted $N_{\delta k_\perp}$, and its factorial moments are averaged over all the anisotropic voxels inside the first Brillouin zone to increase the statistics further:

$$\langle \hat{N}^{(n)}_{\delta k_\perp}\rangle = \sum_{j\in 1\text{BZ}} \langle N_{\delta k_\perp}(N_{\delta k_\perp} - 1)\dots(N_{\delta k_\perp} - n + 1)\rangle_j \tag{3.12}$$

Then, these average factorial moments are normalized to obtain the corresponding correlation amplitudes:

$$g^{(n)}_{\delta k_\perp}(0) = \frac{\sum_{j\in 1\text{BZ}} \langle N_{\delta k_\perp}(N_{\delta k_\perp} - 1)\dots(N_{\delta k_\perp} - n + 1)\rangle_j}{\sum_{j\in 1\text{BZ}} \langle N_{\delta k_\perp}\rangle_j^n} \tag{3.13}$$

Note that because we are interested in the high-order moments of the occupation number, increasing the mean atom number per voxel by increasing the voxel size raises the statistics much more efficiently than averaging over many voxels or experimental runs.

Naturally, this procedure cannot yield the fully-contrasted correlation amplitude $g^{(n)}(0) = n!$ since uncorrelated atoms are added inside the voxels along the two directions $\delta k_\perp > l_c$. This effect is illustrated in Figure 3.4 where a clear suppression of $g^{(n)}_{\delta k_\perp}(0)$ on increasing the transverse voxel size can be seen for any order. However, the 3D Gaussian shape of the correlation volume allows us to decouple the three directions of the momentum space and to quantify the effect of the transverse integration along the two directions $\delta k_\perp$ on the decay of $g^{(n)}_{\delta k_\perp}(0)$ along the longitudinal δk-axis. By repeating the calculation of $g^{(n)}_{\delta k_\perp}(0)$ for different transverse integrations $\delta k_\perp$, the fully-contrasted amplitude $g^{(n)}(0)$ is extracted from extrapolating the value of $g^{(n)}_{\delta k_\perp}(0)$ in the limit $\delta k_\perp \to 0$.

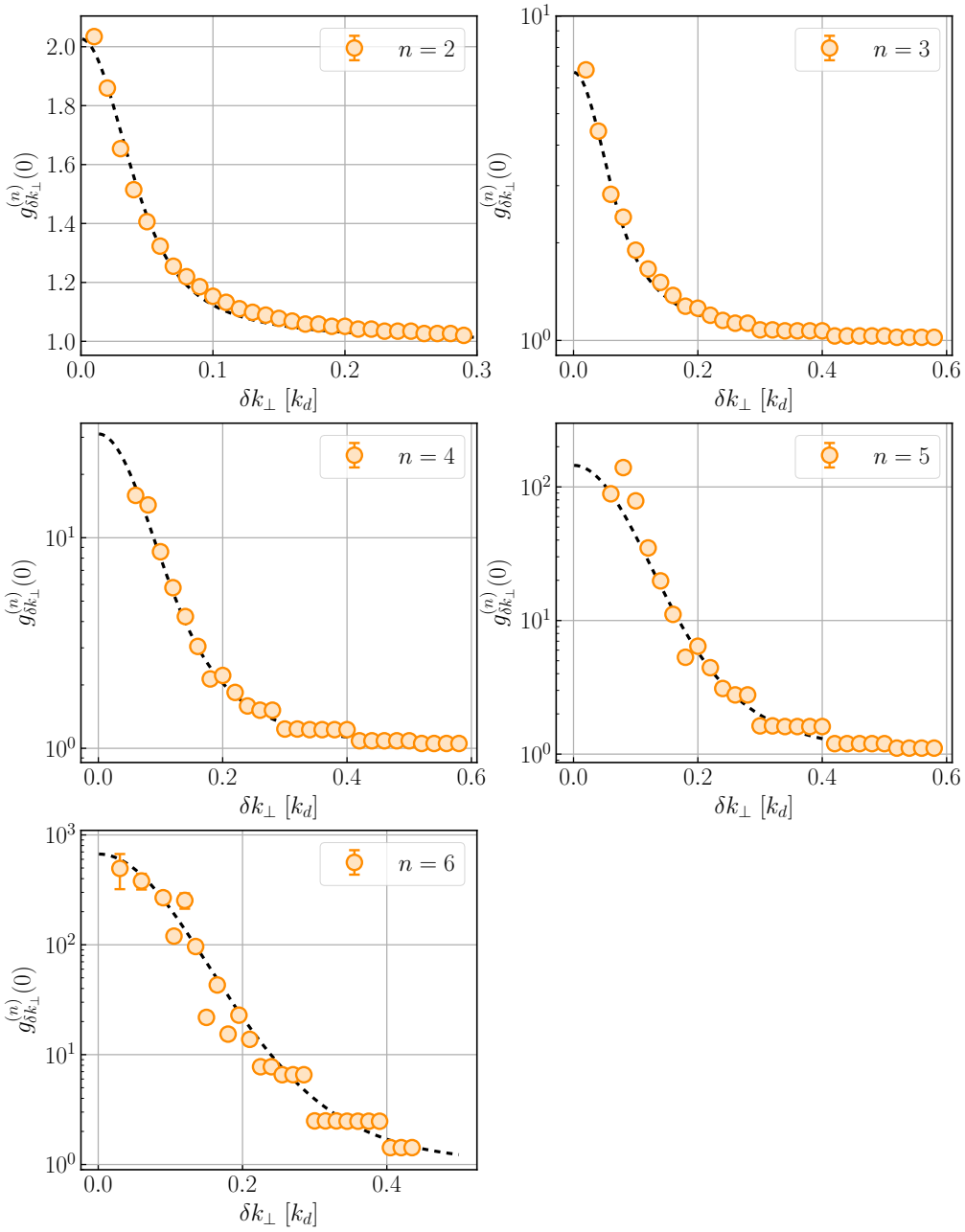

Figure 3.4: **Amplitudes $g^{(n)}_{\delta \boldsymbol{k}_\perp}(\mathbf{0})$ as a function of the transverse integration $\delta \boldsymbol{k}_\perp$.** The different panels correspond to different correlation orders, from $n = 2$ to $n = 6$. The panel $n = 2$ is plotted in linear scale, while all other orders have their vertical axis plotted in log scale. For any orders, the voxel size $\delta k = 1.5 \times 10^{-2} \leq l_c$ is fixed and only the transverse one $\delta k_\perp$ increases. For each order, the dashed black line fits the dependency of $g^{(n)}_{\delta k_\perp}(0)$ with $\delta k_\perp$ to extrapolate the fully-contrasted amplitude $g^{(n)}(0)$ in the limit $\delta k_\perp \to 0$.

3.2.4 Experimental results

The measured amplitudes of the correlation functions $g^{(n)}(0)$ are plotted in Figure 3.5 (in log scale) for Mott insulators and the condensed parts of Bose superfluids. In the former case, the error bars correspond to the fitting error on the extrapolation of the amplitude $g^{(n)}(0)$ in the limit $\delta k_\perp \to 0$. For Bose superfluids, the error bars on $g^{(n)}(0)$ are defined as $\Delta N_\Omega^{(n)}/\langle N\rangle^n$ with $\Delta N_\Omega^{(n)}$ the standard error of the factorial moment of order n:

$$\Delta N_\Omega^{(n)} = \frac{1}{\sqrt{N_{\text{runs}}}}\sqrt{\langle (N_\Omega \dots (N_\Omega - n + 1))^2\rangle - \langle N_\Omega \dots (N_\Omega - n + 1)\rangle^2} \tag{3.14}$$

Up to the sixth order, the correlation amplitudes of Mott insulators are consistent with the scaling $g^{(n)}(0) = n!$ associated with thermal statistics. This finding is a substantial improvement of our previous measurement of the second-order and third-order correlation amplitudes [29], which reported the values $g^{(2)}(0) = 1.065(10)$ and $g^{(3)}(0) = 1.32(5)$. Although the scaling between the magnitudes $g^{(2)}(0) - 1$ and $g^{(3)}(0) - 1$ was compatible with the factor 5 expected for thermal statistics, the absolute correlation amplitudes were quite far from the fully-contrasted ones. This effect was caused by the large transverse integration used in the third-order computation to raise the statistics. Thanks to the improved statistics offered by the Raman transfer, sufficiently small volumes can be probed to retrieve the prediction $n!$. In addition, the extension of this measurement up to the sixth order further confirms the argument presented in Section 3.2.1 along which, up to negligible terms, the Fock state of a perfect Mott insulator leads to thermal statistics of the momentum occupation number. Mott insulators and thermal gases actually differ from their different in-trap sizes and the incompressible (*resp.* compressible) nature of a Mott insulator (*resp.* thermal cloud), which results in different correlation lengths $l_c^{(n)}$

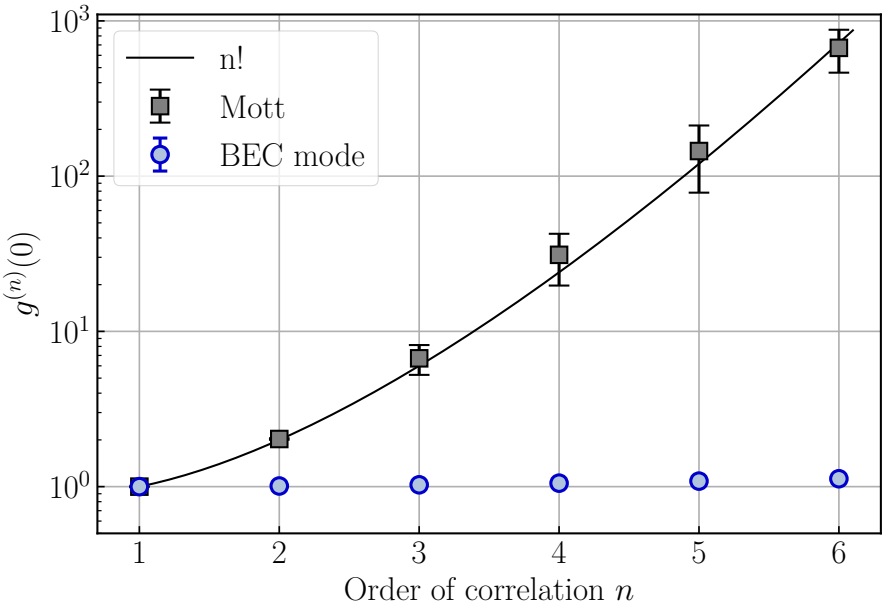

Figure 3.5: **High-order moments of BECs and Mott insulators.** Amplitudes $g^{(n)}(0)$ in log scale versus the order of correlations n for the condensate mode of Bose superfluids and Mott insulators. The Mott data agrees with the $n!$ prediction for thermal state (solid line) while the BEC data seems consistent with Glauber's prediction for a coherent state.

[174]. On the other hand, the correlation amplitude associated with the condensed part of Bose superfluids is $g^{(n)}(0) \sim 1$ for any order up to $n = 6$, consistent with Glauber's prediction for a coherent state. The several orders of magnitude between both cases illustrate the outstanding capabilities of high-order moments to identify quantum states from their many-body coherence.

Zooming in on the amplitude range close to unity (Figure 3.6), our results for the BEC mode of Bose superfluids surprisingly deviate from the exact prediction $g^{(n)}(0) = 1$. This deviation increases the higher the order of correlations and makes our measurement incompatible within error bars with Glauber's prediction already for $n = 2$. To confirm the physical origin of this discrepancy, we repeat our computation of $g^{(n)}(0)$ on a "randomized" data set. The latter is obtained by randomly shuffling the detected atoms between the different distributions while conserving the same number of distributions and number of atoms per distribution. This randomization procedure destroys the many-body coherence within single files. Consequently, our measuring of discrete and independent detection events should lead to a Poisson probability distribution of the occupation number, implying $g^{(n)}(0) = 1$ at any order. As illustrated by the yellow data in Figure 3.6, this is precisely what we observe with the randomized data set. The measured correlation amplitudes are contained within a 2% interval around 1, confirming that the deviation with unity in the non-randomized experimental data is significant. In the next section, we propose an interpretation for our measurement of $g^{(n)}(0) > 1$ which differs from Glauber's prediction for a coherent state.

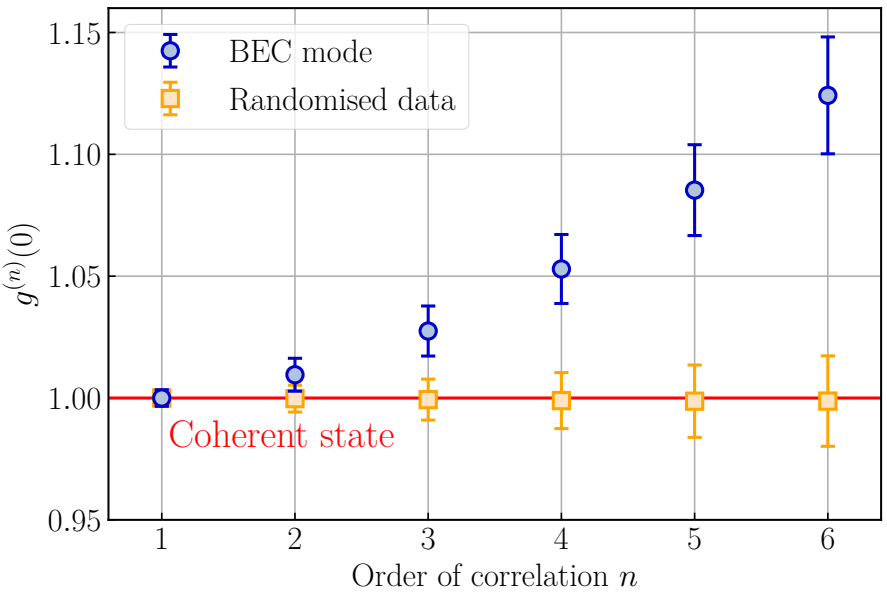

Figure 3.6: **Deviation from Glauber's definition of a coherent state.** The measured amplitude $g^{(n)}(0)$ for the BEC mode actually deviates from Glauber's prediction (in red) $g^{(n)}(0) = 1$. This deviation increases with the order of correlations and is absent from the randomized data set (see text), confirming that it should be statistically meaningful.

3.3 Deviations to the pure-state description for the BEC

The ^{4}He* team in Canberra reported in 2011 the first measurement of second- and third-order momentum correlations for atoms [1]. They demonstrated that a thermal cloud of bosonic atoms and a BEC share, respectively, the coherence properties introduced by Glauber to define incoherent and coherent light fields. Unlike us, they measured $g^{(2)}(0) = g^{(3)}(0) = 1$ for the BECs without any visible deviation from Glauber's prediction. In addition to finding the origin of the deviation in our own data, this section also aims at understanding how our measurement differs from theirs.

3.3.1 Increasing the lattice depth

To understand the deviations $g^{(n)}(0) > 1$, we repeated the measurement of $g^{(n)}(0)$ at various lattice depths corresponding to Bose-Hubbard interaction parameters $U/J \in [2, 22]$. The initial BEC atom number was kept to 5×10^3, for which the corresponding low-entropy Mott transition is around $25-30$ according to the previous chapter. Therefore, the system remains far from entering the Mott regime where the statistics is thermal and yields $g^{(n)}(0) = n!$. The results are plotted in Figure 3.7 for $U/J = 10, 15$, and 20. In a general manner, the data shows that the deviation increases with the lattice depth. This effect is jointly reflected in the increasing deviations with U/J between the FCS of the BEC mode and the expected Poisson distribution. Wondering what else increases with U/J, we naturally thought of the quantum depletion. Indeed, the higher U/J, the stronger the interactions and the more depleted the condensate is. Furthermore, we know from a previous work [146] that both the thermal and quantum depletion of Bose superfluids exhibit

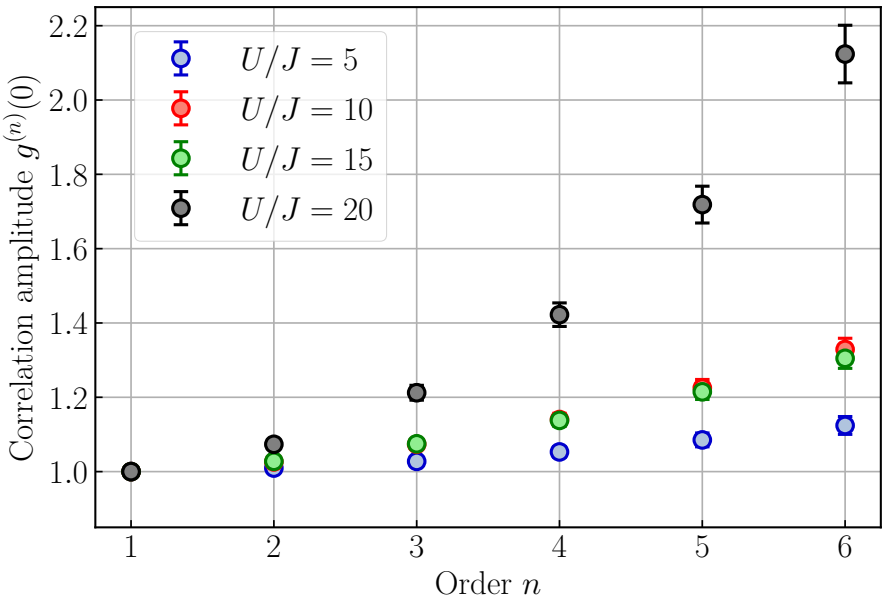

Figure 3.7: **Many-body coherence of Bose superfluids at various U/J.** The correlation amplitudes $g^{(n)}(0)$ for the atoms inside the sphere S_Ω, centered on the condensate mode, are found to deviate from unity. This deviation increases with the order of correlations and the interaction parameter U/J.

perfect bosonic bunching $g^{(2)}(0) = 2$. This result is expected for the thermal depletion because temperature incoherently depletes atoms from the condensate mode. In the case of the quantum depletion, this feature is more subtle to explain and is actually only valid when looking at local correlations. It will be discussed in the next chapter when comparing the local second-order correlations with those at opposite momenta. For the moment, let us focus on the fact that the total depletion contributes to $g^{(n)}(0) = n!$. Naturally, the sphere S_Ω of radius $\delta k = 0.025\ k_d$ centered on the condensate mode $\boldsymbol{k} = \boldsymbol{0}$ essentially contains condensed atoms, since both the thermal and quantum depletion are delocalized over a much larger volume in momentum space. However, a small fraction of the atoms inside S_Ω belongs to the depletion and affects the many-body coherence properties of the condensed ones. We now introduce a simple model to quantify this effect and account for both contributions.

3.3.2 A simple model ...

The volume S_Ω contains essentially condensed atoms and a small fraction of depleted ones, which either belong to the thermal or quantum depletion. Our first assumption is to consider that these two contributions act on the statistical properties of the whole volume S_Ω independently of each other. Naturally, the atom numbers of the BEC and the depletion are correlated in the canonical ensemble since each atom added to the depletion must be removed from the BEC. However, these correlations are assumed to be negligible in the small volume S_Ω considered, whose radius $\delta k = 0.025\ k_d$ is (by far) smaller than the momentum range of the thermal/quantum depletion. This approximation seems reasonable for small interactions corresponding to the Bogoliubov regime, where the condensed fraction remains close to unity. However, nothing says it should remain valid in the strongly-interacting regime, where the (quantum) depletion can no longer be treated as a perturbation of the BEC. Our second assumption consists in considering the BEC as a coherent state and the depletion as a thermal one, assigning $g^{(n)}(0) = 1$ to the former and $g^{(n)}(0) = n!$ to the latter. In our previous work [146], the quantum depletion was found to exhibit (local) thermal statistics when considered at non-zero momenta outside the BEC mode. Whether or not this property holds for small momenta $\boldsymbol{k} \simeq \boldsymbol{0}$ is an assumption, which is difficult to assess in the lattice due to the residual harmonic confinement.

Our goal is to derive the statistical properties of the atom number N_Ω inside the volume S_Ω. In our model, this atom number is associated with the operator $\hat{N}_\Omega = \hat{a}_\Omega^\dagger \hat{a}_\Omega$, whose annihilation operator $\hat{a}_\Omega = \hat{a}_{\mathrm{BEC}} + \hat{a}_{\mathrm{dep}}$ corresponds to the sum of two operators acting respectively on the BEC and the (total) depletion. Our first assumption consist in considering that these two operators are uncorrelated, $\langle \hat{a}_{\mathrm{BEC}}^\dagger\, \hat{a}_{\mathrm{dep}} \rangle = 0$, meaning that the atom number in S_Ω is given by:

$$N_\Omega = \langle \hat{N}_\Omega \rangle = \langle \hat{a}_{\mathrm{BEC}}^\dagger\, \hat{a}_{\mathrm{BEC}} \rangle + \langle \hat{a}_{\mathrm{dep}}^\dagger\, \hat{a}_{\mathrm{dep}} \rangle = N_{\mathrm{BEC}} + N_{\mathrm{dep}} \tag{3.15}$$

with N_{BEC} and N_{dep} the BEC and depleted atom number inside S_Ω. The assumption that $\hat{a}_{\mathrm{BEC}}$ and $\hat{a}_{\mathrm{dep}}$ are uncorrelated implies that the nth power of $\hat{a}_\Omega$ writes:

$$\hat{a}_\Omega^n = \sum_{p=1}^{n} \binom{n}{p} (\hat{a}_{\mathrm{BEC}})^p (\hat{a}_{\mathrm{dep}})^{n-p} \tag{3.16}$$

and the high-order moments of N_Ω is readily derived:

$$\langle \hat{N}_\Omega^{(n)} \rangle = \langle (\hat{a}_\Omega^\dagger)^n \, \hat{a}_\Omega^n \rangle = \sum_{p=1}^{n} \binom{n}{p}^2 \langle \, (\hat{a}_{\mathrm{BEC}}^\dagger)^p \, (\hat{a}_{\mathrm{BEC}})^p \, (\hat{a}_{\mathrm{dep}}^\dagger)^{n-p} \, (\hat{a}_{\mathrm{dep}})^{n-p} \, \rangle \tag{3.17}$$

This expression leads to an analytical formula for the normalized correlation amplitude:

$$g^{(n)}(0) - 1 = \frac{\langle (\hat{a}_\Omega^\dagger)^n \, \hat{a}_\Omega^n \rangle}{\langle \hat{a}_\Omega^\dagger \, \hat{a}_\Omega \rangle^n} - 1 = \sum_{p=1}^{n-1} \left[(n-p)! \binom{n}{p}^2 - \binom{n}{p} \right] (f_{\mathrm{coh}})^p \, (1 - f_{\mathrm{coh}})^{n-p} \tag{3.18}$$

which uniquely depends on the so-called "coherent fraction" f_{coh}. The latter is defined as the fraction of atoms inside S_Ω belonging to the condensate mode, namely $f_{\mathrm{coh}} = N_{\mathrm{BEC}}/N_\Omega = \langle \hat{a}_{\mathrm{BEC}}^\dagger \, \hat{a}_{\mathrm{BEC}} \rangle / \langle \hat{a}_\Omega^\dagger \hat{a}_\Omega \rangle$. Note that even though our simple model can predict the high-order moments of N_Ω, the probability distribution $P(N_\Omega)$ remains out-of-reach as it results from a complex convolution of those of the BEC and the depletion. Obtaining $P(X)$ from the moments of a random variable X is actually a notoriously difficult problem [192, 193].

3.3.3 . . . that works !

The amplitudes $g^{(n)}(0)$ of the BEC mode at $U/J = 5$ are reproduced in Figure 3.8, along with the prediction of our model after adjusting its only variable f_{coh}. Despite the simplicity of our model, an excellent agreement is found between the experimental data and the theoretical prediction. In addition, the fitted coherent fraction $f_{\mathrm{coh}} = 0.9960(5)$ is close to unity, as expected from our assumption that the fraction of depleted atoms inside S_Ω deep into the superfluid regime must be negligible. Nevertheless, our model suggests that such a small fraction is enough to affect the statistical properties in a way that we can resolve experimentally. Furthermore, the uncertainty on the fitted coherent fraction is only at the $\sim 0.1\%$ level (blue shaded area), way below the size of the experimental error bars for the amplitudes $g^{(n)}(0)$. This extreme accuracy is the direct consequence of adjusting our model on the highest orders and illustrates the sensitivity of high-order correlations to probe many-body coherence.

As illustrated in Figure 3.9, we confirmed with the data sets at higher interactions the good agreement between the experimental data and the theoretical prediction of our model. The fitted values of the single adjustable parameter f_{coh} decrease with the interaction strength. This observation is consistent with the physical picture behind the model. Indeed, the coherent fraction expresses the ratio between the condensed atom number inside S_Ω, N_{BEC}, and the total atom number in this volume $N_\Omega = N_{\mathrm{BEC}} + N_{\mathrm{dep}}$. The higher the interactions, the more the BEC gets depleted. Therefore, the *total* number of condensed atoms $N_{\mathrm{BEC}}^{\mathrm{tot}}$ decreases on increasing U/J while the *total* number of depleted atoms $N_{\mathrm{dep}}^{\mathrm{tot}}$ increases. Inside the small volume S_Ω, which mainly contains condensed atoms, the reduction of N_{BEC} is much stronger than the growth of N_{dep}. As a consequence, $\langle N_\Omega \rangle$ decreases (slower than N_{BEC}) at stronger interactions and f_{coh} is thus expected to decrease too.

The following section presents additional certifications of the heuristic model introduced here, based on the comparison of the fitted coherent fraction f_{coh} at various U/J and other observables, such as the momentum density and the condensed fraction. Before that, let us first briefly comment on why we stopped at $n = 6$ when computing the

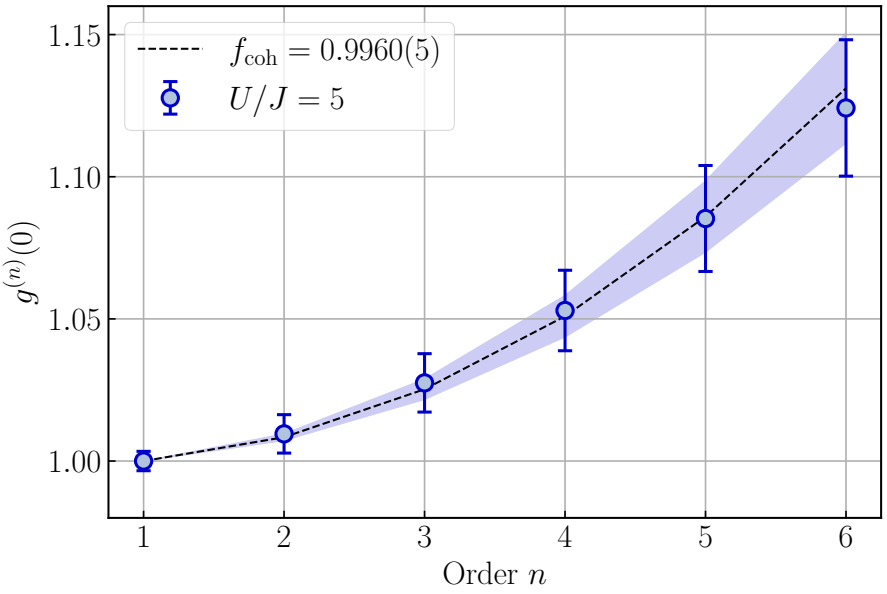

Figure 3.8: **Adjusting the growth of $g^{(n)}(0)$ for $U/J = 5$ with our model.** Same experimental data than the one shown in Figure 3.5 along with the theoretical prediction of our simple model. The latter fits correctly the experimental points, with an adjusted coherent fraction $f_{\mathrm{coh}} = 0.9960$ close to unity (dashed line) and a small uncertainty 5×10^{-4} (shaded area).

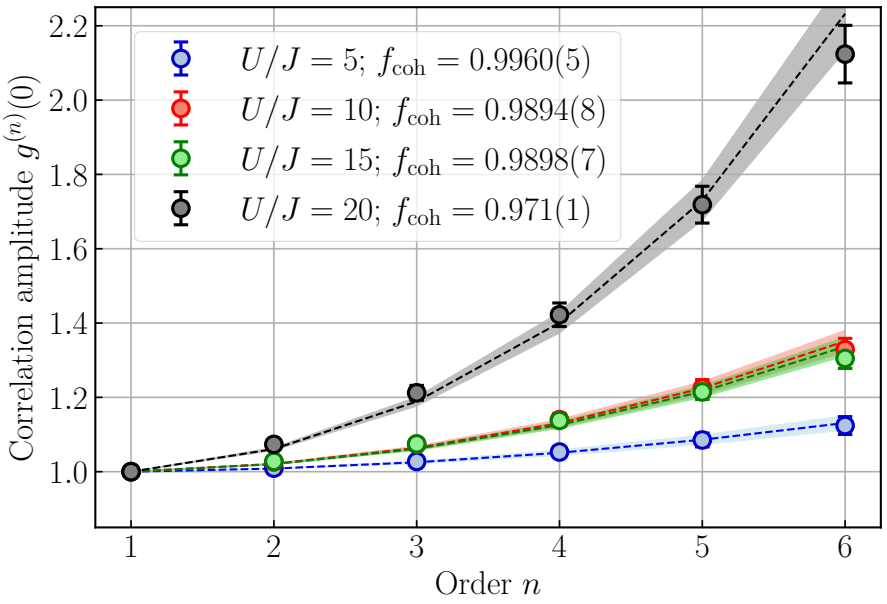

Figure 3.9: **Adjusting the growth of $g^{(n)}(0)$ at increasing lattice depths.** For any interaction strength, our model correctly fits the data with its single adjustable parameter f_{coh}. In addition, the fitted values of f_{coh} decrease at higher interactions, which is qualitatively consistent with our model.

high-order moments of the occupation number. As already mentioned, our randomization procedure yields essentially uncorrelated momentum distributions for which the normal-

ized amplitudes $g^{(n)}(0)$ are compatible with unity up to $n = 6$ (see Figure 3.6). Because this feature only comes from detecting discrete and independent events, a similar result is found when applying this procedure to Mott insulator distributions. There is no order limit to the computations of $g^{(n)}(0)$ from the factorial moments of N_Ω. In practice, however, the finite statistics per voxel limits the maximum order reachable. One way to assess this limit consists in looking at deviations to $g^{(n)}(0) = 1$ in the randomized data sets. As illustrated in Figure 3.10, such deviations appear for $n > 7$ at $U/J = 5$, signaling that there are too few distributions with $N_\Omega > n$ to correctly evaluate the probability of finding $N_\Omega = n$ for $n \geq 7$. This systematic deviation starting from $n \geq 7$ is conjointly found in the amplitudes $g^{(n)}(0)$ of the actual data sets when compared to the predictions of our model adjusted with the orders $n \leq 6$. From this observation (and similar ones at other U/J), we decided to restrict our analysis to $n \leq 6$. To go beyond this limit requires either a larger number of files or a higher detection efficiency η. Increasing η is undoubtedly the most efficient method. Indeed, an imperfect detection efficiency ($\eta < 1$) affects each detection event. Therefore, the joint detection of n atoms depends on a factor η^n whose growth with η is all the more significant than n is large.

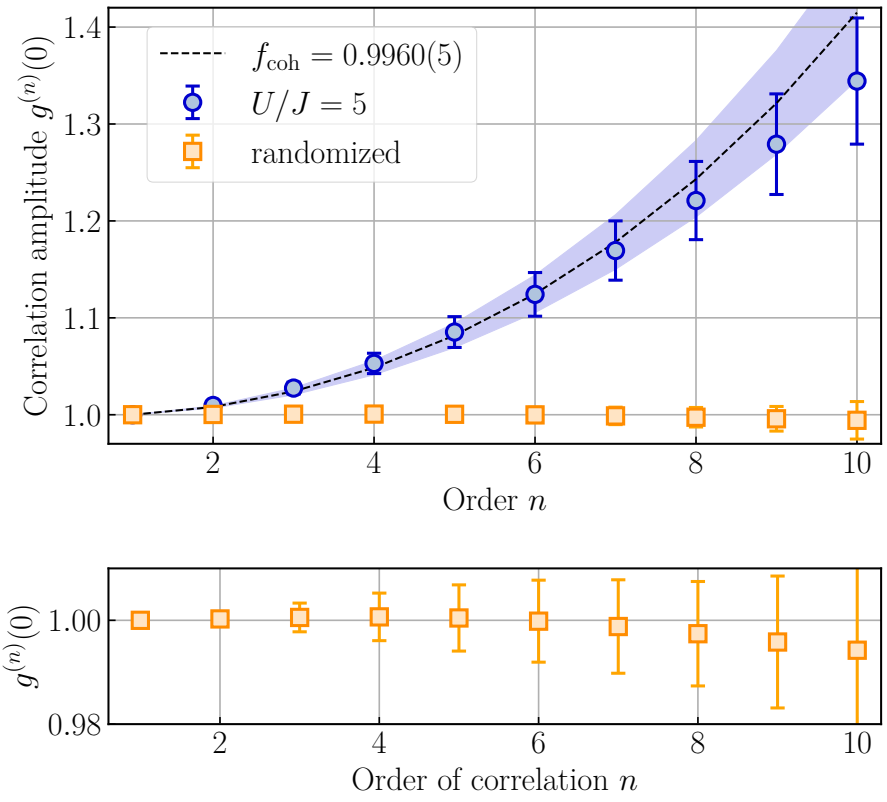

Figure 3.10: **Deviations of the amplitudes $g^{(n)}(0)$ at larger correlation orders.** Top: The computations of the normalized amplitudes $g^{(n)}(0)$ for both the actual and randomized data sets are extended to the tenth order compared to Figure 3.6. The prediction of our model adjusted for the orders $n \leq 6$ is also reproduced to illustrate the systematic deviation starting from $n \geq 7$. Bottom: Zooming in on the randomized correlation amplitudes shows that the lack of statistics is clearly signaled by systematic deviations to $g^{(n)}(0) = 1$ in the randomized data.

3.3.4 Further validating the model

Naturally, an ideal validation of our model would be to quantitatively compare the fitted value of f_{coh} with the experimental value of $N_{\mathrm{BEC}}/N_{\Omega}$. Unfortunately, this is impossible since N_{BEC} is unknown. Indeed, we cannot assign which atoms are condensed and which are not when measuring the number of counts inside the volume S_{Ω}. Furthermore, we are unaware of any analytical prediction that could provide the fraction of depleted atoms inside S_{Ω} for our 3D lattice bosons with additional harmonic confinement.

However, a first quick comparison is amenable by comparing the fitted values of the depleted fraction inside S_{Ω}, $1-f_{\mathrm{coh}}$, with momentum density cuts. This comparison, which is certainly not a certification, simply consists in *(i)* fitting the tails of the momentum density far from the BEC ($k \in [0.2, 0.5]\, k_d$) to have a rough idea of the momentum shape of the depletion, and *(ii)* comparing $1-f_{\mathrm{coh}}$ with the extrapolation of the depletion level at $\boldsymbol{k} = \mathbf{0}$. It is illustrated in Figure 3.11 for $U/J = 5$ and $U/J = 20$. It turns out that a Lorentzian curve fits best the tails of the depletion. Note that one must use 1D cuts of the momentum density with small transverse integration to avoid the momentum tails being distorted by the integration effect. The momentum density cuts in Figure 3.11 are normalized by their value at $\boldsymbol{k} = \mathbf{0}$ so that they can directly be compared with the percentage $1-f_{\mathrm{coh}}$. This analysis shows that the fitted values of $1-f_{\mathrm{coh}}$ are rather consistent with the extrapolated percentage of depleted atoms in S_{Ω}. This agreement is valid over a range of interactions for which both $1-f_{\mathrm{coh}}$ and the extrapolated depletion level have varied by one order of magnitude.

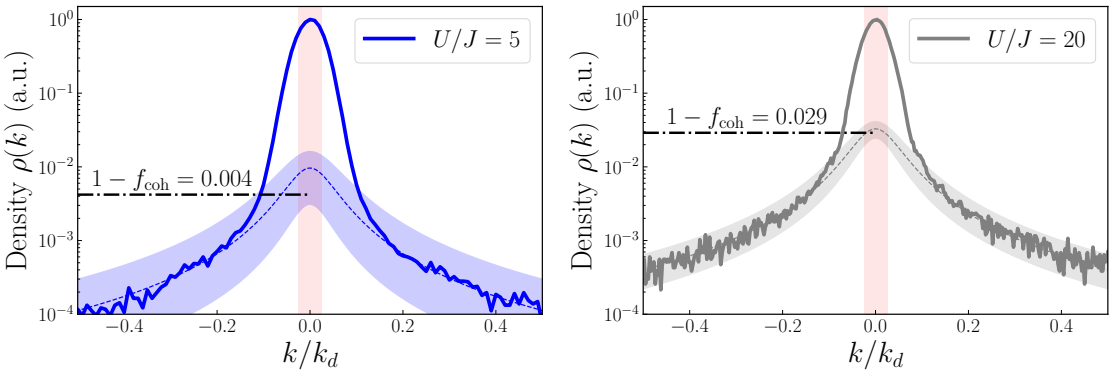

Figure 3.11: **Comparison between $1-f_{\mathrm{coh}}$ and 1D cuts of the momentum densities.** The measured depleted fraction $1-f_{\mathrm{coh}}$ inside the volume S_{Ω} (vertical shaded area) is compared with an extrapolation of the depletion level at $k = 0$. The latter is obtained by fitting the tails of the momentum density cuts with a Lorentzian function, which is an arbitrary choice that matches the data better than a Gaussian one. Within the fit uncertainty (blue/black shaded areas), the agreement between $1-f_{\mathrm{coh}}$ and the extrapolated depletion level at $k = 0$ is rather good, for both the weakly-interacting ($U/J = 5$) and the strongly-interacting ($U/J = 20$) regimes.

A more robust certification for the fitted coherent fraction f_{coh} consists in linking it with the condensed fraction f_c. The latter is measured from a separate and independent procedure described in Appendix A. The relationship between f_{coh} and f_c is not trivial, and particularly not a linear one, since the condensed fraction concerns the whole cloud while the coherent fraction is limited to a small volume centered on $\boldsymbol{k} = \mathbf{0}$ where the condensed contribution *(i)* exceeds by far that of the depletion, and *(ii)* varies much more

abruptly with the interaction strength than the total number of condensed atoms in the whole momentum space. The relationship between f_{coh} and f_c is modeled as follows:

- One assumes that the shape of the BEC in the first Brillouin zone is given by a 3D isotropic Gaussian function [176]:

$$n_{\text{BEC}}(\boldsymbol{k}) = \rho_{\text{BEC}}(0) e^{-k^2/2\sigma^2_{\text{BEC}}} \tag{3.19}$$

  while that of the depletion consists of a Lorentzian function along each (uncoupled) lattice axis:

$$n_{\text{dep}}(\boldsymbol{k}) = \rho_{\text{dep}}(0) \prod_{j=x,y,z} \left(\frac{\sigma^2_{\text{dep}}/4}{k_j^2 + \sigma^2_{\text{dep}}/4} \right) \tag{3.20}$$

- With these assumptions, the coherent fraction in the small volume S_Ω centered on $\boldsymbol{k} = \boldsymbol{0}$ can be approximated by:

$$f_{\text{coh}} = \frac{N_{\text{BEC}}}{N_{\text{BEC}} + N_{\text{dep}}} \simeq \frac{\rho_{\text{BEC}}(0)}{\rho_{\text{BEC}}(0) + \rho_{\text{dep}}(0)} \tag{3.21}$$

  On the other hand, the condensed fraction is given by:

$$f_c = \frac{N^{\text{tot}}_{\text{BEC}}}{N^{\text{tot}}_{\text{BEC}} + N^{\text{tot}}_{\text{dep}}} \simeq \frac{\displaystyle\int_{1\text{BZ}} d\boldsymbol{k}\, n_{\text{BEC}}(\boldsymbol{k})}{\displaystyle\int_{1\text{BZ}} d\boldsymbol{k}\, [n_{\text{BEC}}(\boldsymbol{k}) + n_{\text{dep}}(\boldsymbol{k})]} \tag{3.22}$$

  where 1BZ means that the integration is performed over the first Brillouin zone. However, it can be inferred from Figure 3.11 that σ_{BEC} is much smaller than the momentum extent of the first Brillouin zone since the BEC density decreases by at least four orders of magnitude between $k = 0$ and $k = \pm 0.5\ k_d$.. Therefore, the integration over the first Brillouin zone in the BEC case can be replaced by one over $\pm\infty$ without introducing any significant loss of accuracy. Consequently, the condensed fraction can be conveniently expressed as a function of the maximum densities $\rho_{\text{BEC}}(0)$ and $\rho_{\text{dep}}(0)$:

$$f_c \simeq \frac{\rho_{\text{BEC}}(0)\mathcal{V}_c}{\rho_{\text{BEC}}(0)\mathcal{V}_c + \rho_{\text{dep}}(0)\mathcal{V}_d} \tag{3.23}$$

  with:

$$\mathcal{V}_c \simeq \int_{-\infty}^{\infty} n_{\text{BEC}}(\boldsymbol{k})/\rho_{\text{BEC}}(0) = \left(\sqrt{2\pi}\sigma_{\text{BEC}}\right)^3 \tag{3.24}$$

$$\mathcal{V}_d = \int_{1\text{BZ}} n_{\text{dep}}(\boldsymbol{k})/\rho_{\text{dep}}(0) = \left(\sigma_{\text{dep}} \arctan\left[\frac{k_d}{\sigma_{\text{dep}}}\right]\right)^3 \tag{3.25}$$

  the entire volumes of the BEC and the depletion normalized by their respective densities at $\boldsymbol{k} = \boldsymbol{0}$.
- Finally, it follows from Equations 3.21 and 3.23 that f_{coh} and f_c are linked via the relationship:

$$f_{\text{coh}} \simeq \frac{f_c}{f_c + (1 - f_c)\mathcal{V}_c/\mathcal{V}_d} \tag{3.26}$$

  which only depends on the ratio $\mathcal{V}_c/\mathcal{V}_d$, obtained by fitting the momentum densities to extract σ_{BEC} and σ_{dep}. To estimate f_{coh} from the measured values of f_c, this ratio is fixed in Equation 3.26 to its average value between all the datasets $\mathcal{V}_c/\mathcal{V}_d \simeq 0.3(1)$. The 33% error corresponds to the standard deviation of the list of $\mathcal{V}_c/\mathcal{V}_d$ values.

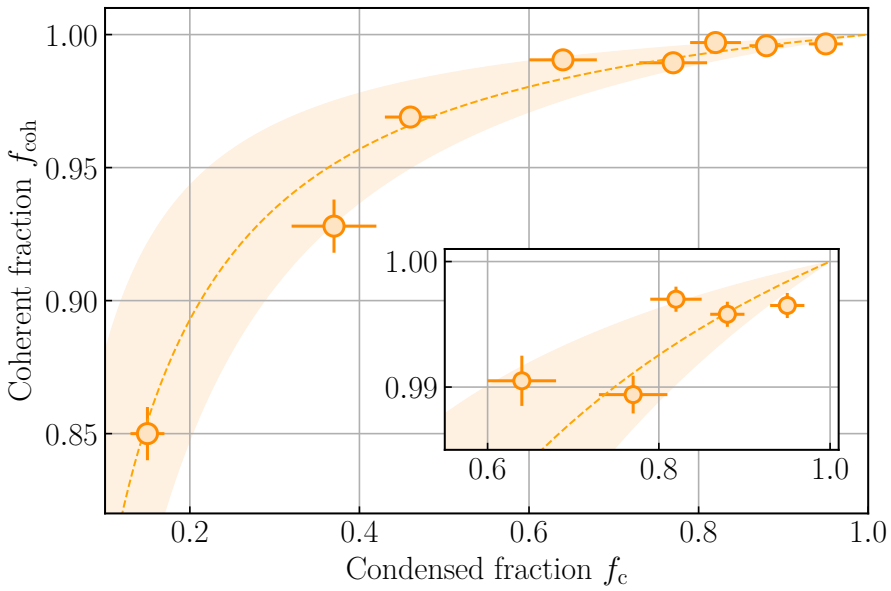

Figure 3.12: **Coherent fraction versus condensed fraction.** The values of f_{coh} extracted from our fitting procedure of the deviations to $g^{(n)} = 1$ are plotted in function of the condensed fractions f_c measured for each data set by a separate procedure (see Appendix A). For comparison, the non-linear prediction of Equation 3.26 is represented by the dotted line and its uncertainty by the shaded area. The inset shows a zoom of the highly-condensed part. The satisfying agreement between experimental and theoretical points confirms the validity of our model with f_{coh} as the only adjustable parameter.

The measured values of f_{coh} and f_c are reported in Figure 3.12 for all the data sets between $U/J = 2$ and $U/J = 20$, along with the quantitative prediction of Equation 3.26. Despite its simplicity, Equation 3.26 correctly captures the non-linear relationship between f_{coh} and f_c without any adjustable parameter, and for a wide range of condensed fractions. This separate measurement further validates the model introduced in Section 3.3.2. As illustrated in both Figures 3.9 and 3.12, this model works even in the strongly-interacting regime where U/J is large and $f_c \ll 1$. This observation is rather surprising considering the key assumption that the BEC and its depletion must be uncorrelated. Understanding this interesting feature would definitely demand a more refined theoretical approach than the one presented here. By attributing the observed deviations from $g^{(n)}(0) = 1$ to the total depletion (quantum and thermal) within the volume probed, our experiment confirms the coherent nature of a BEC up to the sixth order of correlations. A similar conclusion was reached by the Australian team in 2011 up to the third order [1]. However, the effect of the depletion on the system's many-body coherence (visible already for $n = 2$ in Figure 3.8) was not observed at the time. The authors of [1] probably missed it because they probed the statistics in momentum volumes V_Ω larger than the one set by the correlation length associated with the thermal statistics. This choice may have resulted from their smaller detection efficiency $\eta \sim 0.1$, preventing them from reaching sufficient statistics in smaller volumes. As already mentioned, too large volumes V_Ω induce a convolution between uncorrelated atoms that suppresses the amplitude of the correlation functions. This effect is illustrated by the normalized amplitudes $g^{(2)}(0) = 1.022(2)$ and $g^{(3)}(0) = 1.061(6)$ reported by Hodgman *et al.* in the case of a thermal cloud [1], which are significantly smaller than the predictions $g^{(2)}(0) = 2$ and $g^{(3)}(0) = 6$. This shows that, despite its

formidable ability to characterize quantum states, many-body coherence is a complex measurement that requires reaching sufficient statistics in tiny volumes.

3.4 Conclusion

This chapter has presented the measurements of the Full Counting Statistics and high-order moment of the occupation number, up to $n = 6$, in Bose superfluids and Mott insulators. Probed in the far-field regime of the expansion, these quantities identify quantum states from their many-body coherence. Mott insulators and BECs were found to exhibit, respectively, the probability distribution of a thermal and coherent state, with a thermal FCS in the former case and a Poisson FCS in the latter.

The amplitudes of the high-order correlation functions, derived from the factorial moments of the occupation number, corroborated these results. For Mott insulator, finding fully-contrasted correlations $g^{(n)}(0) = n!$ up to the sixth order represents a substantial state-of-the-art improvement compared to previous second-order [175] and third-order [174] correlations measured with significantly smaller amplitudes $g^{(n)}(0) < n!$. Such an improvement is the consequence of the higher detection efficiency used in this work, allowing us to reach high statistics in volumes similar to or smaller than the one set by the system's correlation length.

This capability revealed the effect of the total depletion on the BEC many-body coherence. The resulting deviations from $g^{(n)}(0) = 1$ were successfully captured by a heuristic model introduced to account for the uncorrelated contribution of non-condensed atoms inside the probed volume, that we verified experimentally from studying the coherent fraction at stronger interactions. According to Glauber's definition, we thus conclude that a BEC exhibits a perfect coherence up to $n = 6$, again extending the state-of-the-art [1]. Furthermore, the fact that our simple model work for strongly-interacting gases beyond the Bogoliubov regime ($f_c \ll 1$) was surprising, and this finding calls for further theoretical confirmation.

Overall, we certified quantitatively that a pure-state description correctly describes two iconic states of the Bose-Hubbard phase diagram. Our experimental procedure for measuring the many-body coherence holds promise for studying phase transitions, where fluctuations increase [177] and coherence properties change drastically. Therefore, a natural prospect for us is to extend this technique to investigate the quantum critical region of the low-entropy Mott transition, where the system gets strongly correlated and may exhibit non-trivial (non-Gaussian) correlations at high orders $n \geq 3$.

Chapter 4

4. 2-body correlations at opposite momenta: the fate of Bogoliubov pairs at increasing interactions

Motivated by the discovery of superfluidity in liquid Helium in the late 30s [194, 195], N. Bogoliubov proposed in 1947 [33] a theoretical explanation for the emergence of this phenomenon in ensembles of weakly-interacting bosons. One of the main results of his work is the prediction of the excitation spectrum of the system, whose linear dependency at small momenta implies the existence of a finite critical velocity (according to Landau's criterion [196]) below which the system is superfluid. This feature has been verified in many experimental platforms [197–200], confirming the universal scope of this theory for the description of quantum fluids.

Another prediction of this theory is the existence of a non-condensed fraction in the many-body ground state of the system (at $T = 0$), the so-called quantum depletion. The latter represents the fraction of atoms promulgated outside the condensate mode ($\boldsymbol{k} = \boldsymbol{0}$) by the interactions, whose momentum range extends much further than the condensate [201, 202]. Following the work of Bogoliubov, Lee, Huang, and Yang (LHY) derived in 1957 [203] several properties of the quantum depletion. In particular, they made explicit the quantum depletion-induced energy correction, the linear scaling of the quantum depletion with the interaction strength, and the presence of atom pairs at opposite momenta in the quantum depletion. Measurements of the LHY energy and of the quantum depleted fraction have been reported by other teams [2, 204, 205], confirming the macroscopic predictions of the LHY paper. However, the observation of $\boldsymbol{k}$/-$\boldsymbol{k}$ pairs had never been done until our team made this measurement last year [32], thanks to our ability to detect individual atoms in momentum space.

This chapter is divided into five sections. Section one recalls the main steps of the Bogoliubov theory, particularly how the pairs of atoms at opposite momenta emerge from the effect of (weak) interactions. Sections two and three summarize our experimental work to observe correlations at opposite momenta in the depletion of weakly-interacting Bose gases, and how we ensured that these correlations originate from the Bogoliubov pairs. In the second part of the chapter, we present our undergoing work on investigating this physics in stronger interaction regimes, beyond the validity range of the Bogoliubov theory. Section four presents our recent results on the evolution of the pairing signal with interactions, which is compared to the work of [2]. Finally section five summarizes our

efforts to search for momentum correlations involving three particles that would signal the presence of beyond-Bogoliubov interaction processes.

4.1 The Bogoliubov theory

This section recalls the main steps of Bogoliubov's perturbative approach [33] to describe weakly-interacting Bose gases with two-body contact interactions. Those consist in describing the collision between two atoms at positions $\boldsymbol{r}$ and $\boldsymbol{r'}$ by the two-body contact potential $V = g\delta(\boldsymbol{r} - \boldsymbol{r'})$, with $g = 4\pi\hbar^2 a_s/m$ the coupling constant and a_s the scattering length of the gas [206].

4.1.1 The many-body ground state

In the formalism of second quantization, the Hamiltonian of a homogeneous Bose gas contained in a box of volume L^3 writes:

$$\hat{H} = \int \left(\frac{\hbar^2}{2m} \nabla\hat{\Psi}^\dagger(\boldsymbol{r}) \nabla\hat{\Psi}(\boldsymbol{r}) \right) d\boldsymbol{r} + \frac{g}{2} \int \hat{\Psi}^\dagger(\boldsymbol{r})\hat{\Psi}^\dagger(\boldsymbol{r'})\delta(\boldsymbol{r} - \boldsymbol{r'})\hat{\Psi}(\boldsymbol{r})\hat{\Psi}(\boldsymbol{r'}) d\boldsymbol{r'} d\boldsymbol{r} \tag{4.1}$$

where the field operator $\hat{\Psi}$, $\hat{\Psi}^\dagger$ can be decomposed into the plane wave basis:

$$\hat{\Psi}(\boldsymbol{r}) = \frac{1}{L^{3/2}} \sum_{\boldsymbol{k}} \hat{a}_{\boldsymbol{k}} e^{i\boldsymbol{k}.\boldsymbol{r}} \tag{4.2}$$

$$\hat{\Psi}^\dagger(\boldsymbol{r}) = \frac{1}{L^{3/2}} \sum_{\boldsymbol{k}} \hat{a}^\dagger_{\boldsymbol{k}} e^{-i\boldsymbol{k}.\boldsymbol{r}} \tag{4.3}$$

Here the operator $\hat{a}_{\boldsymbol{k}}$ (resp. $\hat{a}^\dagger_{\boldsymbol{k}}$) annihilates (resp. creates) a particle at momentum $\boldsymbol{k}$. The momentum-space decomposition allows to rewrite the Hamiltonian in the plane wave basis:

$$\hat{H} = \sum_{\boldsymbol{k}} \frac{\hbar^2 k^2}{2m} \hat{a}^\dagger_{\boldsymbol{k}} \hat{a}_{\boldsymbol{k}} + \frac{g}{2L^3} \sum_{\boldsymbol{k'},\boldsymbol{k''},\boldsymbol{q}} \hat{a}^\dagger_{\boldsymbol{k'}+\boldsymbol{q}} \hat{a}^\dagger_{\boldsymbol{k''}-\boldsymbol{q}} \hat{a}_{\boldsymbol{k''}} \hat{a}_{\boldsymbol{k'}} \tag{4.4}$$

At zero-temperature, the ideal Bose gas ($g = 0$) is Bose-condensed with all the bosons in the single-particle ground state, called a Bose-Einstein condensate (BEC). The BEC corresponds to the $\boldsymbol{k} = \boldsymbol{0}$ mode of the momentum space. Assuming interactions are weak, the Hamiltonian 4.4 can be simplified considering that a majority of the N atoms remains in the single-particle ground state. Then, $N_0 = \langle \hat{N}_{\boldsymbol{0}} \rangle = \langle \hat{a}^\dagger_{\boldsymbol{0}} \hat{a}_{\boldsymbol{0}} \rangle \sim N$ and the operators $\hat{a}_{\boldsymbol{0}}$, $\hat{a}^\dagger_{\boldsymbol{0}}$ can be replaced by $\sqrt{N_0}$, which consists in treating the condensate mode as a classical field. In the development of the interacting part of Equation 4.4, the Bogoliubov approach keeps all the terms which are at least quadratic in $\hat{a}_{\boldsymbol{0}}$ and $\hat{a}^\dagger_{\boldsymbol{0}}$. The result is a simplified Hamiltonian:

$$\hat{H}' = \frac{g n_0 N_0}{2} + \sum_{\boldsymbol{k}\neq\boldsymbol{0}} \left(\frac{\hbar^2 k^2}{2m} + 2g n_0 \right) \hat{a}^\dagger_{\boldsymbol{k}} \hat{a}_{\boldsymbol{k}} + \frac{g n_0}{2} \sum_{\boldsymbol{k}\neq\boldsymbol{0}} \left(\hat{a}^\dagger_{\boldsymbol{k}} \hat{a}^\dagger_{-\boldsymbol{k}} + \hat{a}_{\boldsymbol{k}} \hat{a}_{-\boldsymbol{k}} \right) \tag{4.5}$$

with $n_0 = N_0/L^3$. The first term consists of the interaction energy between all condensed atoms. The second term contains the kinetic energy of the non-condensed atoms and the Hartree and Fock terms (hidden in the factor two) of the interaction between the

condensed and non-condensed atoms [207]. Finally, the last term correlates two atoms at momenta $\boldsymbol{k}$ and $\boldsymbol{-k}$ that can either enter or exit the condensate mode $\boldsymbol{k} = \boldsymbol{0}$ as a pair (see Figure 4.1).

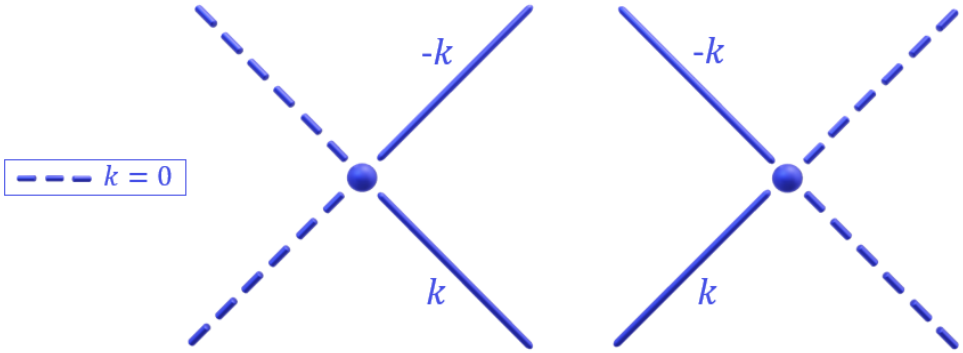

Figure 4.1: **Scheme of the pair creation and annihilation within the Bogoliubov theory.** Left: two atoms in the condensate mode $\boldsymbol{k} = \boldsymbol{0}$ interact via a two-body contact interaction, producing a pair of atoms at opposite momenta to conserve the impulsion. Right: the reversed process where a pair is annihilated back into the condensate mode $\boldsymbol{k} = \boldsymbol{0}$.

This pairing mechanism, referred to as the Bogoliubov or $\boldsymbol{k}$/$\boldsymbol{-k}$ pairing in the following, is a central feature of Bogoliubov's theory. In particular, the system being at equilibrium is a fundamental distinction from other pairing mechanisms occurring in out-of-equilibrium configurations. Examples of the latter include the parametric downconversion in quantum optics [208], dissociation of diatomic molecules in atomic physics [209], and elastic collisions in high-energy physics [210] or with Bose-Einstein condensates [88]. This distinction can be illustrated by considering two atoms initially at rest in the BEC. After the collision process described by the last term in the Hamiltonian 4.5, these two atoms acquire the momenta $\boldsymbol{k}$ and $\boldsymbol{-k}$. Because $\boldsymbol{k}$ can be arbitrarily large, the gain in kinetic energy $2(\hbar^2 k^2/2m)$ may exceed the available interaction energy, inducing an apparent violation of energy conservation. Of course, this is not what is happening here. The oddity comes from the fact that it is conceptually wrong to isolate two atoms from the BEC because of the quantum fluctuations present even without interactions, and quantified by the Heisenberg inequality. As a matter of fact, the existence of the quantum depletion in Bose Superfluids can be derived alternatively to Bogoliubov's approach by a generalization of the Heisenberg uncertainty principle to the case of non-Hermitian operators [211]. In the trap, the atoms in the condensate mode $\boldsymbol{k} \simeq \boldsymbol{0}$ and those of the $\boldsymbol{k}$/$\boldsymbol{-k}$ pairs all belong to the same many-body ground state, whose wavefunction is consequently expressed as a coherent superposition of both contributions [212]:

$$|\Psi_B\rangle \propto \exp\left(\sqrt{N_0}\hat{a}_{\boldsymbol{0}}^\dagger + \sum_{\boldsymbol{k}\neq\boldsymbol{0}} (v_{\boldsymbol{k}}/u_{\boldsymbol{k}})\hat{a}_{-\boldsymbol{k}}^\dagger \hat{a}_{\boldsymbol{k}}^\dagger\right)|0\rangle \tag{4.6}$$

Note that Equation 4.6 is of the same form as the many-body ground state of the Bardeen-Cooper-Schrieffer theory of superconductivity [213], which contains the recently observed (fermionic) Cooper pairs [185]. The coefficients $u_{\boldsymbol{k}}$ and $v_{\boldsymbol{k}}$ are introduced via the Bogoliubov transformation, which we now recall.

4.1.2 Bogoliubov transformation and excitation spectrum

The simplified Hamiltonian H' can be diagonalized using the Bogoliubov transformation [33] that introduces the quasi-particle creation (resp. annihilation) operators $\hat{b}_{\boldsymbol{k}}$ (resp. $\hat{b}^\dagger_{-\boldsymbol{k}}$):

$$\hat{b}_{\boldsymbol{k}} = u_{\boldsymbol{k}}\hat{a}_{\boldsymbol{k}} + v^*_{-\boldsymbol{k}}\hat{a}^\dagger_{-\boldsymbol{k}} \tag{4.7}$$

$$\hat{b}^\dagger_{\boldsymbol{k}} = u^*_{\boldsymbol{k}}\hat{a}^\dagger_{\boldsymbol{k}} + v_{-\boldsymbol{k}}\hat{a}_{-\boldsymbol{k}} \tag{4.8}$$

The latter follow the bosonic commutation rule $[\hat{b}_{\boldsymbol{k}}, \hat{b}^\dagger_{\boldsymbol{k}'}] = \delta_{\boldsymbol{k},\boldsymbol{k}'}$, which implies that the complex numbers $u_{\boldsymbol{k}}$ and $v_{\boldsymbol{k}}$ verify the relation $|u_{\boldsymbol{k}}|^2 - |v_{-\boldsymbol{k}}|^2 = 1$. For these quasi-particle operators to form a basis, the coefficients of the terms $\hat{b}^\dagger_{\boldsymbol{k}}\hat{b}^\dagger_{-\boldsymbol{k}}$ and $\hat{b}_{\boldsymbol{k}}\hat{b}_{-\boldsymbol{k}}$ must be zero. This additional condition allows to write $u_{\boldsymbol{k}}$ and $v_{-\boldsymbol{k}}$ as:

$$u_{\boldsymbol{k}} = \sqrt{\frac{\hbar^2k^2/2m + gn_0}{2\epsilon_{\boldsymbol{k}}} + \frac{1}{2}} \tag{4.9}$$

$$v_{-\boldsymbol{k}} = -\sqrt{\frac{\hbar^2k^2/2m + gn_0}{2\epsilon_{\boldsymbol{k}}} - \frac{1}{2}} \tag{4.10}$$

where $\epsilon_{\boldsymbol{k}}$ is the Bogoliubov dispersion relation (see Figure 4.2):

$$\epsilon_{\boldsymbol{k}} = \sqrt{\frac{\hbar^2k^2}{2m}\left(\frac{\hbar^2k^2}{2m} + 2gn_0\right)} \tag{4.11}$$

The latter contains a linear (phononic) part at low momentum which is the origin of superfluid properties [196]. In particular, it defines the speed of sound $c = \sqrt{gn_0/m}$ below which an impurity can propagate through the gas without scattering. In the opposite large momenta limit, this dispersion relation is quadratic and the quasi-particles are then identical to the real particles ($u_{\boldsymbol{k}} \to 1$ and $v_{\boldsymbol{k}} \to 0$).

In the basis of the quasi-particle operators, the Bogoliubov Hamiltonian is diagonal and writes:

$$\hat{H}_{Bog} = E_{LHY} + \sum_{\boldsymbol{k}} \epsilon_{\boldsymbol{k}}\hat{b}^\dagger_{\boldsymbol{k}}\hat{b}_{\boldsymbol{k}} \tag{4.12}$$

where E_{LHY} contains the Lee Huang Yang energy correction [203] due to the presence of $\boldsymbol{k}$/-$\boldsymbol{k}$ pairs in the many-body ground state. The total energy of the system is simply obtained by adding the contribution of the non-interacting quasi-particles to the LHY energy. These excitations are ideal bosons and are populated by the temperature following the Bose distribution:

$$\langle\hat{b}^\dagger_{\boldsymbol{k}}\hat{b}_{\boldsymbol{k}}\rangle = \frac{1}{e^{\epsilon_{\boldsymbol{k}}/k_BT} - 1} \tag{4.13}$$

Therefore, their statistics is thermal chaotic, in the same way than photons emitted by an incoherent thermal source.

4.1.3 Depleted atoms at finite temperature

Working at finite temperature, the depletion of the condensate has two contributions:

$$\langle\hat{a}^\dagger_{\boldsymbol{k}}\hat{a}_{\boldsymbol{k}}\rangle = (|u_{\boldsymbol{k}}|^2 + |v_{\boldsymbol{k}}|^2)\langle\hat{b}^\dagger_{\boldsymbol{k}}\hat{b}_{\boldsymbol{k}}\rangle + |v_{\boldsymbol{k}}|^2 \tag{4.14}$$

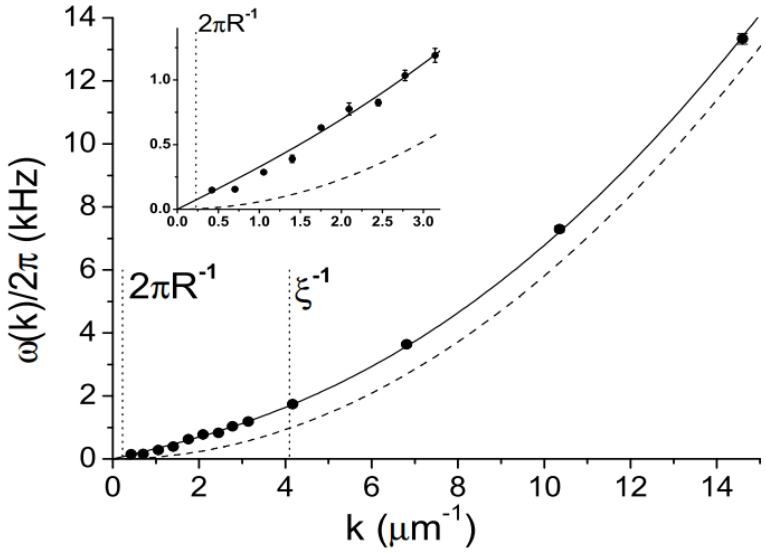

Figure 4.2: **Excitation spectrum of a trapped Bose-Einstein condensate, from [198].** The Bogoliubov prediction (solid line) without free parameters agrees remarkably well with the experimental points. In particular, both the linear phononic regime below ξ^{-1} (in inset) and the free particle regime above ξ^{-1} are clearly visible.

The first one corresponds to the quasi-particles promoted out of the condensed mode by the temperature (thermal depletion) and the second one corresponds to the Bogoliubov pairs present at $T = 0$. Note that the thermal depletion mostly corresponds to single-particle excitations, except at very small momenta $k\xi \ll 1$ for which a quasi-particle has a strong phononic character with $|u_k| \sim |v_k|$. One requirement to detect the Bogoliubov pairs is to work at low temperature for the contribution of the thermally depleted (incoherent) atoms to be reduced. This situation corresponds to reaching the low-temperature regime $k_B T/\mu \ll 1$. In the optical dipole trap, this ratio is of the order of unity $k_B T/\mu \simeq 0.75$ [214] due to the limitation of the evaporative cooling. To decrease the contribution of the thermal depletion, we rather increase the interactions, and consequently the term gn_0 in equation 4.10. As ^{4}He* atoms do not have reachable Feshbach resonance [82] to tune the scattering length and increase the coupling constant g, a 3D optical lattice is used instead. The following section briefly presents the modifications induced by the presence of a lattice, which is assumed not to cause any external trapping confinement for simplicity.

4.1.4 Bogoliubov prediction in the presence of an optical lattice

The Bogoliubov treatment of interactions in the Bose-Hubbard model has been derived, for instance, in [92, 113], and we recall here the main results. The approach is similar to the one of the homogeneous system: starting from the Bose-Hubbard Hamiltonian expanded in the quasi-momentum basis $\hat{a}_{\boldsymbol{q}}$, $\hat{a}^\dagger_{\boldsymbol{q}}$, the high-order terms are grouped into an effective Hamiltonian which is then diagonalized by the use of a Bogoliubov transformation. One ends up with a Hamiltonian of the same form than the one of equation 4.12:

$$\hat{H}^{eff}_{BB} = H_0 + \sum_{\boldsymbol{k}} \epsilon(\boldsymbol{q}) \hat{b}^\dagger_{\boldsymbol{q}} \hat{b}_{\boldsymbol{q}} \tag{4.15}$$

H_0 is the ground state energy and the quasi-particle operators $\hat{b}_{\boldsymbol{q}}$, $\hat{b}^\dagger_{\boldsymbol{q}}$ are similar to those of equations 4.7 and 4.8, except that the coefficients $v_{\boldsymbol{q}}$ and $u_{\boldsymbol{q}}$ now writes:

$$|v_{\boldsymbol{q}}|^2 = |u_{\boldsymbol{q}}|^2 - 1 = \frac{\hbar^2 q^2/2m^* + Un_0}{2\epsilon_{\boldsymbol{k}}} - \frac{1}{2} \tag{4.16}$$

Finally, the dispersion relation $\epsilon(\boldsymbol{q})$ in the presence of an optical lattice becomes:

$$\epsilon(\boldsymbol{q}) = \sqrt{\frac{\hbar^2 q^2}{2m^*}\left(\frac{\hbar^2 q^2}{2m^*} + 2Un_0\right)} \tag{4.17}$$

The effect of the lattice compared to the homogeneous case is twofold:

- the dispersion relation in the ideal case $U \to 0$ now involves the effective mass m^* rather than m [215]. It is therefore not quadratic with q but instead has a sinusoidal shape whose zeros (resp. maxima) are located at the centers (resp. edges) of the Brillouin zones. In the limit of small quasi-momenta, the dispersion relation becomes $\epsilon(\boldsymbol{q}) \simeq \hbar \boldsymbol{q}\sqrt{Un_0/m^*}$. Similarly to the homogeneous case, it is linear in this limit (where $m^* \simeq m$) and the corresponding speed of sound writes $c = \sqrt{Un_0/m^*}$.
- as illustrated by the formula for the speed of sound, the interaction constant g is replaced by the on-site interaction energy $U = g\int |w_{0,0}(\boldsymbol{r})|^4 \mathrm{d}\boldsymbol{r}$ that takes into account the shape of the Wannier functions on the lattice sites. In the limit of a vanishing lattice potential, $U \to g$ and one retrieves the interaction term of the homogeneous case. On the contrary, the higher the lattice potential, the more localized the Wannier functions and the larger the on-site interactions. Therefore, confining the atoms in the lattice sites allows to reach stronger interaction regimes than with the homogeneous system. In particular, it allows us to reach a ratio $k_B T/\mu \simeq 0.3$ at $s = 7.75\, E_r$ which is more favorable than the one of the optical dipole trap.

We should comment here that these results are valid only for homogeneous lattice gases. In our experiment, the optical lattice induces an overall weak harmonic confinement due to the Gaussian shapes of the lattice beams. This external trapping means that the condensate density n_0 is not homogeneous anymore which greatly complicates the resolution of the problem. Actually, an extension of the Bogoliubov theory to the case of 3D lattice bosons in a trap (and at finite temperature) does not exist to our knowledge. It is therefore interesting to provide some first experimental signals for this kind of system.

4.2 Numerical procedure to detect k/-k pairs

This section presents the numerical procedure used to reveal the Bogoliubov pairs in the depletion of weakly-interacting Bose gases released from an optical lattice. The presence of these pairs in the distributions is equivalent to the presence of correlations at opposite momenta between the atoms. In analogy with Quantum Optics [180, 216], these correlations are revealed via a two-body correlator, expressed in second quantization as:

$$G(\boldsymbol{k}, \boldsymbol{k}') = \langle \hat{a}^\dagger_{\boldsymbol{k}} \hat{a}^\dagger_{\boldsymbol{k}'} \hat{a}_{\boldsymbol{k}} \hat{a}_{\boldsymbol{k}'} \rangle \tag{4.18}$$

We recall that the normal ordering of the operators in $G(\boldsymbol{k}, \boldsymbol{k}')$ results from the destruction of a particle upon its detection, which is the case for both the photons in Quantum Optics and the ^{4}He* atoms in our experiment. Similarly to Chapter 3, the pairing signal will

actually be quantified by a normalized version $g^{(2)}(\boldsymbol{k}, \boldsymbol{k}')$ of the two-body correlator 4.19. As explained below, this normalization allows us to identify Bogoliubov's pairs among all possible doublets of atoms within each distribution.

4.2.1 The integration volume Ω_k

When loaded inside a shallow optical lattice, the cloud is in the superfluid phase of the Bose-Hubbard phase diagram. This means that the BEC keeps its coherence and is therefore diffracted by the periodic structure of the optical lattice. In the far-field regime of expansion, condensed atoms are located in the different diffraction peaks whose momentum volume corresponds to $\sim (1/L_{BEC})^3$ [176], with L_{BEC} the in-trap spatial size of the BEC. On the contrary, the typical momentum extent of the quantum depletion is given by the inverse of the healing length $1/\xi \gg 1/L_{BEC}$, and the depleted atoms are delocalized over a much larger momentum space than the BEC. This feature is also true for thermal atoms at the temperature of our experiment [93]. Such a distinction of momentum scales is helpful to detect the $\boldsymbol{k}$/-$\boldsymbol{k}$ pairs. Indeed, one would like to exclude the condensed atoms from the computation as they would hide the signal of interest. This is done by post-selecting only the atoms falling in between the BEC diffraction peaks. Those are k_d-periodically spaced features whose total momentum extent does not exceed $2 \times \Delta k = 2 \times 0.15\, k_d$. Therefore, the post-selected volume Ω_k consists in a cube of side $k_{\max} \leq 0.85\, k_d$, with a smaller cube

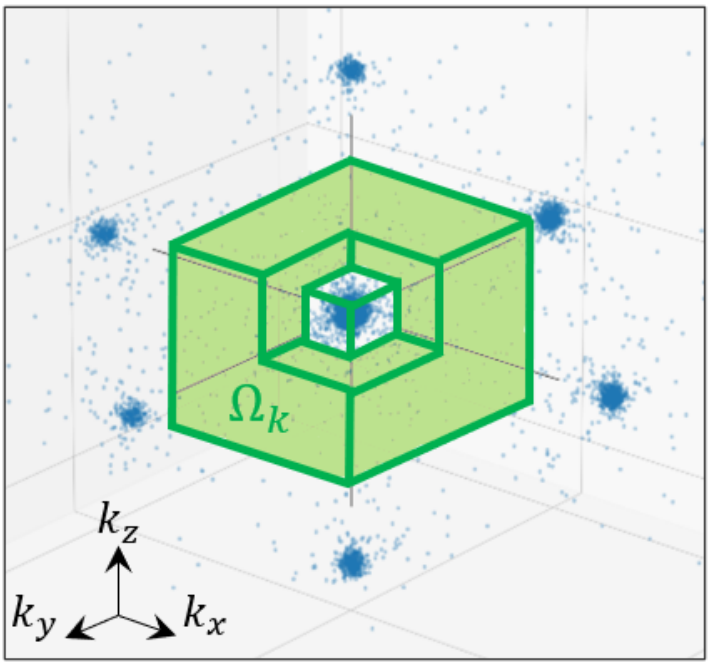

Figure 4.3: **Scheme of the integration volume $\boldsymbol{\Omega_k}$.** The latter is represented as a green shaded area on top of the momentum distribution of lattice bosons detected after time-of-flight. It has a cubic shape whose side can be chosen at will and a cubic hole at the center to exclude the condensed atoms of the zeroth order diffraction peak. The lines between the diffraction peaks are added to represent the orientation of the lattice beams, symbolized by the vectors k_x, k_y and k_z.

of side $k_{\min} \geq 0.15\, k_d$ removed at its center (see Figure 4.3). These dimensions ensure that Ω_k contains exclusively depleted atoms, among which we look for $\boldsymbol{k}$/-$\boldsymbol{k}$ pairs.

4.2.2 Anomalous and normal correlations

Because $\hat{H}_{Bog}$ is diagonal in the quasi-particle basis, all of its eigenstates have Gaussian statistics [155]. As the Bogoliubov transformation is linear, the Gaussian nature of the state is also present in the particle basis where Wick's theorem can be used to decompose $G^{(2)}(\boldsymbol{k},\boldsymbol{k'})$ into [217] :

$$\begin{aligned} G^{(2)}(\boldsymbol{k},\boldsymbol{k'}) &= \langle \hat{a}^\dagger_{\boldsymbol{k}} \hat{a}^\dagger_{\boldsymbol{k'}} \rangle \langle \hat{a}_{\boldsymbol{k}} \hat{a}_{\boldsymbol{k'}} \rangle + \langle \hat{a}^\dagger_{\boldsymbol{k}} \hat{a}_{\boldsymbol{k}} \rangle \langle \hat{a}^\dagger_{\boldsymbol{k'}} \hat{a}_{\boldsymbol{k'}} \rangle + \langle \hat{a}^\dagger_{\boldsymbol{k}} \hat{a}_{\boldsymbol{k'}} \rangle \langle \hat{a}^\dagger_{\boldsymbol{k'}} \hat{a}_{\boldsymbol{k}} \rangle \\ &= |\langle \hat{a}^\dagger_{\boldsymbol{k}} \hat{a}^\dagger_{\boldsymbol{k'}} \rangle|^2 + \rho(\boldsymbol{k})\rho(\boldsymbol{k'}) + |\langle \hat{a}^\dagger_{\boldsymbol{k}} \hat{a}_{\boldsymbol{k'}} \rangle|^2 \end{aligned} \tag{4.19}$$

with $\rho(\boldsymbol{k}) = \langle \hat{a}^\dagger_{\boldsymbol{k}} \hat{a}_{\boldsymbol{k}} \rangle$ the momentum density. The second part of this equation $\rho(\boldsymbol{k})\rho(\boldsymbol{k'}) + |\langle \hat{a}^\dagger_{\boldsymbol{k}} \hat{a}_{\boldsymbol{k'}} \rangle|^2$ is called the normal correlations, as the operators are normally ordered (and conserve particle number). We will come back to it later in this chapter. For the moment, let us focus on the first term of this equation that is referred to as the anomalous part of the two-body correlations $|\langle \hat{a}^\dagger_{\boldsymbol{k}} \hat{a}^\dagger_{\boldsymbol{k'}} \rangle|^2$. This term is non-zero only in the presence of correlations between the modes $\boldsymbol{k}$ and -$\boldsymbol{k}$. Naturally, Bogoliubov pairs contribute to this signal. However, the atoms of the thermal depletion can also contribute to these anomalous correlations. To illustrate that, one can use the Bogoliubov transformation to write the anomalous part in terms of quasi-particle operators [212, 217]:

$$\begin{aligned} |\langle \hat{a}^\dagger_{\boldsymbol{k}} \hat{a}^\dagger_{-\boldsymbol{k}} \rangle|^2 &= |\langle \left(u_{\boldsymbol{k}} b^\dagger_{\boldsymbol{k}} + v_{-\boldsymbol{k}} b_{-\boldsymbol{k}} \right) \left(u_{-\boldsymbol{k}} b^\dagger_{-\boldsymbol{k}} + v_{\boldsymbol{k}} b_{\boldsymbol{k}} \right) \rangle|^2 \\ &= |u_{\boldsymbol{k}} v_{\boldsymbol{k}}|^2 \left(1 + 2 \langle \hat{b}^\dagger_{\boldsymbol{k}} \hat{b}_{\boldsymbol{k}} \rangle \right)^2 \end{aligned} \tag{4.20}$$

The presence of $\langle \hat{b}^\dagger_{\boldsymbol{k}} \hat{b}_{\boldsymbol{k}} \rangle$ implies that quasi-particles can indeed contribute to the anomalous correlations. Looking at equation 4.7, this situation occurs when $|u_{\boldsymbol{k}}| \sim |v_{\boldsymbol{k}}|$, namely when Bogoliubov quasi-particles have a strong phononic character. This condition is fulfilled at low momenta such that $k\xi \ll 1$. In order to unambiguously attribute $\boldsymbol{k}$/-$\boldsymbol{k}$ correlations to atoms from the quantum depletion, we must ensure that the integration volume Ω_k excludes momenta verifying this condition. Fortunately, this is easier to do when atoms expand from a 3D optical lattice compared to the optical dipole trap. Indeed, the higher chemical potential in the optical lattice makes the healing length smaller, and thus the condition $k\xi \ll 1$ becomes less stringent on $\boldsymbol{k}$. Actually, even the smallest lower bound for Ω_k, $k_{\min} = 0.15\, k_d$, already corresponds to $k\xi \simeq 0.85$. It is therefore safe to assume that the thermally depleted atoms in Ω_k do not contribute to the anomalous correlation signal [217].

4.2.3 The integrated and normalized two-body correlator

The two-body correlator of equation 4.19 is not an appropriate quantity to deal with. Firstly because the number of individual modes $\boldsymbol{k}$, $\boldsymbol{k'}$ of volume $(L_{BEC})^{-3}$ inside the integration volume Ω_k is of the order of 10^5. Therefore, reaching a satisfying signal-to-noise ratio for the two-body correlations measurement between all these modes would require a huge amount of experimental realizations. Secondly, $G^{(2)}(\boldsymbol{k},\boldsymbol{k'})$ is a 6D function, and so plotting it in an intelligible way is not straightforward either. To circumvent these

issues, we average the correlations over Ω_k. We first compute the joint probability for any modes $\boldsymbol{k}$ and $\boldsymbol{k'} = \boldsymbol{\delta k} - \boldsymbol{k}$, before summing the contributions of all the modes $\boldsymbol{k}$ inside Ω_k to increase the signal-to-noise ratio. The resulting two-body correlation function only depends on the parameter $\boldsymbol{\delta k}$:

$$G_A^{(2)}(\boldsymbol{\delta k}) = \int_{\Omega_k} G^{(2)}(\boldsymbol{k}, \boldsymbol{\delta k} - \boldsymbol{k}) d\boldsymbol{k} = \int_{\Omega_k} \langle \hat{a}^\dagger_{\boldsymbol{k}} \hat{a}^\dagger_{\boldsymbol{\delta k}-\boldsymbol{k}} \hat{a}_{\boldsymbol{k}} \hat{a}_{\boldsymbol{\delta k}-\boldsymbol{k}} \rangle d\boldsymbol{k} \tag{4.21}$$

With this definition, an enhanced probability at $\boldsymbol{\delta k} = \boldsymbol{0}$ signals the presence of $\boldsymbol{k}$/-$\boldsymbol{k}$ pairs. Note that this definition contains both the anomalous term and the density squared term of Equation 4.19. Therefore, Equation 4.21 also returns the auto-correlation function of the momentum density $\int_{\Omega_k} \rho(\boldsymbol{k})\rho(\boldsymbol{\delta k} - \boldsymbol{k})\rangle d\boldsymbol{k}$. To ease the visualization of the $\boldsymbol{k}$/-$\boldsymbol{k}$ correlation signal on top of this uncorrelated background, we compute the normalized integrated two-body correlator:

$$g_A^{(2)}(\boldsymbol{\delta k}) = \frac{\int_{\Omega_k} \langle \hat{a}^\dagger_{\boldsymbol{k}} \hat{a}^\dagger_{\boldsymbol{\delta k}-\boldsymbol{k}} \hat{a}_{\boldsymbol{k}} \hat{a}_{\boldsymbol{\delta k}-\boldsymbol{k}} \rangle d\boldsymbol{k}}{\int_{\Omega_k} \rho(\boldsymbol{k})\rho(\boldsymbol{\delta k} - \boldsymbol{k})\rangle d\boldsymbol{k}} \tag{4.22}$$

where the normalization ensures that correlated atom pairs are detected if the correlation function $g_A^{(2)}(\boldsymbol{\delta k})$ exceeds one. Therefore, we look at the anomalous amplitude $g_A^{(2)}(0) - 1$ which is non-zero in the presence of $\boldsymbol{k}$/-$\boldsymbol{k}$ pairs. The algorithm used to compute the normalized two-body correlation function $g_A^{(2)}(\boldsymbol{\delta k})$ is presented in the following paragraph.

4.2.4 Brief description of the algorithm

The anomalous correlations $g_A^{(2)}(\boldsymbol{\delta k})$ cannot be calculated from the factorial moments of the occupation number as it was done in Chapter 3, because this method is limited to the measurement of local correlations at close-by momenta $\boldsymbol{k'} = \boldsymbol{k}$. Prior to its implementation, our team studied local (normal) two-body correlations across the Mott transition [146, 174] using a different algorithm. For the purpose of the work reported here, the former Ph.D. student Antoine Ténart adapted this older algorithm to detect two-body correlations at opposite momenta $\boldsymbol{k'} = -\boldsymbol{k}$ [74]. In practice, $g_A^{(2)}$ is a 3D histogram obtained after dividing the 3D histograms of the numerator and denominator of equation 4.22. The numerator computation is schematically described in Figure 4.4. For a given distribution, the momenta of all possible pairs of atoms are summed. The 3D histogram of this list of (sums of) momenta is then computed with an adjustable size of the voxels in the momentum space. If Bogoliubov pairs are contained within an atomic distribution, they "add a click" in the central voxel of this 3D histogram as both atoms i and j of the pair verify $k_x^i + k_x^j = 0$, $k_y^i + k_y^j = 0$, and $k_z^i + k_z^j = 0$.

To get the denominator of equation 4.22, we repeat this procedure with an uncorrelated dataset with the same momentum density. Such dataset can be obtained in two different ways. The first one consists in merging all the atoms of the different atomic distributions into a single file on which the numerator procedure described above is repeated. In that way, the $\boldsymbol{k}$/-$\boldsymbol{k}$ correlations are washed out and one essentially retrieves the auto-correlation of the momentum density. If N_i is the number of atoms detected in each file i, then the number of counts in the denominator with this method is $(\sum_i N_i)\,(\sum_i N_i - 1)$. On the opposite, there are only $\sum_i N_i(N_i - 1)$ counts in the histogram of the numerator. Therefore, the 3D histogram obtained after dividing the numerator by the denominator has to be normalized by the factor $(\sum_i N_i)\,(\sum_i N_i - 1) \,/\, \sum_i N_i(N_i - 1)$ for the voxels in $g_A^{(2)}$ to be

equal to 1 in the absence of $\boldsymbol{k}$/-$\boldsymbol{k}$ pairs. This method gives the auto-correlation of the momentum density with a good signal-to-noise ratio and is used to quantitatively characterize the correlation signals, but it is quite time-consuming (because of the denominator). An alternative approach consists in repeating the numerator procedure on an artificial set of experimental realizations obtained after shuffling the atoms between the different atomic distributions (similarly to the randomization procedure in Chapter 3). Then again, the resulting atomic distributions are essentially uncorrelated since the probability for both atoms of a pair to end up in the same file is small. By keeping the number of distributions and the number of atoms by distribution identical during the mixing, the denominator has exactly the same number of counts than the numerator and then $g_A^{(2)}$ does not need to be rescaled. This method is useful to get a first rapid answer on whether $\boldsymbol{k}$/-$\boldsymbol{k}$ correlations are present.

Algorithm 2-body correlations

```
For each run n
    For each atom i in run n
        For all atoms j ≠ i in run n
            Append k_i + k_j to momentum_sum_list
        End
    End
Compute and store the 3D histogram of momentum_sum_list
End
Average the 3D histograms of all experimental runs
```

Figure 4.4: **Pseudo-code version of the two-body correlations algorithm.** The procedure is identical between the numerator and the denominator of Equation 4.22 except that for the latter, this algorithm is carried out on a distribution for which the anomalous signal has been suppressed (see text).

4.2.5 Transverse integration and absolute amplitude of the correlation signal

A natural way to visualize the information contained in $g_A^{(2)}$ is to plot 1D cuts of the 3D histogram along the directions of the lattice axis $(k_x, 0, 0)$, $(0, k_y, 0)$, and $(0, 0, k_z)$. However, the signal-to-noise ratio is not good enough when plotting such a single line of voxels, so that we usually perform some transverse integration of adjustable width $\delta k_\perp$ to average the neighboring lines. Figure 4.5 illustrates a transverse integration of $\pm\delta k_\perp$ along the axis k_y and k_z. This procedure affects the amplitude of the measured correlation signal. To illustrate this effect, let us assume that the 3D histogram $g_A^{(2)}$ contains on top of the uncorrelated background level a Bell-shaped correlation peak centered at $\boldsymbol{k} = \boldsymbol{0}$ with an amplitude η_0:

$$g_A^{(2)}(\boldsymbol{\delta k}) = 1 + \eta_0 \prod_{i=x,y,z} \exp\left(\frac{-\delta k_i^2}{2\sigma_i^2}\right) \tag{4.23}$$

σ_i are the RMS width of this correlation peak along the three lattice direction. Note that it is assumed here that these axis are separable, a property that was checked experimentally.

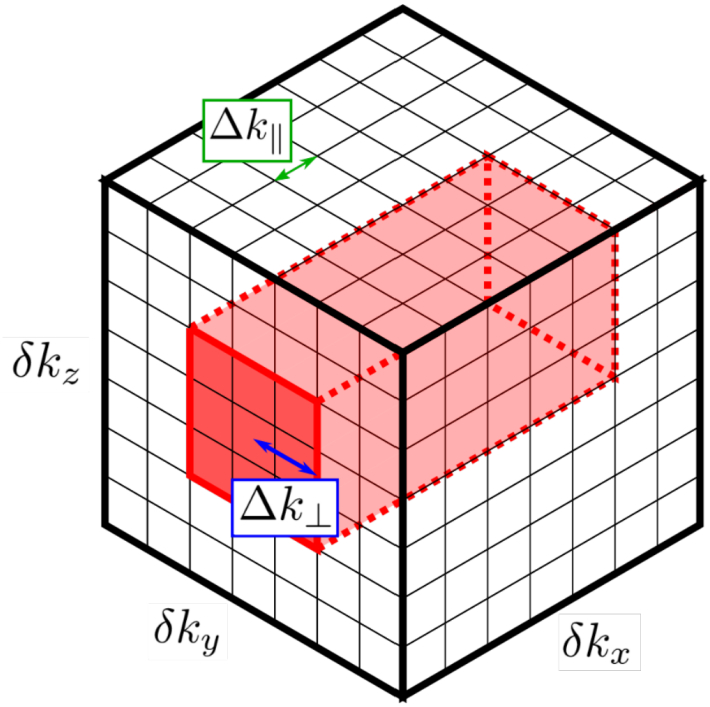

Figure 4.5: **3D visualization of the transverse integration.** The $7 \times 7 \times 7$ matrix represents the 3D histogram $g_A^{(2)}(\boldsymbol{\delta k})$ which has been computed with 3D voxels of volume $(\delta k_{||})^3$. The red parallelogram illustrates a transverse integration of $\pm\delta k_\perp$ along the axis δk_y and δk_z, meaning that all the voxel lines along δk_x inside this red parallelogram are averaged into a single one.

Then, a double transverse integration of $\pm\delta k_\perp$ along the k_y and k_z axis leads to:

$$\begin{aligned} g_A^{(2)}(\delta k_x) &= \frac{1}{(2\delta k_\perp)^2} \iint_{-\delta k_\perp}^{\delta k_\perp} \left(1 + \eta_0 \prod_{i=x,y,z} \exp\left(\frac{-\delta k_i^2}{2\sigma_i^2}\right)\right) d\delta k_y \, d\delta k_z \\ &= 1 + \eta_0 \frac{2\pi\sigma_y\sigma_z}{(2\delta k_\perp)^2} \operatorname{erf}\left(\frac{\delta k_\perp}{\sqrt{2}\sigma_y}\right) \operatorname{erf}\left(\frac{\delta k_\perp}{\sqrt{2}\sigma_z}\right) \exp\left(\frac{-\delta k_x^2}{2\sigma_x^2}\right) \end{aligned} \tag{4.24}$$

with the error function defined as:

$$\operatorname{erf}(x) = \frac{2}{\sqrt{\pi}} \int_0^x \exp\left(-t^2\right) dt \tag{4.25}$$

relthe assumption that the correlation peak is isotropic $\sigma_x = \sigma_y = \sigma_z \equiv \sigma$, the amplitude of the 1D cut of the correlation peak for a given transverse integration, $\eta(\delta k_\perp)$, writes as:

$$\eta(\delta k_\perp) = \eta_0 \frac{2\pi\sigma^2}{(2\delta k_\perp)^2} \operatorname{erf}\left(\frac{\delta k_\perp}{\sqrt{2}\sigma}\right)^2 \tag{4.26}$$

Correcting the transverse integration effect is done in the same spirit than for the previous chapter. The measurement of $\eta(\delta k_\perp)$ is repeated for different transverse integrations, and η_0 is then obtained by fitting the resulting amplitudes with the scaling of Equation 4.26 to extrapolate the amplitude at zero transverse integration. Having described the numerical procedure to reveal the Bogoliubov pairs from the measured momentum distributions, we now move to the experimental signals and their analysis.

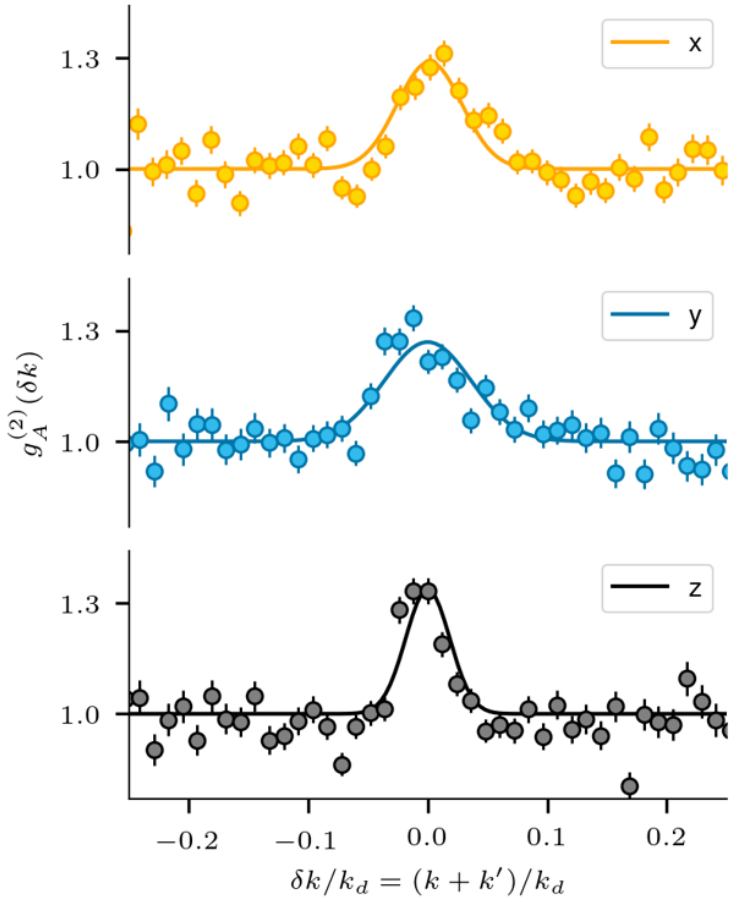

Figure 4.6: **Anomalous correlations revealing pairs of atoms at opposite momenta.** 1D cuts through $g_A^{(2)}(\boldsymbol{\delta k})$ along the three lattice axis. The transverse integration is $\delta k_\perp = 3.0 \times 10^{-2} k_d$ and the longitudinal voxel size is $\delta k_{||} = 1.2 \times 10^{-2} k_d$. The data are fitted by Gaussian functions (solid lines) and the error bars are obtained from the inverse square root of the number of counts in the voxels.

4.3 Observation of k/-k pairs

This section presents the measurements and analysis reported in [32] to validate the observation of the Bogoliubov pairs.

4.3.1 A first signal

To perform the measurement of the Bogoliubov pairs, we calibrate the experiment to prepare BECs of $N_{BEC} = 5 \times 10^3$ atoms that are loaded in a shallow 3D optical lattice of amplitude $s = 7.75\, E_r$ ($U/J = 5$). The lattice is then abruptly switched off, and the gas is let to expand during a 296 ms time-of-flight before reaching our detector. As explained in the first chapter, the expansion from the lattice ensures that the effects of interactions are suppressed during the TOF so that the in-trap many-body wavefunction is mapped onto the momentum basis [90, 146]. The small lattice amplitude allows to keep a high condensed fraction, so that the Bogoliubov approximation should reasonably be valid. The measured condensed fraction for this dataset is about 84% (see Appendix A

for the method), and the latter contains approximately 4000 experimental distributions. Not all of these distributions are retained for calculating the correlations because of shot-to-shot fluctuations in the atom number. In practice, we keep the distributions whose atom number belongs to $[3500; 6500]$, namely a 30% interval around $N_{BEC} = 5 \times 10^3$. At worse, this constraint corresponds to keeping about half of the dataset. The correlation algorithm is computed using a momentum volume Ω_k corresponding to $k_{\min} = 0.15\, k_d$ and $k_{\max} = 0.85\, k_d$, and voxels of dimensions $\delta k_{\parallel} = 1.2 \times 10^{-2}\, k_d$. Figure 4.6 presents the result of this computation. A correlation peak is clearly visible on top of the noise along each 1D cut of $g_A^{(2)}$. Extending the range $\boldsymbol{\delta k}$ of the computations yields additional correlation peaks at momenta $k = \pm k_d$ along each lattice axis, as expected from Bloch's theorem (see 4.7). Such a correlation signal is exactly what we hoped to obtain in searching for signatures of the Bogoliubov pairs. The remaining of Section 4.3 summarizes the list analysis carried out to attribute this pairing signal to Bogoliubov's physics unambiguously.

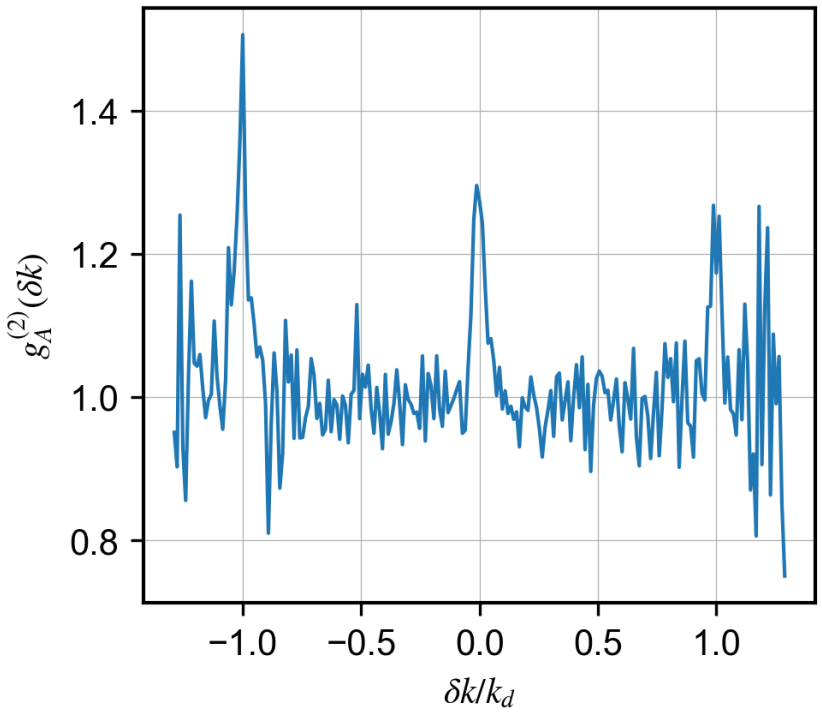

Figure 4.7: **Periodicity of $g_A^{(2)}(\boldsymbol{\delta k})$.** As the diffraction peaks of the momentum density, we observe additional correlations peaks at $\pm k_d$ on the 1D cut of the anomalous function.

4.3.2 Comparison with HBT-like correlations

In the following, we show how interesting it is to compare the anomalous correlations with the normal ones, mentioned earlier in equation 4.19. The term $|\langle \hat{a}_{\boldsymbol{k}}^{\dagger} \hat{a}_{\boldsymbol{k}'} \rangle|^2$ is non-zero only when identical modes $\boldsymbol{k}' = \boldsymbol{k}$ are considered. In this case, the normal correlations become twice the density squared and the normalized correlation amplitude equals two. This enhanced probability for detecting two atoms at close by momenta is commonly referred to as bosonic bunching, a property resulting from the interference between possible detection paths for two indistinguishable bosons with thermal (chaotic) statistics. The first observation of this effect dates back to the Hanbury-Brown and Twiss (HBT) experiment [189] in 1956 (see Chapter 3). Since this first experiment, bosonic bunching has been

observed in various systems [218, 219] and including in cold atoms experiments [26, 28, 146, 174, 175]. Having already explained the computation method for two-body correlations at opposite momenta, the computation of HBT-like correlations is easy to understand. We simply compute the joint probability for two modes $\boldsymbol{k}$ and $\boldsymbol{k'} = \boldsymbol{\delta k} + \boldsymbol{k}$ to be populated, resulting in the two-body correlation function:

$$G_N^{(2)}(\boldsymbol{\delta k}) = \int_{\Omega_k} G^{(2)}(\boldsymbol{k}, \boldsymbol{\delta k} + \boldsymbol{k}) d\boldsymbol{k} = \int_{\Omega_k} \langle \hat{a}^\dagger_{\boldsymbol{k}} \hat{a}^\dagger_{\boldsymbol{\delta k}+\boldsymbol{k}} \hat{a}_{\boldsymbol{k}} \hat{a}_{\boldsymbol{\delta k}+\boldsymbol{k}} \rangle d\boldsymbol{k} \tag{4.27}$$

where, similarly to Equation 4.21, the contributions of all the modes $\boldsymbol{k}$ inside Ωk are summed. Normalizing these correlations yields the 3D normalized and integrated normal correlation function: [1]

$$g_N^{(2)}(\boldsymbol{\delta k}) = \frac{\int_{\Omega_k} \langle \hat{a}^\dagger_{\boldsymbol{k}} \hat{a}^\dagger_{\boldsymbol{\delta k}+\boldsymbol{k}} \hat{a}_{\boldsymbol{k}} \hat{a}_{\boldsymbol{\delta k}+\boldsymbol{k}} \rangle d\boldsymbol{k}}{\int_{\Omega_k} \rho(\boldsymbol{k}) \rho(\boldsymbol{\delta k} + \boldsymbol{k}) \rangle d\boldsymbol{k}} \tag{4.28}$$

In practice, this is done with the same algorithm than the one described in 4.2.4 except that the momenta of all possible pairs of atoms are subtracted rather than summed. Two bunched atoms then "add a click" at the center of the 3D histogram as their momenta verify $k_x^i - k_x^j = 0$, $k_y^i - k_y^j = 0$, and $k_z^i - k_z^j = 0$. Figure 4.8 shows 1D cuts of the normal

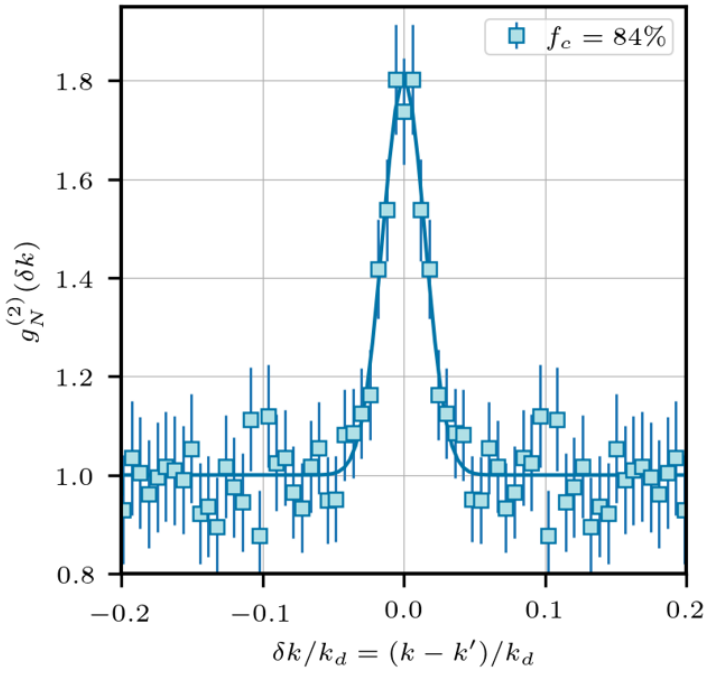

Figure 4.8: **1D cut of the normal correlation function $g_N^{(2)}(\boldsymbol{\delta k})$.** Compared to the anomalous case, the voxel size was reduced to $\delta k_{||} = 6 \times 10^{-3} k_d$ to resolve the thinner bunching peak, resulting in a smaller statistics per voxel and consequently larger error bars. The transverse integration $\delta k_\perp = 1.5 \times 10^{-2}$ reduces the amplitude of the correlation peak compared to the perfect bunching $g_N^{(2)}(0) = 2$. Note that $g_N^{(2)}(\delta k)$ is plotted between -0.2 k_d and 0.2 k_d but is symmetric by construction.

[1] At that time, we did not have at our disposal the algorithm based on the factorial moments of the occupation number.

correlation function $g_N^{(2)}(\boldsymbol{\delta k})$ computed with the same post-selected atoms than in the previous paragraph. As for the anomalous case, a clear correlation peak is visible.

The procedure for correcting the transverse integration effect is identical between the anomalous and normal correlation signals. It is illustrated in Figure 4.9 using the bunching signal of Figure 4.8. For each transverse integration, three amplitudes $g_N^{(2)}(\Delta k_\perp) - 1$ are obtained from fitting the 1D cuts of the correlation peak along each lattice axis with a Gaussian function. The error bars correspond to the confidence interval of the fitted amplitude. The variation of the correlation amplitude with $\Delta k_\perp$ is then adjusted with the scaling of Equation 4.26 (solid lines), from which η_0 is extrapolated. The shaded areas in Figure 4.9 represent the uncertainty on the fitting parameters. Finally, the amplitude $g_N^{(2)}(0)-1$ is obtained by averaging those along each lattice axis, with an error defined as the standard deviation. Applied to the data of Figure 4.8, this procedure yields an amplitude $g_N^{(2)}(0) - 1 = 0.99(2)$ compatible with that expected for bosonic bunching. It is easy to understand that atoms from the thermal depletion at $k\xi \geq 1$ would give a perfect bosonic bunching. In the framework of Bogoliubov theory those atoms correspond to thermally populated quasi-particles and the Bogoliubov transformation being linear, the statistics of the real particles is thermal as well. However, it is not straightforward that atoms pairs of the quantum depletion also contribute to the bunching effect. It actually comes from the fact that a single mode $\boldsymbol{k}$ may contain several atoms from distinct pairs which are not themselves correlated in the Bogoliubov approximation. Therefore, computing local correlations inside a single mode $\boldsymbol{k}$ traces over the partners of the pairs and explains how a chaotic statistics is retrieved from the atoms of the quantum depletion [146, 217, 220]. A similar effect is found in two-mode squeezed states when only one mode is probed [221].

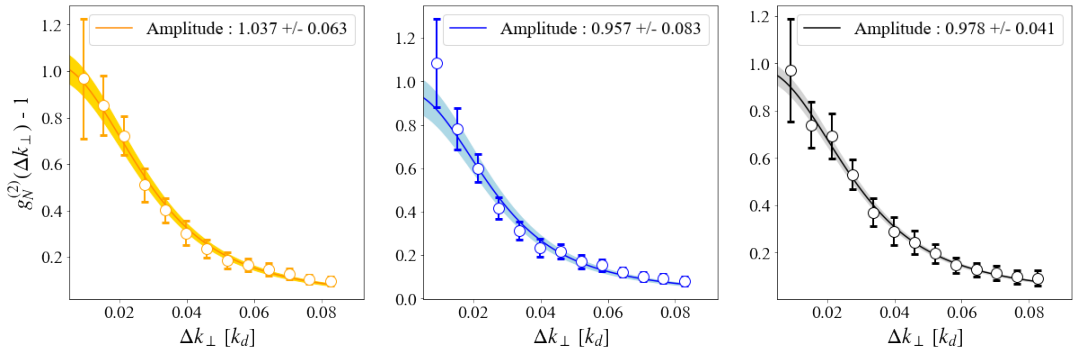

Figure 4.9: **Correction of the transverse integration effect.** Amplitude of the normal correlations function along each lattice axis versus the transverse integration (see text).

In connection with the previous chapter, we have checked that our algorithms for computing both the anomalous and normal correlations led to $g^{(2)}(0) \simeq 1$ when computed with atoms of the BEC mode ($\boldsymbol{k} = \boldsymbol{0}$). This feature is illustrated in Figure 4.10, for which the integration volume Ω_k only keeps the atoms inside a cube of side $0.04\,k_d$ centered on $\boldsymbol{k} = \boldsymbol{0}$. The small modulation (of the order of 1%) visible in the inset of Figure 4.10 is an artifact of the normalization procedure coming from shot-to-shot fluctuations of the BEC width [48]. In the following, the contrasted behaviors between the anomalous and normal correlations is shown to provide signatures of the quantum origin of the anomalous signal.

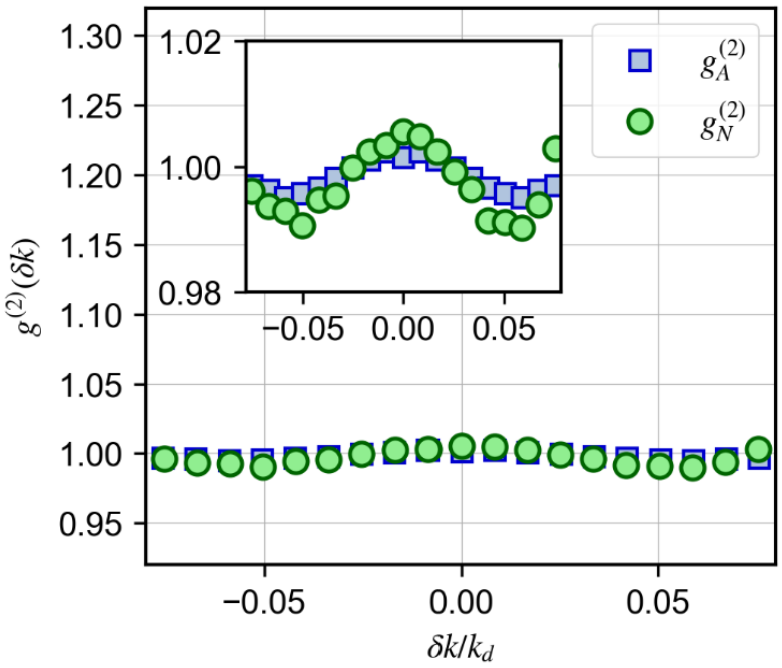

Figure 4.10: **Normal and anomalous correlation functions in the BEC.** The error bars are smaller than the markers.

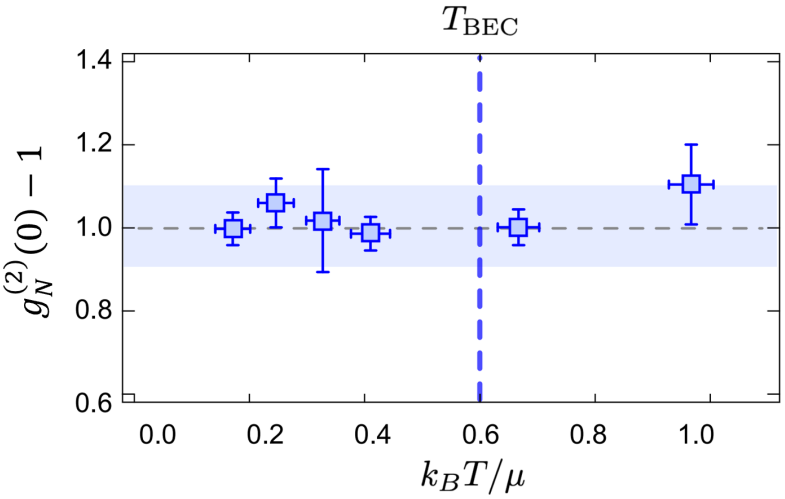

Figure 4.11: **Bunching amplitude versus $k_B T/\mu$, from [146].** The measurements are consistent with $g_N^{(2)}(0) = 2$, namely with a chaotic statistics at any temperature. The vertical blue dashed line in both panels signals T_{BEC}.

4.3.3 Effect of the temperature

The dependency with temperature of both correlation signals $g_N^{(2)}$ and $g_A^{(2)}$ is expected to be quite different. One the one hand, bosonic bunching is independent of temperature as it is a consequence of the Bose statistics. Figure 4.11 illustrates a previous experiment of our team in which the bunching amplitude $g_N^{(2)}(0) - 1$ of lattice bosons was measured for various temperatures across the condensation transition [146]. Starting from the lowest

temperature, the gas is gradually heated up by holding it at the final amplitude of the 3D lattice for an increasing duration. Such heating is attributed to imperfections of the optical lattice, such as spontaneous emission or mechanical vibrations, and is reproducible. All the measurements are compatible with $g_N^{(2)}(0) = 2$. Below the critical temperature T_{BEC}, this perfectly contrasted amplitude is attributed to a bunching of both the thermal and quantum depletion, while above T_{BEC} it consists in the classical HBT bunching of thermal bosons.

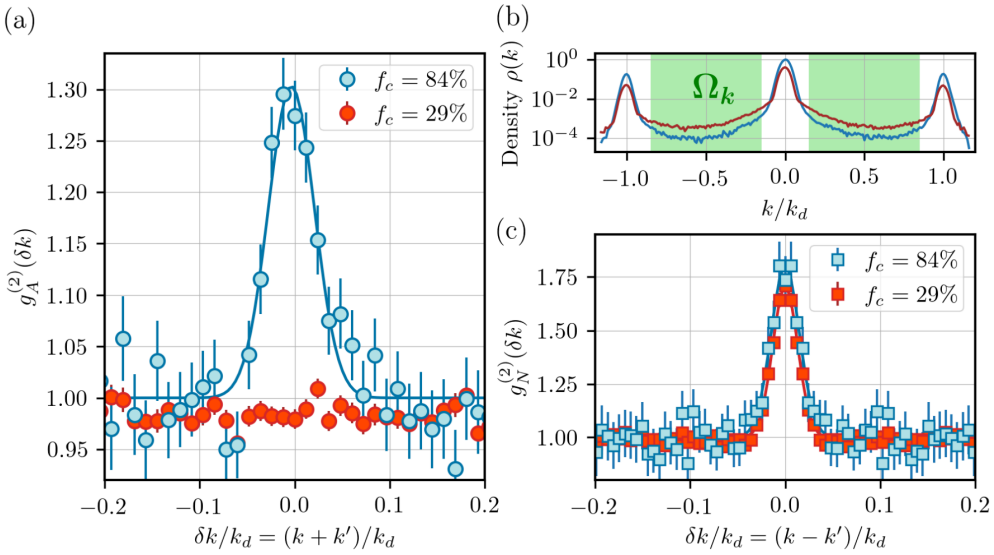

Figure 4.12: **Atom-atom correlations in weakly-interacting BECs at two different temperatures.** The data for the low-temperature ($f_c = 84\%$) and heated ($f_c = 29\%$) BECs are depicted respectively in blue and red. (a) Anomalous correlations $g_A^{(2)}(\boldsymbol{\delta k})$. The $\boldsymbol{k}$/-$\boldsymbol{k}$ peak disappears as the temperature increases, suggesting a $T = 0$ effect. (b) 1D cut of the momentum density $\rho(\boldsymbol{k})$ in semilog scale. The depletion density of the heated BEC is around 4 times larger than that of the low-temperature BEC. According to Equation 4.22, this increase implies a reduction of $g_A^{(2)}(\boldsymbol{\delta k})$ for the heated BEC by a factor 16, which is compatible with the one observed experimentally. The green shaded area shows the integration volume Ω_k over which the correlations are calculated. (c) Normal correlations $g_N^{(2)}(\boldsymbol{\delta k})$ for the same datasets and integration volume. The peak amplitude shows no significant change as the temperature increases, as expected since all depleted particles bunch (see text). All amplitudes shown here are not corrected from the transverse integration effect.

On the other hand, anomalous correlations reflects a zero-temperature feature originating from the interplay between quantum fluctuations and interactions in the many-body ground state of the system [211]. As the cloud is heated up, the $\boldsymbol{k}$/-$\boldsymbol{k}$ pairs are overwhelmed by the increasing number of thermally depleted atoms, and the anomalous correlation signal is expected to disappear. To test this hypothesis, we cannot use the datasets of Figure 4.11 as they were taken with a low transfer efficiency for which no $\boldsymbol{k}$/-$\boldsymbol{k}$ signal could be seen even at low temperature. Therefore, we took a new dataset where the atoms were hold during 500 ms in the optical lattice, a duration corresponding to 225 tunnelling times h/J. The higher temperature between this dataset and the previous one is visible in the momentum density cut in Figure 4.12. The amplitude of the diffraction peaks has decreased while the density level in the depletion has increased by roughly a

factor four. The condensed fraction for this heated dataset is about 29% (it has to be non-zero to keep quantum depleted atoms), and the correlation measurement is reproduced identically for both the normal and the anomalous correlation. As expected, we obtain that the normal correlation signal is identical between the two datasets. In contrast, the anomalous correlation signal has totally disappeared in the heated case. The reduced error bars for the heated dataset result from the larger number of (thermally) depleted atoms. These contrasted behaviors strongly suggest that the anomalous correlation signal is a $T = 0$ feature. To corroborate this conclusion, we took a third dataset at intermediate temperature (corresponding to a condensed fraction of 55%) for which an anomalous correlation peak of intermediate amplitude was observed (see Figure 4.13).

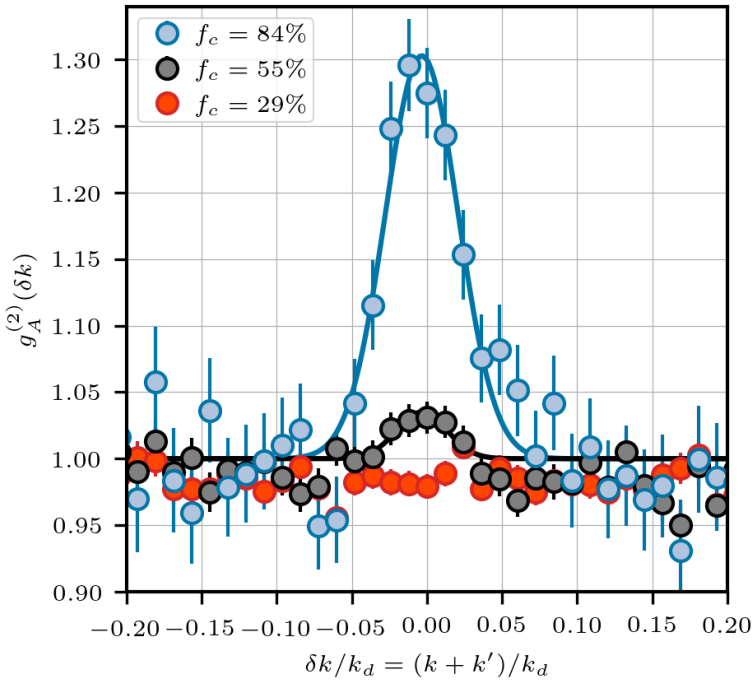

Figure 4.13: **Anomalous correlation function for datasets with different temperatures and condensed fractions.** The amplitude of the ***k*/-*k*** correlation signal is progressively lost as the temperature rises and the condensed fraction diminishes.

4.3.4 Comparison of the widths and center-of-mass fluctuations

To gain further insights into the origin of the anomalous signal, we extend the comparison with the normal correlations to the widths of the associated correlations peaks. In their experiment, Hanbury-Brown and Twiss deduced the angular size of Sirius from the width of the bunching peak [189]. In our case, the width of the two-body correlation function is inversely proportional to the spatial extent of the associated component in the trap [146, 217], which can be used to confirm the quantum origin of the anomalous correlation signal. Indeed, the in-trap spatial extent of the quantum depletion is limited by definition to that of the BEC. As shown by the authors of [217], this property remains valid even in the presence of an external harmonic confinement as in our experiment. Therefore, finding a width of the anomalous peak compatible with the momentum width of the BEC would confirm the origin of these ***k*/-*k*** correlations. In a similar way, we already argued that

both the atoms from the quantum and the thermal depletion contribute to the bunching signal. As the thermal depletion extends on a wider range than the BEC in the trap, the width of the normal correlations is expected to be smaller than that of the BEC, and consequently with that of the anomalous peak.

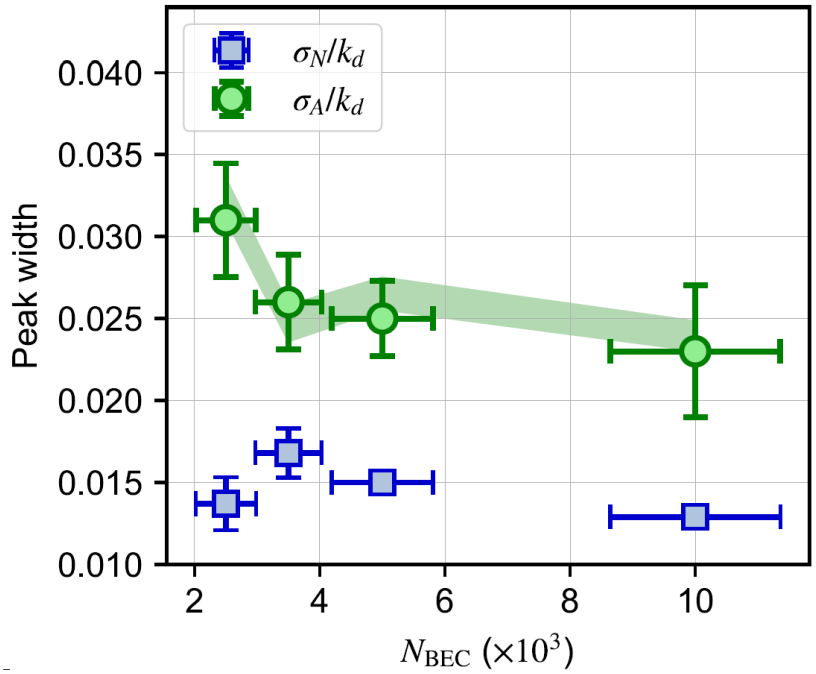

Figure 4.14: **Correlations widths versus the BEC atom number N_{BEC}.** The peak RMS widths of the normal correlations σ_N are represented as blue squares and the anomalous ones σ_A as green circles. The green area represents the expected value of Equation 4.31 based on our estimation of the center-of-mass shot-to-shot fluctuations $\boldsymbol{\delta k}_{com}$ (see text).

The RMS widths of the anomalous (σ_A) and normal (σ_N) correlations peaks are plotted in Figure 4.14 for all the datasets with different atom numbers. The horizontal error bars correspond to the standard deviation of the total atom number, while the vertical error bars corresponds to the standard deviation of the mean over the three 1D cuts of the width along the lattice axis. With this first analysis we always find that $\sigma_N < \sigma_A$ as we would expect from the previous picture. One would also expect σ_A to decrease with the atom number. In the Thomas-Fermi regime, the scaling $L_{BEC} \propto N_{BEC}^{1/5}$ translates into a 30% diminution of the width between the datasets at $N_{BEC} = 2.5 \times 10^3$ and $N_{BEC} = 10 \times 10^3$. Although a decrease of the anomalous width with N_{BEC} is observed, the error bars in Figure 4.14 are too large to reach such conclusion. Additionally, we find that the measured BEC widths (not plotted) are always larger than the ones expected from the Gutzwiller prediction. We attribute this observation to an imperfection of our experiment: the center-of-mass fluctuations from shot to shot of the momentum distributions. To correct this effect, each experimental distribution is manually centered on $\boldsymbol{k} = \boldsymbol{0}$ by fitting the zeroth order diffraction peak with a Gaussian function. However, some residual center-of-mass fluctuations may remain after this centering procedure, explaining the larger BEC widths observed. These fluctuations should then also be reported in the estimation of the correlation width.

If we note $\sigma_{BEC,0}$ the true momentum width of the BEC, the one measured after averaging the signal of all the distributions is enlarged by the center-of-mass fluctuations $\boldsymbol{\delta k}_{com}$ according to:

$$\sigma_{BEC} = \sqrt{\sigma_{BEC,0}^2 + \delta k_{com}^2} \tag{4.29}$$

with $\delta k_{com}^2 = \langle |\boldsymbol{\delta k}_{com}|^2 \rangle$. In a similar way, these center-of-mass fluctuations enlarge the width of the anomalous correlation function. Because the sum of the momenta of two displaced atoms is increased by twice the amount δk_{com}:

$$(\boldsymbol{k} + \boldsymbol{\delta k}_{com}) + (\boldsymbol{k'} + \boldsymbol{\delta k}_{com}) = \boldsymbol{k} + \boldsymbol{k'} + 2\boldsymbol{\delta k}_{com} \tag{4.30}$$

the width of the anomalous correlation peak becomes:

$$\sigma_A = \sqrt{\sigma_{A,0}^2 + 4\delta k_{com}^2} \tag{4.31}$$

On the opposite, it is straightforward to see that $\boldsymbol{\delta k}_{com}$ does not affect the width of the normal correlation peak as the momentum difference of two displaced atoms remains unchanged. The amplitude of the fluctuations $\boldsymbol{\delta k}_{com}$ can be estimated from Equation 4.29. For $N_{BEC} = 5 \times 10^3$, we measured a BEC width of $\sigma_{BEC} \simeq 2.00(4) \times 10^{-2} k_d$. Note that the measurement of the BEC width requires drastically reducing the Raman transfer efficiency to avoid saturating the detector. Otherwise, saturation would flatten the top of the BEC peak, and the Gaussian fit would over-estimate the condensate width σ_{BEC}. Using the Gutzwiller prediction for this atom number, $\sigma_{BEC,0} \simeq 1.7 \times 10^{-2} k_d$, we estimate the center-of-mass fluctuations to be $\delta k_{com} \simeq 1.05(2) \times 10^{-2} k_d$. These fluctuations, which amount to 1% of the separation between the BEC diffraction peaks, are too small to be corrected in post-analysis. We repeated this procedure for all datasets and plotted the theoretical anomalous width of equation 4.31 in Figure 4.14 as a green shaded area. We used for that the theoretical value $\sigma_{A,0} \simeq 0.94\,\sigma_{BEC,0}$ of reference [217], valid for an inhomogeneous 1D system with the same external trapping frequency as ours. We find a good agreement between the experimental widths and the theoretical predictions when accounting for the center-of-mass fluctuations, which is coherent with the hypothesis that the anomalous signal comes from the atom pairs of the quantum depletion. However, we cannot conclude that the anomalous signal is larger than the normal one when comparing the corrected anomalous widths $\sigma_{A,0}$ to the normal ones (Figure 4.15). We conclude from this observation that the temperature is too low for the in-trap extent of the thermal cloud to exceed that of the BEC in a way that the correlation widths can resolve.

4.3.5 Effect of the mode population

In this paragraph we discuss the analogy between the $\boldsymbol{k}$/$\boldsymbol{-k}$ pairs and the emblematic signal and idler modes of the non-degenerate parametric amplifier in Quantum Optics. Theses two modes, labeled as modes 1 and 2 in the following, are populated by correlated pairs of photons just like our modes $\boldsymbol{k}$ and $\boldsymbol{-k}$ are populated by correlated pairs of atoms. However, let us stress that this analogy is incomplete for at least two reasons:

- the pair of photons in the case of Quantum Optics results from a spontaneous parametric down conversion (SPDC) process or a four wave mixing (FWM) process in which the interaction between one or two pump photon(s) and a non-linear medium leads to the creation of a correlated photon pair. Contrary to the Bogoliubov pairs, the SPDC and FWM can be described as a classical interaction process in which both momentum and energy are conserved.

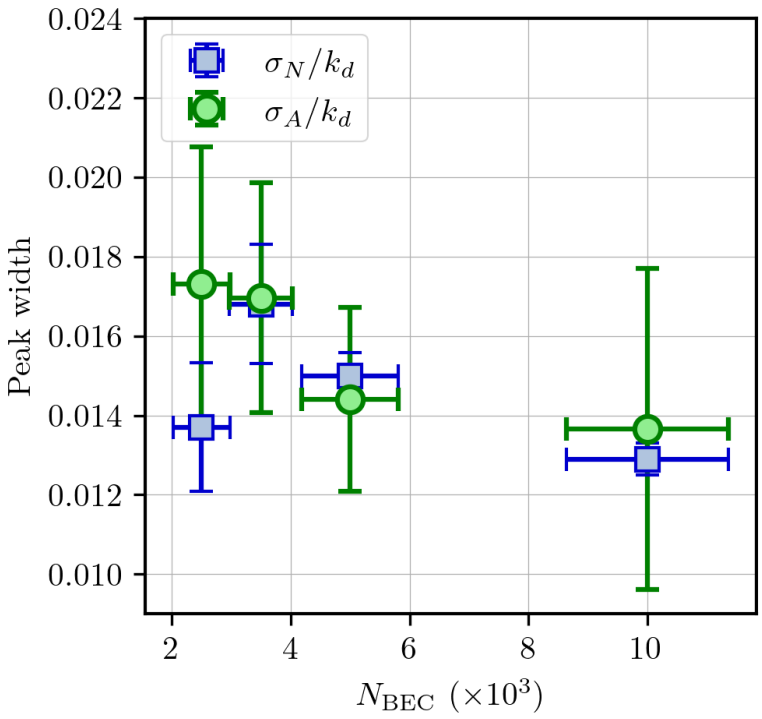

Figure 4.15: **Correlations widths versus the BEC atom number N_{BEC}.** Anomalous (green circles) and normal (blue squares) RMS widths corrected from the center-of-mass shot-to-shot fluctuations δk_{com}. Both measurements cannot be distinguished any more within the error bars, indicating that the temperature might be too low to have a clear distinction between the thermal and the condensed cloud in the trap.

- the two modes signal and idler are exclusively populated by pairs of photons resulting for the SPDC/FWM process. Therefore, the number of photons in those two modes are equal and perfectly correlated. Because we work at finite temperature, this is not the case for the modes $\boldsymbol{k}$ and $\boldsymbol{-k}$ which can be populated by either $\boldsymbol{k}$/$\boldsymbol{-k}$ pairs or thermally depleted atoms. We thus expect the amplitude of the anomalous correlations in our case to be reduced by the presence of these uncorrelated atoms.

The Hamiltonian of the non-degenerate parametric amplifier can be written as [221]:

$$\hat{H} = \hbar\omega_1 \hat{a}_1^\dagger \hat{a}_1 + \hbar\omega_2 \hat{a}_2^\dagger \hat{a}_2 + i\hbar\chi \left(\hat{a}_1^\dagger \hat{a}_2^\dagger e^{-2gi\omega t} - \hat{a}_1 \hat{a}_2 e^{2i\omega t} \right) \tag{4.32}$$

where $\hat{a}_1$ ($\hat{a}_2$) annihilates a photon in the signal (idler) mode and χ is a coupling constant, associated either with a $\chi^{(2)}$ susceptibility (SPDC) or a $\chi^{(3)}$ susceptibility (FWM). Solving the Heisenberg equations of motion in the interaction picture leads to the coupled equations:

$$\hat{a}_1(t) = \hat{a}_1(0)\cosh\chi t + \hat{a}_2^\dagger(0)\sinh\chi t \tag{4.33}$$

$$\hat{a}_2(t) = \hat{a}_2(0)\cosh\chi t + \hat{a}_1^\dagger(0)\sinh\chi t \tag{4.34}$$

from which we can derive the amplitude of the normalized cross-correlations between modes 1 and 2 (using Wick's theorem and initial vacuum conditions):

$$\begin{aligned} g^{(2)}(1,2) &= \frac{\langle \hat{a}_1^\dagger \hat{a}_2^\dagger \hat{a}_1 \hat{a}_2 \rangle}{\langle \hat{a}_1^\dagger \hat{a}_1 \rangle \langle \hat{a}_2^\dagger \hat{a}_2 \rangle} \\ &= \frac{\langle \hat{a}_1^\dagger \hat{a}_2^\dagger \rangle \langle \hat{a}_1 \hat{a}_2 \rangle + \langle \hat{a}_1^\dagger \hat{a}_1 \rangle \langle \hat{a}_2^\dagger \hat{a}_2 \rangle + \langle \hat{a}_1^\dagger \hat{a}_2 \rangle \langle \hat{a}_2^\dagger \hat{a}_1 \rangle}{\langle \hat{a}_1^\dagger \hat{a}_1 \rangle \langle \hat{a}_2^\dagger \hat{a}_2 \rangle} \\ &= 1 + \frac{\cosh^2(\chi t) \sinh^2(\chi t)}{\sinh^4(\chi t)} \\ &= 1 + \frac{\left(1 + \sinh^2(\chi t)\right) \sinh^2(\chi t)}{\sinh^4(\chi t)} \\ &= 2 + \frac{1}{\langle \hat{n}_1(t) \rangle} \end{aligned} \tag{4.35}$$

We see that the amplitude of the cross-correlation for the non-degenerate parametric amplifier scales inversely with the average mode occupancy, a general property of two-mode vacuum squeezed states [222]. Therefore, it would be interesting to test whether our anomalous correlation signal follows a similar scaling. To that end, the average mode occupancy must be varied. In our case, it corresponds to the average momentum density $\rho(\boldsymbol{k}) = \langle \hat{a}_{\boldsymbol{k}}^\dagger \hat{a}_{\boldsymbol{k}} \rangle$ in the integration volume Ω_k:

$$\bar{\rho}_{\Omega_k} = \int_{\Omega_k} \rho(\boldsymbol{k}) d\boldsymbol{k} \tag{4.36}$$

which can be changed easily by repeating the experiment with a different atom number in the BEC. For this purpose, we took two additional datasets at $N_{BEC} = 2.5 \times 10^3$ and $N_{BEC} = 10 \times 10^3$. By changing the post-selection criterion, we could also extract from the dataset originally intended for $N_{BEC} = 2.5 \times 10^3$ a fourth dataset corresponding to $N_{BEC} = 3.5 \times 10^3$. For the datasets at $N_{BEC} = 2.5 \times 10^3$, the integration volume Ω_k was reduced to the momenta $0.3\, k_d \leq |k_{x,y,z}| \leq 0.7\, kd$ to further decrease the average density $\bar{\rho}_{\Omega_k}$. The normal and anomalous correlation amplitudes (corrected from the integration effect) for these new datasets are plotted in Figure 4.16.

While the normal amplitude remains compatible with $g_N^{(2)}(0) = 2$, the anomalous amplitude is found to vary inversely with the average momentum density, with a scaling compatible with a linear one. Observing such an analogous scaling to two-mode squeezed states suggests that the anomalous signal comes from a pair creation term in the Hamiltonian, as predicted by Bogoliubov's theory. It is thus another strong indication that we are indeed measuring the Bogoliubov pairs. Note that our anomalous correlation signal is compatible with $g_A^{(2)}(0) = 1$ when the average density goes to infinity, whereas in this limit the cross-correlations amplitude of equation 4.35 is predicted to reach $g(1,2) = 2$. We attribute this discrepancy to be an effect of the thermal depletion in our experiment. In the limiting case of zero temperature, for which the modes $\boldsymbol{k}$ and $\boldsymbol{-k}$ are only populated by correlated atom pairs according to Bogoliubov theory, we would expect the value $g_A^{(2)}(0) = 2$ as for the Quantum Optics case. In the opposite limit of high temperature where the thermal depletion overwhelm the quantum depletion, we found in the previous paragraph $g_A^{(2)}(0) = 1$. Therefore, we can infer that for intermediate temperature, the anomalous correlations amplitude in the limit of infinite average density is a number between 1 and 2 whose value depends on the balance between the quantum and the thermal

depletions. As explained below, these two contributions are highly unbalanced for the atoms inside Ω_k with which anomalous correlations are computed.

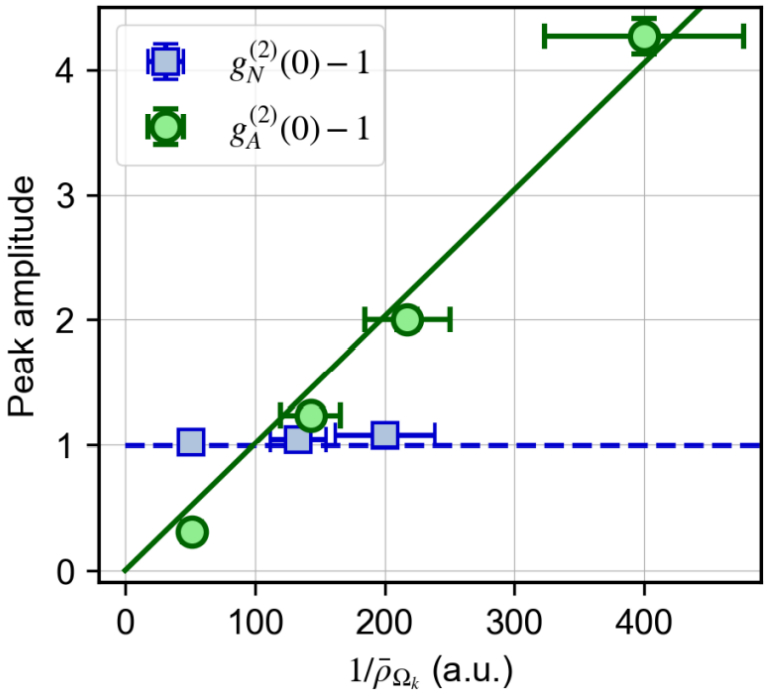

Figure 4.16: **Correlations amplitudes versus the inverse density $1/\bar{\rho}_{\Omega_k}$.** The normal correlations amplitudes $g_N^{(2)}(0)$ are represented as blue squares and the anomalous ones $g_A^{(2)}(0)$ as green circles. All are corrected from the transverse integration effect. While the amplitude of the bunching is perfectly contrasted and constant, $g_N^{(2)}(0) = 2$, the amplitude of the $\boldsymbol{k}$/-$\boldsymbol{k}$ peak increases linearly with $1/\bar{\rho}_{\Omega_k}$. Vertical error bars are mostly hidden behind the symbols and correspond to the standard deviation of the mean over the three lattice directions of the momentum space. Horizontal error bars correspond to one standard deviation and increase with $1/\bar{\rho}_{\Omega_k}$ as the statistics inside the voxels decreases.

The mean number of $\boldsymbol{k}$/-$\boldsymbol{k}$ pairs per shot $\langle N_{pairs}^{k/-k}\rangle$ can be estimated by subtracting the mean number of counts between the numerator and the denominator histograms for the voxels within a volume $(\delta k)^3$ large enough to contain the entire correlation peak. Denoting these numbers $\langle N_{num}\rangle$ and $\langle N_{den}\rangle$, the mean number of pairs per file writes:

$$2\langle N_{pairs}^{k/-k}\rangle = \left(\langle N_{num}\rangle - \langle N_{den}\rangle \times \frac{\sum_i N_i(N_i-1)}{(\sum_i N_i)\,(\sum_i N_i - 1)}\right) \tag{4.37}$$

where the normalization factor $\sum_i N_i(N_i-1)/\,(\sum_i N_i)\,(\sum_i N_i - 1)$ ensures that the *total* number of counts in both histograms is equal (see Section 4.2.4). The factor 2 is here because the correlation algorithm is computed on all post-selected atoms, meaning that each possible pair of atoms is counted twice. For the dataset at $N_{BEC} = 5\times10^3$ we find in average $\langle N_{pairs}^{k/-k}\rangle = 1$ per shot, while the mean atom number in Ω_k for this dataset is $\langle N_{\Omega_k}\rangle \simeq 50$. We thus expect to be closer to the high-temperature limiting case than to the $T = 0$ one, explaining the zero intercept in Figure 4.16.

We should comment here on the mean number of pairs $\langle N_{pairs}^{k/-k}\rangle$ detected in the integration volume Ω_k. Under the assumption that all atoms from the quantum depletion form

$\boldsymbol{k}$/-$\boldsymbol{k}$ pairs, and that these pairs are the only contribution to the anomalous correlations, $\langle N_{pairs}^{k/-k}\rangle$ should be linked to $\langle N_{\Omega_k}\rangle$ through the relation:

$$2\langle N_{pairs}^{k/-k}\rangle = \langle N_{\Omega_k}\rangle \eta_{MCP}\, \alpha_Q \tag{4.38}$$

where α_Q is the proportion of the depletion which is quantum. The additional factor η_{MCP} (a first one being already hidden in $\langle N_{\Omega_k}\rangle$) illustrates that the detection efficiency of the MCP has to be counted twice when considering the joint detection of two atoms of the same pair. With our experimental numbers, we obtain $\alpha_Q \simeq 3.8\%$. The same quantity can be estimated thanks to the $T = 0$ Gutzwiller approach that predicts 5% of quantum depletion at this lattice amplitude for $N_{BEC} = 5 \times 10^3$. Having measured a condensed fraction of $\sim$ 85%, the total depletion corresponds to 15% and the thermal depletion should amount to 10% according to Gutzwiller's prediction for the quantum depletion. Therefore, the proportion of the total depletion that is quantum should be $\alpha_Q \simeq 33\%$, which is one order of magnitude larger than the estimation based on the mean number of pairs per file. There are at least two possible reasons for such discrepancy:

- the distribution of the quantum depleted atoms $|v_{\boldsymbol{k}}|^2$ being the largest in the limit of small momenta $k \to 0$, a non-negligible fraction of the $\boldsymbol{k}$/-$\boldsymbol{k}$ pairs should be located inside the volume of the zeroth order diffraction peak that we exclude in our analysis. We lack a theoretical prediction to estimate the number of pairs missed that way.
- due to the choice of the integration volume Ω_k, the detected $\boldsymbol{k}$/-$\boldsymbol{k}$ pairs are mostly located close to the edge of the first Brillouin zone where the dispersion relation in the presence of a lattice flattens and becomes quite different from the parabolic one of the homogeneous case. Here as well we miss of a quantitative estimate of this effect.

To conclude on this topic, our anomalous correlation signal follows the linear scaling with the inverse momentum density expected from the analogy with the non-degenerate parametric amplifier. Therefore, this feature represents an additional signature of the quantum origin of our anomalous signal, suggesting that we are indeed detecting the Bogoliubov pairs. However, the absence of a theory designed for our system of inhomogeneous lattice bosons at finite temperature prevents us from a quantitative comparison of our results. In particular, it prevents us from fully understanding the discrepancies of the absolute amplitude of the correlation signal and of the total number of pairs detected.

4.3.6 Cauchy-Schwarz inequality and entanglement

As a final remark on the amplitude of the correlation signal, we stress that observing an anomalous amplitude higher than a normal one represents a violation of the Cauchy-Schwarz inequality for classically fluctuating variables. Indeed, the cross-fluctuations between two classical variables I_1 and I_2 is bounded by the well-know Cauchy-Scharwz inequality:

$$\langle I_1 I_2\rangle \leq \sqrt{\langle I_1^2\rangle\langle I_2^2\rangle} \tag{4.39}$$

Its counter part in quantum mechanics is expressed in terms of creation and annihilation operators. Considering the case of two symmetric modes, such as the signal and idler modes of the SPDC, the Cauchy-Schwarz inequality becomes [221]:

$$\langle \hat{a}_1^\dagger \hat{a}_1 \hat{a}_2^\dagger \hat{a}_2\rangle \leq \langle \hat{a}_1^\dagger \hat{a}_1^\dagger \hat{a}_1 \hat{a}_1\rangle \tag{4.40}$$

Normalizing Equation 4.40 leads to:

$$\begin{aligned} \frac{\langle \hat{a}_1^\dagger \hat{a}_1 \hat{a}_2^\dagger \hat{a}_2 \rangle^2}{\langle \hat{a}_1^\dagger \hat{a}_1 \rangle^2 \langle \hat{a}_2^\dagger \hat{a}_2 \rangle^2} &\leq \frac{\langle \hat{a}_1^\dagger \hat{a}_1^\dagger \hat{a}_1 \hat{a}_1 \rangle \langle \hat{a}_2^\dagger \hat{a}_2^\dagger \hat{a}_2 \hat{a}_2 \rangle}{\langle \hat{a}_1^\dagger \hat{a}_1 \rangle^2 \langle \hat{a}_2^\dagger \hat{a}_2 \rangle^2} \\ g^{(2)}(1,2)^2 &\leq g^{(2)}(1,1)\, g^{(2)}(2,2) \end{aligned} \tag{4.41}$$

which for our weakly interacting Bose gas translates into:

$$g_A^{(2)}(0) \leq g_N^{(2)}(0) \tag{4.42}$$

Therefore, three experimental points in Figure 4.16 exhibit a clear violation of the Cauchy-Schwarz inequality, with a maximum violation of $5.27(8) > 2.09(5)$. This observation is analog to what was reported with photons for the spontaneous parametric down conversion [223].

4.3.7 Relative number squeezing

The presence of $\boldsymbol{k}$/-$\boldsymbol{k}$ pairs in the depletion should come along with reduced relative fluctuations of the occupation numbers $N_{\boldsymbol{k}}$ and $N_{-\boldsymbol{k}}$ between modes at opposite momenta. This feature is referred to as relative number squeezing, in analogy with regular squeezing defined as the reduced fluctuations of an operator at the expense of stronger fluctuations of its conjugate operator [221]. If our experiment were performed at $T = 0$, all the modes in the depletion would be populated by $\boldsymbol{k}$/-$\boldsymbol{k}$ pairs. $N_{\boldsymbol{k}}$ and $N_{-\boldsymbol{k}}$ would then be equal for all $\boldsymbol{k}$ and the atom number difference between these two modes would always be zero. At finite temperature, each mode $\boldsymbol{k}$ is mostly populated by uncorrelated thermal atoms and the statistics of $N_{\boldsymbol{k}}$ is Poissonian because of the shot-noise. Still, the effect of the Bogoliubov pairs might be visible in the statistics of the atom number difference between two modes $\boldsymbol{k}$ and $\boldsymbol{k}'$. For uncorrelated modes, such that $\boldsymbol{k}' \neq -\boldsymbol{k}$, we expect the variance and the mean value of this atom number difference to be equal:

$$\sigma^2_{N_{\boldsymbol{k}} - N_{\boldsymbol{k}'}} \equiv \langle (N_{\boldsymbol{k}} - N_{\boldsymbol{k}'})^2 \rangle - \langle N_{\boldsymbol{k}} - N_{\boldsymbol{k}'} \rangle^2 = \langle N_{\boldsymbol{k}} - N_{\boldsymbol{k}'} \rangle \tag{4.43}$$

because the difference of two Poissonian variable is Poissonian as well. However, the $\boldsymbol{k}$/-$\boldsymbol{k}$ pairs should reduce these fluctuations when probing the two modes $\boldsymbol{k}$ and $\boldsymbol{k}' = -\boldsymbol{k}$, leading to sub-Poissonian statistics of the atom number difference in this case. As for the anomalous correlations amplitude, the temperature has to be low enough for the effect of the $\boldsymbol{k}$/-$\boldsymbol{k}$ pairs to be visible.

To detect this signal, we use a squeezing parameter ξ defined as:

$$\xi^2_{\boldsymbol{k},\boldsymbol{k}'} = \frac{\langle (N_{\boldsymbol{k}} - N_{\boldsymbol{k}'})^2 \rangle - \langle N_{\boldsymbol{k}} - N_{\boldsymbol{k}'} \rangle^2}{\langle N_{\boldsymbol{k}} \rangle + \langle N_{\boldsymbol{k}'} \rangle} \tag{4.44}$$

With this definition, $\xi^2_{\boldsymbol{k},\boldsymbol{k}'}$ corresponds to the variance of the atom number difference between modes $\boldsymbol{k}$ and $\boldsymbol{k}'$ normalized by its expectation value if the two modes are uncorrelated. It thus gives $\xi^2_{\boldsymbol{k},\boldsymbol{k}'} = 1$ for uncorrelated modes and $\xi^2_{\boldsymbol{k},\boldsymbol{k}'} < 1$ for sub-Poissonian fluctuations of the atom number difference between the two modes. The procedure to compute this squeezing parameter is represented in Figure 4.17. The first step consists in dividing the integration volume Ω_k into big voxels of volume $(0.3\, k_d)^3$. The voxel size is chosen to be much bigger than the size of a single mode (of the order of σ_N) to increase

the signal. Similarly to the correlation algorithm, the grid of voxels is centered on the origin, so that all the atoms from the zeroth order diffraction peak are contained within a "central" voxel (in black). As represented in Figure 4.17, this voxel is excluded for the analysis and the squeezing parameter $\xi^2_{\boldsymbol{k},\boldsymbol{k}'}$ is computed with the remaining ones for all correlated (orange) or uncorrelated (blue) configurations.

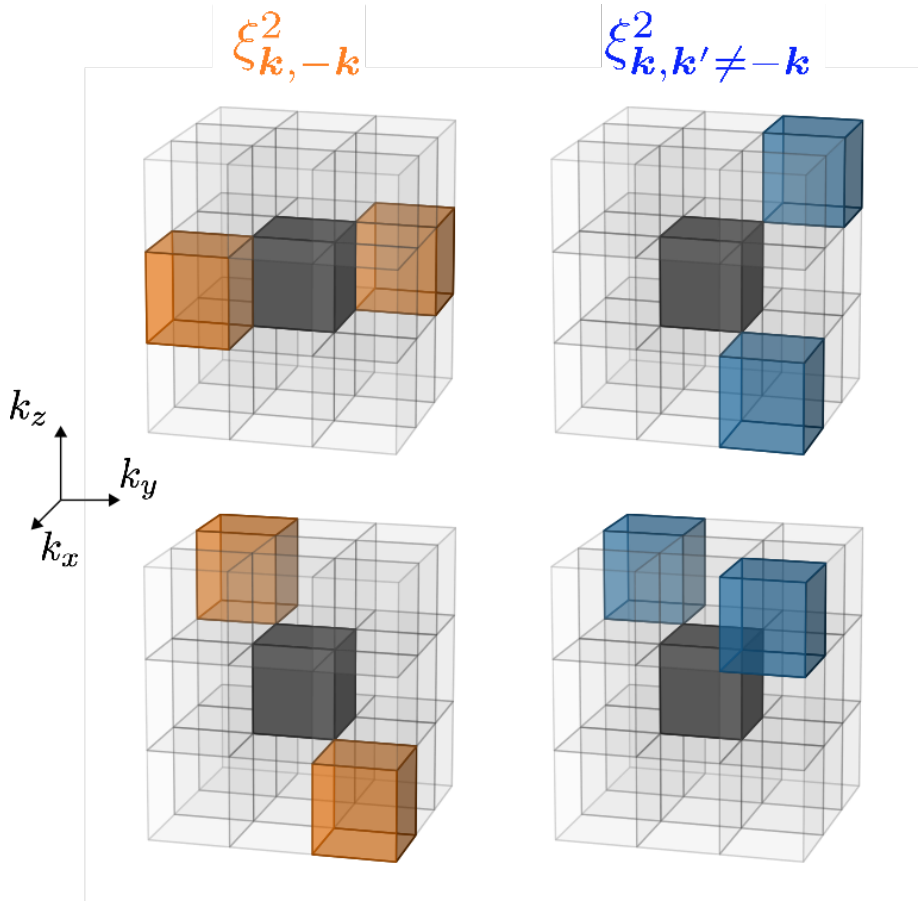

Figure 4.17: **Procedure for detecting relative number squeezing.** Illustration of the momentum-space volumes used to compute the normalized variance $\xi^2_{\boldsymbol{k},\boldsymbol{k}'}$ of Equation 4.44. The BEC is contained in the black voxel centered on $\boldsymbol{k} = \boldsymbol{0}$. The considered voxels are either located at opposite momenta $\boldsymbol{k}$/$\boldsymbol{-k}$ (orange) to compute $\xi^2_{\boldsymbol{k},-\boldsymbol{k}}$ or at random positions such that $\boldsymbol{k}' \neq -\boldsymbol{k}$ to compute $\xi^2_{\boldsymbol{k},\boldsymbol{k}'\neq-\boldsymbol{k}}$ (blue) regions. The values $\xi^2_{\boldsymbol{k},\boldsymbol{k}'}$ are obtained from averaging over all couples of voxels spanning the entire integration volume Ω_k.

The average values of the distributions of the ξ^2 in the uncorrelated and correlated case are plotted in Figure 4.18 for all datasets, with the error bars defined as the standard deviation. Relative number squeezing is observed on the coldest dataset (higher condensed fraction) for which $\xi^2_{\boldsymbol{k},-\boldsymbol{k}} < 1$. Finding for the same dataset a number squeezing slightly above one in the uncorrelated case confirms this measurement. The amplitude of this number squeezing is small compared to what has been reported with discrete (spins) variable systems [25, 224, 225], being limited in our case by the thermally depleted atoms and the detection efficiency. As expected, the relative number squeezing disappears at higher temperatures where we find $\xi^2_{\boldsymbol{k},-\boldsymbol{k}} \simeq \xi^2_{\boldsymbol{k},\boldsymbol{k}'\neq-\boldsymbol{k}}$ within the error bars. The increase of ξ^2 above one in these cases is due to a larger contribution of the total atom number fluctua-

tions. Those add a contribution proportional to $\langle N_{\boldsymbol{k}} \rangle^2$ to the variance of the atom number difference, contrary to the Poisson law whose variance scales as $\langle N_{\boldsymbol{k}} \rangle$. This contribution is negligible as long as the condensed fraction is high, while this is not the case anymore at higher temperature due to the increase of $\langle N_{\boldsymbol{k}} \rangle$.

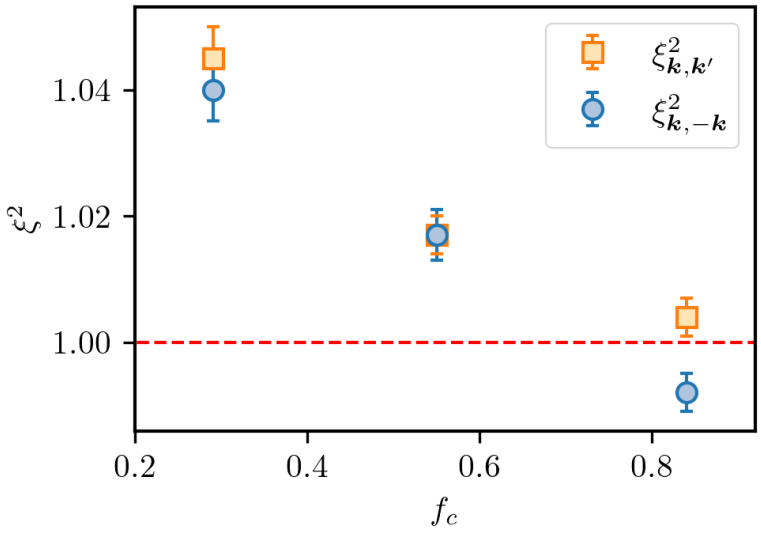

Figure 4.18: **Relative number squeezing results.** Measured values $\xi^2_{\boldsymbol{k},\boldsymbol{k}'}$ for correlated and uncorrelated voxels, and for different values of the condensed fraction f_c. Error bars correspond to one standard error. A small relative number squeezing is observed in the low-temperature data, where $\xi^2_{\boldsymbol{k},-\boldsymbol{k}} < \xi^2_{\boldsymbol{k},\boldsymbol{k}'\neq-\boldsymbol{k}} \simeq 1$. At higher temperatures, no relative number squeezing is visible.

4.3.8 Conclusion of this first part

In the first part of this chapter we have demonstrated the presence of correlations at opposite momenta in the depletion of interacting Bose gases. We verified the quantum nature of these anomalous correlations thanks to several observations:

- their disappearance on increasing the temperature, suggesting a T=0 effect;
- the linear scaling of the their amplitude with respect to the inverse of the average density, in analogy with the two-mode squeezed states produced in Spontaneous Parametric Down Conversion or Four Wave Mixing;
- the violation of the Cauchy-Schwarz inequality for classically fluctuating variables;
- the presence of relative number squeezing induced by the reduced fluctuations of the mode occupancies between modes at opposite momenta.

All these features confirm that the anomalous correlations indeed originate from the presence of pairs of atoms at opposite momenta in the many-body ground state, validating the prediction made by Bogoliubov over 70 years ago. This measurement required the single-atom-resolved detection offered by the ^{4}He* atoms and a 3D optical lattice to enhance the in-trap interactions and make the expansion ballistic. Comparing our results with predictions would require a theory that takes into account: the modified dispersion relation in the lattice, the external confinement induced by the Gaussian beams, the finite temperature, and the fact that we work in 3D. To our knowledge, these constraints are

beyond state-of-the-art computations of second-order correlations.

An interesting perspective for the future would be to further exploit the violation of the Cauchy-Schwarz inequality in order to look for the presence of entanglement in our system. In the context of analogous Hawking radiation [226, 227], the Busch-Parentani criterion [228] states that any two-mode system violating the Cauchy-Schwarz inequality is non-separable, providing that the statistics of the system is chaotic and that no cross-correlations exist between the modes. We have experimentally verified the first condition by finding a perfect bunching amplitude $g_N^{(2)}(0) = 2$. The second condition $\langle \hat{a}_{\boldsymbol{k}}^\dagger \hat{a}_{-\boldsymbol{k}} \rangle = 0$ is fulfilled within Bogoliubov theory and the assumption that it should be valid in our system is therefore reasonable. Thus, we are close to being able to prove the presence of entanglement in the continuous variable $\boldsymbol{k}$ in our system. All that is left is the experimental confirmation of $\langle \hat{a}_{\boldsymbol{k}}^\dagger \hat{a}_{-\boldsymbol{k}} \rangle = 0$. In principle, this correlator could be measured with atom interferometry [40, 229, 230] using Bragg diffraction [231] to produce the required mirrors and beam splitters. This measurement is not immediately feasible because Bragg beams would first have to be implemented, but it may be possible in the near future. Having confirmed the presence of Bogoliubov pairs in the depletion of interacting Bose gases, an exciting and readily achievable prospect is to extend this measurement to stronger interaction regimes. The second part of this chapter details our work on this aspect, which is still an on-going study.

4.4 Increasing the interaction strength

Coming back to the context in which Bogoliubov developed his theory, the original goal was to understand the emergence of superfluid properties in liquid Helium at low-temperature [194, 195]. Bogoliubov successfully explained this phenomenon using the theoretical framework of degenerate Bose gases, for which the description of interactions between the particles is much simpler than for liquids. The approximation of weak interactions allowed him to diagonalized the Hamiltonian of the system and find its excitation spectrum, the phononic part of which verifies the Landau criterion for superfluidity [196]. However, measurements of the condensed fraction in liquid Helium using neutron scattering have converged towards a value of the order of 10% [232–234]. Therefore, the case of liquid Helium is way beyond the validity regime of the Bogoliubov approximation which requires that the condensed fraction should remain close to unity. Interestingly, this theory does not apply to the system for which it was originally designed, and it is natural to ask what happens to its predictions under stronger interactions. Momentum correlations at opposite momenta are rooted within Bogoliubov's theory and are thus a natural candidate to try answering this question. The first part of this chapter highlighted the microscopic description of the many-body ground state provided by the anomalous signal. As explained below, these correlations also ought to contain characteristic signatures of the system becoming strongly correlated, and revealing them is the goal of this second part.

4.4.1 Predictions of Bogoliubov's theory

As aforementioned, an extension of the Bogoliubov theory for 3D lattice bosons at finite temperature and in the presence of an harmonic trap does not exist to our knowledge. To get some insights on how our anomalous signal should evolves when interactions are

increased, we rely on the prediction for a 1D system of homogeneous bosons in this section. Then, the Bogoliubov coefficients $u_{\boldsymbol{k}}$ and $v_{-\boldsymbol{k}}$ (see equations 4.9 and 4.10) can be written as:

$$u_{\boldsymbol{k}} = \sqrt{\frac{1}{2}\left(\frac{1+x}{\sqrt{1+2x}}+1\right)} \tag{4.45}$$

$$v_{\boldsymbol{k}} = -\sqrt{\frac{1}{2}\left(\frac{1+x}{\sqrt{1+2x}}-1\right)} \tag{4.46}$$

where x is the ratio between the interaction energy gn_0 and the free particle energy $\hbar^2k^2/2m$. One can then derive the expressions of the anomalous part of the correlations (cf equation 4.20):

$$\begin{aligned} |\langle \hat{a}^\dagger_{\boldsymbol{k}} \hat{a}^\dagger_{-\boldsymbol{k}} \rangle|^2 &= |u_{\boldsymbol{k}} v_{\boldsymbol{k}}|^2 \left(1 + 2\langle \hat{b}^\dagger_{\boldsymbol{k}} \hat{b}_{\boldsymbol{k}} \rangle\right)^2 \\ &= \frac{x^2}{1+2x}\left(\frac{1}{2} + \langle \hat{b}^\dagger_{\boldsymbol{k}} \hat{b}_{\boldsymbol{k}} \rangle\right)^2 \end{aligned} \tag{4.47}$$

and of the momentum density:

$$\begin{aligned} \rho(\boldsymbol{k}) &= \langle \hat{a}^\dagger_{\boldsymbol{k}} \hat{a}_{\boldsymbol{k}} \rangle \\ &= |u_{\boldsymbol{k}}|^2 \langle \hat{b}^\dagger_{\boldsymbol{k}} \hat{b}_{\boldsymbol{k}} \rangle + |v_{\boldsymbol{k}}|^2 \left(1 + \langle \hat{b}^\dagger_{\boldsymbol{k}} \hat{b}_{\boldsymbol{k}} \rangle\right) \\ &= \frac{1+x}{\sqrt{1+2x}}\left(\frac{1}{2} + \langle \hat{b}^\dagger_{\boldsymbol{k}} \hat{b}_{\boldsymbol{k}} \rangle\right) - \frac{1}{2} \end{aligned} \tag{4.48}$$

The increase of $\rho(\boldsymbol{k})$ with x for any $\boldsymbol{k} \neq \boldsymbol{0}$ reflects the depletion of the condensate mode growing larger the stronger the interactions, assuming the total atom number is fixed. Similarly, the temperature effect on the depletion level is contained within $\langle \hat{b}^\dagger_{\boldsymbol{k}} \hat{b}_{\boldsymbol{k}} \rangle$. We can then derive how the normalized anomalous function, whose numerator contains both the anomalous correlations and the momentum density squared, evolves with x. In the $T = 0$ case where $\langle \hat{b}^\dagger_{\boldsymbol{k}} \hat{b}_{\boldsymbol{k}} \rangle = 0$, it takes a simple form:

$$\begin{aligned} g^{(2)}_A(\boldsymbol{k}, -\boldsymbol{k}) &= \frac{\rho(\boldsymbol{k})\rho(-\boldsymbol{k}) + |\langle \hat{a}^\dagger_{\boldsymbol{k}} \hat{a}^\dagger_{-\boldsymbol{k}} \rangle|^2}{\rho(\boldsymbol{k})\rho(-\boldsymbol{k})} \\ \Leftrightarrow g^{(2)}_A(\boldsymbol{k}, -\boldsymbol{k}) - 1 &= \frac{x^2}{\left(1 + x - \sqrt{1+2x}\right)^2} \end{aligned} \tag{4.49}$$

which is a monotonic decreasing function of x. At finite temperature, the quasi-particle population $\langle \hat{b}^\dagger_{\boldsymbol{k}} \hat{b}_{\boldsymbol{k}} \rangle$ contributes to the behavior of the anomalous amplitude $g^{(2)}_A(\boldsymbol{k}, -\boldsymbol{k}) - 1$. However, the left panel of Figure 4.19 illustrates that in the low-temperature regime $k_B T \ll \mu$, one still expects a monotonic decrease of the anomalous amplitude with the interaction strength, analogous to the $T = 0$ case. At first glance, it may seem confusing that the amplitude of the anomalous correlation decreases at stronger interactions, whereas the condensate gets more strongly depleted. However, the scaling $g^{(2)}_A(0) - 1 \propto \rho(k)$ found in the first part of the chapter corroborates this counter-intuitive result that higher depletion levels lead to smaller anomalous amplitudes. Within Bogoliubov's picture, what is expected to grow with the interaction strength is the probability for a depleted atom to belong to the quantum depletion, *i.e.* to a $\boldsymbol{k}$/$\boldsymbol{-k}$ pair. As explained in Appendix C, this probability is linked to the product of the anomalous amplitude with the mean atom

number in the integration volume $\langle N_{\Omega_k} \rangle$, or equivalently the momentum density $\rho(\boldsymbol{k})$, rather than to the anomalous amplitude alone. At $T = 0$, this product scales with x as:

$$\left(g_A^{(2)}(\boldsymbol{k}, -\boldsymbol{k}) - 1\right) \rho(\boldsymbol{k}) = \frac{1}{2} \frac{x^2}{\sqrt{1+2x}(1+x-\sqrt{1+2x})} \tag{4.50}$$

which is indeed a monotonously increasing function of x. The right panel of Figure 4.19 shows that this increase is also found at finite temperature for an experimentally relevant x range. This increase confirms the naive expectation: when interactions are increased at constant temperature, Bogoliubov's theory predicts that a larger fraction of the depletion belongs to the quantum depletion and contributes to the pairing signal. As this conclusion is independent of $\boldsymbol{k}$, we expect it to remain valid for the average momentum density $\bar{\rho}_{\Omega_k}$.

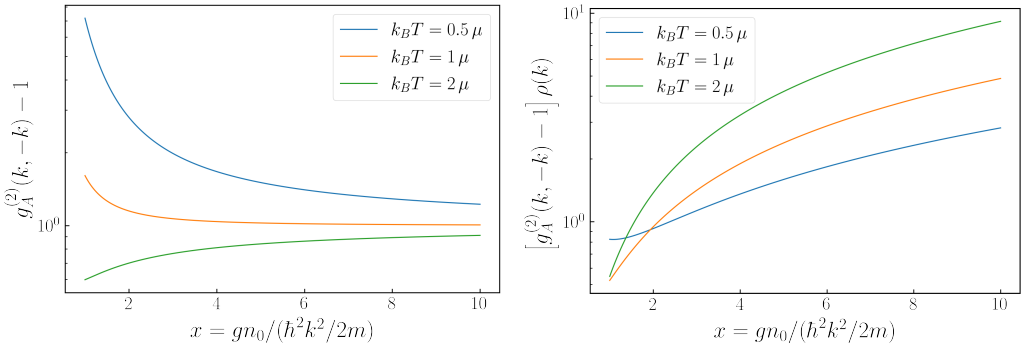

Figure 4.19: **Predictions for the 1D harmonically-trapped system.** Left: Anomalous amplitude as a function of the ratio x between the interaction energy and the free-particle energy for three different temperatures. This amplitude corresponds to Equation 4.47 divided by Equation 4.48 squared. Right: Same predictions for the anomalous amplitude times the momentum density (Equation 4.47 divided by Equation 4.48).

4.4.2 Expectations beyond the Bogoliubov approximation

Bogoliubov's theory is a perturbative approach, so one naturally expects this approximation to fail when the BEC gets strongly depleted. To guess what happens then, we first recall the Hamiltonian of equation 4.4 describing a homogeneous gas of ultracold bosons with two-body contact interaction in the formalism of second quantization:

$$\hat{H} = \sum_{\boldsymbol{k}} \frac{\hbar^2 k^2}{2m} \hat{a}_{\boldsymbol{k}}^\dagger \hat{a}_{\boldsymbol{k}} + \frac{g}{2L^3} \sum_{\boldsymbol{k}', \boldsymbol{k}'', \boldsymbol{q}} \hat{a}_{\boldsymbol{k}'+\boldsymbol{q}}^\dagger \hat{a}_{\boldsymbol{k}''-\boldsymbol{q}}^\dagger \hat{a}_{\boldsymbol{k}''} \hat{a}_{\boldsymbol{k}'} \tag{4.51}$$

To derive the Bogoliubov Hamiltonian in the particle basis (equation 4.5) we made the simplifying approximation of neglecting all the terms of the interaction part containing fewer than two $\hat{a}_{\boldsymbol{0}}$, $\hat{a}_{\boldsymbol{0}}^\dagger$ operators (those were replaced by the real numbers $\sqrt{N_0}$). Naturally, these neglected terms have to be considered to answer the question of which correlations can be expected beyond Bogoliubov's theory. The first terms to be considered are the ones which contain only one $\hat{a}_{\boldsymbol{0}}$ or $\hat{a}_{\boldsymbol{0}}^\dagger$ operator. If we take for instance $\boldsymbol{k}' = \boldsymbol{0}$ in equation 4.51, then it represents the two-body interaction between one atom in the $\boldsymbol{k} = \boldsymbol{0}$ mode and one atom at momentum $\boldsymbol{k}'' \neq \boldsymbol{0}$ [197]. At $T = 0$, the second atom with a non-zero momentum can only come from the quantum depletion, meaning from a Bogoliubov pair. Therefore, one sees that going beyond the Bogoliubov picture consists in allowing the $\boldsymbol{k}$/-$\boldsymbol{k}$ atoms to

interact instead of returning to the condensate. As illustrated in Figure 4.20, this ($T = 0$) third-order process in the development of equation 4.51 creates a triplet of bosons whose total momentum is zero. This can be viewed as the higher-order process analog to the pairing one. Similarly, interactions between two non-condensed atoms, namely atoms from two different Bogoliubov pairs, are neglected in the Bogoliubov approximation. This fourth order process, which is even more unlikely to happen when the condensed fraction is large, is represented in Figure 4.20. This next-order terms leads to the creation of a quadruplet whose total momentum is zero. Similarly to the pairing mechanism, the creation of such momentum-correlated triplets and quadruplets occurs at $T = 0$. Any finite temperature contribution will generate uncorrelated ensembles of atoms and, in turn, finite temperature strongly reduces the probability to find pairs, triplets, and quadruplets.

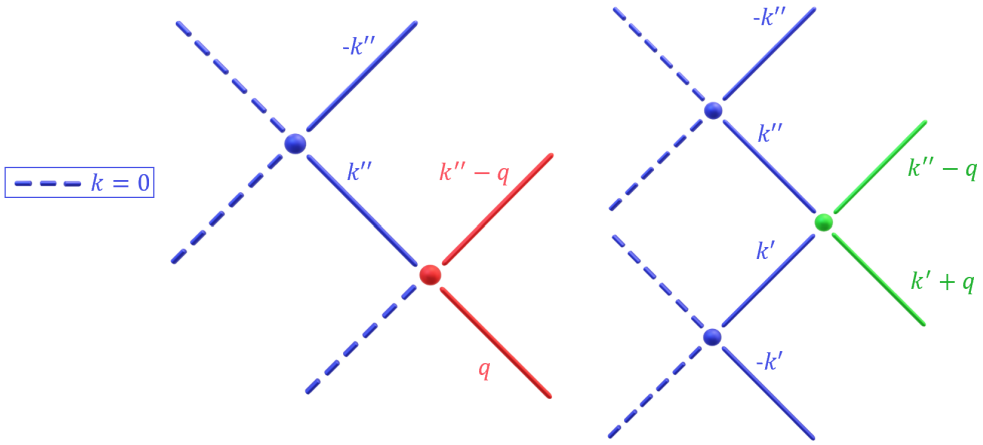

Figure 4.20: **Scheme of some interaction processes beyond the Bogoliubov approximation.** Left: One member of a $\boldsymbol{k}$/$\boldsymbol{-k}$ pair interacts with an atom in the condensate mode $\boldsymbol{k} = \boldsymbol{0}$ (represented as a dashed line). This process yields a pair of correlated atoms with non-zero total momentum (in red) and a triplet of atoms whose total sum is zero. Right: next-order process where two atoms from two different Bogoliubov pairs interact, yielding a correlated quadruplet whose total momentum is zero. Both left and right panels correspond respectively to the third- and fourth-order terms in the development of the interacting part of the Hamiltonian 4.51, which are neglected in the Bogoliubov approximation.

Both kinds of microscopic processes are beyond Bogoliubov's theory and it would be great to reveal them in interacting Bose gases. The question now is the same as for the $\boldsymbol{k}$/$\boldsymbol{-k}$ pairs: are there signatures of this physics that we could detect? Accounting for our capacity to compute correlations between individual particles in momentum space, the answer to that question should be "Yes!". If the Bogoliubov pairs interact before returning to the BEC, an immediate consequence should be a diminution of the anomalous amplitude. Indeed, Figure 4.20 illustrates that each third- and fourth-order process removes two/four atoms that would otherwise contribute to the correlations at opposite momenta. Another possible route to detect high-order processes is to look for correlated triplets and quadruplets whose sum of momenta is zero [235]. These clusters corresponds to $-\boldsymbol{k}'' + (\boldsymbol{k}'' - \boldsymbol{q}) + \boldsymbol{q} = \boldsymbol{0}$ in the third-order case and $-\boldsymbol{k}'' + (\boldsymbol{k}'' - \boldsymbol{q}) + (\boldsymbol{k}' + \boldsymbol{q}) - \boldsymbol{k}' = \boldsymbol{0}$ in the fourth-order case. Detecting them relies on the condition that the partner of each annihilated paired atom has not interacted in turn. Under this assumption, such triplets and quadruplets can be measured in our experiment, provided that we adapt our cor-

relation algorithm. These computations are detailed in the last section of this chapter. Finally, both high-order processes produce correlated pairs at non-zero total momentum, represented in red and green in Figure 4.20. Similarly to the $\boldsymbol{k}/\boldsymbol{-k}$ pairs, these atoms participate to the anomalous signal $g_A^{(2)}$, except that their contribution is not be located at $\boldsymbol{\delta k} = \boldsymbol{0}$ anymore. As there is no preferred $\boldsymbol{\delta k}$ value for observing them, these pairs should induce an overall increase of the baseline of the anomalous signal above one. However, we may anticipate that such a delocalized signal could very well be hidden in the noise of our normalization procedure, depending on the number of events.

4.4.3 Increasing the interactions at fixed temperature

As illustrated in section 4.1.4, changing interactions in our experimental setup is straightforward: we simply have to increase the lattice intensity to increase the on-site interaction energy U. The non-trivial part is to perform this change without heating the gas, to conserve a roughly constant amount of thermal depletion. For that, we rely on the adiabaticity of the ramps with which we change the lattice potential, a property that we have experimentally shown in the second chapter of this thesis. In particular, Figure 2.13 shows that we can prepare clouds at increasing values of U/J in the superfluid regime without changing the reduced temperature T/J by a significant amount. Therefore, increasing the lattice potential is quite analogous to increasing the interactions at fixed temperature (with all energies in units of J). An additional effect that should favor the observation of the quantum depleted atoms on increasing the lattice potential is that the reduced speed of sound $c/J = \sqrt{Un/m^*}/J \propto \sqrt{U/J}$ also increases. If the reduced temperature does not increase in the process, the population of the quasi-particles becomes more phononic, and the temperature contribution in the integration volume becomes smaller. Therefore, we expect our setup to be suited for testing Bogoliubov prediction in stronger interaction regimes via our measurement of anomalous correlations.

dataset	Condensed fraction (%)	Number of files
$U/J = 2$	90(1)	2033
$U/J = 5$	84(1)	2367
$U/J = 7.5$	78(2)	1480
$U/J = 10$	74(1)	2243
$U/J = 12.5$	67(2)	2831
$U/J = 15$	57(4)	3257
$U/J = 20$	41(2)	2876

Table 4.1: **Summary of the datasets taken at different U/J values.** All these datasets were taken at $N_{BEC} = 5 \times 10^3$. The number of files represents the post-selected shots for which the atom number belongs to a 30% interval around the targeted atom number.

To that end, we took several datasets at $N_{BEC} = 5 \times 10^3$, spanning the superfluid region of the phase diagram between $U/J = 2$ and $U/J = 20$. Contrary to the ones used in our previous study of the Mott transition (Chapter 2), all these datasets use the Raman transfer to increase the number of detected atoms. The corresponding condensed fractions and numbers of post-selected files are summarized in table 4.1. Similarly to the first part of the chapter, the distributions kept are the ones whose atom number belongs to a 30%

interval around N_{BEC}. The condensed fraction is estimated according to the procedure described in Appendix A. With the same aim of keeping it non-zero as in the study of the effect of temperature at $U/J = 5$, we have taken care here not to entirely deplete the condensate by staying far from the Mott transition. The resulting condensed fractions are more relevant than U/J for labeling the different datasets since they are directly related to the validity of Bogoliubov's approximation. Figure 4.21 shows normalized 1D cuts of the momentum density for all these datasets. In logarithmic scale, the increase of the depletion level in the integration volume Ω_k is clear and extends over one decade. Finally, the correlation computations are repeated for all these datasets. Due to the limitations induced by the center-of-mass fluctuations, we focus on the amplitude of the correlations in the following. The behavior of the anomalous width with U/J is commented in Appendix B, the conclusion being that it remains essentially constant over the range of U/J values spanned.

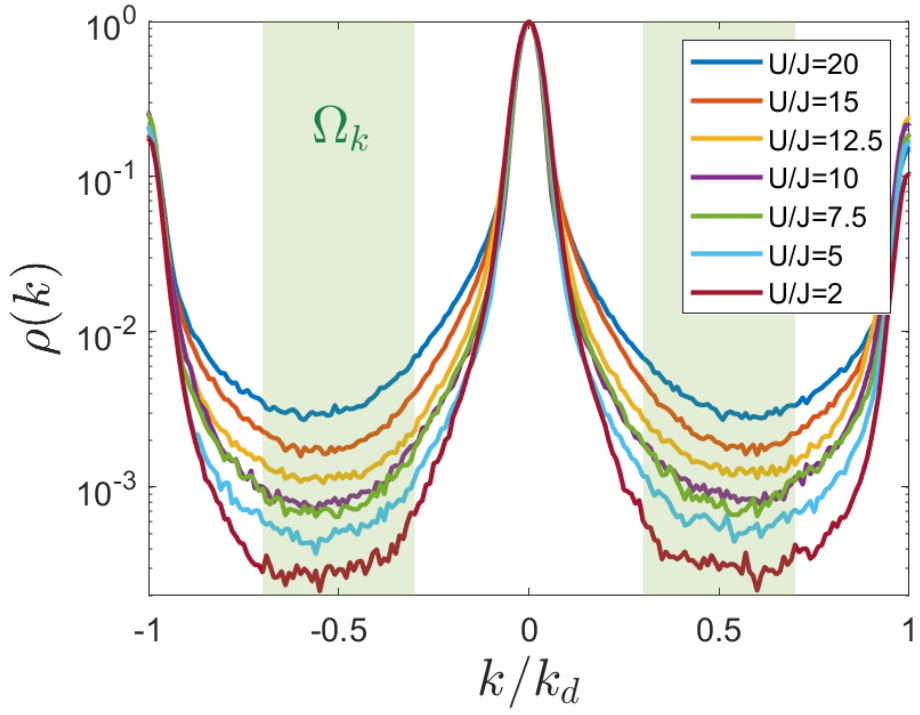

Figure 4.21: **Normalized 1D cuts of the momentum densities versus U/J.** The transverse integration used is $\delta k_\perp = 0.1\, k_d$. The plot is in semilog scale to emphasize the increase of the depletion level with interactions. In particular, the average momentum density in the integration volume $\bar{\rho}_{\Omega_k}$ is varied by more than one order of magnitude in the interaction regime spanned.

4.4.4 Anomalous and normal amplitudes at stronger interactions

The amplitudes of the anomalous correlation peaks, corrected from the integration effect, are plotted in Figure 4.22 as a function of the condensed fraction of the corresponding dataset. We observe a smooth decay of the anomalous amplitude up to $U/J = 20$ where no correlation peak stands out from the noise. The decay of the anomalous amplitude is qualitatively compatible with the behavior expected from the 1D homogeneous system at the temperature regime of our experiment, but a quantitative comparison with theory is not available at the moment. Instead, we compare the decrease of the anomalous amplitude

with that measured when the temperature was increased at fixed $U/J = 5$. As a reminder, we had measured:

- a peak amplitude equal to 0.22(2) for the dataset with an intermediate condensed fraction of 55%,
- no correlation peak in the most heated dataset ($f_c = 0.29$).

These observations are quantitatively compatible with the decay observed in Figure 4.22 as interactions are increased. However, it would be interesting to further compare the decays of the anomalous signal with the condensed fraction depending on whether the temperature or the interaction strength is increased. We would expect a slower decay when the cloud is heated up, because in this case the number of pairs is constant and the anomalous amplitude only decreases due to the larger fraction of uncorrelated (thermal) atoms in the the depletion. On the opposite, an additional contribution to this decay is expected at higher interaction strength if $\boldsymbol{k}/\boldsymbol{-k}$ pairs start interacting. Said differently, only the denominator of $g_A^{(2)}$ increases in the first case, while the decrease of the numerator in the second case would induce a faster decay. For the moment, both heated datasets at $U/J = 5$ do not allow to answer this question since they lie on the right side of Figure 4.22, where the anomalous amplitude is already small for the datasets taken at various lattice depths. To answer this question, we would need to take new heated datasets corresponding to a condensed fraction above 75%, for which a smaller anomalous amplitude than the points in Figure 4.22 would be more easily seen.

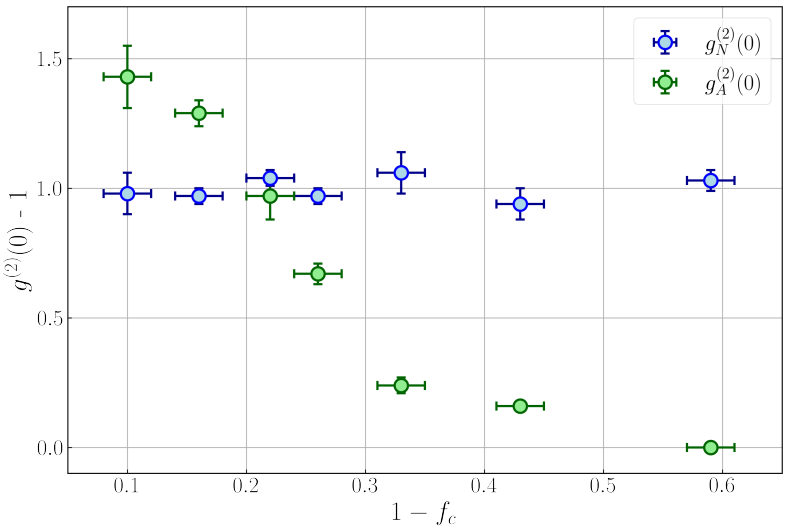

Figure 4.22: **Anomalous and normal amplitudes versus the total depleted fraction.** A smooth decay of the anomalous signal is observed while all normal amplitudes remain compatible with a perfect bosonic bunching $g_N^{(2)}(0) = 2$. Vertical (*resp.* Horizontal) error bars represent the uncertainty in the estimation of the correlation amplitude (*resp.* of the condensed fraction) detailed in Section 4.3.2 (*resp.* in Appendix A).

Similarly to the previous section, we compare the behavior of the anomalous correlations with that of the normal ones. We recall that a perfectly contrasted bosonic bunching $g_N^{(2)}(0) = 2$ was found at $U/J = 5$ once corrected the integration effect. This feature was explained by the fact that all the atoms in the integration volume Ω_k, regardless of whether they belong to the thermal or to the quantum depletion, contributed to the normal corre-

lations. Therefore, we expect a similar result with the new datasets for which the quantum depletion is increased. Figure 4.22 shows the amplitudes $g_N^{(2)}(0)-1$ of the normal correlations versus the condensed fraction for all the datasets between $U/J=2$ and $U/J=20$. Indeed, we always find a perfect bosonic bunching, extending, by the way, the violation of the Cauchy-Schwarz inequality to the dataset with a 90% condensed fraction. This consistent behavior of the normal correlations across the superfluid regime suggests that the decay of the anomalous correlations on the same datasets has a real physical origin.

4.4.5 Anomalous amplitude multiplied by the average density

According to the 1D homogeneous Bogoliubov prediction, the product $(g_A^{(2)}(0)-1)\bar{\rho}_{\Omega_k}$ is expected to increase monotonously with the interaction strength. This increase is easily understood since this quantity is proportional to the probability for a depleted atom to belong to a ***k*/-*k*** pair (see Appendix C). In Bogoliubov's picture, all atoms from the quantum depletion form pairs at opposite momenta. The probability of a depleted atom belonging to one of them should then increase with the quantum depletion level, assuming that the thermal depletion remains constant. The product $(g_A^{(2)}(0)-1)\bar{\rho}_{\Omega_k}$ is plotted for the various datasets at increasing interactions in Figure 4.23. Interestingly, the behavior is not monotonous anymore. It first increases up to a depleted fraction of roughly 20% and then starts decreasing until it reaches zero on the last dataset, for which no correlation peak can be distinguished anymore. The high condensed fraction part of this plot can be interpreted within Bogoliubov theory as being a consequence of an increased number of ***k*/-*k*** pairs at stronger interactions. However, the decay observed at smaller condensed fractions is incompatible with Bogoliubov's picture. The most likely reason is that the Bogoliubov approximation starts to break down at such large depleted fractions because we are gradually moving out of the domain of validity of this perturbative theory. For

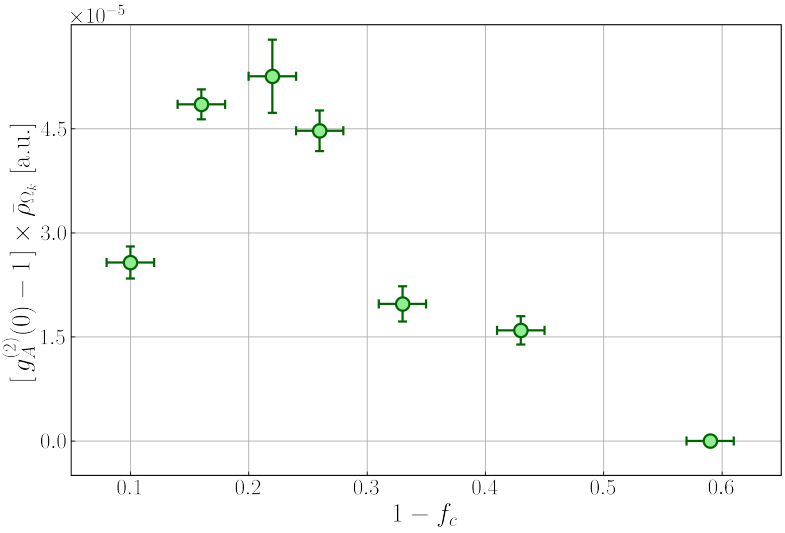

Figure 4.23: **Anomalous amplitude times the average density versus the total depleted fraction.** All amplitudes are corrected from the transverse integration effect. Vertical error bars represent the uncertainty in the estimation of the anomalous amplitude only, as the uncertainty in the average density is negligible. Horizontal error bars represent the uncertainty in the estimation of the condensed fraction (see Appendix A).

this conclusion to be true, we must ensure that the temperature does not play a role in the observed decay of the anomalous signal.

4.4.6 A possible consequence of the temperature?

We should consider the possibility that the decay of the anomalous correlations is simply a consequence of some unintentional heating rather than the limitation of Bogoliubov's regime. Indeed, we have seen with the example of the $U/J = 5$ datasets that temperature drowns out anomalous correlations while it does not affect the normal ones. Note that the heating referred to here is not related to how the lattice intensity is increased - we used the same ramps as the ones with which the adiabatic state preparation was proved in Chapter 2. Its origin would rather be related to the quality of the lattice alignment. Indeed, we took all these datasets several months apart. Due to the inevitable misalignment of the lattice on this timescale, it has been re-aligned before taking each measurement. However, setting the lattice in the optimal configuration is difficult. This hardship is illustrated in Figure 4.24, which shows normalized momentum densities of different datasets at $U/J = 12.5$ and $N_{BEC} = 5 \times 10^3$ that were all taken after different lattice alignments. On a logarithmic scale, the level of the depletion varies over almost one decade between the different datasets while it should, in principle, remain constant. This variation of the depletion level and, consequently, of the condensed fraction, reflects the heating induced by a sub-optimal lattice alignment. Between all these datasets, anomalous correlations were only visible on the coldest one taken on April 28th, 2022. There is thus little doubt that the lattice alignment can affect our measurement of the anomalous correlations across the superfluid

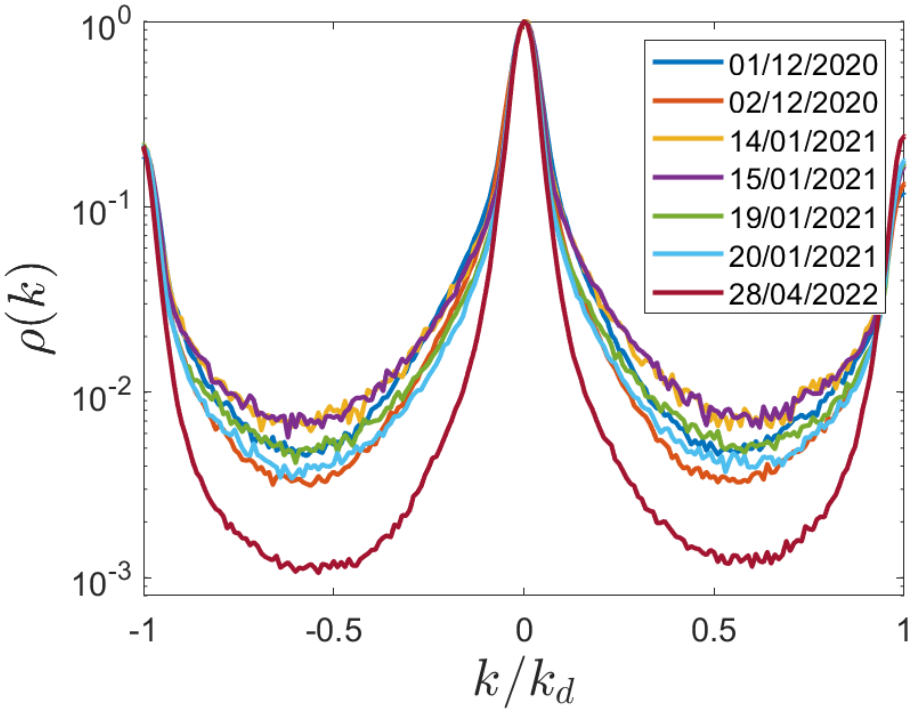

Figure 4.24: **All attempts at $U/J = 12.5$.** The 1D cuts of the momentum densities of all the datasets taken at $U/J = 12.5$ and for $N_{BEC} = 5 \times 10^3$ are superimposed in semilog scale to emphasize how sensible the depletion level is to the lattice alignment. The transverse integration is $\delta k_\perp = 0.1\, k_d$.

phase.

Fortunately, we have at least two observables to convince ourselves that this is not happening here. First, the condensed fractions of the new datasets are consistent with the values found at the same U/J in our previous investigation of the Mott transition with transfer (Chapter 2). As this study led to the observation of the critical scaling $(1-u/u_c)^{2\beta}$ for the maximum momentum density $\rho_0 = \rho(\boldsymbol{k} = \boldsymbol{0})$, there is good reason to trust the associated condensed fractions. Secondly, we empirically observed a linear variation of the average density in the integration volume $\bar{\rho}_{\Omega_k}$ with U/J (see Figure 4.25). This linear variation allows us to identify datasets for which some heating might be induced by a sub-optimal alignment (in red). For instance, all the failed attempts at $U/J = 12.5$ are clearly visible in this plot. We could also identify wrong datasets at $U/J = 5$ and $U/J = 7.5$, for which the anomalous amplitudes were smaller than the ones of the colder datasets at the same U/J. Both observables suggest that the temperature is not the cause of the anomalous amplitude decay. Again, we can hardly comment quantitatively on this decay and, in particular, predict where its onset should be located in our system. However, an alternative can consist in comparing our system with others to provide a first quantitative answer.

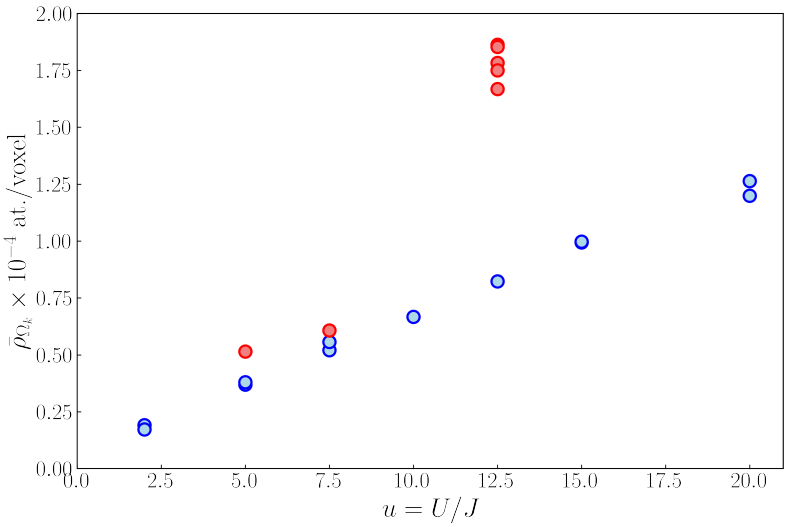

Figure 4.25: **Average density in the integration volume versus U/J.** The average density is obtained by averaging the momentum density belonging to the integration volume Ω_k defined such that all atoms verifying the condition $0.3 \leq |k_{x,y,z}| \leq 0.7$ are kept. Error bars are defined as the standard deviation of the mean over all voxels and are smaller than the marker size.

4.4.7 Comparison with the work of Lopes *et al*

Following Bogoliubov's work that predicted the presence of the quantum depletion in weakly interacting Bose gases, a scaling of the condensed fraction versus the interaction strength was derived by Lee, Huang, and Yang (LHY) in 1957 [203]. They showed that in the homogeneous case this scaling is:

$$f_c = 1 - \gamma \sqrt{n a_s^3} \tag{4.52}$$

with $\sqrt{na_s^3}$ defining the interaction strength of the homogeneous system and $\gamma = 8/(3\sqrt{\pi}) \simeq 1.5$. In 1999, Giorgini *et al.* [236] verified numerically this scaling of the fraction of atoms in the quantum depletion using Monte Carlo simulations. In particular, they showed that it was valid up to $na_s^3 \leq 10^{-3}$. It was only recently that an experimental validation was provided by the group of Zoran Hadzibabic in Cambridge in 2017 [2]. They reproduced the textbook configuration of the LHY paper by producing homogeneous BECs of ^{39}K held in cylindrical optical-box traps [152]. A Feshbach resonance allows them to magnetically tune the scattering length from $a_s = 200\,a_0$ initially, with a_0 the Bohr radius, to any desired value within the range $[700 - 3000]\ a_0$ in order to prepare clouds of varying interaction strength (the largest value of a corresponding to $\sqrt{na_s^3} \simeq 0.04$). Their experiment uses a Doppler-sensitive two-photon Bragg scattering [237] to spatially separate the BEC from the high-momentum tails of the momentum distribution after a 10ms time-of-flight. Prior to this time-of-flight, the interactions are frozen by transferring the atoms from the $|F = 1, m_F = 1\rangle$ to the $|F = 1, m_F = 0\rangle$ hyperfine state for which $a_s \simeq 0$. Finally, the condensed fraction for a given a_s is given by the maximum diffracted fraction η, which is fitted from the ones measured close to a pi-pulse duration of the Bragg pulse. Those η values are shown in Figure 4.26 versus the interaction strength. The linear fit of their experimental data gives $\gamma = 1.5(2)$, which agrees remarkably well with the LHY prediction. The extrapolation of this fit to the limit $a_s = 0$ gives a diffracted fraction slightly below one mostly because of the thermal depletion - which is insensitive to the Bragg pulse - and also to the finite Rabi frequency that prevents a total transfer of the tails of the BEC momentum distribution.

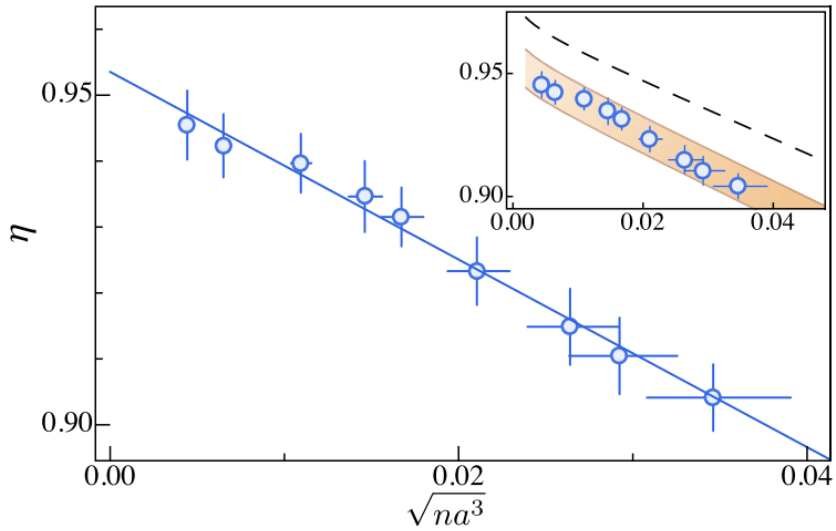

Figure 4.26: **Quantum depleted fraction versus interaction strength, from [2].** This measurement is performed in homogeneous Bose-Einstein condensates using a coherent two-photon Bragg scattering, whose maximum diffracted fraction η is assimilated to the quantum depleted fraction (see text). The interaction strength $\sqrt{na^3}$ is tuned via a Feshbach resonance. The vertical error bars are fitting errors on η, while the horizontal ones reflect the uncertainty on the position of the Feshbach resonance and a 10% error in n. The solid line is a linear fit. The inset shows numerical simulations for $T = 0$ (dashed line) and for initial temperatures between 3.5 and 5 nK (orange shading; see [2] for more details.

The experimental proof of the LHY scaling of the condensed fraction represents the main result of this paper. Of interest to us is that the authors also tried to extend their measurements to the case of higher interaction strengths for which the Monte-Carlo simulations of [236] predicted that deviations to Bogoliubov should be observed. These additional measurements were published in the supplementary material and are shown in Figure 4.27 as brown circles, together with the previous ones (blue circles) and the Monte-Carlo simulations (black diamonds). The larger horizontal error bars on the new experimental points result from the increase of the three-body losses at such high interaction strengths, which also prevents the authors from correctly estimating the effect of the non-zero temperature. Therefore, these new measurements are not entirely conclusive: they suggest that deviations from the Bogoliubov theory are observed. In particular, those deviations would be of the same sign and magnitude as the Monte-Carlo simulations.

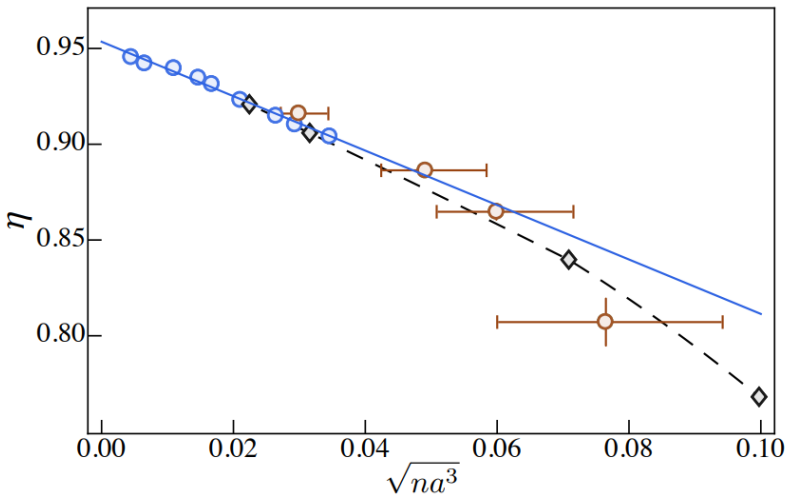

Figure 4.27: **Quantum depleted fraction at higher interaction strength, from the Supplementary of [2].** This plot shows additional measurements (red circles) than the ones presented in Figure 4.26 (blue circles), for which the interaction strength was increased further at the cost of larger error bars in the value of $\sqrt{na^3}$ (see text). In agreement with Quantum Monte-Carlo simulations from [236] (black diamonds and the interpolating dashed line), these new points seem to disagree quantitatively with the Bogoliubov prediction symbolized by the solid line.

We can try to draw a parallel between this measurement and ours, although the system and the quantity traced are different. This link is justified by the fact that Bogoliubov's approach only relies on the assumption $f_c \sim 1$, regardless of whether the interaction strength is quantified by $\sqrt{n\,a_s^3}$ (as in the homogeneous case) or by U/J (for lattice bosons). Let us assume that the deviations in Figure 4.27 are the consequence of the Bogoliubov approximation being invalid at such strong interactions. In that case, we can infer that a quantitative onset for observing such deviations corresponds to a quantum depletion between 5% and 15% (η between 0.90 and 0.80). As our measure of the depleted fraction encompasses both the quantum and the thermal depletion, we must rely on a $T = 0$ Gutzwiller approach to estimate when such quantum depleted fraction is reached with our lattice gases of $N_{BEC} = 5 \times 10^3$. The result of this computation is plotted in Figure 4.28. We can see that a quantum depleted fraction between 5% and 15% corresponds roughly, in our case, to a U/J ratio in the range $[5 - 11.5]$. This interval of U/J values is consistent with the one over which the anomalous amplitude times the average density

starts to decrease. It would then suggest that deviations from Bogoliubov's theory occurs for similar condensed fractions. Naturally, it would be great to confirm this conclusion in our system at the microscopic level via momentum correlations between individual atoms. To this aim, we started to look for momentum correlations that would unambiguously signal the beginning of a breakdown of Bogoliubov's approximation at higher interactions.

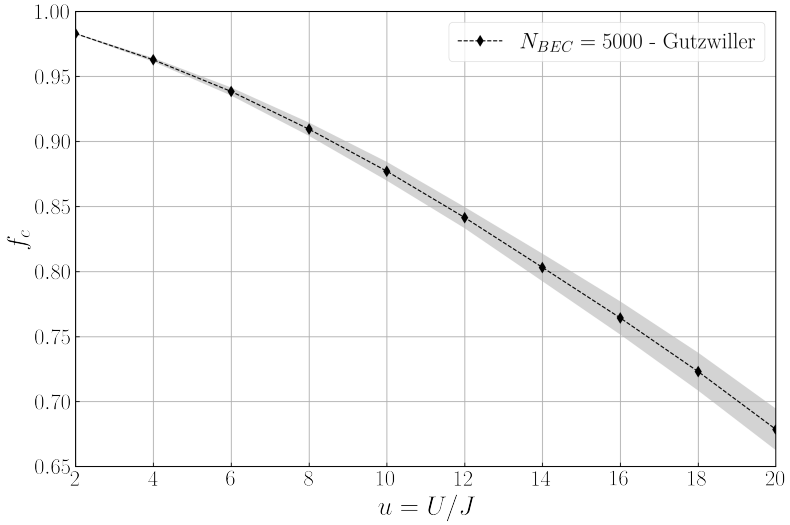

Figure 4.28: **Gutzwiller estimate of the quantum depleted fraction versus U/J.** This $T = 0$ approach returns an estimate of the condensed fraction, which can directly be identified with an estimate of the quantum depleted fraction. The computations are performed with our experimental parameters between $U/J = 2$ and $U/J = 20$, and for $N_{BEC} = 5 \times 10^3$ (black diamonds and interpolating dashed line). The gray shaded area reflects the 30% interval around N_{BEC} allowed on the atom number of the post-selected distributions.

4.5 Attempts to find signatures of momentum-correlated triplets

In this last section we review the tests to look for the high-order interaction processes mentioned in 4.4.2 and illustrated in Figure 4.20. In particular, we have focused on trying to reveal the momentum correlations associated with third-order processes in the development of Equation 4.51 (left panel of Figure 4.20) , *i.e.* atom pairs with non-zero total momentum and momentum-correlated triplets. Unfortunately, observing such momentum correlations has remained elusive so far.

4.5.1 Baseline of the anomalous correlations

As explained in Section 4.4.2, third- and fourth-order interaction processes create pairs of atoms whose sum of momenta is non-zero, which may increase in the baseline of the anomalous correlations. This signature may be hard to detect as it is not localized in the momentum space. To look for this effect, we repeated the anomalous computation with all our datasets at $N_{BEC} = 5 \times 10^3$ while:

- conserving the same holed cubic integration volume Ω_k as for the previous study, for

which any atoms whose momentum coordinates verify the condition $0.3 \leq k_{x,y,z} \leq 0.7$ is kept;

- extending the maximal sum of momenta $\boldsymbol{\delta k}$ up to which the correlations are computed to $0.75\,k_d$ to increase our chances of detecting pairs of atoms with a non-zero sum of momenta. In the previous study, the maximal $\boldsymbol{\delta k}$ was typically smaller than $0.3\,k_d$ as we were looking for correlations centered on $\boldsymbol{\delta k} = \mathbf{0}$ with a typical correlation length on the order of $0.1\,k_d$.
- increasing the voxel size from $(0.012\,k_d)^3$ to $(0.3\,k_d)^3$ to reduce their number and speed up the computations. This is permitted because we are not interested anymore in trying to resolve the $\boldsymbol{k}$/$\boldsymbol{-k}$ correlation signal. We remove the central voxel corresponding to $-0.15\,k_d \leq \delta k \leq 0.15\,k_d$ to be sure not to count the $\boldsymbol{k}$/$\boldsymbol{-k}$ atoms. Finally, the total number of counts in the remaining voxels of the numerator is divided by that of the denominator, obtained from repeating the anomalous computation on a merged file containing all the experimental distributions.

This procedure returns a grid of voxels containing baseline values of the anomalous signal at different $\boldsymbol{\delta k}$. As there should not be any preferred $\boldsymbol{\delta k}$ for the sum of the momenta of the paired atoms, nothing prevents us from averaging the contribution of all voxels to increase the signal. The resulting average baseline is plotted in blue in Figure 4.29 for each datasets at $N_{BEC} = 5 \times 10^3$. Error bars correspond to the standard error of the mean of the distribution of all the baselines computed inside a single dataset.

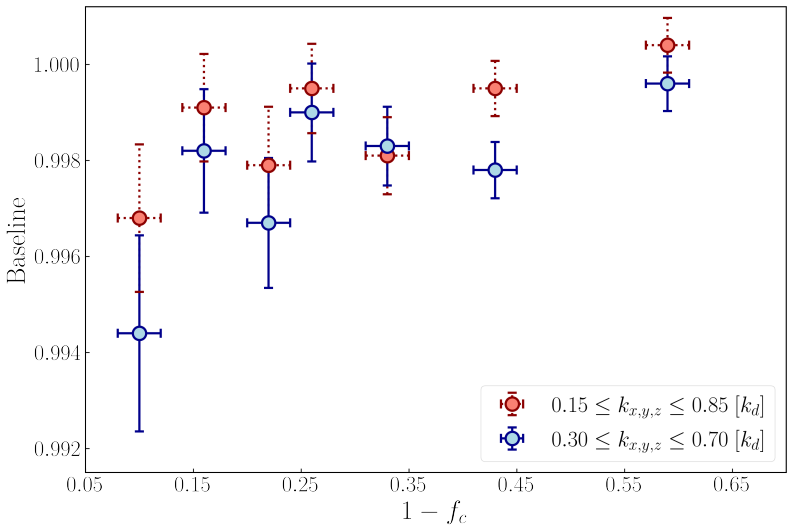

Figure 4.29: **Baselines of the anomalous correlations versus the depleted fraction.** The baselines are computed for two integration volume Ω_k: a first one for the atoms verifying the condition $0.3 \leq |k_{x,y,z}| \leq 0.7\ [k_d]$ (in blue), and a larger one corresponding to $0.15 \leq |k_{x,y,z}| \leq 0.85\ [k_d]$ (in red). Vertical error bars represent the standard deviation of the mean over the ensemble of baselines computed for each experimental run within a single dataset (see text). Horizontal error bars represent the uncertainty in the estimation of the condensed fraction whose measurement is explained in Appendix A.

The baseline is found to increase with the interaction strength, despite the large error bars stemming from the finite statistics in the voxels. At stronger interactions, the larger depletion of the condensate increases the atom number inside the voxels, and the error bars are reduced. As is, the baseline increase cannot be associated with a growing contribution of pairs of atoms whose total momentum is non-zero. Indeed, the baseline always lies below

one, which is, in principle, the smallest value it can take. This measurement instead seems to point out some imperfection in our normalization procedure. For the latter to work best, the statistics must be high enough that mixing all the experimental runs provides an accurate estimate of the momentum density. Only then does the denominator computation correctly reproduce its auto-correlation. As the integration volume Ω_k only keeps the most dilute parts of the distributions, the finite statistics prevent our normalization procedure from working to better than one percent. This effect is worse for highly condensed datasets, where most atoms are located within the diffraction peaks. This hypothesis is verified when repeating the baseline measurement with a larger integration volume Ω_k, which now keeps all the atoms whose momentum coordinates verify the condition $0.15 \leq k_{x,y,z} \leq 0.85$. The new baselines are plotted in red in Figure 4.29, and are closer to 1 than the previous ones. This behavior is consistent with our explanation, and the conclusion is that our resolution does not allow us to distinguish any increase in the baseline of the two-body correlations that would signal the presence of atom pairs with non-zero total momentum.

4.5.2 Three-body correlations: first algorithm

A second approach to finding signatures of interaction processes beyond Bogoliubov's picture is to look for the presence of triplets whose total momentum is zero. As represented in Figure 4.20, such triplet comes from considering the partner of the annihilated $\boldsymbol{k}/\boldsymbol{-k}$ atom together with the pairs with non-zero total momentum. Similarly to the $\boldsymbol{k}/\boldsymbol{-k}$ pairs, this signal should be located at the center of the three-body correlations histogram. However, its observation should be significantly harder than for the $\boldsymbol{k}/\boldsymbol{-k}$ pairs for several reasons:

- the most obvious one is that three correlated particles must now be detected at the same time, which is a factor of η_{MCP} less likely than for the $\boldsymbol{k}/\boldsymbol{-k}$ pairs;
- the most limiting reason may be that such triplets do not exist if the annihilated $\boldsymbol{k}/\boldsymbol{-k}$ atom has interacted with a thermal one. In this case, the total momentum of the resulting triplet would not be zero anymore due to the non-zero momentum of the thermal atom. In the triplet case, not only can thermal atoms hide the signal, but they can also destroy it.
- similarly, two additional conditions are that *(i)* only one member of a $\boldsymbol{k}/\boldsymbol{-k}$ pair interacts, and *(ii)* that this interaction does not involve an atom from another $\boldsymbol{k}/\boldsymbol{-k}$ pair, otherwise a correlated quadruplet is produced rather than a triplet. However, both hypothesis should be fulfilled in a moderately stronger interaction regime.

The identification of these triplets requires an upgrade of the correlation algorithm. As illustrated in Figure 4.30, we simply modified the code to compute the histograms of all the possible sum of triplets - rather than doublets - of momenta within the experimental distributions. Doing this adds a factor $\sim \langle N_{\Omega_k} \rangle$ to the total number of operations, increasing the computation times. The latter are typically several hours long, and the normalization must be calculated by shuffling the atoms between the different experimental distributions instead of merging them into a single file. Unfortunately, we have not distinguished any correlation signal above the noise level while running this algorithm on the different datasets. During these computations, we tried different integration volumes Ω_k and voxel sizes without success. Finally, we also took additional datasets closer to the Mott transition to increase the interactions further, but this did not help us either. As a last attempt, we modified the algorithm to account for the presence of thermally depleted

atoms inside the depletion.

Algorithm 3-body correlations

```
For each run n
    For each atom i in run n
        For all atoms j ≠ i in run n
            For all atoms l ≠ i, j  in run n
                Append k_i + k_j + k_l to momentum_sum_list
            End
        End
    End
Compute and store the 3D histogram of momentum_sum_list
End
Average the 3D histograms of all experimental runs
```

Figure 4.30: **Pseudo-code version of the three-body correlations algorithm.** The procedure is identical to that of the two-body algorithm in Figure 4.4, except that now the 3D histograms are calculated on the sum of the momenta of all possible triplets of atoms in the experimental distributions.

4.5.3 Three-body correlations: second algorithm

As already discussed, triplets such as those in the left panel of Figure 4.20 whose sum of momenta is zero are one of the most natural signatures of interaction processes beyond Bogoliubov's regime we can think of. After a first unsuccessful attempt at observing them, we thought of a different approach: observing the absence of the annihilated $\boldsymbol{k}$/$\boldsymbol{-k}$ atom (the one at momentum $\boldsymbol{k''}$ in the left panel of Figure 4.20). One way to do that is to compute the 3D histogram of the quantity $\boldsymbol{\delta k} = \boldsymbol{k_1} + \boldsymbol{k_2} - \boldsymbol{k_3}$ for all possible triplets of atoms within the experimental distributions. As usual the central voxel $\boldsymbol{\delta k} = \boldsymbol{0}$ of the denominator histogram provides a reference value for the uncorrelated case, which corresponds here to the probability of having three uncorrelated atoms verifying the condition $\boldsymbol{k_1} + \boldsymbol{k_2} - \boldsymbol{k_3}$. In the numerator, when a pair with non-zero total momentum is detected, its atoms are less likely to contribute to the correlations $\boldsymbol{k_1} + \boldsymbol{k_2} - \boldsymbol{k_3}$ since the atom at $\boldsymbol{k_3}$ ($\boldsymbol{k''}$ in Figure 4.20) has been annihilated. The number of counts in the central voxel $\boldsymbol{\delta k} = \boldsymbol{0}$ should then be smaller for the numerator than for the denominator if atom pairs with non-zero total momentum are present in the distributions. With this algorithm, we expect to observe a dip at $\boldsymbol{\delta k} = \boldsymbol{0}$ in the normalized three-body correlations function. It is more likely to observe a signal with this algorithm as the annihilated atom does not need to belong to the quantum depletion. Indeed, a thermally depleted atom interacting with one in the condensate mode $\boldsymbol{k} = \boldsymbol{0}$ may produce a similar correlated pair that does not contribute to the correlations $\boldsymbol{k_1} + \boldsymbol{k_2} - \boldsymbol{k_3}$. The drawback is that if a signal (here, a dip) is detected, we cannot attribute it unambiguously to the higher-order interaction processes we are looking for. The idea behind this algorithm was to get a first signal rather than a conclusive proof. Unfortunately, no clear dip was observed in the normalized correlations function with our datasets.

4.6 Conclusion

After providing experimental evidence for the presence of pairs of atoms at opposite momenta in the depletion of interacting Bose gases, we tested the evolution of this pairing signal at higher interactions beyond the validity regime of the Bogoliubov. Our goal was to gain some insights into the microscopic evolution of the many-body ground state of the system and, in particular, to observe the effect of more complex interaction processes than the one modeled by the Bogoliubov theory. We found that the probability per depleted atom to belong to a $\boldsymbol{k}/\boldsymbol{-k}$ pair evolves non-monotonously with the interaction strength. It starts to increase as one would expect when more $\boldsymbol{k}/\boldsymbol{-k}$ pairs were to be added in the depletion by interactions. It then decreases up to a point where no correlation peak is visible anymore, although the condensed fraction is still about 40%. The onset of the decay corresponds to a quantum depleted fraction between 5% and 15%, which is comparable with recently measured deviations of the Bogoliubov prediction for the linear scaling of the condensed fraction in the homogeneous case [2]. We then tried to link the decay of the pairing correlations with the microscopic picture that Bogoliubov pairs start interacting at higher interactions. More specifically, we searched for signatures of these processes, such as the increase of the baseline of the two-body correlations, or three-body correlations that would either signal the presence of triplets of correlated atoms or the absence of an annihilated $\boldsymbol{k}/\boldsymbol{-k}$ atom. The conclusion is that none of these approaches has yet allowed us to observe a clear signal. We could try accumulating more distributions to reduce the noise level and make such signal visible. An alternative approach would be first to try to maximize the number of $\boldsymbol{k}/\boldsymbol{-k}$ pairs detected for a given interaction strength before searching for signatures of higher-order interaction processes. One way to achieve this would be to increase the trapping frequencies in the ODT to produce BECs with lower entropies. This would further reduce the amount of thermal depletion and bring us closer to the $T = 0$ Bogoliubov physics.

Conclusion

This manuscript reports the experimental investigation of strongly-interacting Bose gases via the high-order moments and correlations in momentum space. We access these quantities exploiting the electronic detection of individual ^{4}He* atoms with Micro-Channel Plates after a long free fall expansion. In addition, this detection method yields the 3D momentum distributions with an unprecedented resolution and dynamical range.

The dynamical range on the 3D momentum densities of lattice gases with a few thousand atoms was essential for the thermometry developed in collaboration with Tommaso Roscilde (ENS Lyon) and presented in Chapter 2. This thermometry was shown to saturate the theoretical limit set by the Fisher information (associated to the comparison of $\rho(\boldsymbol{k})$ with ab-initio QMC simulations). More importantly, this thermometry led us to demonstrate the adiabatic preparation of equilibrium states of the Bose-Hubbard model. In particular, the loading protocol does not suffer from the gapless energy spectrum in the superfluid regime nor from the vicinity of the quantum critical point. From a quantum simulation perspective, these results confirm the capability of cold atom platforms to prepare low-entropy states of strongly-correlated quantum-matter (without a heat bath).

This certification laid the foundations for investigating the critical region of the low-entropy Mott transition. The suppression of $\rho(\boldsymbol{k}=\boldsymbol{0})$ when increasing the lattice depth leads to a critical interaction compatible with that estimated from QMC simulations for the homogeneous system at unit filling and the temperature of the experiment, rather than with the mean-field prediction at $T=0$. In addition, the suppression of $\rho(\boldsymbol{k}=\boldsymbol{0})$ exhibits a critical scaling compatible with that of the $3DXY$ model, a property confirmed by the QMC data. These findings differ from several previous experimental investigations of the critical region of the Mott transition, a specificity that results from our unique access to $\rho(\boldsymbol{k}=\boldsymbol{0})$ and from a careful choice of the lattice filling.

In Chapter 3, we take advantage of an improved detection efficiency to investigate the Full Counting statistics (FCS) and the high-order moments (up to $n=6$) of the momentum occupation number of Bose superfluids and Mott insulators detected in the far-field regime of expansion. The measured FCS are consistent with the Poisson and thermal ones expected from a pure state description of BECs and Mott insulators. These results are

corroborated by the many-body coherence in these systems, quantified by the normalized amplitudes $g^{(n)}(0)$ of the nth-order correlation functions. The latter are measured with perfect contrast via an original approach based on the factorial moments. Concerning the BEC mode ($\boldsymbol{k} = \boldsymbol{0}$) of Bose superfluids, we observe tiny deviations $\left(g^{(n)}(0) > 1\right)$ to the perfect coherence at any order $g^{(n)}(0) = 1$ theorized by Glauber for a coherent state. We introduced a heuristic model to explain these deviations since ab-initio calculations of many-body correlations are not accessible for the strongly-interacting regime of our experiment. Despite its simplicity, the model quantitatively captures the deviations $g^{(n)}(0) > 1$ observed experimentally and attributes them to the depleted fraction. The model also explains why the role of the depletion could not be observed in a previous study [1]. Having identified the cause of the deviations, our measurements confirm the coherent nature of BECs produced in experiments to at least the sixth order of correlations. Reaching this level of certification is of primary importance for further investigations of these fluctuations in the strongly-correlated regime near the Mott transition, where signatures of non-Gaussianity, if present, would appear in the high-order ($n \geq 3$) correlation functions.

In Chapter 4, second-order correlations of the momentum occupation number between opposite modes $\boldsymbol{k}$ and -$\boldsymbol{k}$ reveal atom pairs (at opposite momenta) in the depletion of interacting Bose gases at equilibrium. This observation confirms at the microscopic level the prediction made by N. Bogoliubov more than 70 years ago for the quantum depletion. The presence of these pairs in the many-body ground state results from the interplay between quantum fluctuations and interactions. This quantum origin is confirmed by several observables: the extreme sensitivity with temperature, the scaling of the pairing amplitude analog to that found in two-mode squeezed states, the violation of the Cauchy-Schwartz inequality, and the relative number squeezing between opposite momentum modes. This pairing signal could be observed thanks to the improved detection efficiency and in the low-temperature regime accessed in the optical lattice.

The latter offers the possibility to test the prediction of Bogoliubov's perturbative approach in the strongly-interacting regime by increasing the lattice depth. The probability for a depleted atom to belong to a $\boldsymbol{k}$/-$\boldsymbol{k}$ pair exhibits a non-monotonous variations with the condensed fraction. Its initial growth is compatible with Bogoliubov's approximation, according to which stronger interactions increase the number of pairs in the depletion. However, the suppression of the pairing amplitude at smaller (but non-zero) condensed fractions signals a breaking of this approximation's validity. This appears at condensed fractions compatible with those found in homogeneous systems [2]. Initial searches for momentum-correlated triplets in the depletion that would result from interaction processes beyond Bogoliubov's theory have been unsuccessful. This exploration is so far purely experimental as no theoretical predictions exist for the two-body correlations at opposite momenta in our system, which illustrates the complexity of the physics explored by our quantum simulator.

Appendix

A. Estimation of the condensed fraction

The condensed fraction is evaluated similarly to Cécile Carcy's thesis [49]. From the momentum density, we compute the cumulative distribution function of the number of atoms falling inside the first Brillouin zone N_{BZ}:

$$P(k_r) = \frac{N(|k_x|, |k_y|, |k_z| \leq k_r)}{N_{BZ}} \tag{A.1}$$

where k_r is the side of a cube in momentum space centered on $\boldsymbol{k} = \mathbf{0}$. This fraction is plotted in Figure A.1 for all the datasets at $N_{BEC} = 5 \times 10^3$ between $U/J = 2$ and 20.

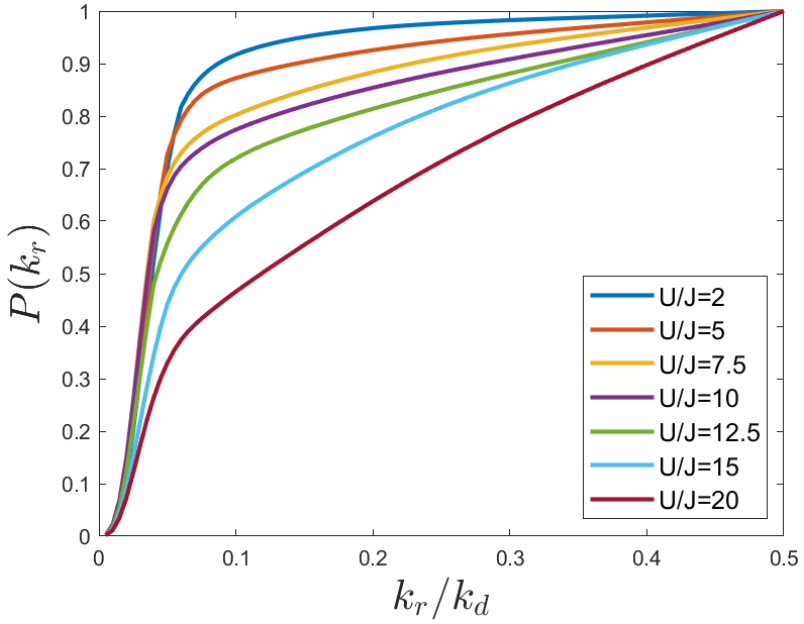

Figure A.1: **Fraction $P(k_r)$ versus k_r for all the different datasets.** This fraction represents the proportion of atoms of the first Brillouin zone within a cube of side k_r. The intersection of both linear parts in $P(k_r)$ gives the condensed fraction with a few percent uncertainties.

The fraction $P(k_r)$ presents two linear behaviors: the first one at low momentum shows a rapid increase as long as k_r is smaller than the condensate size. In contrast, the slow increase at higher momentum is attributed to the depletion. Thanks to this clear distinction, we can infer the condensed fraction from the intersection of these two regions, both fitted with a linear model. This method neglects the contribution of the depleted atoms under the condensate peak, and it provides an accurate estimation (with a few percents uncertainty) as long as the condensed fraction is not too small, namely for roughly $f_c \geq 30\%$. Above this threshold, a condensate can be safely identified from the presence of sharp diffraction peaks on the momentum density cuts. A limitation of this method is that it is affected by the detector's saturation. Indeed, deep in the superfluid region, the central diffraction peak is saturated when working with $N_{BEC} = 5 \times 10^3$. This effect is illustrated by the presence of a saturation cross on the detector for the datasets below $U/J = 15$. Because of this saturation, our measurement of $P(k_r)$ under-evaluates the contribution of the condensate and, thus, the condensed fraction. However, we know from [49] that the diffraction peaks are not saturated when working with a few thousand atoms. From the additional knowledge of the lattice depth s, one can compute the Fourier transform of the corresponding Wannier function. As illustrated in Figure A.2, adjusting it to the diffraction peak amplitudes at $\pm k_d$ allows us to predict what the amplitude of the central peak would be in the absence of saturation.

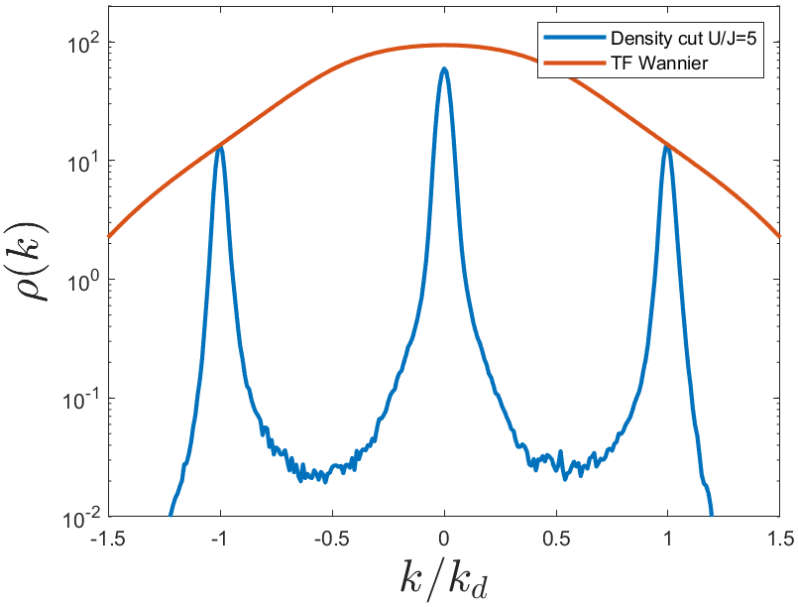

Figure A.2: **Momentum density and Fourier transform of the Wannier function.** A 1D cut of the momentum density at $U/J = 5$ with a transverse integration of $\delta k_\perp = 0.1\, k_d$ is superimposed with the Fourier transform of the corresponding Wannier function. The latter is normalized to coincide with the amplitude of the first-order diffraction peaks. The discrepancy at $k = 0$ reflects the saturation of the central peak from which we deduce the saturation coefficient γ (see text).

The ratio between this expected amplitude and the measured one, $\rho(\boldsymbol{k} = \boldsymbol{0})$, defines the saturation coefficient γ. To correct from the saturation effect, For simplicity, we assume that the saturation evenly affects the momentum region from $\boldsymbol{k} = \boldsymbol{0}$ up to the limit where the density of the central peak reaches that of the first-order diffraction peaks. To correct this effect, the number of atoms detected inside this region is multiplied by γ

in the computation of $P(k_r)$ to infer what the non-saturated atom number would be. The result of this procedure is shown in Figure A.3 for the dataset at $U/J = 5$ ($s = 8$) and $N_{BEC} = 5 \times 10^3$. In the saturated case (in red), the intersection of the linear parts of $P(k_r)$ yields $f_c = 80(1)\%$. As the correction increases artificially the number of atoms at low momenta, $P(k_r)$ increases faster for the corrected data (in blue) and its linear parts cross at a higher condensed fraction $f_c = 85(1)\%$. This correction is reduced at lower condensed fractions, and becomes negligible at $U/J = 15$ where $\gamma \simeq 1$.

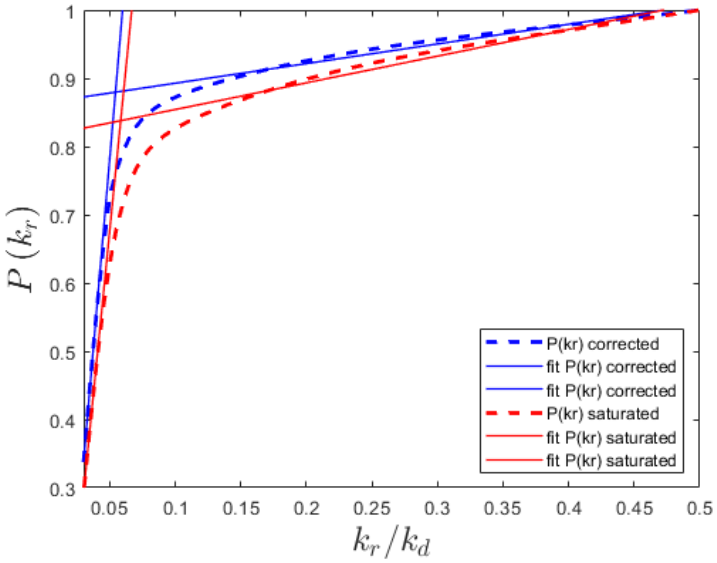

Figure A.3: **Estimation of the condensed fraction from the fraction $P(k_r)$.** The blue (*resp.* red) dashed curve represents the fraction $P(k_r)$ for the $U/J = 5$ dataset with (*resp.* without) the correction of the saturation (see text). The condensed fraction is deduced from the intersection of both linear parts in $P(k_r)$. We obtain$f_c = 85(1)\%$ for in the corrected case and $f_c = 80(1)\%$ for the saturated one.

Appendix

B. Anomalous widths versus U/J

This paragraph briefly comments on the evolution of the anomalous width with the interaction strength. Similarly to the anomalous amplitude, σ_A is obtained from fitting the amplitude of the 1D cuts of the anomalous peak at various transverse integrations (Figure 4.9). The final width is the average of the three fitted values along each lattice axis, and its error is defined as the standard deviation of the mean. The fitted values of σ_A are reported on Table B.1 for all the datasets. A clear trend in the data is hardly distinguishable. Unfortunately, we did not take datasets at low transfer efficiencies, so we cannot quantify the effect of the shot-to-shot center-of-mass fluctuations $\boldsymbol{\delta k}_{com}$ as we did with the dataset at $U/J = 5$. Still, we can compare the experimental values with the theoretical predictions of the trapped system. We estimate the in-trap BEC size L_{BEC} from the Gutzwiller approach with our experimental parameters, from which we derive the expected theoretical size $\sigma_{A,0}$ in the absence of center-of-mass fluctuations. Except for the $U/J = 2$ case, the in-trap BEC size L_{BEC} is found to be globally constant for all. This feature is explained by the competition between external trapping and interaction energy. Indeed, the increase of the on-site interaction energy U tends to increase the spatial extent of the BEC, while this effect is counterbalanced by the increase of the external confinement with the lattice intensity. Therefore, the theoretical width of the anomalous peak should not vary much between $U/J = 5$ and $U/J = 15$. The experimental width σ_A follows a similar trend while its absolute values differ due to the shot-to-shot center-of-mass fluctuations. Although the latter cannot be properly quantified, we expect them to decrease on increasing U/J as the stronger external confinement holds the BEC more tightly. This effect could be at the origin of the larger (resp. smaller) discrepancies between the theoretical and experimental widths for the $U/J = 2$ (resp. $U/J = 15$) datasets. Overall, we consider that the experimental width weakly varies over the U/J values spanned.

dataset	$\sigma_A \times 10^{-3}$ $[k_d]$	L_{BEC} $[d]$	$\sigma_{A,0} \times 10^{-3}$ $[k_d]$
$U/J = 2$	32(1)	20(1)	12(1)
$U/J = 5$	27(2)	15(1)	16(1)
$U/J = 7.5$	27(2)	14(1)	17(1)
$U/J = 10$	30(1)	13(1)	18(1)
$U/J = 12.5$	32(1)	13(1)	18(1)
$U/J = 15$	24(1)	13(1)	18(1)

Table B.1: **Anomalous RMS widths for the different datasets.** The in-trap size of the condensate L_{BEC} is obtained from the $T = 0$ Gutzwiller prediction at $N_{BEC} = 5 \times 10^3$ and the uncertainty reflects the allowed 30% shot-to-shot fluctuations around this atom number. The values of $\sigma_{A,0}$ are obtained from the measured anomalous widths σ_A and the estimated center-of-mass shot-to-shot fluctuations $\boldsymbol{\delta k}_{com}$ via Equation 4.31.

Appendix

C. Linking the probability of a depleted atom belonging to a $k/-k$ pair with the product $\left(g_A^{(2)}(0)-1\right)\langle N_{\Omega_k}\rangle$

The computation of anomalous correlations yields a correlation signal whose non-zero amplitude $g_A^{(2)}(0)-1$ results from the presence of $\boldsymbol{k}/\boldsymbol{-k}$ pairs within the atomic distributions. This part aims at linking explicitly the anomalous amplitude $g_A^{(2)}(0)-1$ to the mean number of $\boldsymbol{k}/\boldsymbol{-k}$ pairs per file $\langle N_{pairs}^{k/-k}\rangle$. More specifically, the final result of this section is the relationship between the probability of a depleted atom belonging to a $\boldsymbol{k}/\boldsymbol{-k}$ pair and the product $\left(g_A^{(2)}(0)-1\right)\langle N_{\Omega_k}\rangle$. The former quantity is expected to increase with the interaction strength according to Bogoliubov's picture and can be compared with the latter that we measure in the experiment. We consider a fictitious dataset containing $\boldsymbol{k}/\boldsymbol{-k}$ pairs, on which we run the anomalous correlations algorithm. The left side of Figure C.1 represents a 1D view of numerator $G_A^{(2)}(\boldsymbol{\delta k})$ of equation 4.22 obtained with this computation. Each voxel i of the histogram contains on average:

- $\langle N_{pairs}^{uncorr}(i)\rangle$ uncorrelated pairs (represented in blue in Figure C.1) originating from the auto-correlation of the part of the momentum density inside Ω_k. This uncorrelated signal corresponds to the result of the denominator computation in Equation 4.22.
- $\langle N_{pairs}^{k/-k}(i)\rangle$ correlated pairs (represented in red in Figure C.1) that denote the number of $\boldsymbol{k}/\boldsymbol{-k}$ pairs whose sum of momenta belongs to the i-th voxel. Of course, $\langle N_{pairs}^{k/-k}(i)\rangle$ is non-zero only at $\boldsymbol{\delta k}\simeq\boldsymbol{0}$ (or multiples of k_d) and decays on the momentum-scale set by the anomalous correlation length σ_A.

The procedure to extract $\langle N_{pairs}^{k/-k}\rangle = \sum_i \langle N_{pairs}^{k/-k}(i)\rangle$ is simple. One first delimits a volume V_0 containing the whole anomalous correlation peak (see Figure C.1). Having defined σ_A as the RMS width of the Bell-shaped anomalous correlation peak, an appropriate choice is $V_0=(6\,\sigma_A)^3$. Then, the mean number of $\boldsymbol{k}/\boldsymbol{-k}$ pairs per file is given by:

$$\langle N_{pairs}^{k/-k}\rangle = \frac{1}{V_0}\left(\int_{V_0}[g_A^{(2)}(\delta k)-1]d(\delta k)\right)\sum_{i=1}^{M}\langle N_{pairs}^{uncorr}(i)\rangle \tag{C.1}$$

with M the number of voxels inside V_0. The interpretation of this equation is straightforward: the number of $\boldsymbol{k}/\boldsymbol{-k}$ pairs corresponds to the integral of the normalized anomalous

amplitude (with a factor $1/V_0$ since $g_A^{(2)}(\delta k)$ has no dimension) times the total background of uncorrelated pairs under the anomalous peak in the numerator histogram. To evaluate this background, one can remark that the momentum density is almost flat inside Ω_k (see Figure 4.21), and can thus be replaced by:

$$\bar{\rho}_{\Omega_k} = \frac{\langle N_{\Omega_k}\rangle}{V_{\Omega_k}} \tag{C.2}$$

This flatness also implies that the uncorrelated signal is approximately constant in the small volume V_0, where it is equal to the auto-correlation of the momentum density C.2 at $\delta k = 0$, namely $\langle N_{\Omega_k}\rangle^2/V_{\Omega_k}$. Under this approximation, the total background of uncorrelated pairs in Equation C.1 becomes:

$$\sum_{i=1}^{M}\langle N_{pairs}^{uncorr}(i)\rangle \simeq \frac{V_0}{V_{\Omega_k}}\langle N_{\Omega_k}\rangle^2 \tag{C.3}$$

Finally, the fact that V_0 has been chosen sufficiently large to contain most of the Gaussian-shaped anomalous correlation peak leads to:

$$\int_{V_0}[g_A^{(2)}(\delta k)-1]d(\delta k) \simeq \left(\sqrt{2\pi}\sigma_A\right)^3\left(g_A^{(2)}(0)-1\right) = \left(\frac{\sqrt{2\pi}}{6}\right)^3 V_0\left(g_A^{(2)}(0)-1\right) \tag{C.4}$$

and Equation C.1 turns into:

$$\langle N_{pairs}^{k/-k}\rangle \simeq \left(\frac{\sqrt{2\pi}}{6}\right)^3 \frac{V_0}{V_{\Omega_k}}\left(g_A^{(2)}(0)-1\right)\langle N_{\Omega_k}\rangle^2 \tag{C.5}$$

Therefore, one sees that $\langle N_{pairs}^{k/-k}\rangle$ can be related to the amplitude of the anomalous correlation function and the mean atom number in Ω_k.

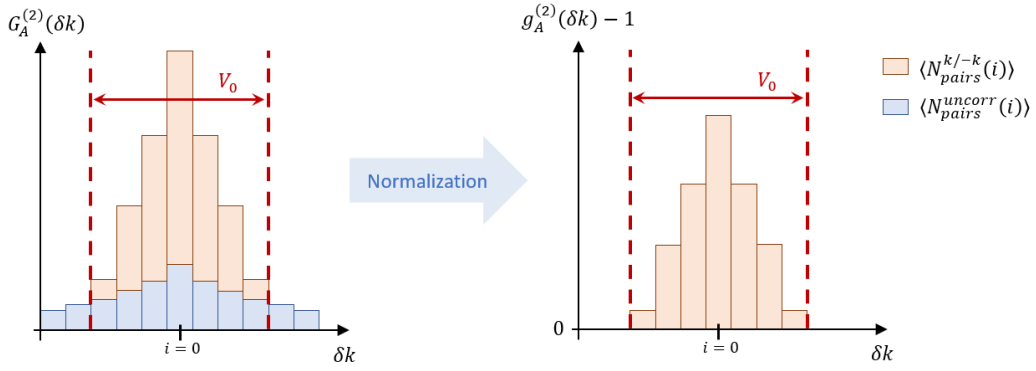

Figure C.1: **1D scheme of the normalization procedure.** Left: 1D histogram $G_A^{(2)}$ whose pixels contain either correlated counts from Bogoliubov pairs (orange shading) or uncorrelated counts (blue shading). Right: After the normalization, each pixel of $g_A^{(2)}$ contains one plus the number of $\boldsymbol{k}$/-$\boldsymbol{k}$ pairs falling inside the corresponding voxel of $G_A^{(2)}$.

To check the validity of this estimate, Figure C.2 shows a comparison with the one of Equation 4.37 where the mean number of pair per file is evaluated by subtracting the number of counts in the numerator and denominator histograms. More specifically, what is plotted in Figure C.2 is the estimate 4.37 (solid black line) computed for a cubic volume

centered on $\boldsymbol{k} = \mathbf{0}$ whose radius corresponds to the x-axis. On increasing this radius, the difference between the number of counts in both histograms is expected to grow as long as the radius considered is smaller than the size of the anomalous correlation peak contained in the numerator. Once the radius exceeds this size, the voxels of the numerator and denominator have more or less the same number of counts, and the number difference saturates at the value of $\langle N_{pairs}^{k/-k} \rangle$. For a typical dataset of 2000 files with 100 atoms per file in Ω_k, the total number of counts in the denominator is $\sim$ 2000 times larger than in the numerator. Therefore, this estimate is highly sensitive to the value of the normalization factor in Equation 4.37. As illustrated in the figure, a 0.3% uncertainty on this normalization factor (gray shaded area) already significantly impacts the estimate's accuracy. On the other hand, the estimate C.5 is plotted as a solid red line, with an uncertainty (red shaded area) reflecting that of the measurements of $\left(g_A^{(2)}(0) - 1\right)$ and $\langle N_{\Omega_k} \rangle$. This figure shows that both estimates are of the same order of magnitude. This agreement is also observed for the other U/J values, confirming the link between $\langle N_{pairs}^{k/-k} \rangle$, $g_A^{(2)}(0) - 1$, and $\langle N_{\Omega_k} \rangle$. Our initial goal is almost met. The last step consists in multiplying Equation C.5 by $2/\langle N_{\Omega_k} \rangle$ to obtain an explicit formula for the probability of a depleted *atom* (hence the factor 2) belonging to a $\boldsymbol{k}$/-$\boldsymbol{k}$ pair:

$$\mathcal{P}_{k/-k} = \frac{2\langle N_{pairs}^{k/-k} \rangle}{\langle N_{\Omega_k} \rangle} \simeq 2 \left(\frac{\sqrt{2\pi}}{6} \right)^3 \frac{V_0}{V_{\Omega_k}} \left(g_A^{(2)}(0) - 1 \right) \langle N_{\Omega_k} \rangle \tag{C.6}$$

The only variable in this formula is the product $\left(g_A^{(2)}(0) - 1\right) \langle N_{\Omega_k} \rangle$ which is accessible experimentally for each dataset.

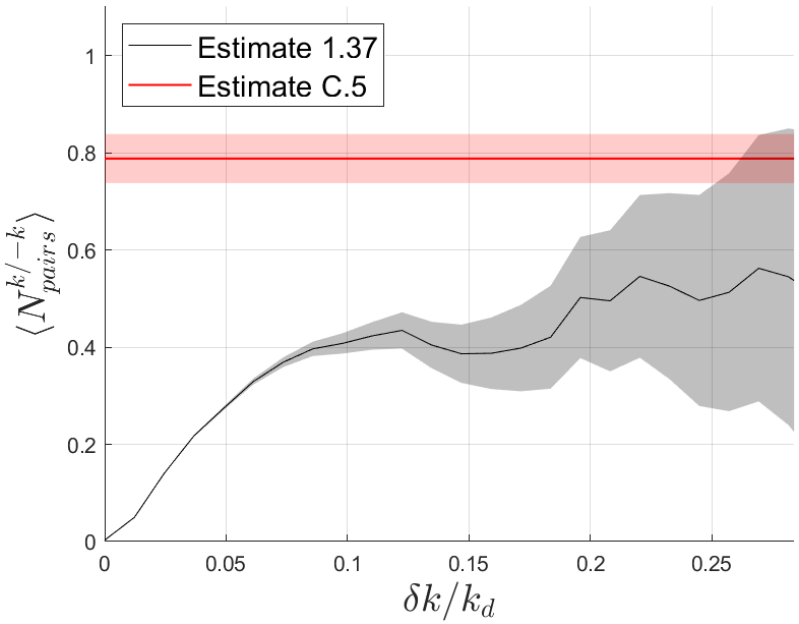

Figure C.2: **Comparison between the estimates 4.37 and C.5 of $\langle N_{pairs}^{k/-k} \rangle$.** Within their uncertainties, both estimates are compatible with each other.

List of Figures

List of Tables

Publications

- H. Cayla, S. Butera, C. Carcy, A. Tenart, G. Hercé, M. Mancini, A. Aspect, I. Carusotto, and D. Clément. **Hanbury-brown and twiss bunching of phonons and of the quantum depletion in a strongly-interacting bose gas**. Physical Review Letters, 125:165301, 2020. Used as reference ecayla2020 in this manuscript.

- C. Carcy, G. Hercé, A. Tenart, T. Roscilde, and D. Clément. **Certifying the adiabatic preparation of ultracold lattice bosons in the vicinity of the mott transition**. Physical Review Letters, 126:045301, 2021. Used as reference [29] in this manuscript.

- G. Hercé, C. Carcy, A. Tenart, J.-P. Bureik, A. Dareau, D. Clément, and T. Roscilde. **Studying the low-entropy Mott transition of bosons in a three-dimensional optical lattice by measuring the full momentum-space density**. Physical Review A, 104:L011301, 2021. Used as reference [30] in this manuscript.

- A. Tenart, G. Hercé, J.-P. Bureik, A. Dareau, and D. Clément. **Observation of pairs of atoms at opposite momenta in an equilibrium interacting bose gas**. Nature Physics, 17:1364–1368, 2021. Used as reference [32] in this manuscript.

- G. Hercé, J.-P. Bureik, A. Tenart, A. Aspect, A. Dareau, and D. Clément. **Full counting statistics of interacting lattice gases after an expansion: quantifying many-body coherence from atom correlations**. Used as reference [31] in this manuscript.

Bibliography

[1] S. S. Hodgman et al. “Direct Measurement of Long-Range Third-Order Coherence in Bose-Einstein Condensates”. In: *Science* 331.6020 (2011), pages 1046–1049.

[2] R. Lopes et al. “Quantum Depletion of a Homogeneous Bose-Einstein Condensate”. In: *Physical Review Letters* 119 (2017), page 190404.

[3] Max Planck. “Ueber das Gesetz der Energieverteilung im Normalspectrum”. In: *Annalen der Physik* 309.3 (1901), pages 553–563.

[4] A. Einstein. “Über einen die Erzeugung und Verwandlung des Lichtes betreffenden heuristischen Gesichtspunkt”. In: *Annalen der Physik* 322.6 (1905), pages 132–148.

[5] Louis de Broglie. “XXXV. A tentative theory of light quanta”. In: *The London, Edinburgh, and Dublin Philosophical Magazine and Journal of Science* 47.278 (1924), pages 446–458.

[6] C. Davisson and L. H. Germer. “Diffraction of Electrons by a Crystal of Nickel”. In: *Phys. Rev.* 30 (6 Dec. 1927), pages 705–740.

[7] Steven Chu. “Nobel Lecture: The manipulation of neutral particles”. In: *Rev. Mod. Phys.* 70 (3 July 1998), pages 685–706.

[8] Claude N. Cohen-Tannoudji. “Nobel Lecture: Manipulating atoms with photons”. In: *Rev. Mod. Phys.* 70 (3 July 1998), pages 707–719.

[9] Wolfgang Ketterle and NJ Van Druten. “Evaporative cooling of trapped atoms”. In: *Advances in atomic, molecular, and optical physics* 37 (1996), pages 181–236.

[10] M. H. Anderson et al. “Observation of Bose-Einstein Condensation in a Dilute Atomic Vapor”. In: *Science* 269.5221 (1995), pages 198–201.

[11] Kendall B Davis et al. “Bose-Einstein condensation in a gas of sodium atoms”. In: *Physical review letters* 75.22 (1995), page 3969.

[12] RichardP Feynman. “Simulating physics with computers”. In: *International Journal of Theoretical Physics* 21.6-7 (1982), pages 467–488.

[13] Ehud Altman et al. “Quantum Simulators: Architectures and Opportunities”. In: *PRX Quantum* 2 (1 Feb. 2021), page 017003.

[14] R. Blatt and C. F. Roos. “Quantum simulations with trapped ions”. In: *Nature Physics* 8.4 (2012), pages 277–284.

[15] Pascal Scholl et al. “Quantum simulation of 2D antiferromagnets with hundreds of Rydberg atoms”. In: *Nature* 595.7866 (2021), pages 233–238.

[16] R. Barends et al. “Digital quantum simulation of fermionic models with a superconducting circuit”. In: *Nature Communications* 6.1 (2015), pages 7654–7660.

[17] Jacob A Blackmore et al. “Ultracold molecules for quantum simulation: rotational coherences in CaF and RbCs”. In: 4.1 (Dec. 2018), page 014010.

[18] Immanuel Bloch, Jean Dalibard, and Sylvain Nascimbène. “Quantum simulations with ultracold quantum gases”. In: *Nature Physics* 8.4 (2012), pages 267–276.

[19] Markus Greiner et al. “Quantum phase transition from a superfluid to a Mott insulator in a gas of ultracold atoms”. In: *Nature* 415.6867 (2002), pages 39–44.

[20] Dieter Jaksch et al. “Cold bosonic atoms in optical lattices”. In: *Physical Review Letters* 81.15 (1998), page 3108.

[21] Herwig Ott. “Single atom detection in ultracold quantum gases: A review of current progress”. In: *Reports on progress in physics. Physical Society (Great Britain)* 79 (Apr. 2016), page 054401.

[22] Joseph W. Britton et al. “A trapped-ion quantum simulator is used to demonstrate tunable long-range spin-spin couplings in two dimensions, relevant to studies of quantum magnetism at a scale that is intractable for classical computers.” In: *Nature* 484.7395 (2012), pages 489–492.

[23] F. Nogrette et al. “Single-Atom Trapping in Holographic 2D Arrays of Microtraps with Arbitrary Geometries”. In: *Phys. Rev. X* 4 (2 May 2014), page 021034.

[24] Waseem S Bakr et al. “A quantum gas microscope for detecting single atoms in a Hubbard-regime optical lattice”. In: *Nature* 462.7269 (2009), pages 74–77.

[25] R. Bücker et al. “Twin-atom beams”. In: *Nature Physics* 7 (2011), pages 608–611.

[26] Anton Öttl et al. “Correlations and counting statistics of an atom laser”. In: *Physical Review Letters* 95.9 (2005), page 090404.

[27] Tatjana Gericke et al. “High-resolution scanning electron microscopy of an ultracold quantum gas”. In: *Nature Physics* 4.12 (2008), pages 949–953.

[28] M. Schellekens et al. “Hanbury Brown Twiss Effect for Ultracold Quantum Gases”. In: *Science* 310.5748 (2005), pages 648–651.

[29] Cécile Carcy et al. “Certifying the adiabatic preparation of ultracold lattice bosons in the vicinity of the Mott transition”. In: *Physical Review Letters* 126.4 (2021), page 045301.

[30] Gaétan Hercé et al. “Studying the low-entropy Mott transition of bosons in a three-dimensional optical lattice by measuring the full momentum-space density”. In: *Physical Review A* 104 (2021).

[31] Gaétan Hercé et al. “Full counting statistics of interacting lattice gases after an expansion: quantifying many-body coherence from atom correlations”. In: *arXiv preprint arXiv:2207.14070* (2021).

[32] Antoine Tenart et al. “Observation of pairs of atoms at opposite momenta in an equilibrium interacting Bose gas”. In: *Nature Physics* 17.12 (2021), pages 1364–1368.

[33] N Bogoliubov. “On the theory of superfluidity”. In: *Journal of Physics (USSR)* 11.1 (1947), page 23.

[34] Alice Robert et al. “A Bose-Einstein condensate of metastable atoms”. In: *Science* 292.5516 (2001), pages 461–464.

[35] F Pereira Dos Santos et al. “Bose-Einstein condensation of metastable helium”. In: *Physical Review Letters* 86.16 (2001), page 3459.

[36] JM McNamara et al. “Degenerate Bose-Fermi mixture of metastable atoms”. In: *Physical Review Letters* 97.8 (2006), page 080404.

[37] Sayan Patra et al. “Proton-electron mass ratio from laser spectroscopy of HD⁺ at the part-per-trillion level”. In: *Science* 369.6508 (2020), pages 1238–1241.

[38] AH Abbas et al. “Rapid generation of metastable helium Bose-Einstein condensates”. In: *Physical Review A* 103.5 (2021), page 053317.

[39] Michael Keller et al. “Bose-Einstein condensate of metastable helium for quantum correlation experiments”. In: *Physical Review A* 90.6 (2014), page 063607.

[40] Pierre Dussarrat et al. “Two-particle four-mode interferometer for atoms”. In: *Physical review letters* 119.17 (2017), page 173202.

[41] F Bardou et al. “Magneto-optical trapping of metastable helium: collisions in the presence of resonant light”. In: *EPL (Europhysics Letters)* 20.8 (1992), page 681.

[42] F Pereira Dos Santos et al. “Penning collisions of laser-cooled metastable helium atoms”. In: *The European Physical Journal D-Atomic, Molecular, Optical and Plasma Physics* 14.1 (2001), pages 15–22.

[43] PO Fedichev et al. “Inelastic decay processes in a gas of spin-polarized triplet helium”. In: *Physical Review A* 53.3 (1996), page 1447.

[44] T. Jeltes et al. “Comparison of the Hanbury Brown–Twiss effect for bosons and fermions”. In: *Nature* 445.7126 (2007), pages 402–405.

[45] Q Bouton et al. “Fast production of Bose-Einstein condensates of metastable helium”. In: *Physical Review A* 91.6 (2015), page 061402.

[46] Lynn Hoendervanger. “A New Metastable Helium Machine : An Investigation into the Attributes of Trapping, Cooling and Detecting Metastable Helium”. 2014IOTA0006. PhD thesis. 2014.

[47] Quentin Bouton. “Etude miscroscopique de la distibution en impulsion de condensats de Bose-Eintein d’Hélium métastable”. Theses. Université Paris Saclay (COmUE), Nov. 2016.

[48] Hugo Cayla. “Measuring the momentum distribution of a lattice gas at the single-atom level”. Theses. Université Paris Saclay (COmUE), Nov. 2018.

[49] Cecile Carcy. “Investigation of the Mott transition with metastable Helium atoms”. Theses. Université Paris Saclay (COmUE), Nov. 2019.

[50] F. Moron et al. “An oscillator circuit to produce a radio-frequency discharge and application to metastable helium saturated absorption spectroscopy”. In: *Review of Scientific Instruments* 83.4 (2012), page 044705.

[51] Steven Chu et al. “Three-dimensional viscous confinement and cooling of atoms by resonance radiation pressure”. In: *Physical review letters* 55.1 (1985), page 48.

[52] Jean Dalibard. “Une brève histoire des atomes froids”. In: *Cours du Collège de France* (2015).

[53] Wim Vassen et al. “Cold and trapped metastable noble gases”. In: *Rev. Mod. Phys.* 84 (1 Feb. 2012), pages 175–210.

[54] Rockson Chang et al. “Three-dimensional laser cooling at the Doppler limit”. In: *Physical Review A* 90.6 (2014), page 063407.

[55] C Valentin et al. “One-Dimension Sub-Doppler Molasses in the Presence of Static Magnetic Field”. In: *Europhysics Letters (EPL)* 17.2 (Jan. 1992), pages 133–138.

[56] William D Phillips and Harold Metcalf. “Laser deceleration of an atomic beam”. In: *Physical Review Letters* 48.9 (1982), page 596.

[57] E. L. Raab et al. “Trapping of Neutral Sodium Atoms with Radiation Pressure”. In: *Phys. Rev. Lett.* 59 (23 Dec. 1987), pages 2631–2634.

[58] Jean Dalibard and Claude Cohen-Tannoudji. “Laser cooling below the Doppler limit by polarization gradients: simple theoretical models”. In: *JOSA B* 6.11 (1989), pages 2023–2045.

[59] A. S. Tychkov et al. “Metastable helium Bose-Einstein condensate with a large number of atoms”. In: *Phys. Rev. A* 73 (3 Mar. 2006), page 031603.

[60] R.G. Dall and A.G. Truscott. “Bose–Einstein condensation of metastable helium in a bi-planar quadrupole Ioffe configuration trap”. In: *Optics Communications* 270.2 (2007), pages 255–261. ISSN: 0030-4018.

[61] Ettore Majorana. “Atomi orientati in campo magnetico variabile”. In: *Il Nuovo Cimento* 9.2 (1932), pages 43–50.

[62] M. D. Barrett, J. A. Sauer, and M. S. Chapman. “All-Optical Formation of an Atomic Bose-Einstein Condensate”. In: *Phys. Rev. Lett.* 87 (1 June 2001), page 010404.

[63] J.-F. Clément et al. “All-optical runaway evaporation to Bose-Einstein condensation”. In: *Phys. Rev. A* 79 (6 June 2009), page 061406.

[64] Y.-J. Lin et al. “Rapid production of ^{87}Rb Bose-Einstein condensates in a combined magnetic and optical potential”. In: *Phys. Rev. A* 79 (6 June 2009), page 063631.

[65] GV Shlyapnikov et al. “Decay kinetics and Bose condensation in a gas of spin-polarized triplet helium”. In: *Physical review letters* 73.24 (1994), page 3247.

[66] Rudolf Grimm, Matthias Weidemüller, and Yurii B Ovchinnikov. “Optical dipole traps for neutral atoms”. In: *Advances in atomic, molecular, and optical physics* 42 (2000), pages 95–170.

[67] William. Aberth. “Microchannel plate for surface-induced dissociation in mass spectrometry”. In: *Analytical Chemistry* 62.6 (1990), pages 609–611.

[68] Wesley H Smith. “Triggering at LHC experiments”. In: *Nuclear Instruments and Methods in Physics Research Section A: Accelerators, Spectrometers, Detectors and Associated Equipment* 478.1 (2002). Proceedings of the ninth Int.Conf. on Instrumentation, pages 62–67. ISSN: 0168-9002.

[69] Lars von der Wense et al. “Direct detection of the 229Th nuclear clock transition”. In: *Nature* 533.7601 (2016), pages 47–51.

[70] Yoshiya Harada, Shigeru Masuda, and Hiroyuki Ozaki. “Electron spectroscopy using metastable atoms as probes for solid surfaces”. In: *Chemical reviews* 97.6 (1997), pages 1897–1952.

[71] AL Hoendervanger et al. “Influence of gold coating and interplate voltage on the performance of chevron micro-channel plates for temporally and spatially resolved single particle detection”. In: *Review of Scientific Instruments* 84.2 (2013), page 023307.

[72] O. Jagutzki et al. “Multiple hit readout of a microchannel plate detector with a three-layer delay-line anode”. In: *IEEE Transactions on Nuclear Science* 49.5 (2002), pages 2477–2483.

[73] F Nogrette et al. “Characterization of a detector chain using a FPGA-based time-to-digital converter to reconstruct the three-dimensional coordinates of single particles at high flux”. In: *Review of Scientific Instruments* 86.11 (2015), page 113105.

[74] Antoine Ténart. “Momentum-space correlations in the depletion of weakly interacting lattice Bose gases”. Theses. Université Paris-Saclay, Dec. 2021.

[75] Michael L Edgar, JS Lapington, and Alan Smith. “The spatial extent of gain depression for MCP-based photon detectors”. In: *Review of scientific instruments* 63.1 (1992), pages 816–819.

[76] Chao Zhang. *Building and characterizing an external cavity laser at 1083 nm*. Internship report. 2019.

[77] C. Cohen-Tannoudji, F. Laloe, and B. Diu. *Mécanique quantique - tome III*. SAVOIRS ACTUELS. EDP sciences, 2017. ISBN: 9782759821518.

[78] Olivier Sirjean. “Collisions ionisantes : un nouveau diagnostic pour les condensats de Bose-Einstein d’hélium métastable”. J.F. Roch Rapporteur J. Vigué Rapporteur D. Boiron Examinateur A. Lahmam-Bennani Examinateur-Président M. Leduc Examinateur A. Aspect Directeur de These. Theses. Université Paris Sud - Paris XI, June 2003.

[79] Shina Tan. “Large momentum part of a strongly correlated Fermi gas”. In: *Annals of Physics* 323.12 (2008), pages 2971–2986.

[80] Tangi Morvan. *Dynamique des pertes à deux corps dans les gaz de Bose unidimensionnels en interaction*. Internship report. 2021.

[81] Y. Castin and R. Dum. “Bose-Einstein Condensates in Time Dependent Traps”. In: *Phys. Rev. Lett.* 77 (27 Dec. 1996), pages 5315–5319.

[82] T. M. F. Hirsch, D. G. Cocks, and S. S. Hodgman. “Close-coupled model of Feshbach resonances in ultracold ^{3}He* and ^{4}He* atomic collisions”. In: *Phys. Rev. A* 104 (3 Sept. 2021), page 033317.

[83] Fabrice Gerbier et al. “Phase Coherence of an Atomic Mott Insulator”. In: *Phys. Rev. Lett.* 95 (5 July 2005), page 050404.

[84] Joern N Kupferschmidt and Erich J Mueller. “Role of interactions in time-of-flight expansion of atomic clouds from optical lattices”. In: *Physical Review A* 82.2 (2010), page 023618.

[85] Shiang Fang, Ray-Kuang Lee, and Daw-Wei Wang. “Quantum fluctuations and condensate fraction during time-of-flight expansion”. In: *Phys. Rev. A* 82 (3 Sept. 2010), page 031601.

[86] Markus Greiner et al. “Exploring phase coherence in a 2D lattice of Bose-Einstein condensates”. In: *Physical Review Letters* 87.16 (2001), page 160405.

[87] Paweł Ziń, Jan Chwedeńczuk, and Marek Trippenbach. “Elastic scattering losses from colliding Bose-Einstein condensates”. In: *Physical Review A* 73.3 (2006), page 033602.

[88] Aurélien Perrin et al. “Observation of atom pairs in spontaneous four-wave mixing of two colliding Bose-Einstein condensates”. In: *Physical Review Letters* 99.15 (2007), page 150405.

[89] Roman I Khakimov et al. "Ghost imaging with atoms". In: *Nature* 540.7631 (2016), pages 100–103.

[90] Antoine Tenart et al. "Two-body collisions in the time-of-flight dynamics of lattice Bose superfluids". In: *Physical Review Research* 2.1 (2020), page 013017.

[91] F Gerbier et al. "Expansion of a quantum gas released from an optical lattice". In: *Physical review letters* 101.15 (2008), page 155303.

[92] E Toth, AM Rey, and PB Blakie. "Theory of correlations between ultracold bosons released from an optical lattice". In: *Physical Review A* 78.1 (2008), page 013627.

[93] Hugo Cayla et al. "Single-atom-resolved probing of lattice gases in momentum space". In: *Physical Review A* 97.6 (2018), page 061609.

[94] J H de Boer and E J W Verwey. "Semi-conductors with partially and with completely filled $_3d$-lattice bands". In: *Proceedings of the Physical Society* 49.4S (Aug. 1937), pages 59–71.

[95] N. F. Mott and R Peierls. "Discussion of the paper by de Boer and Verwey". In: *Proceedings of the Physical Society* 49.4S (Aug. 1937), pages 72–73.

[96] N F Mott. "The Basis of the Electron Theory of Metals, with Special Reference to the Transition Metals". In: *Proceedings of the Physical Society. Section A* 62.7 (July 1949), pages 416–422.

[97] N. F. Mott. "On the transition to metallic conduction in semiconductors". In: *Canadian Journal of Physics* 34.12A (1956), pages 1356–1368.

[98] N. F. Mott. "The transition to the metallic state". In: *The Philosophical Magazine: A Journal of Theoretical Experimental and Applied Physics* 6.62 (1961), pages 287–309.

[99] Masatoshi Imada, Atsushi Fujimori, and Yoshinori Tokura. "Metal-insulator transitions". In: *Rev. Mod. Phys.* 70 (4 Oct. 1998), pages 1039–1263.

[100] J. Hubbard and Brian Hilton Flowers. "Electron correlations in narrow energy bands". In: *Proceedings of the Royal Society of London. Series A. Mathematical and Physical Sciences* 276.1365 (1963), pages 238–257.

[101] J. Hubbard and Brian Hilton Flowers. "Electron correlations in narrow energy bands. II. The degenerate band case". In: *Proceedings of the Royal Society of London. Series A. Mathematical and Physical Sciences* 277.1369 (1964), pages 237–259.

[102] J. Hubbard and Brian Hilton Flowers. "Electron correlations in narrow energy bands III. An improved solution". In: *Proceedings of the Royal Society of London. Series A. Mathematical and Physical Sciences* 281.1386 (1964), pages 401–419.

[103] Robert Jördens et al. "A Mott insulator of fermionic atoms in an optical lattice". In: *Nature* 455.7210 (2008), pages 204–207.

[104] U. Schneider et al. "Metallic and Insulating Phases of Repulsively Interacting Fermions in a 3D Optical Lattice". In: *Science* 322.5907 (2008), pages 1520–1525.

[105] Jean Dalibard. "Des cages de lumière pour les atomes: la physique des pièges et des réseaux optiques". In: *Cours du Collège de France* (2013).

[106] Fabrice Gerbier. "Quantum gas in optical lattices". In: *Lecture notes* (2015).

[107] Neil W Ashcroft, N David Mermin, et al. *Solid state physics*. 1976.

[108] Gregory H Wannier. "The structure of electronic excitation levels in insulating crystals". In: *Physical Review* 52.3 (1937), page 191.

[109] Matthew PA Fisher et al. "Boson localization and the superfluid-insulator transition". In: *Physical Review B* 40.1 (1989), page 546.

[110] Subir Sachdev. *Quantum Phase Transitions*. 2nd edition. Cambridge University Press, 2011.

[111] Matthias Vojta. "Quantum phase transitions". In: *Reports on Progress in Physics* 66.12 (Nov. 2003), pages 2069–2110.

[112] Massimo Campostrini et al. "Critical behavior of the three-dimensional XY universality class". In: *Phys. Rev. B* 63 (21 May 2001), page 214503.

[113] D Van Oosten, Peter van der Straten, and HTC Stoof. "Quantum phases in an optical lattice". In: *Physical Review A* 63.5 (2001), page 053601.

[114] K Sheshadri et al. "Superfluid and insulating phases in an interacting-boson model: Mean-field theory and the RPA". In: *EPL (Europhysics Letters)* 22.4 (1993), page 257.

[115] J. K. Freericks and H. Monien. "Strong-coupling expansions for the pure and disordered Bose-Hubbard model". In: *Phys. Rev. B* 53 (5 Feb. 1996), pages 2691–2700.

[116] K. Sengupta and N. Dupuis. "Mott-insulator–to–superfluid transition in the Bose-Hubbard model: A strong-coupling approach". In: *Phys. Rev. A* 71 (3 Mar. 2005), page 033629.

[117] Daniel S Rokhsar and BG Kotliar. "Gutzwiller projection for bosons". In: *Physical Review B* 44.18 (1991), page 10328.

[118] Werner Krauth, Michel Caffarel, and Jean-Philippe Bouchaud. "Gutzwiller wave function for a model of strongly interacting bosons". In: *Phys. Rev. B* 45 (6 Feb. 1992), pages 3137–3140.

[119] Wilhelm Zwerger. "Mott Hubbard transition of cold atoms in optical lattices". In: *Journal of Optics B: Quantum and Semiclassical Optics* 5.2 (Apr. 2003), S9–S16.

[120] Lode Pollet. "Recent developments in quantum Monte Carlo simulations with applications for cold gases". In: *Reports on progress in physics* 75.9 (2012), page 094501.

[121] Ghassan George Batrouni, Richard T. Scalettar, and Gergely T. Zimanyi. "Quantum critical phenomena in one-dimensional Bose systems". In: *Phys. Rev. Lett.* 65 (14 Oct. 1990), pages 1765–1768.

[122] Richard T. Scalettar, Ghassan George Batrouni, and Gergely T. Zimanyi. "Localization in interacting, disordered, Bose systems". In: *Phys. Rev. Lett.* 66 (24 June 1991), pages 3144–3147.

[123] W Krauth and N Trivedi. "Mott and Superfluid Transitions in a Strongly Interacting Lattice Boson System". In: *Europhysics Letters (EPL)* 14.7 (Apr. 1991), pages 627–632.

[124] Werner Krauth, Nandini Trivedi, and David Ceperley. "Superfluid-insulator transition in disordered boson systems". In: *Phys. Rev. Lett.* 67 (17 Oct. 1991), pages 2307–2310.

[125] Ghassan George Batrouni and Richard T. Scalettar. "World-line quantum Monte Carlo algorithm for a one-dimensional Bose model". In: *Phys. Rev. B* 46 (14 Oct. 1992), pages 9051–9062.

[126] B. Capogrosso-Sansone, N. V. Prokof'ev, and B. V. Svistunov. "Phase diagram and thermodynamics of the three-dimensional Bose-Hubbard model". In: *Phys. Rev. B* 75 (13 Apr. 2007), page 134302.

[127] Jongchul Mun et al. "Phase Diagram for a Bose-Einstein Condensate Moving in an Optical Lattice". In: *Phys. Rev. Lett.* 99 (15 Oct. 2007), page 150604.

[128] C Becker et al. "Ultracold quantum gases in triangular optical lattices". In: *New Journal of Physics* 12.6 (June 2010), page 065025.

[129] Claire K. Thomas et al. "Mean-Field Scaling of the Superfluid to Mott Insulator Transition in a 2D Optical Superlattice". In: *Phys. Rev. Lett.* 119 (10 Sept. 2017), page 100402.

[130] M. J. Mark et al. "Precision Measurements on a Tunable Mott Insulator of Ultracold Atoms". In: *Phys. Rev. Lett.* 107 (17 Oct. 2011), page 175301.

[131] T. A. Savard, K. M. O'Hara, and J. E. Thomas. "Laser-noise-induced heating in far-off resonance optical traps". In: *Phys. Rev. A* 56 (2 Aug. 1997), R1095–R1098.

[132] S. Friebel et al. "CO_2-laser optical lattice with cold rubidium atoms". In: *Phys. Rev. A* 57 (1 Jan. 1998), R20–R23.

[133] Fabrice Gerbier. "Boson Mott insulators at finite temperatures". In: *Physical Review Letters* 99.12 (2007), page 120405.

[134] Tosio Kato. "On the Adiabatic Theorem of Quantum Mechanics". In: *Journal of the Physical Society of Japan* 5.6 (1950), pages 435–439.

[135] Nikolai Il'in, Anastasia Aristova, and Oleg Lychkovskiy. "Adiabatic theorem for closed quantum systems initialized at finite temperature". In: *Phys. Rev. A* 104 (3 Sept. 2021), page L030202.

[136] J Hecker Denschlag et al. "A Bose-Einstein condensate in an optical lattice". In: *Journal of Physics B: Atomic, Molecular and Optical Physics* 35.14 (July 2002), pages 3095–3110.

[137] T. Gericke et al. "Adiabatic loading of a Bose–Einstein condensate in a 3D optical lattice". In: *Journal of Modern Optics* 54.5 (2007), pages 735–743.

[138] Jacob F Sherson et al. "Single-atom-resolved fluorescence imaging of an atomic Mott insulator". In: *Nature* 467.7311 (2010), pages 68–72.

[139] Sara Bergkvist, Patrik Henelius, and Anders Rosengren. "Local-density approximation for confined bosons in an optical lattice". In: *Physical Review A* 70.5 (2004), page 053601.

[140] S. Trotzky et al. "Suppression of the critical temperature for superfluidity near the Mott transition". In: *Nature Physics* 6.12 (2010), pages 998–1004.

[141] Tommaso Roscilde. "Bosons in one-dimensional incommensurate superlattices". In: *Phys. Rev. A* 77 (6 June 2008), page 063605.

[142] S Yoshimura, S Konabe, and T Nikuni. "Adiabatic cooling and heating of cold bosons in three-dimensional optical lattices and the superfluid-normal phase transition". In: *Physical Review A* 78.1 (2008), page 015602.

[143] Lev Pitaevskii and Sandro Stringari. *Bose-Einstein condensation and superfluidity.* Volume 164. Oxford University Press, 2016.

[144] Adriaan Van den Bos. *Parameter estimation for scientists and engineers.* John Wiley & Sons, 2007.

[145] Ronald A Fisher. "On the mathematical foundations of theoretical statistics". In: *Philosophical Transactions of the Royal Society of London. Series A, Containing Papers of a Mathematical or Physical Character* 222.594-604 (1922), pages 309–368.

[146] Hugo Cayla et al. "Hanbury-Brown and Twiss bunching of phonons and of the quantum depletion in a strongly-interacting Bose gas". In: *Physical Review Letters* 125 (2020), page 165301.

[147] Ping Nang Ma et al. "Influence of the trap shape on the detection of the superfluid—Mott-insulator transition". In: *Phys. Rev. A* 78 (2 Aug. 2008), page 023605.

[148] Kenji Harada and Naoki Kawashima. "Kosterlitz-Thouless Transition of Quantum XY Model in Two Dimensions". In: *Journal of the Physical Society of Japan* 67.8 (1998), pages 2768–2776.

[149] Thilo Stöferle et al. "Transition from a Strongly Interacting 1D Superfluid to a Mott Insulator". In: *Phys. Rev. Lett.* 92 (13 Mar. 2004), page 130403.

[150] Simon Braun et al. "Emergence of coherence and the dynamics of quantum phase transitions". In: *Proceedings of the National Academy of Sciences* 112.12 (2015), pages 3641–3646.

[151] Alexander Keesling et al. "Quantum Kibble–Zurek mechanism and critical dynamics on a programmable Rydberg simulator". In: *Nature* 568.7751 (2019), pages 207–211.

[152] Alexander L. Gaunt et al. "Bose-Einstein Condensation of Atoms in a Uniform Potential". In: *Phys. Rev. Lett.* 110 (20 May 2013), page 200406.

[153] Yoav Sagi et al. "Measurement of the Homogeneous Contact of a Unitary Fermi Gas". In: *Phys. Rev. Lett.* 109 (22 Nov. 2012), page 220402.

[154] Ya.M. Blanter and M. Büttiker. "Shot noise in mesoscopic conductors". In: *Physics Reports* 336.1 (2000), pages 1–166. ISSN: 0370-1573.

[155] Crispin Gardiner and Peter Zoller. *Quantum noise: a handbook of Markovian and non-Markovian quantum stochastic methods with applications to quantum optics.* Springer Science & Business Media, 2004.

[156] E. A. Burt et al. "Coherence, Correlations, and Collisions: What One Learns about Bose-Einstein Condensates from Their Decay". In: *Phys. Rev. Lett.* 79 (3 July 1997), pages 337–340.

[157] Ehud Altman, Eugene Demler, and Mikhail D. Lukin. "Probing many-body states of ultracold atoms via noise correlations". In: *Phys. Rev. A* 70 (1 July 2004), page 013603.

[158] T. Schweigler et al. "Experimental characterization of a quantum many-body system via higher-order correlations". In: *Nature* 545 (2017), page 323.

[159] Leonid S. Levitov, Hyunwoo Lee, and Gordey B. Lesovik. "Electron counting statistics and coherent states of electric current". In: *Journal of Mathematical Physics* 37.10 (1996), pages 4845–4866.

[160] T. Cubel Liebisch et al. "Atom Counting Statistics in Ensembles of Interacting Rydberg Atoms". In: *Phys. Rev. Lett.* 95 (25 Dec. 2005), page 253002.

[161] N. Malossi et al. "Full Counting Statistics and Phase Diagram of a Dissipative Rydberg Gas". In: *Phys. Rev. Lett.* 113 (2 July 2014), page 023006.

[162] Johannes Zeiher et al. “Many-body interferometry of a Rydberg-dressed spin lattice”. In: *Nature Physics* 12 (12 July 20116), pages 1095–1099.

[163] Maxime Perrier et al. “Thermal counting statistics in an atomic two-mode squeezed vacuum state”. In: *arXiv preprint arXiv:1904.04135* (2019).

[164] D. A. Ivanov and A. G. Abanov. “Phase transitions in full counting statistics for periodic pumping”. In: *Europhysics Letters* 92.3 (Nov. 2010), page 37008.

[165] Fernando J. Gómez-Ruiz, Jack J. Mayo, and Adolfo del Campo. “Full Counting Statistics of Topological Defects after Crossing a Phase Transition”. In: *Phys. Rev. Lett.* 124 (24 June 2020), page 240602.

[166] P. Devillard et al. “Full counting statistics of the momentum occupation numbers of the Tonks-Girardeau gas”. In: *Phys. Rev. A* 101 (6 June 2020), page 063604.

[167] Viktor Eisler. “Universality in the Full Counting Statistics of Trapped Fermions”. In: *Phys. Rev. Lett.* 111 (8 Aug. 2013), page 080402.

[168] Izabella Lovas et al. “Full counting statistics of time-of-flight images”. In: *Phys. Rev. A* 95 (5 May 2017), page 053621.

[169] Israel Klich and Leonid Levitov. “Quantum Noise as an Entanglement Meter”. In: *Phys. Rev. Lett.* 102 (10 Mar. 2009), page 100502.

[170] Massimiliano Esposito, Upendra Harbola, and Shaul Mukamel. “Nonequilibrium fluctuations, fluctuation theorems, and counting statistics in quantum systems”. In: *Rev. Mod. Phys.* 81 (4 Dec. 2009), pages 1665–1702.

[171] Steven T Flammia et al. “Quantum tomography via compressed sensing: error bounds, sample complexity and efficient estimators”. In: *New Journal of Physics* 14.9 (Sept. 2012), page 095022.

[172] Eric Brunner, Andreas Buchleitner, and Gabriel Dufour. *Many-body coherence and entanglement from randomized correlation measurements*. 2021.

[173] Piero Naldesi et al. *Fermionic correlation functions from randomized measurements in programmable atomic quantum devices*. 2022.

[174] Cécile Carcy et al. “Momentum-space atom correlations in a Mott insulator”. In: *Physical Review X* 9.4 (2019), page 041028.

[175] S. Fölling et al. “Spatial quantum noise interferometry in expanding ultracold atom clouds”. In: *Nature* 434 (2005), pages 481–484.

[176] J Stenger et al. “Bragg spectroscopy of a Bose-Einstein condensate”. In: *Physical Review Letters* 82.23 (1999), page 4569.

[177] M. A. Kristensen et al. “Observation of Atom Number Fluctuations in a Bose-Einstein Condensate”. In: *Phys. Rev. Lett.* 122 (16 Apr. 2019), page 163601.

[178] Y. Castin and R. Dum. “Low-temperature Bose-Einstein condensates in time-dependent traps: Beyond the $U(1)$ symmetry-breaking approach”. In: *Phys. Rev. A* 57 (4 Apr. 1998), pages 3008–3021.

[179] Joseph W Goodman. “Statistical optics”. In: *New York, Wiley-Interscience, 1985, 567 p.* 1 (1985).

[180] Roy J Glauber. “The quantum theory of optical coherence”. In: *Physical Review* 130.6 (1963), page 2529.

[181] Roy J Glauber. “Coherent and incoherent states of the radiation field”. In: *Physical Review* 131.6 (1963), page 2766.

[182] Alain Aspect. *Current Trends in Atomic Physics*. Edited by Antoine Browaeys et al. Oxford University Press, May 2019. ISBN: 9780198837190.

[183] R. G. Dall et al. "Ideal n-body correlations with massive particles". In: *Nature Physics* 9.6 (2013), pages 341–344.

[184] A. Bergschneider et al. "Experimental Characterization of Two-Particle Entanglement through Position and Momentum Correlations". In: *Nature Physics* 15 (2019), pages 640–644.

[185] M. Holten et al. "Observation of Cooper pairs in a mesoscopic two-dimensional Fermi gas". In: *Nature* 606.7913 (2002), pages 287–291.

[186] Pavel E. Dolgirev et al. "Non-Gaussian correlations imprinted by local dephasing in fermionic wires". In: *Phys. Rev. B* 102 (10 Sept. 2020), page 100301.

[187] C. Fabre and N. Treps. "Modes and states in quantum optics". In: *Rev. Mod. Phys.* 92 (3 Sept. 2020), page 035005.

[188] Mattia Walschaers. "Non-Gaussian Quantum States and Where to Find Them". In: *PRX Quantum* 2 (3 Sept. 2021), page 030204.

[189] R. Hanbury-Brown and R. Q. Twiss. "A test of a new type of interferometer on Sirius". In: *Nature* 178 (1956), pages 1046–1048.

[190] V. Degiorgio. "About photon correlations". In: *American Journal of Physics* 81.10 (2013), pages 772–775.

[191] K. Laiho et al. "Measuring higher-order photon correlations of faint quantum light: A short review". In: *Physics Letters A* 435 (2022), page 128059. ISSN: 0375-9601.

[192] Gerassimos A. Athanassoulis and P. N. Gavriliadis. "The truncated Hausdorff moment problem solved by using kernel density functions". In: *Probabilistic Engineering Mechanics* 17 (2002), pages 273–291.

[193] N. I. Akhiezer. *The Classical Moment Problem and Some Related Questions in Analysis*. Philadelphia, PA: Society for Industrial and Applied Mathematics, 2020.

[194] P. Kapitza. "Viscosity of Liquid Helium Below the λ Point". In: *Nature (London)* 141 (1938), page 74.

[195] J. F. Allen and A. D. Misener. "Flow of Liquid Helium II". In: *Nature (London)* 141 (1938), page 75.

[196] L. Landau. "Theory of the Superfluidity of Helium II". In: *Phys. Rev.* 60 (4 Aug. 1941), pages 356–358.

[197] A. Miller, D. Pines, and P. Nozières. "Elementary excitations in liquid helium". In: *Physical Review* 127 (1962), pages 1452–1464.

[198] J Steinhauer et al. "Excitation spectrum of a Bose-Einstein condensate". In: *Physical review letters* 88.12 (2002), page 120407.

[199] Q. Fontaine et al. "Observation of the Bogoliubov Dispersion in a Fluid of Light". In: *Physical Review Letters* 121 (2018), page 183604.

[200] P. Stepanov et al. "Dispersion relation of the collective excitations in a resonantly driven polariton fluid". In: *Nature Communications* 10 (2019), page 3869.

[201] L. P. Sokol. *Bose-Einstein condensation*. Edited by D. W. Snoke A. Griffin and S. Stringari. Cambridge University Press, 1995, page 51.

[202] K. Xu et al. “Observation of Strong Quantum Depletion in a Gaseous Bose-Einstein Condensate”. In: *Physical Review Letters* 96 (2006), page 180405.

[203] Tsin D Lee, Kerson Huang, and Chen N Yang. “Eigenvalues and eigenfunctions of a Bose system of hard spheres and its low-temperature properties”. In: *Physical Review* 106.6 (1957), page 1135.

[204] Nir Navon et al. “The equation of state of a low-temperature Fermi gas with tunable interactions”. In: *Science* 328.5979 (2010), pages 729–732.

[205] Thomas G Skov et al. “Observation of a Lee-Huang-Yang Fluid”. In: *Physical Review Letters* 126.23 (2021), page 230404.

[206] Lev Davidovich Landau and Evgenii Mikhailovich Lifshitz. *Quantum mechanics: non-relativistic theory*. Volume 3. Pergamon Press, 1977.

[207] Jean Dalibard. “Les interactions entre atomes froids dans les gaz quantiques (II)”. In: *Cours du Collège de France* (2022).

[208] David C Burnham and Donald L Weinberg. “Observation of simultaneity in parametric production of optical photon pairs”. In: *Physical Review Letters* 25.2 (1970), page 84.

[209] M. Greiner et al. “Probing Pair-Correlated Fermionic Atoms through Correlations in Atom Shot Noise”. In: *Physical Review Letters* 94 (2005), page 110401.

[210] G Arnison and al. “First observation of correlations between high transverse-momentum charged-particules in events from the CERN proton and anti-proton collider”. In: *Physical letters* 118 (1982), page 173.

[211] Lev Pitaevskii and Sandro Stringari. “Uncertainty principle, quantum fluctuations, and broken symmetries”. In: *Journal of low temperature physics* 85.5-6 (1991), pages 377–388.

[212] L Mathey, A Vishwanath, and E Altman. “Noise correlations in low-dimensional systems of ultracold atoms”. In: *Physical Review A* 79.1 (2009), page 013609.

[213] J. Bardeen, L. N. Cooper, and J. R. Schrieffer. “Theory of Superconductivity”. In: *Physical Review* 108 (5 1957), pages 1175–1204.

[214] R Chang et al. “Momentum-resolved observation of thermal and quantum depletion in a Bose gas”. In: *Physical review letters* 117.23 (2016), page 235303.

[215] M Krämer, L Pitaevskii, and S Stringari. “Macroscopic dynamics of a trapped Bose-Einstein condensate in the presence of 1D and 2D optical lattices”. In: *Physical review letters* 88.18 (2002), page 180404.

[216] C. K. Hong, Z. Y. Ou, and L. Mandel. “Measurement of subpicosecond time intervals between two photons by interference”. In: *Phys. Rev. Lett.* 59 (18 Nov. 1987), pages 2044–2046.

[217] Salvatore Butera, David Clément, and Iacopo Carusotto. “Position-and momentum-space two-body correlations in a weakly interacting trapped condensate”. In: *Physical Review A* 103 (2021), page 013302.

[218] G Baym. “The physics of Hanbury-Brown and Twiss intensity interferometry : from stars to nuclear collisions”. In: *Acta. Phys. Pol. B* 29 (1998), pages 1839–1884.

[219] William Oliver et al. “Hanbury Brown and Twiss-Type Experiment with Electrons”. In: *Science* 284 (Apr. 1999), pages 299–301.

[220] B Yurke and M Potasek. "Obtainment of thermal noise from a pure quantum state". In: *Physical Review A* 36.7 (1987), page 3464.

[221] D. F. Walls and G. J. Milburn. *Quantum Optics*. Springer-Verlag, Berlin, 2008.

[222] R. Loudon and P. L. Knight. "Squeezed light". In: *Journal of Modern Optics* 34 (1987), page 709.

[223] XY Zou, LJ Wang, and L Mandel. "Violation of classical probability in parametric down-conversion". In: *Optics communications* 84.5-6 (1991), pages 351–354.

[224] J Esteve et al. "Squeezing and entanglement in a Bose–Einstein condensate". In: *Nature* 455.7217 (2008), pages 1216–1219.

[225] L. Pezzè et al. "Quantum metrology with nonclassical states of atomic ensembles". In: *Reviews of Modern Physics* 90.3 (2018), page 035005.

[226] W. G. Unruh. "Experimental Black-Hole Evaporation?" In: *Phys. Rev. Lett.* 46 (21 May 1981), pages 1351–1353.

[227] D. Boiron et al. "Quantum Signature of Analog Hawking Radiation in Momentum Space". In: *Phys. Rev. Lett.* 115 (2 July 2015), page 025301.

[228] Xavier Busch and Renaud Parentani. "Quantum entanglement in analogue Hawking radiation: When is the final state nonseparable?" In: *Physical Review D* 89.10 (2014), page 105024.

[229] Mark Kasevich and Steven Chu. "Atomic interferometry using stimulated Raman transitions". In: *Physical review letters* 67.2 (1991), page 181.

[230] Raphael Lopes et al. "Atomic hong–ou–mandel experiment". In: *Nature* 520.7545 (2015), pages 66–68.

[231] Peter J Martin et al. "Bragg scattering of atoms from a standing light wave". In: *Physical review letters* 60.6 (1988), page 515.

[232] P. E. Sokol and W. M. Snow. *Momentum Distributions in Liquid Helium*. Edited by A. F. G. Wyatt and H. J. Lauter. Boston, MA: Springer US, 1991, pages 47–58. ISBN: 978-1-4684-5937-1.

[233] H. R. Glyde, R. T. Azuah, and W. G. Stirling. "Condensate, momentum distribution, and final-state effects in liquid ^{4}He". In: *Phys. Rev. B* 62 (21 Dec. 2000), pages 14337–14349.

[234] H. R. Glyde et al. "Atomic momentum distribution and Bose-Einstein condensation in liquid ^{4}He under pressure". In: *Phys. Rev. B* 84 (18 Nov. 2011), page 184506.

[235] M. Kira. "Hyperbolic Bloch equations: Atom-cluster kinetics of an interacting Bose gas". In: *Annals of Physics* 356 (2015), pages 185–243. ISSN: 0003-4916.

[236] S. Giorgini, J. Boronat, and J. Casulleras. "Ground state of a homogeneous Bose gas: A diffusion Monte Carlo calculation". In: *Phys. Rev. A* 60 (6 Dec. 1999), pages 5129–5132.

[237] Raphael Lopes et al. "Quasiparticle Energy in a Strongly Interacting Homogeneous Bose-Einstein Condensate". In: *Phys. Rev. Lett.* 118 (21 May 2017), page 210401.